

EXPLORING PROPERTY-STRUCTURE-PERFORMANCE RELATIONSHIP FOR ADDITIVE MANUFACTURED Ti-6Al-4V ALLOY THROUGH EXPERIMENTAL STUDIES

ALOK GUPTA
(BEng, MSc, CEng, FIMechE, CPhys, MInstP)

Thesis submitted to The University of Nottingham
for the Degree of Doctor of Philosophy

Department of Mechanical, Materials and Manufacturing Engineering
University of Nottingham

August 2022

ABSTRACT

Additive Manufacturing (AM) offers design freedom and ability to fabricate parts of complex shapes which are not often possible with the conventional methods of manufacturing. AM has gained a widespread attention within the aerospace and bio-medical industries to make parts in Ti-6Al-4V, an $\alpha + \beta$ alloy. A thorough understanding of the relationship between the AM process, microstructure, mechanical and fatigue properties, and performance of AM parts is therefore critical to establish AM as an alternative and preferred route to manufacture safety critical parts. The AM components designed for aerospace applications need to be compliant against the certification requirements of EASA (e.g. CS-E 650, CS-E 810 and CS-E100). Therefore, the main purpose of this research study was to verify that the carefully designed weight optimised AM bracket meets the targeted fatigue performances under LCF and HCF loadings to be in line with the aerospace standards and to build confidence amongst the practicing engineers, researchers and certification authorities to adopt this novel technology for safety critical applications such as the aerospace.

To achieve this objective, the main focus of the present study was thus to analyse the mechanical and fatigue properties of Powder Bed Fusion Ti-6Al-4V through a series of experiments performed at specimen and component levels, and to evaluate the effect of characteristic microstructure, defects, surface roughness, micro-hardness and characteristic features present on the fracture surfaces of the specimen and component, on these properties. Firstly, the tensile behaviour of Ti-6Al-4V was studied for both Electron Beam Powder Bed Fusion (EPBF) and Laser Powder Bed Fusion processes (LPBF), at Room Temperature (RT) and at Elevated Temperatures (ETs), and at two different strain rates. The characterisation of defects and its role in relation to the mechanical strength of the EPBF and LPBF Ti-6Al-4V has also been presented.

Further, for the first time, this research presents a detailed investigation on the Low Cycle Fatigue (LCF) and High Cycle Fatigue (HCF) performances of an aero-engine LPBF Ti-6Al-4V bracket in struts and connectors design. The novel bracket design was tested for its fatigue performance which was evaluated in relation to the fatigue behaviour of LPBF Ti-6Al-4V, tested at RT and at ETs. Additionally, the cyclic softening behaviour seen during the LCF testing of LPBF Ti-6Al-4V was studied in detail to understand and identify the micro-mechanisms responsible for cyclic softening. The features of fracture surface and evolution of microstructure and dislocation density near the fracture surface have also been discussed.

For machined EPBF Ti-6Al-4V, decrease in tensile strengths but increase in material ductility were observed for the tests at ETs on machined specimens. The poor surface finish of the as-built specimen and presence of defects are the two significant contributors to reduce material ductility of as-built EPBF Ti-6Al-4V at ETs. Furthermore, the tensile strengths of LPBF Ti-6Al-4V were higher, owing to its fine microstructure with α' needles in high aspect ratio, but the ductility was lower than the EPBF Ti-6Al-4V. Orientation of defects and columnar β grains in the microstructure of PBF Ti-6Al-4V causes anisotropy in material properties.

During cyclic deformation, formation of Low Angle Boundaries inside the prior α' grains, progressively leads to nucleation and eventually to fracture. With increase in fatigue cycles, the free dislocation density increases resulting into cyclic softening of LPBF Ti-6Al-4V. It was found that the bracket in struts and connectors design for aerospace application has redundancies in the load paths due to its particular design and it meets the set performance targets, in terms of number of cycles to failure and its g capability against the LCF and HCF test loading conditions, respectively.

Finally, a fatigue crack growth life prediction method which considers the small crack growth behaviour, has also been proposed. The proposed method includes a Finite Element based crack growth simulation and the calculations utilise an approach based on the modified NASGRO equation.

ACKNOWLEDGEMENTS

First, I would like to acknowledge the support and motivation given by my supervisors, Dr Chris Bennett and Prof. Wei Sun. Their expert advice, guidance and continuous support during my studies were fundamental for me to complete this research study and the thesis. Both my supervisors have been the beacon of light cutting through the dark. Their 'keep going' approach has made me to sail through the several difficult situations throughout this course.

I would like to give my sincere thanks to Rolls Royce Plc., UK for sponsoring my PhD. My sincere thanks to Dr Rob Mitchell (Head of Engineering, ITP Aero UK, Hucknall) for his encouragement towards my professional development. Also, my sincere thanks to my friends Mr. Daniel Cousins, Dr Jian Ding and Mr. Ulaganathan, for providing encouragement to keep my motivation going during the entire period of my studies.

I would like to extend my sincere thanks to my university staff Dr Nigel Neate, Dr Elisabeth Steer, Dr Marco Simonelli and Mr. Jason Greaves, and to all other technicians of the Workshop for their kind support towards the laboratory examinations and preparation of specimens. The technical support with the experiments provided by Mr. Shane Maskill is greatly acknowledged.

Father is like a banyan tree which provides shade to the people for them to feel safe and protected. In its absence, one feels alone, lost and at the mercy of people surrounding like I felt when my father had passed away. My sincere gratitude to my father (Late Shri Jitendra Kumar Gupta), a quiet influencer, who inspired me to live a simple and honest life and to put best efforts and achieve excellence in my professional and personal lives. Also, my gratitude to my mother (Smt. Sarala Gupta) who have always been close to my heart and passing on the attributes like adaptability, decisiveness, and situational awareness.

My greatest thank to my lovely wife Pragati Gupta, a kinder, for her friendship, encouragement, deep care and concern for my health during the PhD course. Thank you Pragati for being a brilliant partner and for being with me all the time and helping me to achieve a work-life balance which was difficult at times to maintain during the course. A special mention to both my lovely children Aprova Varshney and Riddhima Varshney whose presence in the house has kept energising me.

LIST OF PUBLICATIONS

[1] A. Gupta, W. Sun, C.J. Bennett, Simulation of fatigue small crack growth in additive manufactured Ti–6Al–4V material, Continuum Mechanics and Thermodynamics 32 (2020) 1745–1761. https://doi.org/10.1007/s00161-020-00878-0.

[2] A. Gupta, C.J. Bennett, W. Sun, The role of defects and characterisation of tensile behaviour of EBM additive manufactured Ti-6Al-4V : An experimental study at elevated temperature, Engineering Failure Analysis (2020) 105115. https://doi.org/10.1016/j.engfailanal.2020.105115.

[3] D. Li, M. Li, D. Shang, A. Gupta, W. Sun, Physically-based modeling of cyclic softening and damage behaviors for a martensitic turbine rotor material at elevated temperature, International Journal of Fatigue 142 (2021) 105956. https://doi.org/10.1016/j.ijfatigue.2020.105956.

[4] A. Gupta, C.J. Bennett, W. Sun, Fatigue response of selective laser melted Ti-6Al-4V bracket: an experimental study, Procedia Structural Integrity 31 (2021) 15–21. https://doi.org/10.1016/j.prostr.2021.03.004.

[5] A. Gupta, C.J. Bennett, W. Sun, Fatigue property-performance relationship of additively manufactured Ti-6Al-4V bracket for aero-engine application: An experimental study, Procedia Structural Integrity 38 (2021) 40–49. https://doi.org/10.1016/j.prostr.2022.03.005.

[6] A. Gupta, C.J. Bennett, W. Sun, An experimental investigation on the progressive failure of an additively manufactured Laser Powder Bed Fusion Ti-6Al-4V aero-engine bracket under Low Cycle Fatigue, Engineering Failure Analysis 139 (2022) 106455. https://doi.org/10.1016/j.engfailanal.2022.106455.

[7] A. Gupta, C.J. Bennett, W. Sun, High Cycle Fatigue performance evaluation of a laser powder bed Fusion Manufactured Ti-6Al-4V Bracket for Aero-Engine Applications, Engineering Failure Analysis 140 (2022) 106494. https://doi.org/10.1016/j.engfailanal.2022.106494.

[8] A. Gupta, C.J. Bennett, W. Sun, N. Neate, On the microstructural evolution and failure mechanism in laser powder bed fusioned Ti-6Al-4V during low cycle fatigue at room and elevated temperatures, J. Mater. Res. Technol. 21 (2022) 4299–4319. https://doi.org/10.1016/j.jmrt.2022.10.141.

[9] A. Gupta, C.J. Bennett, W. Sun, Low cycle fatigue performance of SLM Ti-6Al-4V aero-engine bracket at 200°C: An experimental study, Procedia Structural Integrity, under publication.

[10] A. Gupta, C.J. Bennett, W. Sun, Evaluation of elevated temperature low cycle fatigue performance of a LPBF Ti-6Al-4V aero-engine bracket through an experimental study, Engineering Failure Analysis, currently being drafted.

CONFERENCES

Conferences with Presentation

1. 29th International Workshop on Computational Mechanics of Materials (IWCMM29), September 15-19 2019.

2. ICSID 2020: 4th International Conference on Structural Integrity and Durability, September 15-18 2020 and Summer School 14-15 September 2020.

3. 2021 Cornerstone Prosperity Partnership & Doctoral Training Conference, Mechanical Engineering Science to Enable Aero Propulsion Futures is a co-investment by Rolls-Royce, EPSRC, Imperial College, Nottingham and Oxford University Technology Centres, 28th June to 30th of June, Online.

4. ICSID 2021: 5th International Conference on Structural Integrity and Durability, September 7-10- 2021 and Summer School 6-7 September 2021.

5. Fatigue Design 2021, 17 & 18 November 2021, Senlis, France,

6. 12th EASN International Conference on "Innovation in Aviation & Space for opening New Horizons" 18 - 21st of October 2022, Barcelona, Spain.

Conferences with Attendance only

7. 2020 Conference on Advancing Analysis & Simulation in Engineering (CAASE20). Virtual Conference, NAFEMS, 16th of June – 18th of June 2020.

8. Additive Manufacturing for Aerospace and Space, 23-25th Feb 2021, Virtual Organiser: Defence IQ.

Trainings Attended

9. Robust design for analysts (through R-R)

10. Lean Six Sigma Green Belt (through R-R)

LIST OF ABBREVIATIONS

3D	Three Dimensional
AB	As-Built
AC	Air Cooling
ACR	Adjusted Compliance Ratio
AFM	Abrasive Fluid Machining
ALM	Additive Layer Manufacturing
AM	Additive Manufacturing
AN	Annealing
ASTM	American Society for Testing and Materials
BA	Beta (β) Annealing
BCC	Body Centred Cubic
BCV	Beam Current Value
BOR	Burgers Orientation Relationship
BTF	Buy to Fly
CAD	Computer Aided Design
CAGR	Compound Annual Growth Rate
CBO	Core Blade Off
CCF	Current Compensation Function
CCV	Calculated Current Value
CDM	Continuum Damage Mechanics
CP	Cavitation Peening
CRSS	Critical Resolved Shear Stress
CT	Computed Tomography
DA	Duplex Annealing
DED	Direct Energy Disposition
DMLS	Direct Metal Laser Sintering
DR	Displacement Rate
EASA	European Aviation Safety Agency
EB	Electron Beam
EBM	Electron Beam Melting
EBSD	Electron backscatter diffraction

EIFS	Equivalent Initial Flaw Size
ELI	Extra Low Interstitial
EPBF	Electron Beam Powder Bed Fusion
ET	Elevated Temperature
FAA	Federal Aviation Administration
FBO	Fan Blade Off
FC	Furnace Cooling
FCC	Face Centred Cubic
FCG	Fatigue Crack Growth
FDT	Fatigue and Damage Tolerance
FE	Finite Element
FEM	Finite Element Method
FEG-SEM	Field Emission Gun Scanning Electron Microscope
FOV	Focus Offset Value
FRC	Frequency Response Curve
HCF	High Cycle Fatigue
HCP	Hexagonal Closed Pack
HIP	Hot Isostatic Pressing
HT	Heat Treatment
IC	Investment Casting
IOS	Interlayer Offset Staggered
IPF	Inverse Pole Figure
ISO	International Organisation for Standardization
KAM	Kernel Average Misorientation
KT	Kitagawa-Takahasi
LAB	Low Angle Boundaries
LCF	Low Cycle Fatigue
LEFM	Linear Elastic Fracture Mechanics
LENS	Laser Engineering Net Shaping
LOF	Lack of Fusion
LOV	Line Offset Value
LPBF	Laser Powder Bed Fusion
LSF	Laser Solid Form

LSP	Laser Shock Peening
LVDT	Linear Variable Differential Transformer
MC	Machined
MCV	Maximum Current Value
MP	Machined or Machined Polished
MRO	Maintenance Repair and Overhaul
NDT	Non-Destructive Test
OEM	Original Equipment Manufacturer
OoB	Out of Balance
OL	Oxygen Layer
ODZ	Oxygen Diffusion Zone
OS	Orthogonal Staggered
PBF	Powder Bed Fusion
PBG	Prior Beta Grain
PS	0.2% Proof Strength
R-R	Rolls Royce Plc.
RT	Room Temperature
SB	Sand Blasting
SEM	Scanning Electron Microscope
SIF	Stress Intensity Factor
SFC	Specific Fuel Consumption
SLM	Selective Laser Melting
SMaRT	Separating Morphing and Adaptive Remeshing Technology
SP	Shot Peened
SR	Strain Rate
SRE	Strain Range
SRL	Stress Relieving
STA	Solution Treatment and Aging
STR	Strength Ratio
SWT	Saw Tooth
TRL	Technology Readiness Level
UTS	Ultimate Tensile Strength
VP	Vibratory Polished

VMH	Vickers Micro-Hardness
WQ	Water Quenching

Note: Where s is added to an abbreviation as suffix it indicates a plural quantity.

CONTENTS

Abstract i

Acknowledgements iii

List of Publications iv

Conferences v

Abbreviations vi

Contents x

1 Introduction 1

1.1 Aims and Objectives 3
1.2 Thesis Structure 5

2 Literature Review 6

2.1 Powder Bed Fusion Process: Additive Manufacturing of Ti-6Al-4V 6
2.1.1 Laser Powder Bed Fusion (LPBF) Process 6
2.1.2 Electron Beam Powder Bed Fusion (EPBF) Process 8

2.2 Physical Characterisation of Ti-6Al-4V 9
2.2.1 Material Composition of Ti-6Al-4V 9
2.2.2 Crystallographic Information of Ti-6Al-4V 10
2.2.3 Microstructure and Phases 12

2.3 Issues related to AM Process 16
2.3.1 Smoking 16
2.3.2 Oxygen Content and Oxygen Layer in Ti-6Al-4V 17
2.3.3 Defects 19
2.3.4 Surface Roughness 25
2.3.5 Residual Stresses 28
2.3.6 Heat Treatment and Microstructure of AM Ti-6Al-4V 29
2.3.7 Texture and Anisotropy 31

2.4 Tensile Behaviour of AM Ti-6Al-4V 35
2.5 Fatigue Behaviour of Ti-6Al-4V 41
2.6 Crack Growth Behaviour of AM Ti-6Al-4V 45
2.6.1 Regime 1: Near Threshold Properties (ΔK_{th}) 46
2.6.2 Regime 2: Fatigue Crack Growth Properties (C and m) 47
2.6.4 Regime 3: Fracture Toughness (ΔK_{IC}) 47
2.7 AM Components for Aerospace Application 52
2.8 Applications to Aerospace 56
2.9 Knowledge Gaps and Opportunities 61

3 Materials and Methods 63

3.1 Materials 64
3.1.1 EPBF Specimen Manufacturing 64
3.1.2 LPBF Specimens and Bracket Manufacturing–Phase 2 64
3.1.3 LPBF Specimens and Bracket Manufacturing–Phase 3 65
3.2 Physical Characterisation 65
3.2.1 Material Microstructure 65
3.2.2 Surface Roughness 66
3.2.3 Defects Distribution 66
3.2.4 Micro-Hardness Mapping 67
3.3 Manufacturing Details 68
3.3.1 Phase 1: EPBF Specimens 68
3.3.2 Phase 2: LPBF Test Specimens and Bracket 69
3.3.2.1 Dog-Bone Specimens – Tensile Testing 69
3.3.2.2 Dog-Bone Specimens – LCF Testing 70
3.3.2.3 Dog-Bone Specimens – HCF Testing 70
3.3.2.4 Brackets 71
3.3.3 Phase 3: LPBF Test Specimens and Bracket 73
3.3.3.1 Dog-Bone Specimens 73
3.3.3.2 Bracket 73
3.4 Test Matrix and Testing Details 73
3.4.1 Phase 1: EPBF Tensile Tests 73
3.4.2 Phase 2 and Phase 3: LPBF Test Campaign 75
3.4.2.1 Tensile Tests 75
3.4.2.2 Low Cycle Fatigue Testing 76
3.4.2.3 High Cycle Fatigue Testing 79

4 Tensile Behaviour of EPBF Ti-6Al-4V 86

4.1 Tensile Test Results 86
4.2 Characterization 89
4.2.1 Microstructure 89
4.2.2 Defects 90
4.2.3 Fractography 93
4.2.4 Hardness Mapping 94
4.3 Discussion 96
4.3.1 Effect of Strain Rate 96
4.3.2 Effect of Temperature 96
4.3.3 Effect of Build Orientation 97
4.3.4 Effect of Surface Roughness 97
4.3.5 Role of Defects 99
4.3.6 Role of Microstructure and Crystallographic Texture 100
4.4 Further Discussion 105
4.5 Conclusions 105

5 Tensile Behaviour of LPBF Ti-6Al-4V 108

5.1 Tensile Test Results 108
5.2 Characterization 111
5.2.1 Macrostructure and Microstructure 111
5.2.2 Defects 113
5.2.3 Fractography 114
5.2.4 Hardness Mapping 116
5.3 Discussion 117
5.3.1 Effect of Strain Rate 117
5.3.2 Effect of Temperature 118
5.3.3 Effect of Surface Roughness 118
5.3.4 Role of Defects 119
5.3.5 Role of Microstructure 119
5.4 Conclusions 120

6 LCF Behaviour of LPBF Ti-6Al-4V at Specimen Level 122

6.1 Test Results 124
6.1.1 Test at RT 124
6.1.2 Test at ET 125
6.1.3 Cyclic Softening 128
6.2 Discussion 128
6.2.1 Fractography 128
6.2.2 Evolution of Low Angle Boundaries and Increase in Free Dislocation Density 130
6.2.3 Changes in Micro-hardness 133
6.2.4 Effect of Temperature and SRE 135
6.2.5 Defects in LCF Tested Samples 137
6.2.6 Additional Considerations 138
6.3 Conclusions 139

7 LCF Performance of LPBF Ti-6Al-4V Aeroengine Bracket at RT 140

7.1 Test Results 141
7.2 Discussion 143
7.2.1 Fractography 143
7.2.2 KAM Distribution Plots 145
7.3 Conclusions 147

8 LCF Performance of LPBF Ti-6Al-4V Aeroengine Bracket at ET 148

8.1 Test Results 148
8.2 Discussion 149
8.2.1 Microstructure Characterization 149
8.2.2 Fractography 149
8.2.3 KAM Distribution Plots 152
8.2.4 Additional Considerations 153

8.3 Conclusions 153

9 High Cycle Behaviour of LPBF Ti-6Al-4V 155

9.1 HCF Test Results 157
9.1.1 Uniaxial HCF Tests at RT 157
9.1.2 Uniaxial HCF Tests at ET 157
9.1.3 Shaker table Tests at RT 158
9.2 Discussion 160
9.2.1 Fractography of Failed Bracket Struts 160
9.2.2 g Load Capability and Compliance against the Design Target 161
9.2.3 Micro-Hardness and Fatigue Limit Relationship 163
9.2.4 Safe Life Design Curve 164
9.3 Conclusions 166

10 Simulation of Fatigue Small Crack Growth 168

10.1 Introduction 168
10.2 Small Crack Growth Behaviour and Modified NASGRO Equation 169
10.3 FE Based Crack Growth Simulation and Lifing Calculation 171
10.3.1 Source of Material, Additive Process and Experimental Data 172
10.3.2 Small Crack Growth Data 173
10.3.3 FE Based Crack Growth Simulation 174
10.3.4 Small Crack Growth Lifing Calculation 176
10.4 Results and Discussion 177
10.4.1 Case A: No Internal Designed Defect, Crack Initiating at the Surface 177
10.4.2 Case B: With Internal Designed Defect of Cylindrical Shape, Crack Initiating at the Surface 180
10.4.3 Case C: With Internal Designed Defect of Cylindrical Shape, Crack Initiating at the Cylindrical Defect 181
10.5 Conclusions 183

11 Conclusions and Future Works 185

11.1 Conclusions 185
11.2 Future Work 186

References 189

CHAPTER 1

1 Introduction

The American Society for Testing and Materials (ASTM) has defined Additive manufacturing (AM) as "a process of joining materials to make objects from three Dimensional (3D) model data, usually layer by layer, as opposed to subtractive manufacturing methodologies [1]. The typical synonyms for AM process are 'Free Form Fabrication', 'Additive Layer Manufacturing (ALM)', '3D Printing', 'Additive Fabrications', 'Additive Processes/Techniques', 'Rapid Prototyping', 'Near Net Shape Fabrications' etc. Over the past 10 years, the AM industry has seen an average growth of 27.5% to nearly US$ 12.8 billion in 2020 [2]. Where the total revenue for independent service providers worldwide within the AM industry grew to nearly US$ 5.3 billion in 2020 [2]. With recent technological advancement, this technology is now being widely used within the industry utilising metals and polymers because of its several benefits including (but not limited to): Freedom of design with ability to manufacture complex structures, mass customisation, minimisation of material waste and as well as fast prototyping [3]. In addition, the AM enables designers and engineers to create unique and bespoke products, where conventional assemblies can be redesigned in a single complex structure in functional geometries that can be manufactured at low volumes in an economical, environment friendly and ecologically promising way [4]. In addition, the AM additive manufacturing offers opportunities to do repair of used costly parts, and fabricate customized parts on demand at remote locations, thus reducing the overall inventory cost [5].

Ti-6Al-4V, an α + β titanium alloy, has a wide range of applications in aerospace, automobile, chemical, marine, energy and medical industries. In Ti-6Al-4V, both α and β microstructural phases coexist at room temperature, offering the combination of the strength of α alloys and the ductility of β alloys [6, 7]. The microstructure of the alloy and the properties can be suitably varied by performing heat treatment and thermo-mechanical processing [8]. Due to its high strength to weight ratio, Ti-6Al-4V is being increasingly used to make weight sensitive parts [7]. AM of Ti-6Al-4V, an alloy which accounts for nearly half of the Ti market share around the world, is of interest in aerospace industry due to its elevated set of physical, mechanical and metallurgical properties, corrosion resistance and its galvanic compatibility with composites [7, 8]. High fuel costs, continuous demand for efficiency improvement, growing demand of new aircrafts (commercial, military and private jets), and stringent environmental standards (i.e. less noise pollution and less CO_2 emission) and recyclability of materials are the few factors which continuously demands that the aero engine parts are designed using Ti-6Al-4V alloy [9].

However, to fully exploit the above listed benefits and capabilities of AM processes, the structural integrity of parts fabricated using AM must be understood and fully characterized. Although, the complex geometries and assemblies using AM may be possible to design through topological optimization, the mechanical behaviour of AM parts and overall trustworthiness is not yet fully studied and reported in detail. This is causing a widespread delay in a confident deployment of AM in

aerospace, biomedical and automotive industries [5]. Furthermore, the mechanical and fatigue properties of AM parts may vary from the parts manufactured using the conventional methods of manufacturing. The powder used in AM process may have higher degree of variation of quality, porosity, cleanliness, shape/size, etc. The AM process itself involves highly localized heating and cooling. Higher cooling rates and complex thermal history during the AM process leads to material microstructures evolving under the non-equilibrium conditions, ending with significant anisotropy, potentially significant residual stresses and distortion. The tracks and layers being deposited are subjected to repeated heating and remelting during the build, producing defects such as spherical pores, lack of fusion voids and un-melted powder, which could serve as the fatigue crack initiation sites and significantly influence fatigue behaviour [5]. Therefore, the data gathered in the laboratory environment may not be fully representative of the fatigue performance of AM part, even when built using the same process parameters. Lack of standardization, in terms of process and manufacturability of specimens and parts, could cause variation in mechanical properties, fatigue properties and performance of AM parts. Hence to gain repeatability and consistent performance and also to increase reliability and durability of the product, this variation needs to be minimised and statistically understood. Furthermore, there may be differences between performance results of testing AM coupons and of AM functional component, which need to be accounted for by means of property–performance relationships, and this becomes a necessity for certification of AM structural components [5].

The AM components designed for aerospace applications need to be compliant against the certification requirements of EASA (e.g. CS-E 650, CS-E 810 and CS-E100). Therefore, the main aim of this research study was to verify that the carefully designed weight optimised AM bracket meets the targeted fatigue performances under LCF and HCF loadings (against EASA CS-E 650 requirements), to be in line with the aerospace standards. Therefore, to achieve this aim, to make this research study relevant to the aero-engine application and be in line with the AM strategy of Rolls Royce Plc. (R-R), the testing campaign under this research includes the mechanical, Low Cycle Fatigue (LCF) and High Cycle Fatigue (HCF) testings on AM Ti-6Al-4V, both at specimen and at component levels. This experimental study starts with a mechanical testing on the Electron Beam Powder Bed Fusion (EPBF) Ti-6Al-4V specimens. All subsequent experimental studies were on the Laser Powder Bed Fusion (LPBF) Ti-6Al-4V specimens, where the experimental results were analysed for its mechanical strength and LCF and HCF properties, both at Room temperature (RT) and at Elevated Temperature (ET). Furthermore, the LCF and HCF performances of LPBF Ti-6Al-4V at component level were studied using a weight optimised LPBF Ti-6Al-4V bracket which was designed for aero-engine application. The mechanical and fatigue studies on EPBF and LPBF processed Ti-6Al-4V were comprehended using the results of material composition, examination of microstructure, analysis of fracture surface, presence of defects and material micro-hardness.

1.1 Aims and Objectives

The main aim of this research study was to demonstrate that the carefully designed weight optimised AM bracket in Ti-6Al-4V would be acceptable under the EASA requirements (e.g. EASA CS-E 100 and CS-E 650 requirements) and also to explore the property-structure-performance relationship for AM Ti-6Al-4V, particularly for LPBF Ti-6Al-4V. Therefore, to achieve this aim, the main objectives of this research studies were set as follows:

- Firstly, explore the mechanical properties (0.2% Proof Strength (PS), Ultimate Tensile Strength (UTS) and Ductility) of EPBF and LPBF processed Ti-6Al-4V at specimen level at RT and at ET. Study the material microstructure, micro-hardness and role of defect of Ti-6Al-4V obtained from the two Powder Bed Fusion (PBF) processes and relate it to the observed mechanical properties. Study the effect of temperature, strain rate, build orientation and surface roughness. Examine the fracture surfaces of the specimens and identify the critical features responsible for causing the respective type of failures in the EPBF and LPBF specimens.
- Explore the LCF test performances of LPBF Ti-6Al-4V at specimen level at RT and at ET. Study the microstructural mechanisms responsible for material softening observed under the cyclic loading. Analyse the effect of temperature and cyclic strain range on cyclic performance of LPBF Ti-6Al-4V. Examine the fracture surfaces of the LCF tested specimens and identify the critical features responsible for LCF fracture of the specimens.
- Perform a detailed testing and characterisation study to explore the LCF performance of a weight optimised LPBF bracket, designed to support a sensor unit on an aeroengine, at RT and ET. Link the LCF performance of the bracket to the desired performance targets needed for the typical LCF load case experienced by the bracket during engine normal operation and under an extreme event defined for the aeroengine component design and certification.
- Perform HCF test on LPBF Ti-6Al-4V at specimen level at RT and ET. Perform shaker table testing to study the HCF performance of the LPBF bracket at RT to demonstrate fatigue performance of the bracket under vibratory loading. Based on the test results, check the HCF test performance of the LPBF Ti-6Al-4V bracket against the initially set design objectives and determine the vibration g load capability of the bracket in order to ensure that the g capability of the bracket is higher than the target g capability defined in the engine vibration spectra for accessories.
- To analyse the crack growth behaviour of AM Ti-6Al-4V parts with presence of small cracks (defects), suggest a crack growth life prediction method which effectively considers the small crack growth behaviour.
- Ensure that the results and outcome of the research study have been peer reviewed and bought off by R-R, the end customer.

1.2 Thesis Structure

Based on all the studies performed under this research work, this thesis is structured as follows:

- Firstly, a detailed literature review on the mechanical, fatigue and crack growth properties of EPBF and LPBF Ti-6Al-4V, performance of AM parts and physical characterisation of AM Ti-6Al-4V is presented in detail in Chapter 2. Additionally, the use of AM together with the key challenges and benefits of AM for the aerospace industry have been discussed. Based on the literature review carried out, this Chapter also highlights the identified knowledge gaps and opportunities which has helped us to establish the aims and objectives of this research study.
- In Chapter 3, the details of Ti-6Al-4V powder, build machines and parameters used for manufacturing of test specimens and brackets, and also the methodologies followed for physical characterisation, including material microstructure, surface roughness, defects distribution, micro-hardness mapping and fracture surface are presented. Furthermore, the details of test methods used for the uniaxial tensile testing, and LCF and HCF testings are also described in this chapter.
- In Chapter 4, the details of test results obtained from mechanical testing together with a detailed discussion on material microstructure, characterisation of defects, material hardness, surface roughness and fracture surface examination, carried out on uniaxial tensile specimens / samples of EPBF Ti-6Al-4V are provided.
- Chapter 5 presents the tensile test results and a discussion covering the material microstructure and characterisation of defects, material hardness, and fracture surface, carried out on uniaxial tensile specimens / samples of LPBF Ti-6Al-4V.
- Based on the results of uniaxial LCF testing, the LCF performance of LPBF Ti-6Al-4V at RT and ET have been discussed in Chapter 6.
- The LCF performance of a weight optimised bracket in the struts and connectors design, made using the LPBF process in Ti-6Al-4V material, was explored through the displacement controlled LCF testing at RT and ET. The results of which together with the characterisation of local microstructure and fracture surfaces are presented in Chapter 7 and Chapter 8 for the component testing at RT and ET, respectively.
- In chapter 9, a detailed discussion on HCF performances of LPBF Ti-6Al-4V has been presented based on the uniaxial HCF testing and the component testing. Also, in Chapter 9, a safe-life regime which links the stress levels with size of defects, was established and recommended to support the property-performance relationship for LPBF component design.
- Chapter 10 presents a small crack growth life prediction method which includes a detailed FE based crack growth simulation and lifing calculations using the modified NASGRO equation and small crack growth data.

- At the end, in Chapter 11 of this thesis, the key conclusions based on the overall results and discussions reported in individual chapters of this thesis are highlighted. This Chapter also provides recommendation for future studies to further investigate and resolve the pending technical issues related to meeting challenges associated with adoption of AM in the aerospace industry.

-----x x x x x x-----

CHAPTER 2

2 Literature Review

According to the International Organisation for Standardization (ISO)/ASTM52900 [10], metallic AM processes could be categorised based on the; (i) material feed stock (e.g, powder bed, powder/wire feed, sheet lamination etc.), (ii) source of energy (Laser, Electron Beam (EB), arc etc.), and (iii) build volume (small vs large volumes) [11].

Out of the seven process categories defined in [10], the PBF and Direct Energy Deposition (DED) processes have made advances in terms of technology readiness levels (TRL) and allow the fabrication of metallic components with near full density [10]. Historically, a number of terms have been used to refer to the various AM processes. Most often a manufacturer would adopt its own term and, in some cases, a registered trademark. The most common terms related to PBF process are outlined in Table 2.1 which have been adapted from the ASTM classifications [12].

Table 2.1. The common terms used in the PBF process [12]

ASTM Classification	AM Process	Machine Manufacturer	Commercial Name
Powder bed fusion	Laser Powder Bed Fusion	EOS	Direct metal laser sintering (DMLS)
		Concept Laser	LaserCUSING
		Renishaw	Selective Laser Melting (SLM)
		Realizer	Selective laser melting
		Phenix	Selective laser melting
		Matsuura	Selective laser melting
	Electron Beam Powder Bed Fusion Process	ARCAM	Electron beam melting

2.1 Powder Bed Fusion Process: Additive Manufacturing of Ti-6Al-4V

This section provides an overview of the LPBF and EPBF processes which are the two most popular PBF methods currently being utilised to manufacture parts for aerospace application [13];

2.1.1 Laser Powder Bed Fusion (LPBF) Process

Amongst the PBF processes, the LPBF process, also known as Selective Laser Melting (SLM), is gaining traction due to its high resolution, higher quality and repeatability of parts, and ability to include fine features with parts in varying sizes and quantities [13]. As shown in the schematic diagram in Fig. 2.1, the LPBF system is composed of powder delivery and energy delivery sub-systems. The powder delivery sub-system has a fabrication piston to supply powder, a coater to create the powder layer, and a piston that holds the fabricated part. The energy delivery sub-system consists of a laser and a scanner system with optics to provide the delivery of a focused spot to each point in the build platform. The build

chamber has a flow of a gas (usually nitrogen or argon) which passes over the powder bed to protect the part from oxygen and to clear any "spatter" and metal fumes developed from the laser path [14]. The high laser power density is used to melt and solidify individual layers of metal powders. The powder feedstock is delivered and coated on to a build platform where powder is selectively melted according to the Computer Aided Design (CAD) deign geometry which subsequently solidifies to form a solid layer [13, 14]. Once a layer is complete, the fabrication piston moves down by a layer thickness and a new layer of powder is spread over it by the coater. The process continues until the entire part is constructed. Upon completion the fabrication piston lifts up the final part when the excess unused powder is brushed away, the part is cut from the substrate and then the part is taken for further processing, machining etc. as required. Post machining/processing, an inspection usually is carried out to check the dimensional accuracy, material quality and for any defects etc. The LPBF process produces AM parts with high precision in a relatively short duration and typically used in the industries with high value components, such as aerospace, where higher performance can provide significant cost savings. The maximum size of the part which can be build is about 300-400 mm with typical minimum feature size ranging between 0.2 - 0.4 mm. The larger LPBF systems with build volumes of 500 x 280 x 850 with multiple laser sources are also now available to provide flexibility to build larger size parts with enhanced productivity [13].

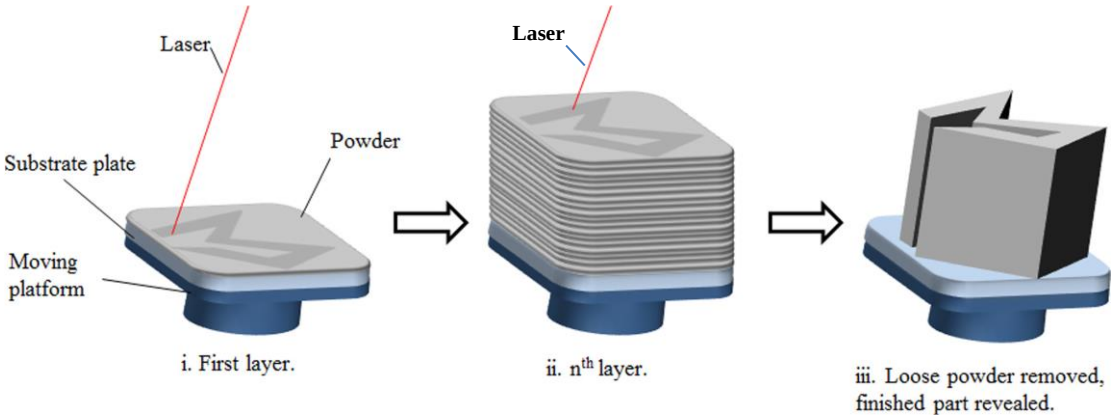


Fig. 2.1. A schematic of LPBF process: (i) first layer being selectively melted, (ii) n_{th} layer being selectively melted, (iii) finished part ready to be removed after removal of powder [14].

Typical process parameters for an EOS M280 LPBF machine for typical applications are as below [15]:

Laser	: Yb (Ytterbium) fibre
Building volume	: 250 x 250 x 325 mm (H)
Laser beam diameter	: 80 μm – (maximum 500 μm)
Scanning speed	: 1400 m/s (maximum 7000 m/s)
Laser power	: 200 W or 400 W
Hatch width	: 5 mm
Hatch spacing	: 100 μm
Average layer thickness	: 20 μm - 100 μm
Environment	: Argon

2.1.2 Electron Beam Powder Bed Fusion (EPBF) Process

In the EPBF process, also known as the Electron Beam Melting (EBM) process, an EB with high kinetic energy of about 60 keV is utilised for selective melting of the metal powder layers, using information received from the CAD models to fabricate 3D parts [16, 17]. As shown in the schematic diagram in Fig 2.2, the EPBF system generally contains a computer controlling system, a tungsten filament for emitting the EB and a powder feeder system. EPBF is a complex metallurgical process related to the interaction of heat source and material and it involves micro-zone melting and cooling at specific rate. This complex metallurgical process makes a microstructure which often differs from those processed by the traditional metallurgical techniques, resulting into different mechanical properties [16]. Since the EB requires vacuum, the vacuum (at 10^{-4} – 10^{-5} mbar) is maintained within the build chamber which also helps to reduce oxygen contamination in metals, such as titanium, which have high affinity towards oxygen. The build plate is preheated via rapid scanning through an EB gun with a typical power of 4 kW, prior to the actual melting taking place aiding to reduce the residual stress in the part [16, 17]. Furthermore, the high scanning speed and high power of the EPBF system offer improved supply chain, providing productivity with shorter build times [17]. The maximum build chamber size of an EPBF system is 350 mm (diameter) x 380 mm (height) [18]. The EPBF process produces functional parts with superior mechanical properties more rapidly and with greater energy efficiency than the laser based AM techniques [16]. However, the EPBF build parts come with larger surface roughness due to larger powder size used in the process. A schematic of EPBF process is shown in Fig. 2.2. The powder stored in powder cassette is brought into the chamber via gravity where it is raked on the build plate to form a powder layer (typically 50 - 70 μm thick). The electron gun emits the EB with a peak power of 3 kW (at a voltage of 60 kV and a current of 1 - 50 mA). The focus of the EB is achieved using a lens and beam deflection coils. To avoid the smoke effect, a small amount of helium gas with a pressure of 10^{-3} mbar is inducted into the build chamber. Each successive layer goes through the following four steps; (i) deposition of new powder layer, (ii) preheating, (iii) melting, (iv) lower down the build plate. After completion of build, the part is cooled down within the build chamber to RT which typically takes 2 h in helium environment [16, 17].

Typical process parameters for an Arcam A2X EPBF machine for typical applications are as below [18]:

Beam	: Electron Beam
Building volume	: 200 x 200 x 380 mm (H)
Beam spot size	: 200 μm – (maximum 1000 μm)
Scanning speed	: up to 8000 m/s
Beam power	: 50 W or (maximum 3000 W) continuously variable
Hatch width	: 5 mm
Line offset	: 100 μm – 500 μm
Average layer thickness	: 50 μm - 200 μm
Environment	: Vacuum

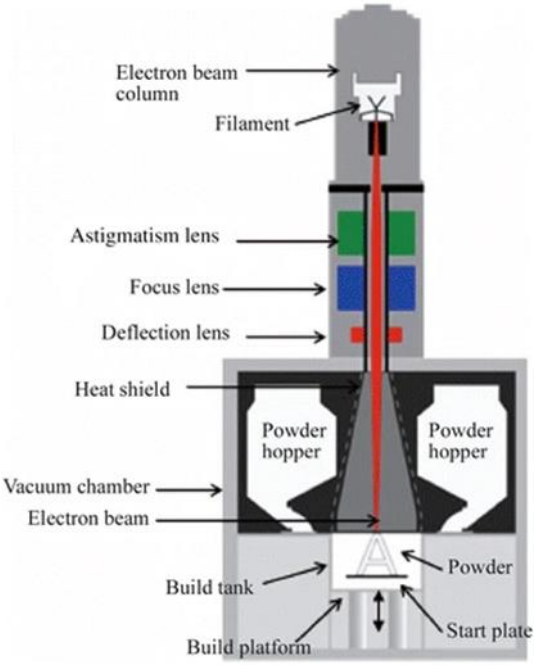


Fig. 2.2. A schematic of EPBF process [17].

2.2 Physical Characterisation of Ti-6Al-4V

2.2.1 Material Composition of Ti-6Al-4V

Ti-6Al-4V features excellent strength, low modulus of elasticity, high corrosion resistance, and good weldability. Different heat treatments (HTs) and thermo-mechanical processing can be deployed to control and, therefore, achieve the desired mechanical properties and volume fraction of the α and β phases in the microstructure of Ti-6Al-4V [19]. In general, Ti-6Al-4V is obtained by alloying pure Ti (~90%) with average 6% wt Aluminium (an α stabiliser) and average 4% wt Vanadium (a β stabiliser). The addition of V causes lowering of transition temperature and therefore a mixture of α + β equilibrium phases is observed in the microstructure of Ti-6Al-4V at RT. ASTM B348 provides standard specifications for titanium and titanium alloy bars and billets and lists a total of 38 different grades of titanium alloy [20]. Ti-6Al-4V grade 5 and grade 23 are the two widely used alloys in the aerospace industry [21]. Ti-6Al-4V (grade 5) is a standard Ti-6Al-4V alloy whereas Ti-6Al-4V (grade 23) is an alloy with Extra Low Interstitial (ELI) elements i.e. with reduced interstitial elements (oxygen and iron) to achieve improved ductility and fracture toughness but with some reduction in strength. The chemical composition of these two grades of Ti-6Al-4V material are prescribed in the Table 2.2 below [20].

Table 2.2. Composition of alloying elements of Ti-6Al-4V material [20]

Ti-6Al-4V	C (max.)	O (max.)	N (max.)	H (max.)	Fe (max.)	Al (range)	V (range)	Other (max)	Ti
Grade 5	0.08	0.35	0.05	0.015	0.4	5.5 – 6.75	3.5 – 4.5	0.4	balance
Grade 23 (ELI)	0.08	0.13	0.03	0.0125	0.25	5.5 – 6.5	3.5 – 4.5	0.4	balance

2.2.2 Crystallographic Information of Ti-6Al-4V

Although titanium has highest strength to weight ratio, due to its higher cost, it is used only in high end niche applications such as the aerospace and biomedical industries [3]. The high reactivity of titanium with oxygen limits the maximum use temperature of titanium alloys to 400°C [22]. Above this temperature, the diffusion of oxygen through the oxide surface layer becomes too fast resulting in excessive growth of oxide layer and embrittlement of the adjacent oxygen rich layer of titanium alloy. The pure titanium has allotropic phase transition at 882°C where it changes from a Body Centered Cubic (BCC) crystal structure (β phase) at higher temperatures to a Hexagonal Close Packed (HCP) crystal structure (α phase) at lower temperatures. The HCP unit cell of α phase is shown in Fig. 2.3(a) and the BCC unit cell of β phase is shown in Fig. 2.3(b). For titanium, the RT lattice parameters as shown in Fig. 2.3(a), are; 'a' = 0.295 nm and 'c' = 0.468 nm giving a 'c/a' ratio of 1.587 (an ideal ratio is 1.633 [21]) for the HCP crystal structure [21]. Also as shown in Fig. 2.3(a) the HCP cell has 3 basal planes denoted by {0001} which are the most densely packed planes, three prismatic planes denoted by $\{10\bar{1}0\}$ and 6 pyramidal planes denoted by $\{10\bar{1}1\}$. The three 'a1', 'a2' and 'a3' axes, separated by 120°, are the closed packed direction with indices $<10\bar{2}0>$. The unit cell of a BCC crystal structure, shown in Fig. 2.3(b), has six most densely packed lattice planes denoted by {110} and the four close packed directions are denoted by <111>. For pure titanium, the lattice parameter value for the BCC structure is a = 0.332 nm [21].

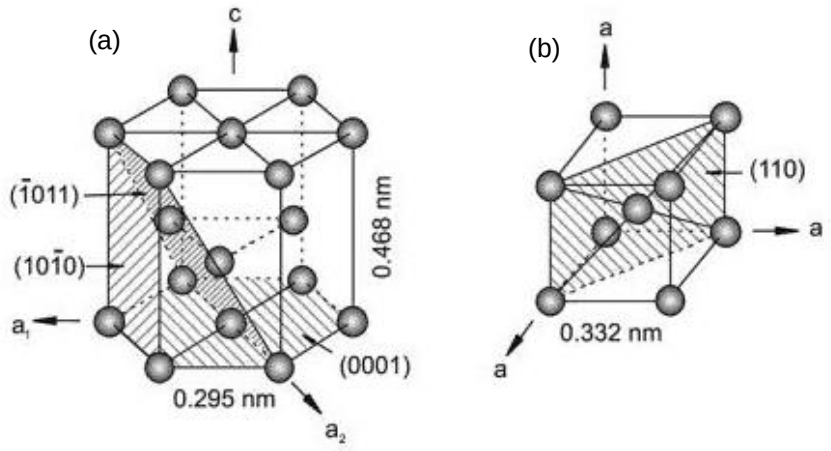


Fig 2.3. Unit cells of: (a) HCP α phase, (b) BCC β phase [21].

The phase composition and the arrangement of phase constituents at the microscopic scale governs the mechanical properties of titanium alloys [21]. The classification of titanium alloys is typically based on the volume fraction of main phases present at RT, which again is dependent on the elemental composition of the titanium alloy. The titanium alloys are, hence, classified into three types, namely, α alloys, β alloys and α + β alloys. These alloys are stabilized by the solute elements that have strong effect on the transformation temperature. Elements increasing the transformation temperature are referred to as the α stabilizers, while the elements that decrease it, thereby increasing the β phase

region, are referred to as the β stabilizers. The most common α stabilizers are Al, O, C and N, whereas many heavy and high melting transition elements, such as Fe, Cr, Nb, Mo, Ta, V, and Si etc. are the β stabilizers. For the β stabilizers, a minimum concentration of β is required to fully stabilize the β phase following a quench from high temperature. The β stabilising elements are divided into β isomorphous elements and β eutectoid forming elements, depending upon the details of the resulting binary phase diagram. Sufficient concentration of isomorphous elements in titanium alloys makes it possible to stabilise β phase at RT. Cr, Si and Fe are the most commonly used β eutectoid forming elements. Fig. 2.4 shows the effect of alloying elements on phase composition.

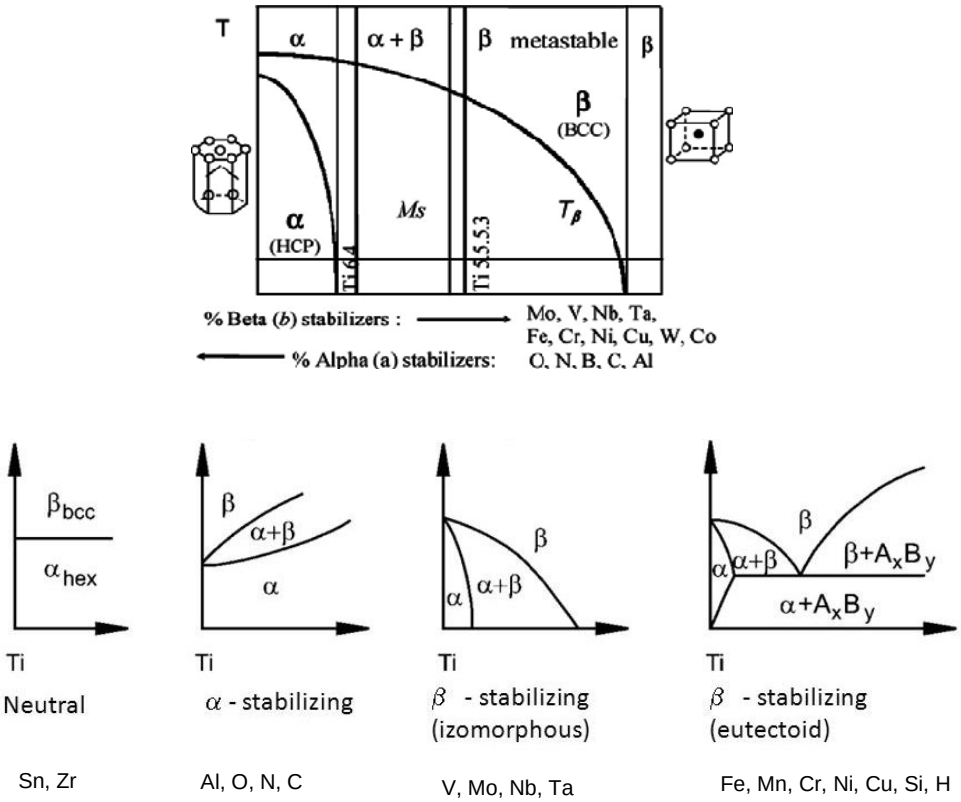


Fig. 2.4. Effect of alloying elements on phase composition [21].

The transformation of the BCC β phase to the hexagonal α phase in titanium can either occur martensitically or by a diffusion controlled nucleation and growth process, depending upon the cooling rate and the alloying elements present. A BCC crystal can transform into 12 hexagonal variants which will have different orientations with respect to the parent β crystal, in accordance with Burgers Orientation Relationship (BOR) as below [21], and is obeyed for both martensitic transformation and the conventional nucleation and growth process.

$$\{110\}_\beta \parallel \{0001\}_\alpha$$

$$\langle 1\,1\,1\rangle_\beta \,||\, \langle 1\,1\,\bar{2}\,0\rangle_\alpha$$

2.2.3 Microstructure and Phases

Microstructure plays a significant part to achieve the desired properties of Ti-6Al-4V. By doing the thermo-mechanical processing on Ti-6Al-4V, the following three distinctly microstructure can be achieved;

(a) Fully Lamellar

The α phase in this microstructure has shape of a lamellar or plate as shown in Fig. 2.5 (a). The lamellar microstructure can be achieved in final steps of the four step processing route by an annealing (AN) treatment in the β phase field (BA treatment) and therefore the lamellar microstructure is also known as the β-annealed microstructure. The four steps processing route to achieve this microstructure is shown in Fig. 2.6. The recrystallisation phase in the β phase field comes in step 3. In step (i), the microstructure of the billet / ingot is homogenized in the β phase field. Subsequently, in step (ii), the rolling/forging is carried out at high temperature around the β transus temperature of Ti-6Al-4V. In step (iii), the component is then heated by 30°C to 50°C above β transus temperature and then cooled down to RT at a controlled cooling rate and environment. Finally, the alloy is annealed in the α + β phase (step 4) as a stress relieving (SRL) treatment to enable a solid phase transformation of martensitic phase to α + β phase mixture in equilibrium.

Steps (iii) and (iv) are the two main steps to generate fully lamellar microstructure. The size of Prior Beta Grain (PBG) is determined by the temperature and the time treatment given to the β phase field. The cooling rate at step (iii) determines the arrangement and size of the α lamellar grains/laths, and also the amount of β phase. The finer α grains with limited amount of β grains are produced at higher cooling rates. At a slower cooling rate (i.e. Furnace Cooling (FC)) a fully lamellar microstructure with colonies of thick α grains/laths arranged in parallel manner are produced, where typically the α colonies originate at the PBG boundaries and grow interior of the PBG [23]. The fully lamellar microstructure produced with the FC comes out with the largest possible α colony size (see Fig. 2.5(a)).

Air cooling of Ti-6Al-4V generates another type of microstructure, also known as widmanstätten microstructure, where α laths are arranged similar to the weave pattern of a basket. This microstructure has very limited retained β phase located around the α grain boundaries [23] (see Fig. 2.5(b)).

If the cooling rate is further increased, using oil or Water Quenching (WQ), a martensitic microstructure with fine needles, designated as α', is produced without the retained β phase as shown in Fig. 2.5(c) [24]. This martensitic phase is produced when the α phase is supersaturated in β stabilizing elements and occurs by shear transformation, where atoms transform homogenously in a collaborative ordered movement [23]. Sometimes, it is difficult to locate the initiation of β phase in widmanstätten and martensitic microstructures. Also, the martensitic microstructures are rarely present in the structural component of Ti-6Al-4V [21]. The martensitic phase comes in two similar morphologies; acicular and massive. The acicular martensite α' grains have shape of pointed needles, and have a thin lenticular aspect in 3D, which tend to cross each other and are difficult to discern at the optical level. Each lath

carries a distinct crystal orientation and therefore the α' colony size is denoted by the thickness of a single α' lath.

For relative lower cooling rates, massive α' tends to form, which consists of irregular zones of laths, with size in the range of 50 – 100 nm. The massive α' laths share the same crystallographic orientation. The α' laths possess high density of dislocation of crystal defects such as staking faults and twins as compared to the equilibrium α phase. Furthermore, the α' martensitic phase has a higher content of Vanadium as compared to the equilibrium α phase [25].

During the step (iv) (the AN phase), depending on the choice of the AN temperature, the following different effects are possible to take place; (1) stress relieve the microstructure that may have resulted from a non-homogenous quenching from the β phase field, (2) trigger a solid phase transformation during which the martensitic phase transforms into the equilibrium mixture of the α+β phase, and (3) eliminate compounds that are micro-segregated within the material.

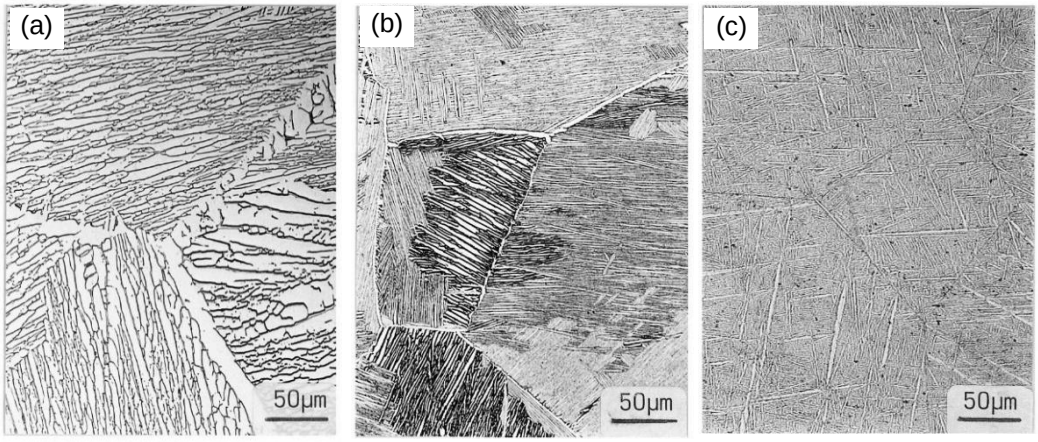


Fig. 2.5. Optical micrographs of three different fully lamellar microstructures produced at different cooling rates: (a) slow cooling rate, (b) intermediate cooling rate, and (c) quenching [6].

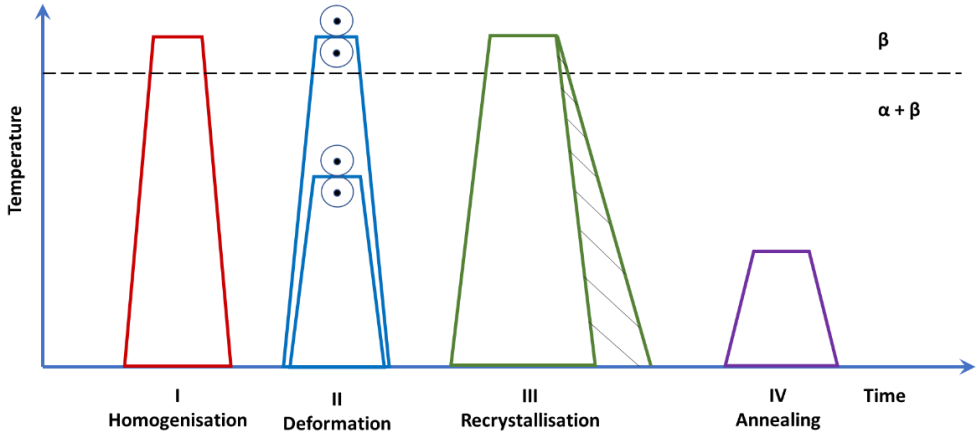


Fig. 2.6. A schematic of process route for the formation of fully lamellar microstructure [21].

(b) Bimodal Microstructure

This form of microstructure, also known as duplex microstructure, consists of a mixture of lamellar and equiaxed α grains as shown in Fig. 2.7. The processing route for Bimodal microstructure is similar to that followed for fully lamellar microstructure, but in this case, the recrystallisation step (the step (iii)), is conducted in the α+β phase. The microstructure of the ingot is initially homogenized in the β phase field (step (i)) and then cooled down to RT. The cooling rate in this step sets the width of the lamellar α grains and the size of equiaxed grains [21]. During step (ii), generally conducted in the α+β phase field, the α lamellar grains are plastically deformed and a preferred crystallographic texture is obtained prior to carrying out the recrystallisation step (iii). The new undeformed equiaxed α grains ($\alpha_{primary}$) are then formed at the expense of the deformed α lamellar grains. The volume fraction of equiaxed grains in the microstructure is dependent on the recrystallisation temperature. The typical lath width of the retained α lamellar grains ($\alpha_{secondary}$) will be determined based on the cooling rate chosen. Again, the final AN step (iv) is carried out to remove the micro-segregates and residual stresses in the microstructure [21].

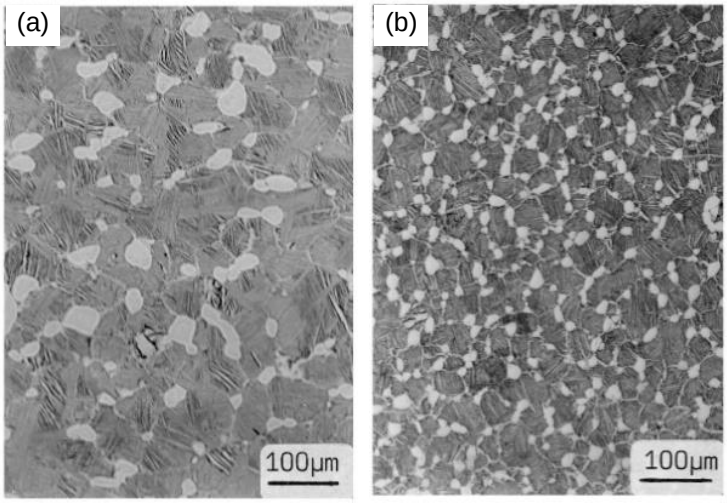


Fig. 2.7. The optical micrographs showing examples of bimodal microstructures: (a) bigger grains formed at slow cooling rate, and (b) smaller grains formed at fast cooling rate [6].

(c) Fully Equiaxed Microstructure

The fully equiaxed microstructure has only equiaxed grains of α phase as shown in Fig. 2.8. The fully equiaxed microstructure is created when a slow cooling rate is imposed during step (iii) [21]. The volume fraction of primary α dominates at the expense of a lamellar α grains. Another method to obtain fully equiaxed microstructure is to conduct the recrystallisation stage (step (iii)) at a relatively low temperature so that the equiaxed grains are formed directly during the recrystallisation of the deformed grains. The size of the equiaxed grains determines the mechanical properties of Ti-6Al-4V with fully equiaxed microstructure [21].

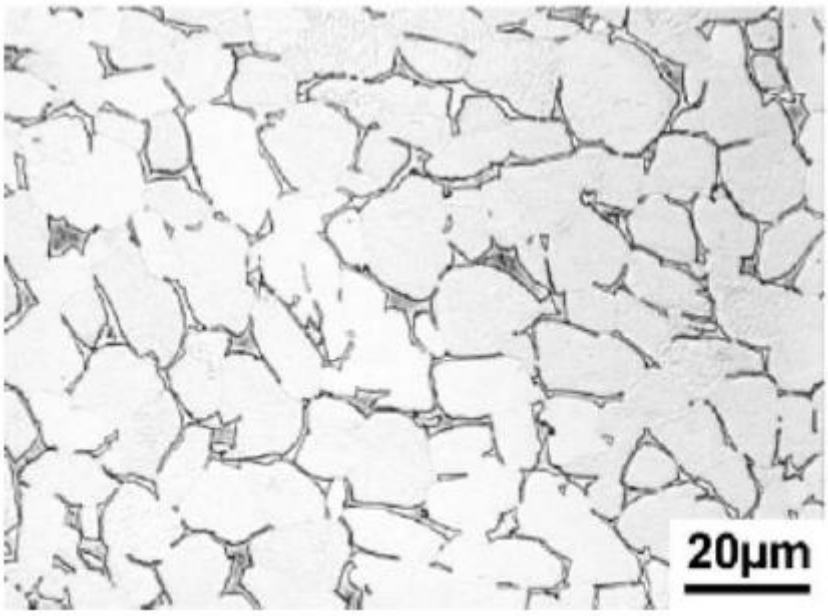


Fig. 2.8. The optical micrograph showing example of fully equiaxed microstructures [21].

(d) Secondary α Precipitation

In addition, depending on the cooling process followed in step (iii), fine secondary α platelets can be precipitated in the β phase during the heat treatment in step (iv) of the processing route [21]. This precipitation of secondary α platelets in the β phase field is possible in all three different types of micro-structures viz. fully lamellar, bimodal and fully equiaxed. The prime factor which leads to formation of secondary α platelets is the β phase composition which is directly connected to the volume fraction of β present in the microstructure before the final annealing treatment in step (iv) – see Fig. 2.9. The hardening of the β phase by precipitated secondary α platelets has a significant positive impact on the mechanical properties of Ti-6Al-4V. It is suggested to add an intermediated HT before the final stage annealing treatment to ensure hardening of β phase field through the precipitation of secondary α. The temperature of this intermediated HT must be high enough to create a metastable β phase that could precipitate the secondary α platelets. An example of fully lamellar microstructure of a titanium alloy with fine secondary α platelets within the β lamellae is shown in Fig. 2.9(c), which was obtained by adding an intermediate HT in the α+β phase field, and this type of microstructure is popularly known as bi-lamellar [21, 26]. The effective slip length in the bi-lamellar micro-structure with fine secondary α platelets reduces, causing higher barriers to slip transfer which then leads to a positive impact on the mechanical properties. The presence of secondary α platelets in β phase improves tensile, HCF and LCF strengths and but reduces ductility of Ti-6Al-4V. Due to the increase in strength of the bi-lamellar matrix, the soft continuous α layers at β grain boundaries will deform preferentially, leading to ductile fracture [21, 27]. The propagation rate of micro-cracks is much slower in the in the bi-lamellar microstructure as compared to the fully lamellar microstructure, because the hardened β lamellae are the effective barriers for micro-crack propagation [21].

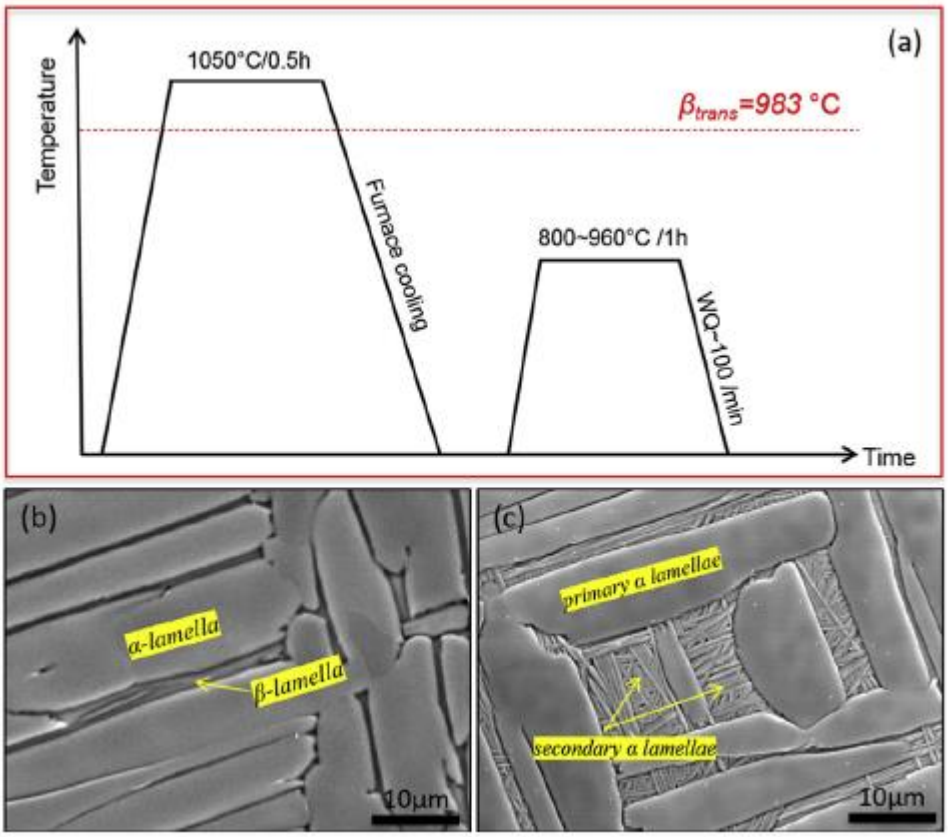


Fig. 2.9. (a) Heat treatment process route to obtain bi-lamellar microstructure, (b) SEM micrograph of processed Ti-6Al-4V showing lamellar microstructure, (c) SEM micrograph of processed Ti-6Al-4V showing bi-lamellar microstructure [26].

2.3 Issues related to AM Process

2.3.1 Smoking

In the EPBF process, under certain conditions, the electrons injected into the feedstock by the high energy density electron beam can get accumulated on the irradiated particles, causing them to electrostatically repel each other. In extreme cases, these electrostatic forces can grow so large that they eject the particles from the powder bed and this process is often known as “smoking” [28, 29]. Smoking is generally undesirable because it can cause failure of the EPBF build process [28]. The sequence and a strong development of sudden smoking was captured using the high speed camera imaging and is shown in Fig. 2.10 [29]. According to the study by Sigl et al. [29], the electrostatic charge, water residue in the powder and momentum of electrons are the prime reasons of smoking during the EPBF process.

Cordero et al. [28] have developed an analytical model of powder bed charging. In this model, the particle and its substrate were approximated as the electrodes, each powder particle was approximated as a capacitor, and the oxide overlayer as the dielectric. From this analytical study, they approximated the charge distribution in the powder bed, the electrostatic forces acting on the particles, and the conditions at which the powder bed smoking will happen. It was found that the electrical resistivity of the oxide overlayer strongly influences the charging behaviour of the powder bed. A high resistivity

promotes the accumulation of charge which then leads to smoking. From the modelling predictions, Cordero et al. [28] also concluded that the higher powder bed temperatures, bigger particle sizes and higher beam speeds should generally help to suppress smoking.

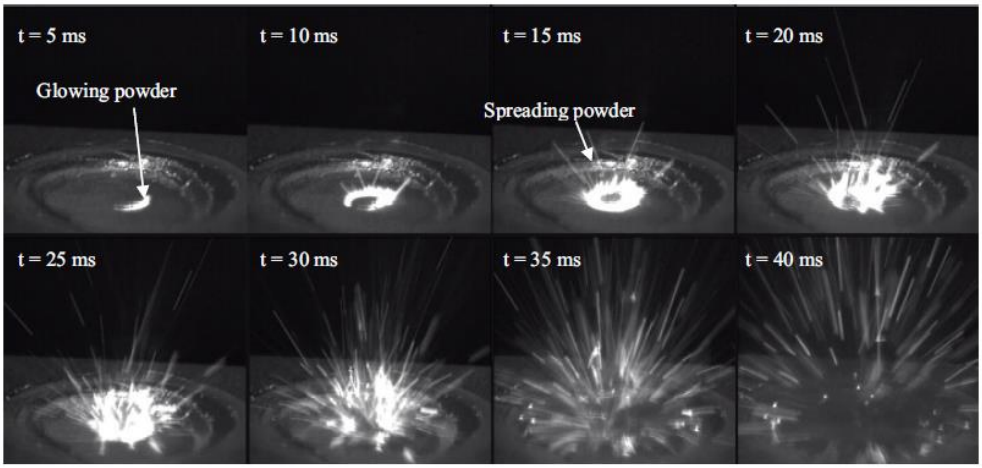


Fig. 2.10. Smoking phenomenon during the EPBF process [29]

2.3.2 Oxygen Content and Oxygen Layer in Ti-6Al-4V

Exposure of titanium and its alloys to any oxygen containing atmosphere at ETs leads to formation of an oxide layer (OL) on the surface with an oxygen diffusion zone (ODZ) beneath it, which therefore limits the use of Ti-6Al-4V at ETs. Rutile and anatase are the most common phases of TiO_2 that lead to formation of an OL. Irreversible transition of anatase phase to rutile phase takes place within the OL at about 700 ◦C [30]. Dissolution of oxygen in the underlying substrate as a result of inward diffusion of oxygen develops a continuous, hard and brittle ODZ with higher oxygen content, commonly referred to as alpha-case (α-case) [31, 32]. Formation of ODZ is because of higher solid solubility of oxygen in α-titanium (i.e. 14.5 wt.% [31]), and is critical because it leads to a loss of tensile ductility, fracture toughness and fatigue life of Ti-6Al-4V. Additionally, the presence of ODZ also affects its deformation mode (slip or twinning), and formation of phase precipitation and secondary alpha in Ti-6Al-4V [30, 32, 33, 34, 35]. The formation of ODZ is critical to the life expectancy of Ti-6Al-4V particularly when used in aeroengines [30, 33]. A typical OL on the surface with an ODZ beneath it, can be seen in Fig. 2.11(a) [31]. Also, a normalised oxygen concentration profile along the thickness of alpha case for a sample, exposed for 500 h at 593°C, is shown in Fig. 2.11(b) [34]. Presence of aluminium, having a detrimental effect on ductility, considerably enhances the oxidation behaviour of titanium which forms a thermodynamically stable and protective Al_2O_3 phase causing a mixture of TiO_2 and Al_2O_3 in the OL [30]. Above 200 °C the thickness of the OL significantly increases. ODZ develops above 400 °C. At temperatures above 600 °C, increase of oxidation rate causes formation of a thicker but defective OL leading to easy penetration of oxygen into the substrate. According to Guleryuz et al. [30], oxidation at temperatures above 800 °C would significantly degrade the performance of titanium alloys because of possible thinning due to detachment of thick OL and also due to formation of wider ODZ.

From the published research studies, if the AB microstructure of AM Ti-6Al-4V consists of α' martensite then it would show a significant reduction in ductility beyond 0.20 wt-% Oxygen [33, 35]. On the other hand, if it consists of a microstructure with α and β, it can tolerate up to 0.40 wt-% oxygen while still maintaining a decent ductility (>20%) [33].

According to Dietrich et al. [35], by increasing the oxygen concentration within the build chamber from 2 ppm to 977 ppm, the oxygen concentration in the final parts increases (from 1670 ppm to 1848 ppm) which then was found to increase the tensile strength and decrease the fatigue resistance of AM Ti-6Al-4V. They also summarised that if the build atmospheres is not precisely controlled, then it tends to cause a greater deviation in tensile and fatigue strengths of LPBF Ti-6Al-4V. Furthermore, Pauzon et al. [36] have found that if the oxygen concentration is varied within the build chamber, then the absorption of oxygen in the LPBF Ti-6Al-4V also varies along the height of the specimens [36], which then affects the mechanical responses of LPBF Ti-6Al-4V specimens built at different elevations in the build chambers.

In aerospace applications, the α-case is often removed/avoided using the machining or chemical milling processes and also by using high temperature coatings [34]. Since the jet engines do thousands of flight hours during its service life, the exposure time at the maximum allowed temperature can be quite significant, and can lead to infusion of critical amount of oxygen to form α-case within the Ti-6Al-4V alloy [34]. Therefore, the maximum service temperature for Ti-6Al-4V is limited to 350°C. It is partly because of possible degradation of mechanical properties above this temperature due to simultaneous formation OL and ODZ [31]. From their research study, Gaddam et al. [31] concluded that the growth of α-case layer in Ti-6Al-4V follows a parabolic relationship at 593°C and 700°C. They found a depth of 200 μm for α-case layer in Ti-6Al-4V after 500 hours of exposure at 700°C in an oxygen containing environment. If a thick α-case layers is found to be present then the AM part can be etched or machined prior to putting it in service to achieve an improved life [32].

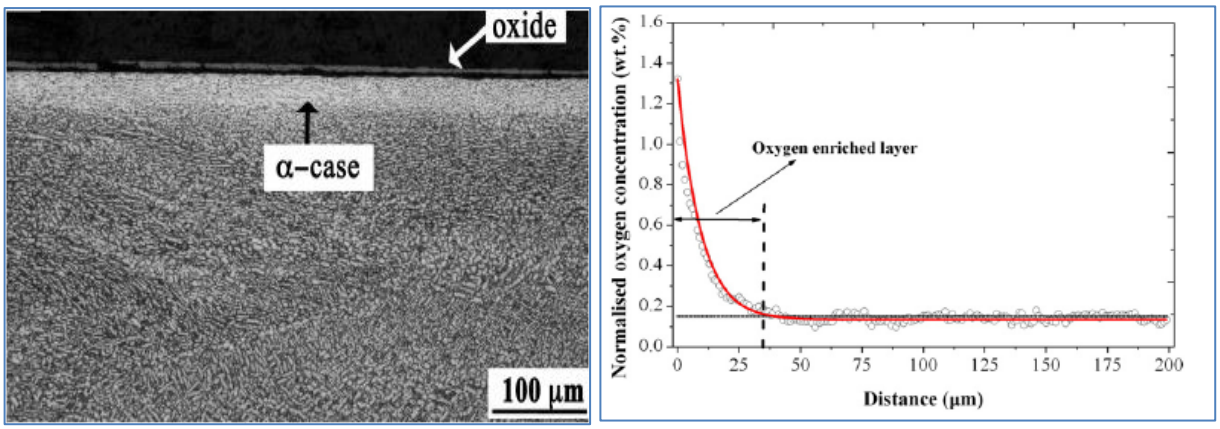


Fig. 2.11. Formation of oxide and α-case layers in Ti-6Al-4V, held at 593°C for 500 h in dry air: (a) Optical micrographs showing α-case layer in Ti-6Al-4V [10] (b) Normalised oxygen content profile along the thickness of α-case in Ti-6Al-4V [9].

ASTM F3001-F14 [37] allows a maximum oxygen content of 0.13 % wt after AM processing, whereas AMS 4999A [38] defines an overall compositional requirement for oxygen in the range of 0.12 – 0.2% wt %. Used powder is allowed but the maximum number of times any portion of a powder lot can be processed in the build chamber should be agreed upon between the manufacturers and the customer [37].

2.3.3 Defects

During the AM build process, the part experiences a unique and complex thermal history with a highly localised and asymmetric temperature field, resulting in a non-uniform cooling rate and formation of non-homogenous material [39]. The anomalies in the AM parts and specimens are inherent to the AM process and produced due to deviation from the optimum melting conditions. These defects could significantly deteriorate the mechanical and fatigue properties of AM build parts [40]. These anomalies are of two types; (i) gas pores and (ii) Lack of Fusion (LOF) voids. The majority of the gas pores are spherical or elliptical in shape and randomly distributed (see Fig. 2.12(a)). During the AM process, the gas gets trapped in the melt pool and remains stuck in the solidified metal to form pores [41]. Additionally, the gas trapped in the powder particles during the gas atomisation process used to make the powder particles could also lead to formation of gas pores during the AM process. The formation of irregular shape voids, see Fig. 2.12(b), is due to multiple pockets of gas coalescing or areas experiencing LOF [40, 42]. These irregular shape voids are typically formed in between the adjacent layers and take the shape of a thin/collapsed flat crack with its longitudinal axis aligned perpendicular to the build direction [40, 41].

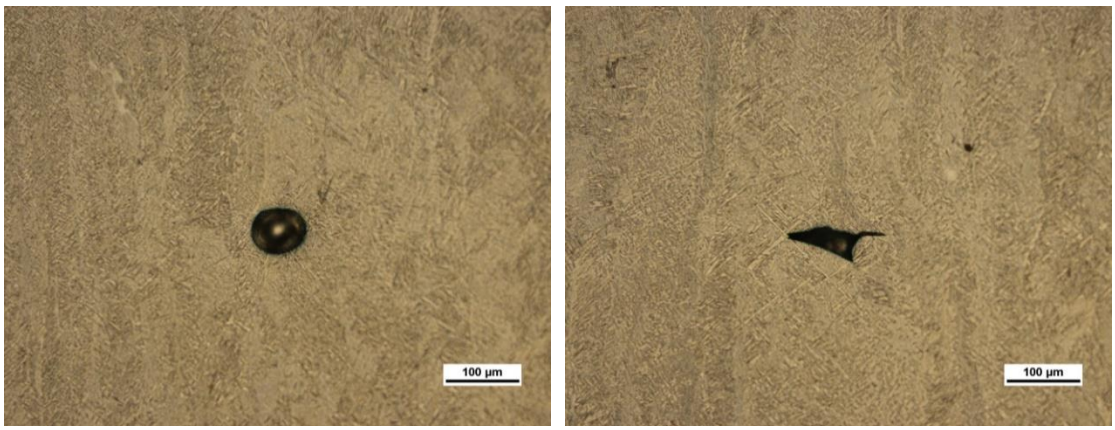


Fig. 2.12. Defects in AM parts: (a) spherical shaped gas pores, (b) irregular shaped voids.

The presence of anomalies/defects are heavily influenced by the AM process parameters [40, 42]. Discontinuities in the hatch lines and lack of overlap between the hatch lines result in porosity and entrapped powder particles (see Fig. 2.13). In the LPBF process, the energy density (E) is usually used to calculate the applied average energy per unit volume of material during scanning of a layer. For the LPBF process, it can be expressed by Eq. (2.1) [43];

$$E = \frac{P}{v.h.t} \quad (2.1)$$

Where, E = Energy density (J/m^3), P = laser power (J/s), V = scan velocity (m/s) , h = hatch spacing (m) and t = layer thickness (m). These processing parameters of LPBF process have significant direct impact to produce defects in the LPBF parts. When some or all of these parameters are varied simultaneously, some complicated interaction effects can be seen [40, 42 44, 45, 46]. Laser power and scan speed have direct but inverse impact on energy density. The combined effect of laser power and scan speed on to generate two defect types, i.e. pores and voids, is shown in Fig. 2.13.

If scanning is too fast with little power, then this can form regions within the part which do not fully melt, leading to 'lack of fusion' porosity. By contrast, if too much power is applied for the chosen speed, then it may overheat the melt pool, causing deeper energy penetration and leading to an effect known as the 'keyhole formation' [44, 45, 46].

The central operating window in the interaction diagram in Fig. 2.13 is where the right combination of speed and power will generate a stable melt pool of optimum size. It is where the laser energy is being efficiently absorbed by the powder, creating a melt pool of sufficient depth to fuse strongly with the layer below whilst avoiding excessive re-melting. In this processing window, the laser recoil pressure creates a shallow cavity. The laser heats the front face of this cavity as it moves, creating a metal vapour plume that is ejected normal to the surface – i.e. upwards and backwards. The shallow cavity does not allow for internal reflections, so no additional melting occurs. Heat energy is conducted into the melt pool, which experiences a degree of turbulent flow due to the high temperature gradients within it and the surface tension. This flow will result in some matter being ejected in the form of weld spatter. The moving vapour plume creates an environment around the melt pool that is analogous to a weather system. It can entrain powder from next to the weld track, drawing it towards the laser beam through the Bernoulli effect and then ejecting it outwards. Some of this material will be heated as it passes through the laser, while the other material is blown around by the induced gas flow in the form of 'winds' adjacent to the laser beam [44, 45, 46].

If we use less power for a given speed, then the melt pool will be smaller. This means that it is likely to experience less turbulence and generate less spatter as it solidifies more rapidly. The vapour plume will also be less vigorous and so entrainment of neighbouring powder will also be reduced. The bad news is that now the lower laser energy may not penetrate deeply enough to fully melt the powder layer and the top surface of the solid metal below. This leaves unmelted powder beneath the melt pool, resulting in excessive porosity and risk of delamination as illustrated in Fig. 2.14 (a) [44, 45, 46].

When higher power is used for a given speed, we see excess penetration of the laser into the metal under the layer of powder, forming a keyhole (Fig. 2.14 (b)). This deep melt cavity in the surface sees metal vapour being ejected more vertically than before. Internal reflections of the laser energy within the cavity trap more heat deeper in the material, leading to a deeper, longer-lasting melt pool. This increase in energy input will increase the melt pool turbulence and spatter formation, whilst a stronger 'weather system' will lead to more powder entrainment [40, 42, 44, 45, 46, 47]. Where the keyhole

becomes unstable (affected by power, scan velocity and melt pool dynamics), the melt pool can collapse on the cavity to form a pore of inert gas at the base. Such pores may not close up as the melt pool solidifies, generating sub-surface porosity in the welded metal (Fig. 2.14(c)) [44, 45, 46]. A greater degree of re-melting of the layers below will also occur, affecting the microstructure of the solidified material. In addition to the process parameters, the geometry of part, material of construction and machine architecture will also affect the formation of defects in the AM builds [40, 42, 44, 45, 46].

Thijs et al. [43] also did some tests where they varied v, h and scanning strategy to study the microstructural evolution during selective laser melting of Ti-6Al-4V. They found that the lower relative energy densities introduce large pores, with dimensions of 200 x 100 μm, appearing in a certain order. These pores were elongated along the scanning direction and located at certain scanning vectors and at certain layers. Thijs et al. [43] also observed accumulation of powder particles due to LOF around the melt pool within a layer and an accumulation of surface roughness across the layers. The energy supplied to the melt pool should also be optimized so that it partially melts the previously deposited layer and creates a bond between the two sequential layers. Any deviation from this optimized amount of energy could create insufficient melting or a highly unstable melt pool and vaporization [47]. Furthermore, the lack of wetting of the solid particles and the underlying substrate may result in the balling phenomenon in Ti-6Al-4V, leading to formation of discontinuous tracks and voids, poor interline bonding and even delamination [47], see Fig. 2.15.

From the research investigation by Kasperovich et al. [45], the typical defect types they observed at three different energy density level are shown in Fig. 2.16. The binding defects due to lack of fusion observed were in the form of complex, elongated and sharp crack-like voids, formed between layers and were aligned parallel to them (see Fig. 2.16(a) for the energy of 58 J/mm^3 [45]). Whereas, the kind of porosity, keyhole induced porosity, can be seen in Fig. 2.16 (c) [44, 45].

According to Chen et al. [48], the laser scanning strategy adopted in the LPBF builds can significantly influence the mechanical properties of AM parts. From their experimental study, they suggested that, with the Interlayer Offset Stagger (IOS) scan strategy, the internal defects within the AM parts were reduced because the laser energy input at the neighbouring layers was distributed in a uniform manner, whereas the orthogonal stagger (OS) scan strategy was effective to reduce the stress accumulation along a single direction, thus preventing deviations from the intended component shape. As per Qiu et al. [49], an unstable melt flow is responsible for increased porosity level and surface roughness, and recoil pressure is the driving forces to cause instability of melt flow during the SLM process.

In the EPBF process, there are various factors which could aid to produce LOF voids in the EPBF parts. The EPBF process uses a speed function index which is directly proportional to the scan speed to achieve the desired melt pool size. The Arcam system controls the scan speed dynamically according to the max current and powder bed temperature. A higher scan speed increases porosity by creating entrapped un-melted powder particles [42]. Further, the Current Compensation Function (CCF) in the Arcam system calculates the beam current (i_m) for a given scan as a function of the scan line length in a way

that the variation required in the input beam power when melting small and large areas is considered [50].

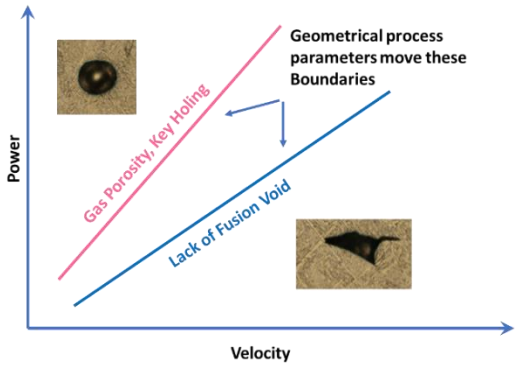


Fig. 2.13. Defects in AM parts: effect of power and velocity on defect formation [46, 47].

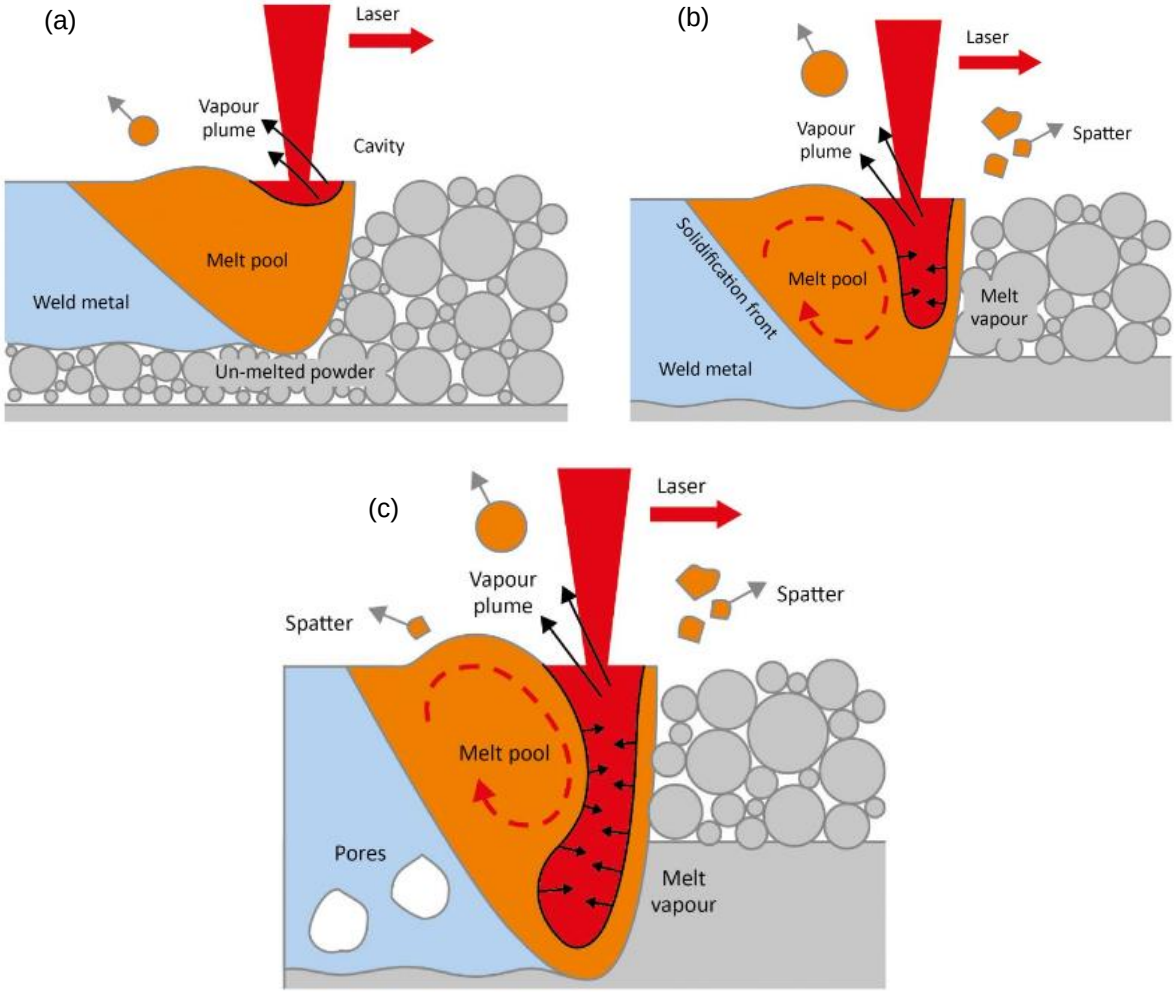


Fig. 2.14. Effect of energy density on defect formation in LPBF process: (a) insufficient penetration of the laser causing unmelted powder, (b) moderate keyhole effect – indicating formation of a deep cavity by an intense laser spot, (c) excessive keyhole effect causing a very deep cavity to trap gas in a pore below the surface layer [46].

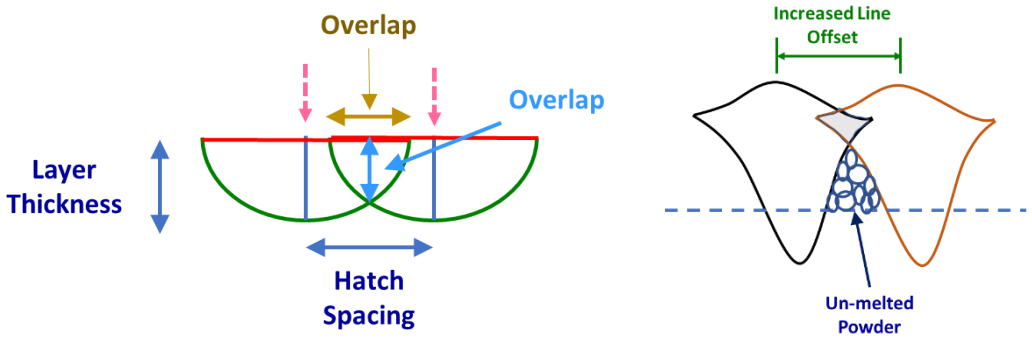


Fig. 2.15. Defects in AM parts due to layer thickness: formation of LOF voids where layer thickness is > overlap depth [47].

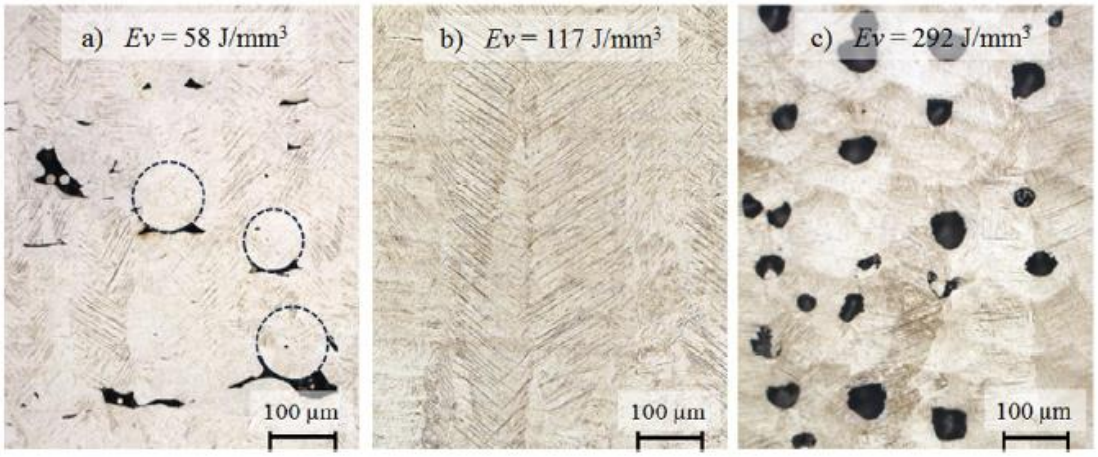


Fig. 2.16. Optical micrographs showing pores morphology in LPBF Ti-6Al-4V under different energy densities (E_v = E in equation 2.1) , (a) E_v = 58 J/mm^3, (b) E_v = 117 J/mm^3 and (c) E_v = 292 J/mm^3 [45].

The CCF changes the input current (i_m) according to equation (2.2) below [50].

$$i_m = i_i \left(1 + K \frac{l - l_{ref}}{l_{ref}}\right) \quad (2.2)$$

Where,

i_m = current used during the hatch melt,

i_i = current set by the user in the build process,

K = proportionality constant,

l_{ref} = reference scan length, and

l = length of the scan line to be melted per CAD geometry.

With many individual parts in a build, only the melt segments in the same line are added to calculate the total scan length of that beam scan path. The upper value of the Calculated Current Value (CCV, i_m) is limited by the Maximum Current Value (MCV) of the Arcam system. In case of CCV exceedance, the MCV is used by the Arcam system to melt the scan line length rather than the CCV, leaving the scan line

deprived of sufficient energy required for melting and thus assisting to generate voids. Arcam recommended maximum scan length is 90–100 mm to avoid insufficient melting [50]. An increase in the Line Offset Value (LOV) and Focus Offset Value (FOV) also influence defect generation. The distance between two hatch lines is known as LOV and an increase in LOV decreases the energy density between the melt lines. A bigger FOV means a bigger beam diameter and enlarged beam spot with lesser energy density. A lower energy density would mean discrete regions between the hatch lines [51]. These discontinuous regions with an un-melted powder offer slower cooling and surface tension effects help to form voids [40, 42]. Furthermore, the EB power fluctuations, surface gas flows, thermal history and raw material characteristics are some other contributing factors towards causing defects in the EPBF built parts [42].

For materials under fatigue loading, the crack initiation and propagation between the surface and internal defects remain competitive depending upon their size and stress levels [52, 53]. Typically, the surface cracks occur at high stress levels and the associated fatigue life is relatively short because of the environmental effects [52, 53]. The crack initiations from interior defects generally lead to long life because of crack growth in a quasi-vacuum environment [52, 53]; however, interior crack initiation not associated with any internal defects can also occur in titanium alloys, meaning that the crack initiation can shift from surface to interior (subsurface) [52].

Defects can be minimized by using high quality powder and optimization of the process parameters such as the layer thickness, input energy, build direction, scanning strategy, hatch spacing, and scanning speed during the process [47]. To enhance density, remove internal pores and voids, and improve fatigue properties of PBF parts, the Hot Isostatic Pressing (HIP) process is frequently used after an AM build. The HIP process is specifically used for sintering of powders, diffusion bonding or densification of castings. Under HIP, a high pressure of a gas and a high temperature are applied simultaneously, through an inert gas, to the component [54, 55]. Since, the 0.2% Proof Strength (PS) reduces and diffusion rates are higher at ETs, the pores and voids collapse through a small scale plastic flow under the applied pressure leads, and, under ideal conditions, it may also bond the pore interface [55]. However, the application engineer should also realise that the HIP process may not be effective for defects approaching or intersecting a free surface or for the defects which are likely to encroach a free surface due to post build machining process [56, 57]. Both the machining and the HIP processes are expensive and increase the lead time to the customer. Other methods such as preheating of the base plate and keeping it at a certain temperature during the build process and maintaining appropriate cooling rates could also influence the formation of defects in the end product [47]. Whichever process is chosen, the effort should be such that the part's performance is proven without carrying out any costlier post-processes. Furthermore, it should be noted that the HIP treatment may not always lead to a superior performance. Xu et al. [58] observed that a significant intergranular precipitation in LPBF Inco 718 took place under the HIP condition. These precipitates caused intergranular cracking due to void nucleation/ coalescence and decohesion between contiguous grains leading to poor creep performance.

The Archimedes method according to ASTMB962-17 [59] has been used by the researchers to calculate the density of an AM part with defects [42]. Alternatively, a suitable post processing of X-ray Computed Tomography scan (CT scan) data to calculate total volume of defects could be utilised to determine the density of an AM part [56, 60].

2.3.4 Surface Roughness

The rough surface, possibly having the stress raising feature or the existing surface cracks, could significantly deteriorate fatigue performance of metal AM parts [61, 62, 63, 64]. A rough surface, intrinsic to AM process, is due to the layer-by-layer nature of the AM build process. The surface roughness of an AM part can be affected by the process type, type of equipment, powder size, utilized process parameters etc. [61, 62]. In general, the surface roughness of AM parts typically increases with an increase in hatching pitch, layer thickness, powder size and support structure [61, 62]. Additionally, as shown in Fig. 2.17, the build rate (i.e. laser beam energy or speed) can also affect the surface quality, i.e. as the build rate increases the surface quality decreases [63]. The surface roughness is higher in AM build parts relative to conventionally manufactured metallic parts, possibly due to the partially melted powder existing along the outer surfaces or periphery [62]. Even between the two PBF approaches, the LPBF process generally creates a smoother surface for the part compared to the EPBF process which is due to the lower layer thicknesses and lower powder particle sizes used in the LPBF process [65]. Additionally, the specimen geometry and build orientation of different parts of a complex shape component would also drastically change the resulting surface roughness. The surfaces which are not parallel to the build plate or its normal direction are often affected due to the stair casing effect [61] and the inclination angle, an angle between the surface of the part and build direction, also influences and surface roughness. The stair step size decreases proportionally with the cosine of the wall angle, meaning that the staircase effects can be reduced by increasing the wall angle. Overhanging surfaces with a build angle below 60° will typically have a high surface roughness [62]. The parts which are built diagonally have even higher surface roughness on the surfaces facing downward compared to the surfaces facing upward – see Fig. 2.18 [62]. This is due to the reason that the down-skin is built on the powder with a lower thermal conductivity compared to the solidified material. This results in less dissipation of heat and more powder particles being partially melted and attached to the surface. The gravity is the second contributing factor which causes sagging of melt pools of unsupported layers into the un-melted powder underneath. Sagging of the down-skin could be prevented by introducing more build supports but then removal of these supports could cause the formation of burrs, nicks and dents giving rise to even higher final roughness. The build orientation of a complex part should therefore be optimized to minimize such situations [61, 62].

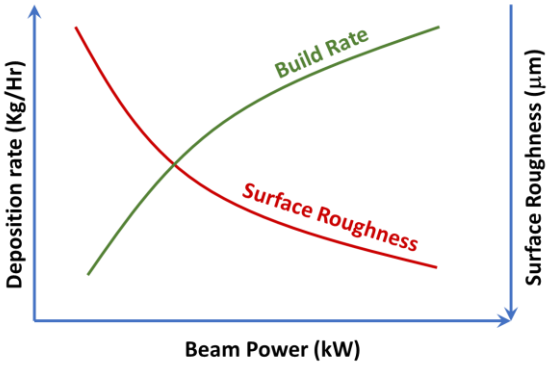


Fig. 2.17. Relationship between power, build rate and surface roughness [63].

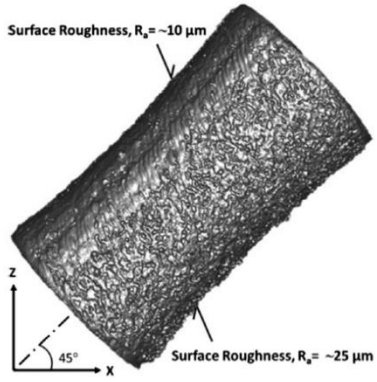


Fig. 2.18. 45° build AM sample showing higher surface roughness for the downward facing side (i.e. toward the build-plate) relative to the upward facing side [62].

A common method used to characterise surface roughness of AM parts is the standard stylus profilometry [62]. It is a direct and inexpensive method and gives reproducible results. However, this method can be used only on the accessible surfaces. Stylus profilometry provides a linear image or profile of the surface being investigated, as shown in Fig. 2.13. The limits for the features (such as deep valleys with sharp angles) that could be measured are dependent upon the size of the probes. The radius of the stylus tip, the cone angle, and the exerted force are carefully chosen to achieve reliable surface information under different conditions.

The amplitude parameters, R_a, R_v and R_t as shown in Fig. 2.19, are characterized based on the vertical deviations of the roughness profile from the mean line of the surface roughness measurements, taken over a constant length for each specimen. Amongst the most commonly used roughness parameters, R_a is the arithmetic average value of filtered roughness profile determined from deviations about the center line within the evaluation length, R_t is the range and R_v is the depth of the deepest valley of the collected roughness data points [61]. It should be noted that the parameter R_a sometimes could be heavily influenced by the partially melted powder particles attached to the surface which are not bearing any load and do not contribute significantly to the stress concentration induced by the rough surface. However, due to the nature of the surfaces produced by AM, the contact profilometry fails to spot some very critical features that are not accessible to the tip and could act as the existing cracks [61].

The conventional 2D imaging by optical microscopy, which is a contactless technique, is also used to evaluate surface roughness of AM parts [61, 66]. However, the optical technique also has limitations where optical disturbances from the environment or the illumination of the specimen can alter any surface measurements and analysis [66]. Furthermore, the material specific structure of AM surfaces can create optical scattering reflections which could cause misinterpretations by the optical sensors. Additionally, due to the high reflectivity of metal AM surfaces, an overexposure induces illumination peaks which could falsify the information regarding surface texture and therefore the calculation of the

roughness parameters. Due to the limitations with each surface measurement technique, a combination of different techniques may be required to obtain surface roughness [61, 66]. The Scanning Electron Microscopy (SEM), another contactless technique, is also used to examine the surface features within the AM samples. However, the SEM technique requires significant efforts to prepare a representative flat sample which includes cross-section of AM built material with surface and it is difficult to calculate the roughness parameters [61].

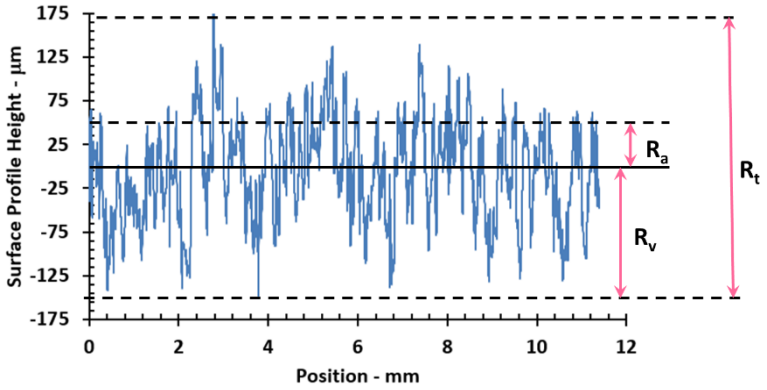


Fig. 2.19. Characterisation of surface roughness of as-build AM sample using stylus profilometry - parameters commonly used to describe roughness.

The surface roughness could have more detrimental effects to fatigue performance of AM parts, particularly on HCF performance, than the effect of internal defects i.e. pores, voids, un-melted particles [65, 67, 68]. Pegues et al. [64] studied the effect of AM part size in relation to surface roughness and gage diameter on the fatigue behaviour of LPBF Ti-6Al-4V specimens in As-Built (AB) condition, and concluded that the crack initiation behaviour was found to be highly sensitive to surface roughness. The specimens with higher gage diameter (> 4.90mm) had significantly lower surface roughness for down-skin surfaces which was due to the bigger solidified part volume beneath the layer edge which was efficiently dissipating the supplied heat. According to Fatemi et al. [69], the fatigue cracks in AB AM specimens initiate either from the surface or from internal defects. Whereas the internal defects form the crack initiation sites in machined (MC) AM specimens. In addition to improving fatigue performance of AM material, the removal of surface defects/features through surface machining can also lead to improvement in material ductility [69]. Zhang et al. [70] have suggested a significant improvement in fatigue life after completing the machining operation to remove rough surface. However, the improvement by surface machining could be lower if near surface defects remain after machining [70, 71]. The rough surface also controls the crack initiation and crack growth direction in AM parts, and according to Molaei et al. [71], the crack growth occurs in mode (I) direction when the rough surface is present. Researchers have used fracture mechanics based modelling methods to assess the effect of surface roughness on crack growth life of AM parts [65, 68, 70, 71]. From the viewpoint of fracture mechanics, Masuo et al. [68] have proposed a method to estimate the effective size $\sqrt{area}_{effmax}$ of irregularly shaped defects and interacting adjacent defects including near

and surface breaking defects/features. The HIP process is ineffective to remove detrimental effects of surface roughness of AM surface [68, 71]. The surface roughness values noted for the EPBF and LPBF processes from various published studies are reported in Table 2.3. As can be seen in Table 2.3 that the average surface roughness observed for EPBF built Ti-6Al-4V ranges between 27 μm to 42 μm whereas the average surface roughness for LPBF built Ti-6Al-4V ranges between 6 μm to 38.5 μm. As mentioned above and seen in Table 2.3, the LPBF process has, in general, created a smoother surface compared to the EPBF process due to the lower layer thicknesses and lower powder particle sizes used in the LPBF process.

Table 2.3. Measured average surface roughness for the EPBF and LPBF Ti-6Al-4V

Process	Build Orientation	Surface Roughness, R_a (μm)	References
EPBF	Vertical	27	[72]
		42	[68]
		35	[73]
LPBF	Diagonal	23	[64]
	Vertical	13	[72]
		38.5	[74]
		15.5	[75]
		6.8	[76]
		13	[68]
		17	[73]
		17.9	[77]
		10.5	[78]
		15	[79]
	Horizontal	32	[74]
		30.5	[74]
		13	[80]

2.3.5 Residual Stresses

In the LPBF process, the residual stresses are seen which may cause build failure, cracking, delamination and warpage within the part being built. The localised nature of the heating and cooling cycle results in residual stress field through the volume of the part being built [81, 82]. The expansion of a localized zone when it gets heated quickly by a high energy density beam is typically suppressed by the neighbouring material resulting into compressive plastic strains, whereas a subsequent rapid cooling of the molten metal and its contraction results in high tensile stresses, see Fig. 2.20 [81]. In the EPBF

process, where the build platform is kept heated during the process, the residual stresses can be lower by an order of magnitude in comparison to the LPBF process [83].

The magnitude of residual stresses in AM build can be process dependent on the scan strategy (i.e. the scan line) and layer thickness. The most common approach to reduce the residual stress is to follow a scan strategy where each layer is divided into smaller strip segments so that the longest uninterrupted line of travel remains small. The scan direction of the heat source is rotated in the PBF systems after each layer [82]. A finer scan layer results in higher stress gradients compared to a thicker layer [82]. Furthermore, the overall residual stress levels can also be dependent on the size of the part being built. For example, the tensile residual stresses in taller and narrower LPBF Ti-6Al-4V specimens were higher and penetrated deeper from the surface as compared to the residual stresses in short and wider parts, according to Edwards et al. [74]. Also, a more substantial delamination type defects were formed between the layers due to residual stresses [84]. The built up of significant tensile stresses in larger parts caused delamination at support structures or at the build platform [47, 84]. Additionally, the delamination type defects have also been observed near the stress concentration feature such as the support structures [85]. The dimensional tolerances are also significantly affected due to part distortion which can result into significant non-conformances in applications such as aerospace or bio-medical, where tight geometric tolerances are necessary. Furthermore, the residual stresses, if tensile in nature, can act as the crack driving force and thereby accelerating the initiation of crack and its propagation under fatigue loading [85].

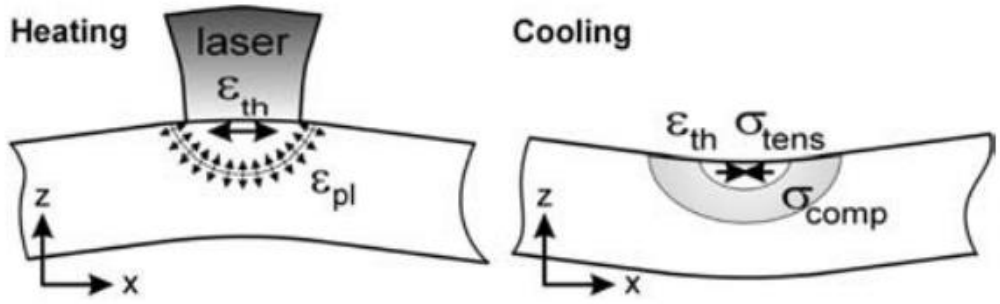


Fig. 2.20. Temperature gradient mechanism responsible for residual stresses in the LPBF process [81].

2.3.6 Heat Treatment and Microstructure of AM Ti-6Al-4V

The standard approach to transform the metastable microstructure that could be in the AB state of AM Ti-6Al-4V is through the use of post-processing HTs, during which Vanadium diffuses out of the saturated α' to facilitate the formation of β along the α lath boundaries when the cooling rates are sufficiently low [86]. The HT of AM Ti-6Al-4V generally falls into three distinct groups; (i) SRL treatment performed between 480°C to 650 °C, (ii) recrystallisation AN treatment carried out from 705 °C to ~975

°C, i.e., just below the β transus temperature (T_β), and (iii) β Annealing (BA) performed above 975 °C [54, 87]. While the HTs performed below T_β do not alter the PBGs meso-structure, the HT conducted above T_β results in recrystallisation, globularisation and significant growth of PBG [88, 89]. The microstructural responses to HTs taken from literature are summarised in Table 2.4 and Table 2.5 for EBPF and LPBF processes, respectively.

The typical microstructure observed in EPBF Ti-6Al-4V is the lamella $\alpha + \beta$ phases in columnar PBGs (see Fig. 2.21, [90]), which is as a result of ET maintained inside the chamber during the build process which not only affects the thermal history of the previously built layers but also maintains a slow cooling rate post EPBF build [90, 91, 92]. The BA treatment results in α colonies in globular PBGs. The cooling rate affects the size of α lath structure where FC post HT has produced coarse α colonies and WQ has produced acicular α' within PBGs [93]. The Duplex Annealing (DA) HT (i.e AN at 950 °C for 1 h followed by WQ and then a second SRL treatment at 500 °C followed by air cooling (AC)) has kept the microstructure of LPBF same as for AB EPBF Ti-6Al-4V, i.e. Lamella α + β in columnar PBGs [94].

Raghavan et al. [95] and Galarraga et al. [93] have studied the effect of HT in super β transus temperature regime onto the development of microstructure in EPBF Ti-6Al-4V. In the study by Raghavan et al. [95], they studied the effect of HT in the β phase field followed by FC. The grain structure after HT completely changed to a uniform equiaxed shape and the α-β morphology contained both widmanstätten and colony microstructure. Raghavan et al. [95] also observed a significant amount of α phase precipitation on the β grain boundaries after HT, but no significant change in α lath thickness was noticed and the final α morphology depended primarily on the cooling rate (also see Table 2.4). Galarraga et al. [93] studied the cooling rate effects (FC, AC and WQ) on EPBF Ti-6Al-4V from temperatures above β transus and they reported the resultant microstructure. From their study, the thickness of α grains present in the α colonies within the PBG were observed to be progressively thinner from FC to AC then to WQ. With reduction in α lath thickness, the tensile strength values reduced but the ductility value was observed to increase significantly [93].

The rapid solidification during the LPBF process results in a fine microstructure of Ti-6Al-4V with metastable martensitic α' phase within the PBGs, leading to a hierarchical microstructure (see Fig. 2.22, [96]), and constituent phases with enhanced solid solubility [91]. Repeated heating and cooling of the previously deposited layer, during the fabrication of next layer over it, make the solidified LPBF Ti-6Al-4V to experience a complex thermal cycle history, which is important both in terms of the microstructure development (i.e. columnar grains) and residual stresses [83]. Another inherent feature of AM, the line-by-line and layer-by-layer nature of manufacturing, imparts a meso-structure that often reflects into the line hatch spacing, layer thickness and the scanning strategy [83, 86, 97]. The combination of all these microstructural features, which span several length scales, i.e. from nanometres to millimetres scale, and could make the mechanical performance of AM Ti-6Al-4V unique and significantly different from the conventionally manufactured Ti-6Al-4V [83, 86, 97].

The solidification cellular structure is a distinct feature in AM Ti-6Al-4V, which can range from ~0.1 to 1 μm in LPBF process and ~5 μm in EPBF process [83]. Formation of these structures is a consequence

of constitutional undercooling during solidification and is controlled by the ratio of the temperature gradient and the solidification rate. The size of cellular structure depends on the process parameters used [83]. The meso-structures in AM alloys can manifest not only in terms of the scanning methods used, but also in terms of texture, grain boundaries and formation of defects [83]. The crystallographic variants of α grains form randomly from the parent β grains and a weak α crystallographic texture with a distinct structural morphology orientated at ∼45 °to the build direction (Z) in the fabricated alloy is commonly reported [98]. It has been suggested that an elongated/columnar grain and primary lath morphology will have a larger influence on anisotropy than the crystallographic texture itself [98]. Hence, the underlying properties are affected by the PBG meso-structure and the subsequent α lath formation. The texture of α laths depends on texture of the PBGs and the extent of variant selection [99].

The primary α grains tend to extend across an entire PBGs and additionally finer secondary, tertiary, and quartic grains form between the primary laths (due to the repeated heating cycles that the solidified layers of Ti-6Al-4V experience), forming a basketweave structure [86, 92]. The columnar PBGs, oriented along the build direction (Z), in LPBF Ti-6Al-4V form due to epitaxial growth along the < 001 > direction, which occurs due to the absence of nucleation sites of heterogeneous grain within the melt pool and the domination of the growth of grains that are at the bottom of the melt pool during solidification [92, 86]. An elongated/columnar grain and primary lath morphology causes a significant influence on anisotropy, hence, the underlying properties are affected by the PBGs meso-structure and formation of subsequent α lath [86]. In the LPBF process, the α' can start to transform into α grains post HT [86, 100]. At higher SRL temperatures, β precipitates start to form along the α lath boundaries [100]. The AN treatment results in coarsening of α lath structure and formation of β along the lath boundaries in significant amounts. The BA treatment results in a colony type structure, which is commonly seen in conventionally produced Ti-6Al-4V. Duplex HTs (i.e AN at 910 °C followed by WQ and then a second AN at 750 °C followed by AC has produced a bimodal microstructure consisting of fragmented equiaxed primary α grains in a matrix of lamellar secondary α + β in LPBF Ti-6Al-4V [101]. The bimodal microstructure of Ti-6Al-4V offers a good compromise between strength and ductility, and enhances the near-threshold fatigue crack growth (FCG) resistance [101]. According to Tammas-Williams et al. [102], the application of high temperature BA treatment at 1035 °C caused pores to reappear in HIPed EPBF Ti–6Al–4V component after 10 minutes of BA treatment [102]. The expansion of pores was due to high pressure within the pores which remained after the HIP process due to low diffusivity of argon in titanium [102]. Additionally, the surface connected porosity was found to be retained, which possibly expanded after the HIP process [55]. Also, the HIP process involves treatment at high temperature which may sometime coarsen the microstructure and thus reduce the mechanical strength of AM Ti-6Al-4V [103].

2.3.7 Texture and Anisotropy

It is widely accepted that even though the existence of columnar grains and molten pool behaviour would influence to cause anisotropy in mechanical properties of LPBF Ti-6Al-4V, the crystallographic texture, which usually controls the slip mode and plastic flow, also exhibits a strong link with the mechanical anisotropy of LPBF Ti-6Al-4V [104, 105]. A dominant $\{100\}_{\beta}$ texture typically forms in the Ti-6Al-4V, while α' texture could be relatively weak due to the high number of α' variants within each prior β grain [104]. The ability of the material to deform plastically can be characterized by the Schmid factor, which is the ratio of the maximum resolved shear stress to the maximum contact pressure. The larger the Schmid factor, the larger the critically resolved shear stresses will be and more easily the slip system can be activated [104]. The Schmid factor values for several typical slip systems under different stress states are different, and therefore it can lead to anisotropy in material properties due to different α variants present in LPBF Ti-6Al-4V. Yang et al. [104] concluded that the horizontally built Ti-6Al-4V samples depicted higher tensile strengths, but the vertically built ones got better elongations, confirming the existence of mechanical anisotropy in LPBF Ti-6Al-4V. Also, the anisotropy in tensile properties of the LPBF Ti-6Al-4V can be weakened by reducing the laser energy density [104].

Chang et al. [105] noticed a distinct strong texture feature in the pole figures on the {0001} plane of α grains of LPBF Ti-6Al-4V. The crystallographic texture of LPBF Ti-6Al-4V indicates the preferred orientation growth of the α phase, which will cause non-uniformity of the slip band distribution and resulting into anisotropic tensile behaviour. Furthermore, the presence of trans-granular α phases destroys the microstructure integrity of PBGs because it acts like a weak band connector [105]. When the tension was applied along the long axes of PBGs, the trans-granular α tends to fracture and cause a preferential source for damage accumulation, resulting in a relatively lower tensile strength in the build direction of LPBF Ti-6Al-4V. On the contrary, when exposed to the tension forces in the horizontal direction, the tensile loads are exerted on the short axes of PBGs and only a relatively small quantity of α_{GB} acts to separate adjacent β grains, resulting in a superior tensile properties. Therefore, the anisotropic tensile behaviour is formed due to the microstructural anisotropy [104].

Chang et al. [105] successfully manufactured the near-fully dense Ti-6Al-4V parts with considerably low porosity of 0.034% vol. by the LPBF process, coupled with the AN treatment. The XY plane showed typical near-cellular PBGs whereas the PBGs on XZ plane exhibited a columnar morphology grown along the building direction. The typical α+β microstructure with a mean width of lath-like α of 1.55 μm was formed by the AN treatment. The annealed Ti-6Al-4V part had an obvious crystallographic texture with the intensity of 5.56 and 5.28 on XY and XZ planes, respectively (Fig. 2.23). The strong morphological feature of PBG and crystallographic texture gave rise to the anisotropic tensile behaviour and the UTS, PS and ductility in horizontal direction were all higher than that in the vertical direction. However Not any obviously anisotropic behaviour for hardness was found, due to the formation of similar diphasic microstructure on XY and XZ planes [105].

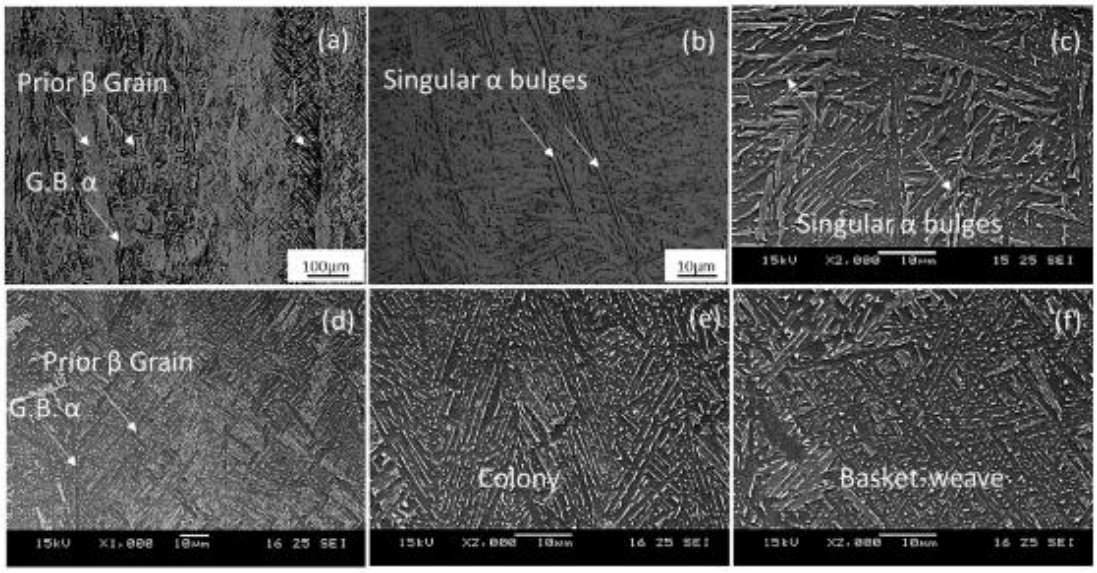


Fig. 2.21. Optical micrographs of EPBF Ti-6Al-4V on vertical section (XOZ) showing; (a) wavy columnar PBGs and (b) singular α grains (bulges). Also, SEM images of EPBF Ti-6Al-4V sample showing; (c) singular α grains (bulges), (d) transformed α + β microstructure with (e) colony and (f) basket-weave morphologies [90].

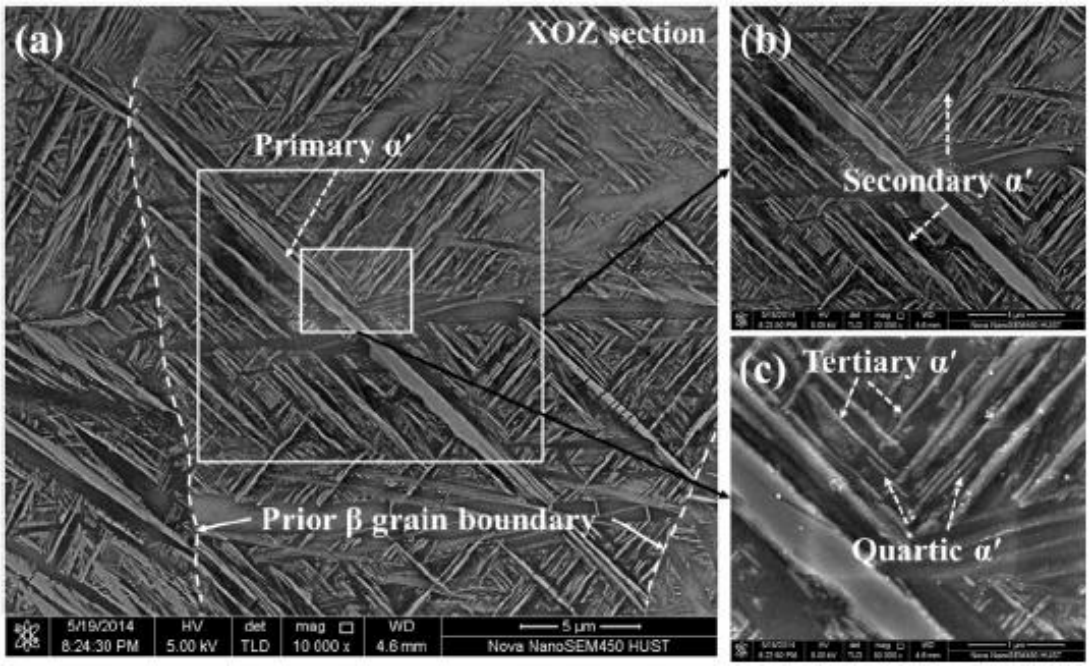


Fig. 2.22. SEM images of LPBF Ti-6Al-4V cuboid sample on vertical section (XOZ) showing primary, secondary, tertiary and Quartic α′: (b) and (c) are the zoomed in areas indicated by the white boxes [96].

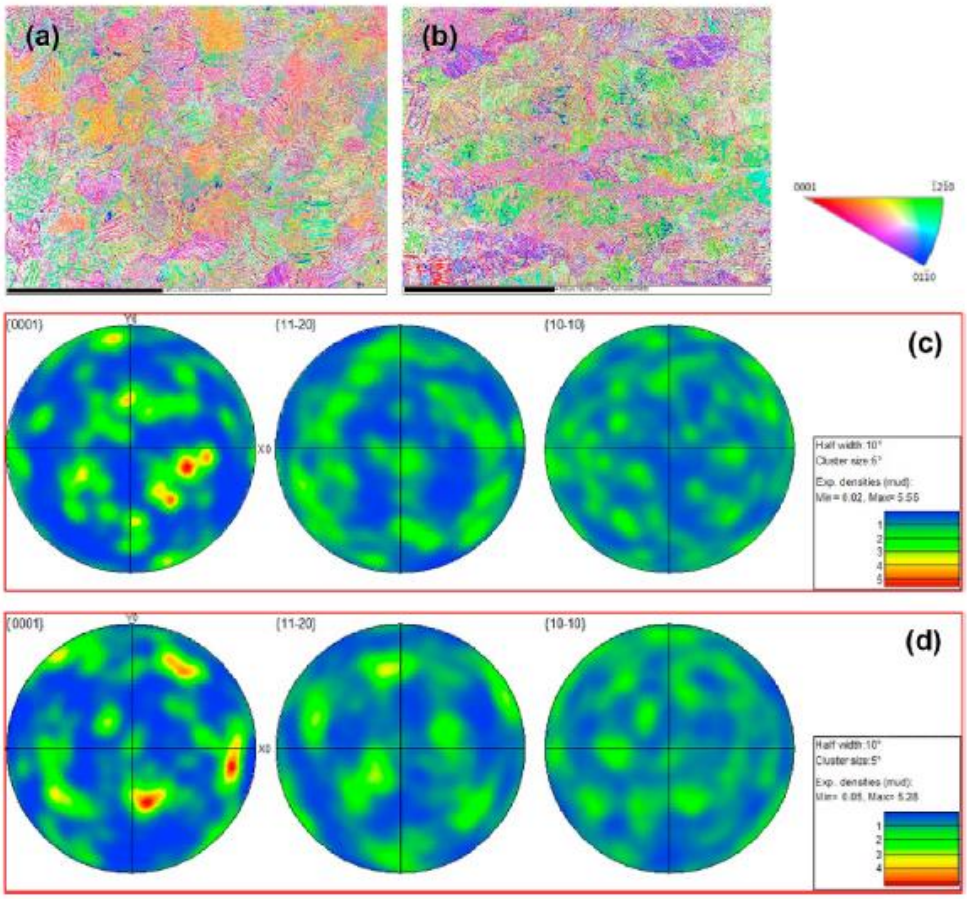


Fig. 2.23. LPBF Ti-6Al-4V: orientation map of (a) XY and (b) YZ planes. (c) is the pole figure corresponding (d) is the pole figure corresponding to microstructure in (b) [105].

Table 2.4. Effect of HT on microstructure of EPBF Ti-6Al-4V.

State	Microstructure	Reference
AB	Fine lamella α + β in columnar PBG	[90]
MC	Fine lamella α + β in columnar PBG	[91]
AB	Fine lamella α + β in columnar PBG	[92]
BA (1100 °C for 30 min, FC)	Coarse α colonies + in globular PBG	[93]
BA (1100 °C for 30 min, AC)	α colonies + in globular PBG	
BA (1110 °C for 30 min, WQ)	Accicular α' + in globular PBG	
AB	Lamella α + β in columnar PBG	
AB, horizontal build	Lamella α + β in columnar PBG	[94]
AN (950 °C for 1 h, WQ) + SRL (500 °C for 7 h, AC)	Lamella α + β in columnar PBG	

Table 2.5. Effect of HT on microstructure of LPBF Ti-6Al-4V.

State	Microstructure	Reference
Wrought, Solution Treatment and Aging (STA)	Globular α + β	[19]
MC, vertical and horizontal built	Accicular α' in columnar PBG	[91]
AB	Accicular α' in columnar PBG	[106]
HIP (820 °C for 2 h at 109 MPa in argon, FC)	Lamella α + β in columnar PBG	
HIP (950 °C for 3 h at 109 MPa in argon, FC)	Coarse lamella α + β in columnar PBG	
BA (1020 °C for 0.5 h, AC)	α colonies, α + β in globularised PBG	
SRL (650 °C for 3 h)	Ultrafine lamellar α + α' in columnar PBG	[107]
HIP (920 °C at 100 MPa for 2 h	Coarse lamella α + β in columnar PBG	
AB	Accicular α' in columnar PBG	[108]
AN (700 °C for 4 h in vaccum, FC)	Fine lamella α + β in columnar PBG	
AN (955 °C for 2 h in argon, WQ) + SRL (550°C for 5 h, AC)	Equiaxed α with secondary lamella α + β in columnar PBG	
SRL (650 °C for 3 h, FC)	Accicular α' in columnar PBG	[86]
SRL (650 °C for 3 h, FC)	Accicular α' in columnar PBG	
AB	Accicular α' in columnar PBG	[100]
SRL (480 °C for 1 h)	Accicular α in columnar PBG	
SRL (610 °C for 1 h)	Ultrafine lamellar α + α' in columnar PBG	
AN (750 °C for 8 h, FC)	Fine lamella α + β in columnar PBG	[109]
AN (910 °C for 8 h, FC)	Lamella α + β in columnar PBG	
AN (910 °C for 8h, WQ) + AN (750°C for 4 h, FC)	Equiaxed α with secondary lamella α + β in columnar PBG	
HIP (920 °C for 2 h, FC)	Lamella α + β in columnar PBG	[110]
HIP (920 °C for 2 h, WQ) + (500°C for 1 h)	Lamella α with partially decomposed α' in columnar PBG	
HIP (920 °C for 2 h, WQ) + (700°C for 1 h)	Lamella α with fine secondary α + β in columnar PBG	

2.4 Tensile Behaviour of AM Ti-6Al-4V

In Table 2.6 and Table 2.7, the tensile properties of Ti-6Al-4V taken from the published studies have been compiled for the EPBF and LPBF processes, respectively. The properties reported are PS, UTS and ductility. Additionally, these Tables also show the build orientation of the specimen, i.e. horizontal (X

and/or Y directions) and vertical (Z or the building direction). It has also been specified whether the material was tested in the AB, heat treated and/or in HIP condition.

The mechanical property data in Table 2.6 and Table 2.7 indicates orientation-dependent values for PS, UTS and ductility and these strength parameters are also affected by the machining operations, postprocessing HTs and/or the HIP process performed on the test samples. Since the samples for the test results in Table 2.6 and Table 2.7 were produced with different machines and different processing parameters, there is a good amount of scatter seen in the dataset in each of the two Tables.

Size of the α colony is a key parameter that affects the mechanical properties of Ti-6Al-6V with a fully lamellar microstructure. The slip length is dependent upon the size of the α colony which in turn determines the onset of plastic deformation in Ti-6Al-4V. Also, because the tensile strength of material depends upon the resistance to dislocation motion, a decrease in the size of α colony, and thus the slip length, corresponds to an increase in PS and UTS of Ti-6Al-4V. For this reason, the Ti-6Al-4V with lamellar microstructure has lower tensile strength as compared to the Ti-6Al-4V microstructure with fine martensitic α' needles where slip length is essentially the size of a single α needle. However, the martensitic α' needles offer lower ductility as compared to ductility of fully lamellar microstructure [21].

On comparing the strength data in Tables 2.6 and 2.7, the strength property values (PS an UTS) of LPBF Ti-6Al-4V are better than those of EPBF produced Ti-6Al-4V, which is typically due to acicular α' microstructure of LPBF Ti-6Al-4V as compared to lamellar α + β microstructure typically observed in EPBF built Ti-6Al-4V. However, the ductility of EPBF produced Ti-6Al-4V is typically better as compared to that obtained from the LPBF process. This is a result of the in-situ tempering of microstructure caused by heating of the build platform in the EPBF process. Also, by careful adjustment of LPBF parameters such as the layer thickness and volume energy, the temperature cycle during the build might be controlled in a way that α' decomposes in-situ so that a more favourable high strength - high ductility combination is obtained [110]. Oxygen pickup by titanium may also increase its strength but reduce its ductility [89, 111]. Vrancken et al. [89], who studied the effect of heating the build platform (to 400 °C), observed a drop in ductility of Ti-6Al-4V from 7 % to 4% and decomposition of martensitic α' into α'+ α + β. The observed changes in microstructure and ductility were due to the oxygen pickup during the LPBF build process. Therefore, such variations in the chemical composition, even if they are minor, may produce the observed scatter in the reported properties.

This suggests that the process parameters chosen to build the specimens have significant effect on mechanical properties of Ti-6Al-4V, which indicates that the process parameters need to be optimised to get the desirable mechanical properties of Ti-6Al-4V [83]. Similar PS and UTS values between LPBF and EPBF are achievable after carrying out an appropriate HT post an AM build [83]. The post build HTs result in the transformation of fine α' (or α) into coarsened and lamellar α in a PBGs matrix, to form an α + β structure, similar to the microstructure obtained by the EPBF process or through the conventional methods of manufacturing. These microstructural changes lead to a reduction in PS and UTS and an improvement in ductility.

Table 2.6. Tensile properties of EPBF Ti-6Al-4V

State	Young's Modulus (MPa)	PS (MPa)	UTS (MPa)	Elongation (%)	References
AB	N/A	851.8 ± 5.8	964.5 ± 0.3	16.3 ± 0.8	[90]
MC, vertical	115000 ± 0.7	869± 7.2	928 ± 9.8	9.9 ± 1.7	[91]
MC, horizontal	113500 ± 2.5	899± 4.7	978 ± 3.2	9.5 ± 1.2	
AB, vertical	N/A	812 ± 12	851 ± 19	3.6 ± 0.9	[92]
AB, horizontal	N/A	783 ± 15	833 ± 22	2.7 ± 0.4	
BA (1100 °C for 30 min, FC)	N/A	774 ± 112	913 ± 38	13 ± 2.0	[93]
BA (1100 °C for 30 min, AC)	N/A	847 ± 90	998 ± 52	13 ± 7.0	
BA (1110 °C for 30 min, WC)	N/A	932 ± 80	1200 ± 50	1.8 ± 1.5	
AB	N/A	1001 ± 42	1073 ± 45	11 ± 1.0	
AB, horizontal	N/A	1006	1066	15	[94]
AB, horizontal	N/A	1001	1073	11	
AN (950 °C for 1 h, WQ) + SRL (500 °C for 7 h, AC)	N/A	1039	1294	10	
AB, AN (710 °C for 2 h, FC) horizontal	N/A	869 ± 7	965 ± 5	6 ± 0	[65]
AB, vertical	N/A	928.7 ± 13.3	1011.7 ± 14.8	13.6 ± 1.4	[112]
HIP (920 °C at 100 MPa for 2 h), vertical	N/A	813.3 ± 14.3	908.8 ± 3.2	17.7 ± 0.9	
AB, horizontal	N/A	975	1033	16.78	[113]
AB, horizontal	N/A	881.5 ± 12.5	978.5 ± 11.5	10.7 ± 1.5	[114]
AB, HIP, horizontal	N/A	876.5 ± 12.5	978 ± 9.5	13.5 ± 1.5	
AB, horizontal	N/A	982.9 ± 5.7	1029.7 ± 7	12.2 ± 0.8	[115]
AB,vertical	N/A	984.1 ± 8.5	1032.9 ± 12.9	9 ± 2.9	
AB, vertical	N/A	1150	1200	25	[116]
AB	118000 ± 5	830 ± 5	915 ± 10	13.1 ± 0.4	[117]
MC, HIP (915 °C at 100 MPa for 2 h)	117000 ± 4	795 ± 10	870 ± 10	13.7 ± 1	
AB, vertical	93000 ± 2	735 ± 28	775 ± 26	2.3 ± 0.8	[118]
AB	114000 ± 6	1135 ± 12	NA	NA	[119]
MC, vertical	121000 ± 3	962 ± 4	1012 ± 3.0	8.8 ± 1.6	[40]

Table 2.7. Tensile properties of LPBF Ti-6Al-4V.

State	Young's Modulus (MPa)	PS (MPa)	UTS (MPa)	Ductility (%)	References
STA	120000	900	970	17	[19]
AB	120000	896	1000	8	[19]
MC, vertical	N/A	1143 ± 30	1219 ± 20	4.9 ± 0.6	[91]
MC, horizontal	N/A	1195 ± 19	1269 ± 9	5 ± 0.5	
AB, horizontal	N/A	1028 ± 9.1	1151 ± 1.8	-	[106]
AB, vertical	N/A	1010 ± 8.2	1150 ± 4.2		
AB, HIP (820 °C for 2 h at 109 MPa in argon, FC), horizontal	N/A	972 ± 7.1	1052 ± 4.1	-	
AB, HIP (820 °C for 2 h at 109 MPa in argon, FC), vertical	N/A	913 ± 6.4	1011 ± 8.3	-	
AB, HIP (950 °C for 3 h at 109 MPa in argon, FC), horizontal	N/A	847 ± 7.8	907 ± 2.1	-	
AB, HIP (950 °C for 3 h at 109 MPa in argon, FC), vertical	N/A	812 ± 4.7	904 ± 6.9	-	
AB, BA (1020 °C for 0.5 h, AC), horizontal	N/A	717 ± 2.4	840 ± 3.5	-	
AB, BA (1020 °C for 0.5 h, AC), vertical	N/A	715 ± 4.1	832 ± 5.9	-	
MC, SRL (650 °C for 3 h), vertical	N/A	1076 ± 14	1189 ± 16	13.6 ± 1.3	[107]
MC, HIP (920 °C at 100 MPa for 2 h), horizontal	N/A	907 ± 4	1022 ± 5	17.7 ± 0.8	
AB	N/A	1003 ± 20	1232 ± 15	7.4 ± 0.1	[108]
AB, AN (700 °C for 4 h in vaccum, FC)	N/A	1015 ± 4	1083 ± 4	7.9 ± 1.1	
AB, AN (955 °C for 2 h in argon, WQ) + SRL (550 °C for 5 h, AC)	N/A	1036 ± 37	1115 ± 39	3.9 ± 1.2	
MC, SRL (650 °C for 3 h, FC), vertical	N/A	1161 ± 30	1237 ± 30	7.6 ± 1.0	[86]
MC, SRL (650 °C for 3 h, FC), horizontal	N/A	1029 ± 8	1091 ± 6	7.8 ± 0.8	
AB, horizontal	N/A	1093 ± 64	1279 ± 13	6 ± 0.7	[120]
AB, vertical	N/A	1125 ± 22	1216 ± 8	6 ± 0.4	

State	Young's Modulus (MPa)	PS (MPa)	UTS (MPa)	Ductility (%)	References
SRL (650 °C for 4 h), horizontal	N/A	1145 ± 17	1187 ± 10	7 ± 2.7	
SRL (650 °C for 4 h), vertical	N/A	1132 ± 13	1156 ± 13	8 ± 0.4	
AN (890 °C for 2 h), horizontal	N/A	973 ± 8	996 ± 10	3 ± 0.4	
AN (890 °C for 2 h), vertical	N/A	964 ± 7	998 ± 14	6 ± 2	
AB, vertical	109900	736	1051	11.9	
MC vertical	112400	986	1155	10.9	
MC, vertical, HIP ((900 °C and 100 MPa for 2 h in argon atmosphere, AN at 700 °C for 1 h, AC)	115400	885	973	19	[121]
MC, vertical, AN (700 °C for 1 h, AC)	117400	1051	1115	11.3	
AB, horizontal	N/A	910 ± 9.9	1035 ± 29	3.3 ± 0.76	[74]
MC, vertical	N/A	NA	1314 ± 15.6	4 ± 1.2	[122]
MC, HIP (920 °C at 100 MPa), vertical	N/A		1088 ± 26.3	13.8 ± 1.3	
MC, AN (800 °C for 2 h), vertical	N/A		1288 ± 32.4	8 ± 1.5	
AB, horizontal	115000 ± 6	978 ± 5	1143 ± 6	11.8 ± 0.5	[123]
AB, vertical	119000 ± 7	967 ± 10	1117 ± 3	8.9 ± 0.4	
AB, horizontal	113000 ± 5	1075 ± 25	1199 ± 49	7.6 ± 0.4	
SRL (730 °C for 2 h), horizontal	113000 ± 9	958 ± 6	1057 ± 8	12.4 ± 0.7	
SRL (730 °C for 2 h), vertical	117000 ± 6	937 ± 9	1052 ± 11	9.6 ± 0.9	
SRL (730 °C for 2 h), horizontal	112000 ± 6	974 ± 7	1065 ± 21	7.0 ± 0.5	
AB, vertical	N/A	1008	1080	1.6	[124]
HIP (920°C at 100 MPa), vertical	N/A	912	1005	8.3	
AN (800 °C for 2 h), vertical	N/A	962	1040	5	
AB, vertical	119000 ± 7	967 ± 10	1117 ± 3	8.9 ± 0.4	[125]
SRL, vertical	117000 ± 6	937 ± 9	1052 ± 11	9.6 ± 0.9	

State	Young's Modulus (MPa)	PS (MPa)	UTS (MPa)	Ductility (%)	References
MC	109200 ± 3.1	1110 ± 9	1267 ± 5	7.28 ± 1.12	[126]
MC, horizontal	110000 ± 5	990 ± 5	1095 ± 10	8.1 ± 0.3	[127]
MC, HT, horizontal	104000 ± 2	790 ± 20	870 ± 10	18.1 ± 0.8	
MC, vertical	109000 ± 2.1	1098 ± 15	1237 ± 13	8.8 ± 0.6	[40]
AB, vertical	N/A	1333	1407	4.54	[128]
AB, horizontal	105000 ± 5	1137 ± 20	1208 ± 8	7.6 ± 2	[129]
AB, vertical	102000 ± 7	962 ± 47	1166 ± 25	1.7 ± 0.3	
AB, horizontal	103000 ± 11	944 ± 8	1036 ± 30	8.5 ± 1	
AB, vertical	98000 ± 3	925 ± 14	1040 ± 4	7.5 ± 2	
AB	94000	1125	1250	6	[130]
AB, AN	110000	920	1000	12	
AB, STA	110000	1100	1200	10	
AB, horizontal	N/A	1166 ± 6	1321 ± 6	2.0 ± 0.7	[131]
AN (640 C for 4h), horizontal	N/A	1104 ± 8	1225 ± 4	7.4 ± 1.6	
AN (640 C for 4h), vertical	N/A	1152 ± 11	1256 ± 9	3.9 ± 1.2	
MC	118000 ± 2.3	1100 ± 12	1211 ± 31	6.5 ± 0.6	[132]
MC, AN (950 °C for 0.5 h)	118000 ± 2.3	960 ± 19	1042 ± 20	13.0 ± 0.6	
AB, horizontal	N/A	1050	1230	5	[133]
AB, vertical	N/A	1025	1180	8	
Hipped (920°C, 103 MPa, 4 h, FC), horizontal	N/A	985	1025	12.5	
Hipped (920°C, 103 MPa, 4 h, FC), vertical	N/A	900	980	16	
AN (710°C for 2h, FC), vertical	N/A	1017 ± 7	1096 ± 7	12 ± 0.5	[65]

A significant grain growth at high temperatures can reduce PS to 715 MPa, which is well below that of the wrought alloy [106]. The ductility of LPBF Ti-6Al-4V is often lower than that of wrought Ti-6Al-4V [135, 135]. A bimodal microstructure consisting of equiaxed primary α phase and lamellar secondary α

+ β structure can be obtained in LPBF Ti-6Al-4V by using a duplex HT, where ductility of this alloy is substantially enhanced to 16–20% [109].

The anisotropy is most notable in the ductility of AM Ti-6Al-4V. For example, ductility is observed to be generally lower for AM builds in the horizontal orientation (i.e. X or Y directions) [134]. An elongated/columnar grain and primary lath morphology causes a significant influence on anisotropy, hence, the underlying properties are affected by the meso-structure with PBGs and subsequent α lath formation in AM Ti-6Al-4V [86]. A suitable combination of powder layer thickness and hatch strategy can be adopted to reduce anisotropy and enhance ductility of AM Ti-6Al-4V to some extent [134].

2.5 Fatigue Behaviour of Ti-6Al-4V

The HCF properties play a critical role in the safe design of components installed on aeroengines where designing against the vibration loading is one of the critical requirement [135]. In such safety critical applications, the objective of getting a good HCF strength drives to selecting appropriate materials and AM process types while doing the design of structural components. Hence, the HCF properties of AM materials should be characterised in detail, and strategies for achieving an improved HCF strength should be explored.

The process related attributes of AM, such as defects, surface roughness, residual stresses etc. typically have negative impact on its HCF performance. The asperities in the rough surface and internal defects (in size and number), in particular LOF defects with a high AR, act as the fatigue crack initiation sites and lead to reduce HCF strength of AM Ti-6Al-4V [40, 64, 68, 74, 77, 121]. The microstructure of Ti-6Al-4V relates to the fatigue crack initiation period, whereas the residual stress get added to the mean stress, increasing the net effect of mean stress in parallel to the vibration stress and thus reducing the safety margins. Typically, the HCF strength of AM materials is improved by applying the HIP treatment that transforms the microstructure of AM materials and reduces porosity. The HCF strength is also affected by the α colony size. It has been demonstrated that the Ti-6Al-4V microstructure with fine α' needles and with small α colonies better retard the propagation of micro-cracks than the microstructure with large colonies [98]. Whereas, the propagation of large cracks is mainly retarded by the deflection of crack tip, therefore the large α colonies provide better resistance to propagation of large cracks [98].

Also, the post build machining operations are carried out to improve the surface finish. The HCF strength is defined by the stress amplitude at which fatigue failure did not occur even after 10^7 cycles. In most cases, it is evaluated either at R Ratio (minimum stress/maximum stress) of R = -1 (fully reversed) or at R = 0.1 (axial fatigue testing in tension-tension). The HCF data for EPBF and LPBF Ti-6Al-4V taken from the published literature are summarised in Table 2.8 and Table 2.9, respectively.

From Table 2.8, the HCF strength value of EPBF Ti-6Al-4V (at R = -1) was observed to be quite low at 130 MPa. The HCF strength improved with the DA HT and went up to 220 MPa. Furthermore, the HCF strength improved by improving the surface finish with Shot Peening (SP) operation and the HCF

strength value went up to 450 MPa. Also, both SP and HIP can take the HCF strength of EPBF up to 575 MPa, which is comparable to the HCF strength of the wrought Ti-6Al-4V [136].

From Table 2.9, in the AB condition, the HCF strength of LPBF Ti-6Al-4V (at R = -1) is considerably lower (98 - 360 MPa) compared to the wrought alloy (500 – 650 MPa) [136]. By improving the surface finish, the HCF strength improves significantly (200 – 370 MPa) [40, 68, 121]. For SRL specimens, the improvement in the HCF strength is small [137], which suggests that the effect of residual stresses on HCF strength is small.

As seen in Table 2.8 and Table 2.9, the flaws on the surface or near surface flaws formed the crack initiation sites for AB specimens, and also for specimens which were post processed with MP, HIP and HT processes. Whereas the crack initiation sites in the AM specimens with post build processes like SP, Cavitation Peening (CP) and Sand Blasting (SB) were observed to be from the flaws internal to the bulk material [138], which was possibly due to the compressive residual stresses generated on or near the surface of the specimen, which discouraged the initiation of cracks.

The HIP and SP processes increase the HCF strength significantly by closing the defects within the bulk volume and near the surfaces, respectively. However, the effect of HIP is limited if the high surface roughness of an AM part is not improved [68, 139]. With SP, the surface finish improves which increases the fatigue strength to 450 MPa. The HCF strength goes up to 550 MPa post HIP, whereas a combination of HIP and machining can take the HCF strength of LPBF Ti-6Al-4V up to 590 MPa which is comparable to the HCF strength of wrought Ti-6Al-4V [136]. The SP offers the advantage of introducing compressive residual stresses near the surface and thus reduces the sensitivity related to the surface roughness [76, 140].

Table 2.8. Fatigue properties of EPBF Ti-6Al-4V.

Condition	R Ratio	HCF Strength (MPa)	Crack Initiation Site	References
Machined Polished (MP), vertical	-1	375 ± 25	Near surface flaw	[141]
DA, (935°C for 1.75 h, AC), 705°C for 2 h, AC), horizontal	-1	221 ± 11	Surface flaw	[142]
DA, CP, horizontal		406 ± 11	Internal flaw	
DA, Laser Shock Peening (LSP), horizontal		450 ± 3	Internal flaw	
SP, horizontal		371 ± 7	Internal flaw	
MP, vertical	0.1	50	Internal flaw	[40]
MP, vertical		270	Internal flaw	
AB, vertical	-1	130	Surface flaw	[68]
HIP (920°C for 2 h, 100 MPa), vertical		185	Surface flaw	
MP, vertical		250	Near surface flaw	
MP, HIP (920°C for 2 h, 100 MPa), vertical		575	Internal flaw	
MP	0.1	340	Near surface flaw	[91]

Table 2.9. Fatigue properties of LPBF Ti-6Al-4V

Condition	R Ratio	HCF Strength (MPa)	Crack Initiation Site	References
MP, SRL (650 °C for 3 h, AC), Vertical	-1	340	Near surface flaw	[140]
MP, DA (920 °C for 0.5 h, FC) + (700 °C for 2h, AC), Vertical		375	Near surface flaw	
MP, DA (920 °C for 0.5 h, FC) + (700 °C for 2h, AC), SP, vertical		450	Internal flaw	
AB, vertical	-0.2	80	Internal flaw/porosity	[74]
MP, horizontal		200	Internal flaw/porosity	
AB, (SRL 700 °C for 1 h, AC), 45° to vertical	-1	98 ± 23	Surface flaw	[64]
MP, AN (820°C for 4 h, 820°C for 1.5 FC)	-1	220	Near surface flaw	[139]
AB, HIP (920 °C for 2 h at 102 MPa)		230	Surface flaw	
MP, HIP (920°C for 2 h at 102 MPa)		350		
AB, SRL (650°C for 3 h, AC), vertical and 45° to vertical	0.1	210	Surface flaw	[137]
MP, SRL (650°C for 3 h, AC), vertical and 45° to vertical		500	internal defects	
SRL (800°C for 2 h), MP, vertical	-1	310 ± 40	Surface and internal flaw	[141]
SRL, HIP (920°C for 2 h, 100 MPa), MP, vertical		550	Internal flaw	
AB, HIP (900°C for 2 h at 100 MPa)	-1	200	surface	[121]
MP		350	internal flaw	
HIP (900°C for 2 h at 100 MPa), MP		500	surface	
MP, vertical	0.1	350	LOF flaw	[40]
SRL + HIP (810°C for 2 h, 200 MPa), 45° to vertical	0.1	300	Surface flaw	[77]
SRL + HIP (810°C for 2 h, 200 MPa), Vibratory polishing, 45° to vertical		467	Surface flaw	
SRL + HIP, Milling, 45° to vertical		690	Internal flaw	
SRL + HIP, SB, 45° to vertical		510	Internal flaw	
SRL + HIP, Micro-polishing, 45° to vertical		520	Surface flaw	
AB, vertical	-1	155	Surface flaw	[68]
AB, HIP (920°C for 2 h, 100 MPa), vertical		200		
MP, vertical		370	Near surface flaw	

Condition	R Ratio	HCF Strength (MPa)	Crack Initiation Site	References
HIP, MP, vertical		590		[68]
SRL (670 °C for 5 h), vertical	-1	213	Near surface flaw	[76]
SRL (670 °C for 5 h), vertical	0.1	140	Near surface flaw	
SRL (670 °C for 5 h), vertical	-3	310	Near surface flaw	
SRL, AN (920 °C for 2 h, FC), vertical	-1	191	Internal flaw	
SRL (670 °C for 5 h), EP, vertical	-1	250	Surface flaw	
SRL (670 °C for 5 h), SP, vertical	-1	325	Near surface flaw	
HIP (920 °C for 2 h, 100 MPa), Vibratory Polish (VP), vertical	-1	375	Near surface flaw	
AB	0.1	550	Internal flaw	[91]

2.6 Crack Growth Behaviour of AM Ti-6Al-4V

Understanding FCG characteristics is important for successful deployment of AM Ti-6Al-4V in safety-critical applications such as the aerospace industry. This enables the engineers and practitioners to use the damage tolerance analysis methodologies to assess structural integrity and reliability of AM components in presence of defects for the cases where assessment against the fluctuating loads is an essential design requirement. Therefore, a good understanding of the damage tolerance life of AM components under fluctuating loads becomes critical for part certification against the regulatory requirements. This also implies that the structural integrity assessment of AM parts requires an in-depth understanding of fracture properties and its relationship to the AM build process, build orientation and HTs. The FCG behaviour in metals is divided into three regimes;

Regime 1: Near-threshold behaviour,

Regime 2: Steady-state growth or Paris regime, and

Regime 3: Fast fracture regime.

Regime 1 indicates the near threshold FCG behaviour and is represented as the threshold stress intensity ΔK_{th}. Regime 2 of the FCG behaviour in metals is analysed using the Paris relationship;

$$\frac{da}{dN} = C\Delta K^m$$

Where,

$\frac{da}{dN}$ is the crack length advancement per load cycle,

ΔK is the cyclic Stress Intensity Factor (SIF) range,

m is the FCG rate exponent and (material specific constants),

C is the intercept (material specific constants).

The steady state FCG behaviour of AM Ti-6Al-4V, which is heat treated, is generally similar to their wrought or cast Ti-6Al-4V. This is because the steady-state FCG rates are less sensitive to the microstructure and the exponent m is observed to be independent of microstructural features. However, the AM Ti-6Al-4V in the AB state generally exhibit higher FCG rates, [74, 86, 143], which generally is due to the higher C values.

Regime 3 entails unstable and rapid crack growth that is sensitive to variations in microstructure and stress state and is directly related to the fracture toughness of the material.

2.6.1 Regime 1: Near Threshold Properties (ΔK_{th})

In the AB condition, the LPBF Ti-6Al-4V has a relatively low ΔK_{th} (1.5 – 1.8 MPa$\sqrt{m}$ for R > 0.5). In contrast, the ΔK_{th} values for EPBF Ti-6Al-4V are significantly higher (2.7 to 3.4 MPa$\sqrt{m}$ for R > 0.5). which is attributed to the α + β microstructure with a bigger lath size in the AB state. After HT, ΔK_{th} values for both EPBF and LPBF Ti-6Al-4V increase (3.1 to 4.6 MPa$\sqrt{m}$ at R > 0.5). Zhai et al. [143] have reported ΔK_{th} for heat treated AM Ti-6Al-4V and have found values similar to those for the wrought Ti-6Al-4V (3 – 4 MPa$\sqrt{m}$).

The near threshold FCG behaviour depends upon the microstructure, loading conditions which possibly could cause closure of crack, crack propagation behaviour in terms of its deflection and / or branching, plasticity level, residual stresses around the crack tip, and effects arising due to the operating environment [144]. Furthermore, the contacting cracked faces absorb some portion of the load during each loading cycle, therefore, decrease the driving force locally [83].

The fine α' microstructure, typically observed in the AB LPBF Ti-6AL-4V, produces a relatively low FCG threshold value as compared to that for the wrought / cast Ti-6Al-4V with relatively coarse microstructure. This suggests, that in AM Ti-6Al-4V, the near-threshold behaviour, and associated anisotropy can be improved through HT and resulting grain growth. This is particularly relevant, as most of the component life is in the crack initiation period, i.e. the time spent in Regime 1. With improved near-threshold behaviour, the overall impact of defects and surface roughness on damage tolerance. life of AM Ti-6Al-4V reduces.

The anisotropy is possible in AM Ti-6Al-4V, both in terms of the measured ΔK_{th} and crack closure behaviour. Anisotropy in the near-threshold FCG behaviour is most apparent in the AB state. For understanding this, both ΔK_{th} and closure effects need to be considered and this could be attributed to the microstructural texture [145]. Additionally, the PBG structure has a direct influence on the FCG behaviour in the near-threshold region in LPBF Ti-6Al-4V [140]. The crack deflection is observed along the lath boundaries and through the β phase along the grain boundary α (after HT). Such deflections reduce the crack driving force (mode (I)) significantly, which leads to the arrest of the crack from propagating altogether. Furthermore, at low R ratio, the factors such as the interaction between

asperities in the crack surface and other crack shielding mechanisms reduce the effective crack driving force and hence improve the near-threshold FCG behaviour.

In some instances, a preferential crack path along the PBGs is visible, which is perpendicular to the crack plane, causing shear type of cracking (mode (II) / mode (III)) to occur over that of the opening mode (I).

2.6.2 Regime 2: Fatigue Crack Growth Properties (C and m)

In most cases, a m value of ~3.5 is reported after HT, which is similar to that of the wrought material [146] and the FCG behaviour is similar between HIP, AN and DA states. In the AB state, a relativity lower m of ~2.7 is reported and is attributed to the presence of the fine α' in LPBF Ti-6Al-4V as compared to an α + β microstructure in the heat treated condition having more ductility.

The higher FCG rates observed for AM Ti-6Al-4V are partly due to presence of high and nonuniform tensile residual stresses which provides an additional crack driving force causing a shift to a higher R ratio [74, 120, 124, 145]. This also results in anisotropic behaviour because residual stresses are known to be dependent on the printing machine, scanning strategy, part size and part orientation. Leuders et al. [124] showed that the flaws have little influence on the FCG behaviour in LPBF Ti-6Al-4V with relatively low levels of porosity, as localised stress concentration associated with the porosity do not provide any significant additional crack driving force. However, the defects significantly affect the fracture toughness of AM Ti-6Al-4V. Also, in the relatively brittle α' phase, the fatigue cracks would propagate predominantly in trans-granular manner between the alpha laths aligned parallelly, which would possibly deflect at the boundaries of primary α' lath, leading to a slower FCG rate [147].

Additionally, the PBGs also affect the crack growth properties. The grain boundaries are the weak points in the microstructure where cracks can propagate. Fully lamellar microstructure with long PBG boundaries offers a weak resistance to short crack propagation. Long PBG boundaries can retard the propagation of large cracks as these boundaries induce crack deflection, where the large cracks are deflected along the grain boundaries causing crack path to be torturous and is associated with higher energy expense [98, 148].

2.6.3 Regime 3: Fracture Toughness (ΔK_{IC})

Fracture toughness (K_{IC}) defines the resistance offered by a material to cracking (or crack propagation) and is an essential property in the damage tolerance assessment [83]. The parameters such as the microstructure, porosity and high residual stresses can adversely affect (individually or in combination) the ability of AM alloys to resist propagation to fracture. Hence, the HT of AM parts is often necessary to achieve higher fracture toughness. Broadly, the K_{IC} depends on the following factors; the size of plastic zone ahead of the crack tip (r_p), crack tip blunting, and crack tortuosity in the cracking mode [83]. For example, a larger plastic zone size, often accompanied by the blunting of crack tip leads to higher fracture toughness.

Likewise, a mixing of crack failure modes (mode (II) or mode (III)) which could cause defection of propagating crack under mode (I) significantly increases the fracture toughness. Furthermore, an increase in ductility of AM Ti-6Al-4V would lead to an improvement in K_{IC}, but at the cost of PS and UTS

[149]. Also, a torturous crack propagation increase the fracture toughness but without affecting the strength [149].

FCG properties for EPBF and LPBF Ti-6Al-4V gathered from various published sources are presented in Table 2.10 and Table 2.11, respectively. Depending upon the microstructure of wrought Ti-6Al-4V, its typical K_{IC} ranges between 30 to 100 MPa√m [146]. Whereas, the K_{IC} for LPBF AB Ti-6Al-4V is significantly reduced due to presence of defects and residual stresses and ranges between 16 – 52 MPa√m. The K_{IC} increases to a value between 48 – 86 MPa√m after improving the density of LPBF Ti-6Al-4V to a value higher than 99.5% and also by performing HTs.

The typical value of K_{IC} for EPBF AB Ti-6Al-4V falls in the range of 48 – 82 MPa√m. The lower bound of the fracture toughness range improves and the range narrows down to 74 – 82 MPa√m after HT and/or HIP processes performed. In general, the K_{IC} for EPBF Ti-6Al-4V is higher than that of LPBF Ti-6Al-4V which is because of its lamellar α+β microstructure. The effect of HIP is two fold, where it not only closes the internal defects but also reduces any residual stresses within the EPBF Ti-6Al-4V specimens.

In LPBF Ti-6AL-4V, the increase in fracture toughness upon HT is due to formation of lamella α+β microstructure which has higher ductility. The anisotropy observed in the fracture toughness values is said to be caused by the columnar PBG boundaries which also cause defection of propagating cracks giving rise to the torturous crack path [97]. For the LPBF Ti-6Al-4V, the microstructure with equiaxed PBG boundary will result in near isotropoic K_{IC} values. Similarly, a weak texture typically observed in the microstructure suggests that the anisotropy observed in the fracture toughness is independent of the texture for both types of PBF process.

Generally, for R > 0.5 these effects are less prevalent, and an intrinsic threshold value is measured.

The strong influence of the underlying microstructure in the near-threshold regime means that through HT and subsequent grain growth, the threshold values can be increased and anisotropy in ΔK_{th} can be reduced.

Leuders et al. [124] concluded that the residual stress and porosity do not cause significant adverse influence on the fast fracture toughness values. Cain et al. [120] have suggested that for the residual stress and anisotropy in fracture toughness of LPBF Ti-6Al-4V are inversely correlated.

Table 2.10. Fatigue crack growth properties of EPBF Ti-6Al-4V.

Condition	R-Ratio	Orientation	ΔK_{th} (MPa√m)	Paris slope - m	C (m/cycle)	K_{IC} (MPa√m)	References
AB	0.1	Z-X	3.7	-		49.7	[150]
	0.5	Z-X	2.7				
	0.8	Z-X	2.2				
	0.1	X-Z	4.2			56.6	
	0.5	X-Z	3			28.8	
	0.8	X-Z	2.9			17.7	
	0.1	Z-X	6			82	

Condition	R-Ratio	Orientation	ΔK_{th} (MPa√m)	Paris slope - m	C (m/cycle)	K_{IC} (MPa√m)	References
BA (1100 °C for 0.5 h, FC)	0.5	Z-X	4.8				
	0.8	Z-X	4.5				
	0.1	X-Z	6				
	0.8	X-Z	4.6				
AB	0.1	X-Z	5.7	3.1		74	[151]
		X-Y	3.8	3.9		74	
	0.3	X-Z	3.6	2.1		74	
		X-Y	3.8	2.7		74	
		Z-X	3.8	2.6		65	
		Y-X	5.1	2.9		67	
	0.7	X-Z	3.5	1.4		74	
		X-Y	3.4	1.9		74	
AB	0.1	Z-X	3.5	-	-	-	[143]
		X-Z	3.2				
AN (950 °C for 2 h, WQ) + SRL (500 °C for 7 h, AC)	0.1	Z-X	5	-	-	-	
		X-Z	3.4				
AB	0.1	X - Z	5.7	4.1	-	82	[87]
		X - Y	3.8	2.9	-	-	
	0.3	X - Y	3.4	2.4	-	60	
		Z - X	4	2.6	-	65	
	0.7	X - Z	3.5	1.4	-	-	
		X - Y	3.4	1.9	-	60	
HIP (950 °C for 3 h at 100 MPa, FC	0.3	X - Y	4.8	1.1	-	61	
		Z - X	5.1	1.4	-	55	
AN (720 °C for 2 h, FC)	0.1	Z - X	4.2	-	-	60	[72]
HIP (920 °C for 2 h at 105 MPa, FC)	-	-	4.8	-	-	60	
AN (720 °C for 2 h, FC)	0.7	Z - X	2.9	-	-	30	

Table 2.11. Fatigue crack growth properties of LPBF Ti-6Al-4V.

Condition	R-Ratio	Orientation	ΔK_{th} (MPa$\sqrt{m}$)	Paris slope - m	C (m/cycle)	K_{IC} (MPa$\sqrt{m}$)	References
-	0.1		4.0 - 5.0	3 - 4.8		65 ± 35	[146]
AB	0.1	Z-X	1.5	-	-	-	[106]
HIP (820°C for 3 h, FC at 3°C/min)	0.1	Z-X	3.3				
		X-Z	3.5				
HIP (950°C for 3 h, FC at 3°C/min)	0.1	Z-X	4.1				
		X-Z	4.5				
BA (1020°C for 1 h, AC)	0.1	Z-X	6.2				
		X-Z	7.3				
AB	0.1	X-Y	2.7	2.77	-	-	[147]
	0.3	Z-X	2.0				
		X-Y	2.1				
	0.45	X-Z	1.7				
	0.6	Z-X	1.9				
		X-Z	1.6				
		X-Y	1.7				
	0.77	X-Z	1.5				
	0.8	X-Y	1.6				
	0.84	X-Z	1.5				
	0.85	X-Y	1.5				
	0.88	Z-X	1.8				
	0.92	Z-X	1.8				
SRL (480°C for 8h, FC)	0.1	Z-X	2.7	2.77	-	-	[147]
		X-Z	2.1				
		X-Y	3.1				
	0.3	Z-X	2.2				
		X-Z	2				
		X-Y	2.7				
	0.6	Z-X	2				
		X-Z	1.8				
		X-Y	2				
	0.75	Z-X	1.9				
	0.85	X-Y	1.6				
SRL (480°C for 8h, FC)	0.86	X-Z	1.5	2.77	-	-	[147]
	0.88	Z-X	1.9				

Condition	R-Ratio	Orientation	ΔK_{th} (MPa$\sqrt{m}$)	Paris slope - m	C (m/cycle)	K_{IC} (MPa$\sqrt{m}$)	References
AN (910°C for 8h, WQ) + AN (750°C for 4h, FC	0.1	Z-X	5.6	3.51	-	-	[147]
		X-Z	6				
		X-Y	6.2				
	0.3	Z-X	4.5				
		X-Z	4.9				
		X-Y	5.3				
	0.6	Z-X	3.1				
		X-Z	3.7				
		X-Y	4.1				
	0.77	X-Y	4.3				
	0.82	Z-X	2.7				
	0.88	X-Z	3.3				
	0.91	X-Y	3.7				
	0.92	X-Z	2.8				
SRL (650 °C for 3 h, FC)	0.1	Z-X	5.6	2.53	-	52	[86]
		X-Z	5.7	3.31	-	55	
SRL (650 °C for 3 h)	0.1	Z-X	4.12	-	-	-	[152]
		X-Z	3.07				
SRL + HIP	0.1	X - Y	3.74 ± 1.1	-	-	-	
AN (720 °C for 2 h, FC)	0.1	Z - X	3.2	-	-	49.5 ± 1.5	[72]
HIP (920 °C for 2 h at 105 MPa , FC)			4.4	-	-	60	
AN (720 °C for 2 h, FC)	0.7	Z - X	2	-		30	
AB	0.1	X-Y	-	3.37	5.79E-12	28 ± 2	[120]
		X-Z		4.17	7.51E-12	23 ± 1	
		Z-X		4.41	2.08E-12	16 ± 1	
SRL (650 °C for 4 h, FC)	0.1	X-Y	-	5.84	9.93E-15	28 ± 2	
		X-Z		3.24	1.16E-11	30 ± 1	
		Z-X		3.35	8.85E-12	31 ± 2	
AN (890 °C for 2 h, FC)	0.1	X-Y	-	3.83	2.04E-12	41 ± 2	[120]
		X-Z		3.11	1.71E-11	49 ± 2	
		Z-X		2.94	2.58E-11	49 ± 1	

Condition	R-Ratio	Orientation	ΔK_{th} (MPa√m)	Paris slope - m	C (m/cycle)	K_{IC} (MPa√m)	References
AB	0.1	X-Y	6.3	2.61 ± 0.25	1.20E-07	33.3 ± 3.9	[153]
		X-Z	5.8	2.37 ± 0.27	5.80E-08	36.0 ± 22.6	
		Z-X	5.9	2.45 ± 0.63	1.60E-07	33.4 ± 3.6	
AB	-	X-Y	-	-	-	37	[88]
AN (950°C for 1 h, FC)		X-Y	-	-	-	86	
HIP (915°C for 2 h at 105 MPa , FC at 11°C/min)		X-Y	-	-	-	58	
SRL (650°C, 3 h, FC)	0.1	Z-X	3.48	-	-	73	[137]
AB	0.1	X-Y	-	3.376	5.00E-12	52.4 ± 3.5	[154]
AB	0.1	Z-X	1.4	-	-	-	[124]
		X-Z	1.7	-	-	-	
AN (800°C for 2 h, FC)		Z-X	3.9	-	-	-	
		X-Z	3.7	-	-	-	
BA (1050°C for 2 h, FC)		Z-X	3.7	-	-	-	
		X-Z	6.1	-	-	-	
HIP (920°C for 2 h, FC)		Z-X	4.2	-	-	-	
		X-Z	3.9	-	-	-	

2.7 AM Components for Aerospace Application

The Topology Optimisation (TO) technique refers to a mathematical design method often used to optimize the material layout in structural applications for the given boundary conditions, set of loads and constraints [155]. The TO methods are based on simulations and iterative shape optimization, and utilize the Finite Element Method (FEM) to improve design performances [155]. The TO technique allows optimization of shape and geometry for highly efficient designs with components internal and intricate features that are not feasible otherwise [156]. The fundamental opportunities for metal additive manufacturing in aerospace applications include: significant cost and lead-time reductions, novel materials and unique design solutions, mass reduction of components through highly efficient and lightweight designs, and consolidation of multiple components for performance enhancement or risk management, e.g. through internal cooling features in thermally loaded components or by eliminating traditional joining processes [157]. These opportunities are being commercially applied in a range of high-profile aerospace applications including liquid-fuel rocket engines, propellant tanks, satellite components, heat exchangers, turbomachinery, valves, and sustainment of legacy systems

[157]. The TO methods and guidelines to achieve optimised designs of AM parts and brackets have been studied by various researchers as one of the key steps to adopt the AM technology in the aerospace industry, where design goals, product price, and time to market are all independent and important considerations [158]. Therefore, the advanced high-performance components designed with complexity and built using AM see beneficial applications in aerospace application. A few examples of using the TO technique to design AM parts for aerospace application are discussed below.

Emmelmann et al. [159] defined a novel approach which effectively considered the structural optimisation tools, bionic structures and guidelines to adopt the LPBF technology. Based on the innovative design process adopted, they achieved > 40% weight saving for the LPBF bracket design, see Fig. 2.24 [159].

A successful manufacturing of a complex thrust chamber assembly for the demonstrator AM rocket engine designed by Cellcore is shown in Fig. 2.25 [160]. The thrust chamber was built in Inco 718 material with integrated lattice internal cooling channels which demonstrated the current capability to manufacture a complex thrust chamber assembly through AM. The structural cooling design provides an optimal relationship between stability and mass application of the thrust chamber [160].

Similarly, GE Aviation have successfully produced the fuel nozzle tips using AM where the number of parts in a single fuel nozzle tip was reduced from about 20 pieces previously welded together to a one whole piece. Furthermore, the nozzle tip's weight was cut by about 25 % [161]. The nozzle tips were developed for the LEAP engine, GE commercial aviation's best-selling engine with fuel efficiency up to 15 percent better than the best CFM56 engines. Utilizing the LPBF technology with a Cobalt-Chrome alloy, the fuel nozzle tip, shown in Fig. 2.26, is installed on several engines currently in service on commercial aircraft [161].

Fetisov et al. [162] used the TO technique to produce a lightweight aerospace part to be built using the LPBF process. As a result, the optimised part for LPBF build was 5 times less in weight as compared to the conventional design, and, in this novel design, 25 sub-parts were replaced by only one part, see Fig. 2.27 [162].

Furthermore, Plocher et al. [163] carried out a detailed optimisation study and concluded that the Design for AM (DfAM) with holistic design approach, aspects of digitisation, improvement in CAD/CAM software, loads conforming geometries and required performance parameters form a key part to the product optimisation for AM [163]. Plocher et al. [163] used the density based approach with isotropic properties in the product optimisation exercise and recommended to optimise the geometries with functionally graded structures which has better conformance to the load trajectories.

Xiao et al. [164] did a detailed structural optimisation study on an antenna bracket manufactured by selective laser melting. The optimisation study was aimed to improve its natural frequencies and reduction in deformation compared to its baseline design. The fully optimised antenna bracket achieved a mass decrease of 30 % percent and a fundamental frequency increase of 50 %, with desired forming accuracy and improvements in strength, stiffness and dynamic characteristics and improved overall performance of structures. The optimised antenna bracket is shown in Fig. 2.28 [164].

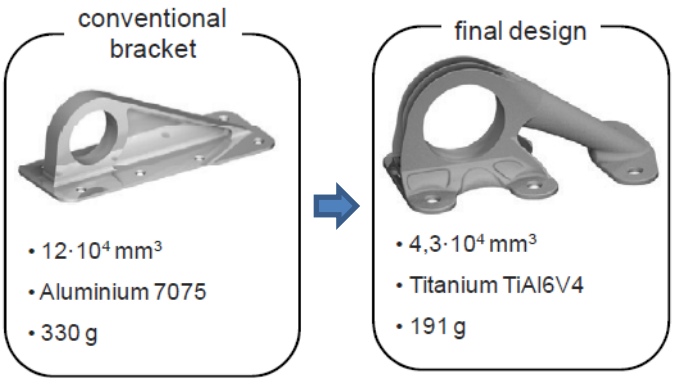


Fig. 2.24. Development of a weight optimised bracket with > 40% weight savings, based on the innovative design process considered by Emmelmann et al. [159] for LPBF build.

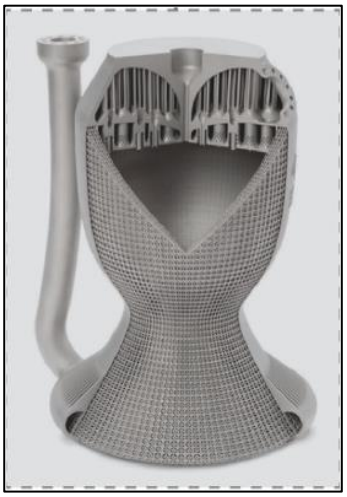


Fig. 2.25. A complex thrust chamber assembly with integrated lattice internal cooling channels built using AM [160].



Fig. 2.26. A single part fuel nozzle tip assembly built using the LPBF technology in Cobalt-Chrome alloy, developed by GE aviation [161].



Fig. 2.27. A single part weight optimised geometry developed for LPBF build using the topology optimisation technique by Fetisov et al. [162].

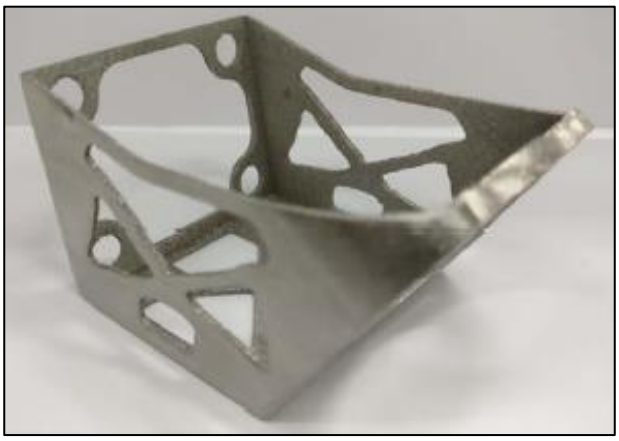


Fig. 2.28. A weight optimised antenna bracket developed and analysed by Xiao et al. [164].

Furthermore, a joint study between EOS and Airbus was carried out on to optimise the Airbus A320 nacelle hinge bracket shown in Fig. 2.29 [165]. The optimised hinge bracket offered > 60% weight savings compared to the conventionally manufactured hinge bracket, and was designed to be manufactured from Ti-6Al-4V using the LPBF technique (see Fig. 2.29(a)).

(a)

(b)



Fig. 2.29. Original nacelle hinge bracket (top) and final TO optimized design (bottom). Original steel bracket mass = 0.918 Kg; AM bracket in Ti-6Al-4V = 0.326 Kg [165].

Hence, an optimal design of AM components is often needed for cost, weight and efficiency purposes [166, 167]. Additionally, for safety critical applications, it becomes essential that these part designs are assessed in detail and qualified against the defined service goals/life. The mechanical and fatigue properties obtained by testing of laboratory specimens may not be directly suitable for consideration in the lifing assessment of AM parts, which is due to possible differences in geometry and size, which would directly affect the thermal histories experienced during the AM building process. As a result, this will affect the microstructural features, surface roughness, defects, residual stresses etc. [62]. Although, the HCF performance of LPBF Ti-6Al-4V has been studied widely at specimen level, studies on the fatigue performance (LCF and HCF) of geometrically complex AM parts are very limited [124]. Brusa et al. [168] studied the fatigue performance of a structural bracket design and suggested that a bracket made using the DMLS process was better than the one made using the EPBF process. The poor performance of EPBF bracket was due to the larger number of internal defects and higher surface roughness found in the EPBF bracket, but the fatigue performance of the brackets was not established within this study. Leuders et al. [169] did an experimental study to compare the fatigue performance of a topologically optimised component made using the LPBF and Investment Casting (IC) processes, and showed that the fatigue performance (at R = 0.1, where loading ratio R = minimum stress / maximum stress) of the IC component was ~50% better, studied using the fatigue load at 10^6 cycles, than the LPBF component. Mardaras et al. [170] have suggested a structural analysis approach to perform Fatigue and Damage Tolerance (FDT) assessment for AM parts for aerospace applications. They concluded that the effects of internal defects, surface roughness, and loading ratio R, including the overload effect, are critical to establish design limits and material properties needed for FDT assessments. However, they did not present an actual case study on FDT [170].

2.8 Applications to Aerospace

The aerospace sector covers the civil aerospace sector including business jets, military aircrafts, space launch systems, satellites and missiles systems. Despite several challenges (including the recent decline in air travel due to Covid-19 pandemic), the revenue of aerospace sector is predicted to grow to US$ 430.87 billion by the year 2025 [13]. The long-term order books for commercial aircrafts, greater military expenditure globally, newer projects in the space sector and increased research allocations in the aerospace sector are the main factors behind this optimistic growth prospects [13].

In the aerospace sector, high-performance materials are used to manufacture parts with increasingly complex designs in lightweight which is frequently and responsibly done to meet commercial orders or mission requirements while adhering to stringent regulatory requirements of Federal Aviation Administration (FAA)/ European Aviation Safety Agency (EASA) [11]. The conventional manufacturing systems and strategies have been developed over many decades to accommodate these aerospace design objectives for numerous application types. In aerospace sector, AM is rapidly becoming a desired process for designing, testing, tooling and production of the aircraft and engine parts, ground support systems, and also for repair of parts and assemblies. AM is helping the aerospace supply chain to become more cost effective, agile and efficient in bringing new products into market with stricter timescales [11, 171, 172]. Over the last decade, the research into AM in aerospace sector has also witnessed exponential growth with significant number of scholarly publications and technical reports [13, 172]. The AM is predicted to have a profound impact on the design and manufacturing of aerospace parts and this digital manufacturing transformation will increase its market size in the aerospace sector to US$ 3.2 billion by the year 2025 [173, 174] in both product and services, with an average Compound Annual Growth Rate (CAGR) of 26% [174]. The overall global AM market is forecasted to be around US$ 21.5 billion by the year 2025 [174]. There are 20,000 commercial aircrafts and 15,000 business jets currently in service and this fleet size is expected to double in the next 20 years' time horizon [174]. Due to this growing number of aircrafts, the through-life-support services in the aerospace industry are estimated to go beyond US$ 1.9 trillion by the year 2035, which therefore puts AM into a strong position [174]. Consequently, the leaders of the aerospace industry have been constantly exploring the possible use of AM to produce parts, and, in recent times, they have started to test the performance of AM parts of different types including hinges, brackets, latches, light-weight support structures, blades and combustor tiles with intricate flow channels, fuel nozzles and integrated piping system, all of them targeting for better fuel efficiencies [171, 172].

Due to the high market entrance barriers, complexity, experience and skill level involved, there are only a few Original Equipment manufacturers (OEM) who are designing and manufacturing the engines, aircrafts and their main component systems. Furthermore, due to the stringent standards, the maintenance process for the engines and aircrafts are highly regulated, and therefore the Maintenance Repair and Overhaul (MRO) organizations need to be approved by the aviation authorities such as the FAA and EASA. The complex supply chain for the OEMs requires faster maintenance system and thus a higher level of inventory. The overall inventory cost in the aircraft industry globally is estimated to be

around US$ 50 billion [172]. Manufacturing in the aerospace sector is driven by several objectives such as;

Functional Performance: The components and systems in aerospace sector are safety critical components that must operate in their intended complex operating environments for challenging and complex flight profiles.

Light-Weighting: The component mass reduction directly relates to enhanced economical and technical performances, including reduction in fuel cost, lower emissions, larger payloads and increased flight ranges. Each kilogram of weight reduced on commercial aircraft can roughly save around US$ 3000 worth of fuel and corresponding reduction in the carbon emissions per year [172].

Complexity: Aerospace component designs are often complex and involve several parts in an assembly with complex and competing design and performance parameter requirements in the intended environment.

Certification: The regulatory bodies (such as EASA and FAA) need to be confident that the components and assembly designs are fundamentally well understood, and can be repeatably designed and inspected such that the compliance against reliability and safety expectations are demonstrated. These certification requirements vary according to the criticality of the system (i.e. its criticality against safety, mission or functional).

Lead Time Reduction: The production volumes in aerospace sector is usually small but with relatively stricter delivery schedule needed for rapid product certification and flexibility in design and manufacturing of high value components.

Cost Management: throughout the product life cycle, the cost management applies to component design, manufacturing, supply chain efficiency and maintenance in service.

Sustainability: Sustainment challenges include part availability for ageing aircraft, remanufacture/repair, and re-certification of systems/aircrafts for alternate usage.

Each of these objectives have strong interactive relationship between them and the relative importance of these factors would depend upon the specific aerospace application. Each of these factors must therefore be considered carefully for an optimal product design solution meeting the life cycle requirements. Furthermore, the capabilities, benefits and results offered by AM are also highly interacting, shown in Fig. 2.30, and are discussed below [172, 174];

Mixed Materials: The use of multiple/composite materials or functionally graded materials using the hybrid manufacturing technique is a key attribute offered by AM, which allows for a possible and selective variation in material composition for the part being built. Additionally, to achieve functionality and improved part performance, conductive sensors and electronic devices could also be embedded within the printed parts through AM builds.

Complex Geometries: AM enables functional part designs which are unconstrained by the geometric parameters imposed by the conventional methods of manufacturing. This encourages the designers and practicing engineers to explore the novel and complex geometries and topologically optimised parts which meet the functional requirements and optimal parts utilisation leading to reduced number

of assemblies in a system / sub-system, offering significant cost savings in terms of weight and assembly times. Furthermore, the AM allows for a high degree of personalisation whereby enabling bespoke products to be delivered at speed and produce items in small batches at a reasonable cost even in serial production. Novel and intricate geometries such as cellular structures, lattice, honeycomb, and optimised parts with bionic features are being designed for AM to improve overall performance of aircraft structures. Optimization of parts for specific functions and requirements such as stress distribution, cooling patterns, air flow channelling etc. can also be achieved via optimisation of parts design for AM.

Material Process Efficiency: AM build parts are the near net shape solutions leading to reduction in material scrap and an improved Buy to fly (BTF) ratio. Furthermore, in the PBF process, the un-melted metal powder can still be used in the next build cycles meaning that the metal powder remains mostly in recycling loop, possibly leading to 90% reduction in material wastage, compared to the conventional machining process. The BTF ratio is a weight ratio between the original raw material and a finished component, which for the traditional methods of manufacturing sits around 15-20 compared to a BTF ratio of 1, achievable through AM. The aerospace materials are often expensive, and the global market for aerospace materials is estimated to be at US$ 21.9 billion in the year 2020 and is projected to reach to a revised size of US$ 32.4 billion by 2027 [175]. Furthermore, the aerospace materials are expensive which makes the AM an attractive and preferred solution to minimise material wastage.

On-Demand Manufacturing: The cost of tools and jigs in the conventional methods of manufacturing can often limit the desired improvement in part designs over its life cycle. The AM process removes the need for bespoke tooling and provides encouragement towards a continuous improvement in part design to derive efficiency in part performance, and save cost and weight as the part design is gets matured [172, 174]. The production volumes for aircraft parts are usually limited, which makes AM a great choice to produce quality parts in limited quantity. Since, AM parts are built using the CAD files, the part (new and spare) builds and repair of parts can be done near the end users' sites on-demand which not only saves the cost of transportation but also reduces the lead time.

Additionally, the materials and machines can easily be distributed and installed globally which once done, along with growth in digital architecture, provides a significant opportunity for MRO. For maintenance of legacy products, cases where legacy manufacturing tools have retired, AM can be used for repairs and low volume replacements. AM is also being utilised to produce rapid tooling such as mandrels, dies, moulds, jigs and fixtures, which is an essential part of the conventional methods of manufacturing and are often produced in limited quantities.

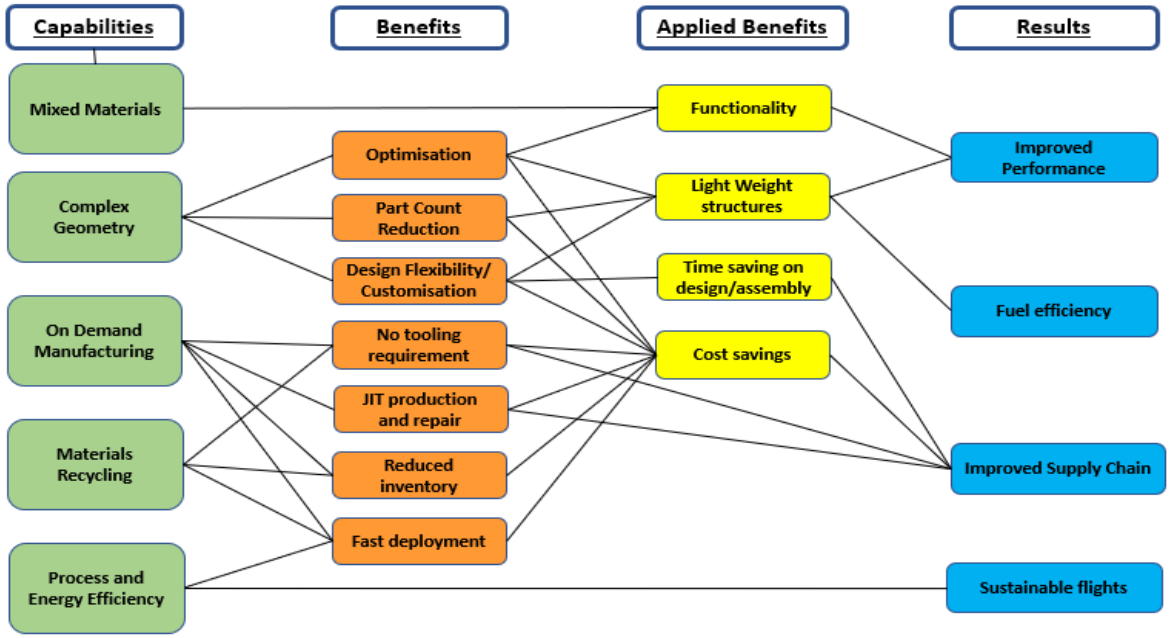


Fig. 2.30. Additive manufacturing within the aerospace industry: key attributes covering AM capabilities, its benefits, applied benefits and results

Despite of wide applications and various benefits of AM discussed above, there are still several challenges which need to be discussed and gradually worked upon to mitigate the identified risks and shortcoming, and build confidence of practicing engineers and researchers for a smooth and efficient adoption of AM in the aerospace sector [8, 13, 172].

Certifications and Standards: The engine components are safety critical and often require stringent assessment plans to certify these components and make them airworthy. Failure of these components can lead to extreme loading events, such as a Fan Blade Off (FBO) or a Core Blade Off (CBO) event. The certification process requires demonstrating the quality of the part, consistency in manufacturing and repeatability in the production process to the certification authorities. Development of a quality product requires an enormous amount of resources and investments in research and development, and manufacturing process. Furthermore, the demonstration towards certification compliance involves acquiring quality data related to parts within the regulatory framework prescribed by the certification authorities. The limitations associated with the dimensional non-conformances, process limitations, poor surface, lack of part-to-part repeatability and life limitations indicate some of the challenges in the certification routes of AM parts. The certification agencies like EASA and FAA have been working with the OEMs, the aerospace market leaders, academia, researcher and the organisations involved in developing the standards (ISO, ASTM, SAE etc.) to develop the policies, guideline documents and standards for applying AM into the aerospace sector and to ensure the continued safety in operation [176]. The standards specific to AM are still evolving and are in parallel, some OEMs have developed specific solution guidelines for certifying specific components in their sub-systems using the data and practices derived from their independent research [172]. For AM, the published report [176] details the key aspects and current industry best practices in the areas of; development of materials and processes,

inspection techniques, acceptance routes and quality control, part and system qualification, consolidation of material allowable and design values, and different means of compliance to applicable regulations. As a conclusion this suggests that the part qualification and its certification can successfully be achieved using the proven established methodologies as a baseline, supplemented with additional focus on issues which are specific to AM.

Structural Integrity: For mission critical aerospace applications, ensuring structural integrity of parts during flight is critical for the safety of flight. The dynamic loading types, which causes fatigue damage accumulations, and is of particular interest within the aerospace applications include; LCF and HCF, thermal cycling, impact and subsequent run-down, and wind-milling. The static mechanical properties for AM metallic materials are well researched and are observed to be exceeding that of conventionally manufacture materials. However, there remains a lack of robust design data for the dynamic material properties like creep and fatigue. The LCF and HCF fatigue properties of AM metals are in general substandard compared to the conventional manufacturing methods owing to the defects, residual stress and poor surface roughness observed in the AM products. Effect of these factors to establish the fatigue design allowable for lifing purposes become important while assessing the AM parts.

Design for AM: To achieve the best manufacturing quality, and to minimise the requirement of build supports, the design for AM shall be optimised. Additionally, the build simulations can be performed in parallel to determine optimal orientation of part on the build platform to minimise residual stresses and resulting deformation of part, and also to minimise the number of build support structures. A good simulation would require a skilled engineer, computational power and well defined material properties; both mechanical and thermophysical. The loading paths, and structural, thermal and dynamic environments are often not well defined during the design optimisation stage, which could result either in an inadequate design or in a non-optimised product with high safety margins.

Powder Recycling: Post an AM build, the powder is typically removed from the part using the rotational movements, or by tapping and blowing the powder out of surface cavities, channels and intricate features. The powder particles within the intricate features of the AM part can sometimes be difficult to remove and it may permanently be trapped if not removed prior to HT. Also, to produce a conforming part, care must be taken to not damage or distort the AM part while carrying out the support removal, HT, surface machining and handling during assembly.

Non-Destructive Testing (NDT): The NDT techniques are used for identifying flaws such as pores and cracks in AM parts, and the conventional NDT techniques such as the radiographic testing, dye penetrant, eddy current and ultrasonic testings may not be suitable to inspect complex features of AM parts [13]. The X-ray Computed Tomography (CT) scan has been shown to be successful for inspection of anomalies within the AM parts, however, its poor resolution for bigger and thicker parts, cost and scanning time could be the limiting factors. If the material is highly absorbing for X-rays then it can make the CT scans ineffective and, in these cases, use of high energy x-ray sources are used which can sometimes be expensive and can be less readily available. To mitigate these limitations, many in-

process monitoring tools are being developed to scan through the anomalies being developed during the process itself rather than during the post processing stage.

Size of AM Parts: The challenges associated with scaling up of the AM parts come due to the low printing speed, resolution and size of the build chamber. The LPBF builds must have an optimal printing speed to minimise the size and distribution of defects due to LOF, and to produce better surface finish of the part. The multi-laser machines and efforts to build the machines with bigger size build chambers will help to build the AM parts in bigger size and with faster speed.

Simulation Methods: To predict the performance of AM parts, including the characteristics such as stresses/strains, surface finish, residual stresses, distortion etc., using simulation based techniques would require reliable methodologies. The optimisation of parameters for different structural and load bearing applications without over-simplification is required, which will then be required to included in the CAD and Finite Element (FE) packages to achieve a good accuracy in the stress predictions and lifing assessments of AM parts.

Thin Wall AM Structures: For thin wall hollow structures, controlling the deformation due to thermal stresses, thermal movements and sagging could be quite difficult. Furthermore, the low surface finish of AM parts means that the thin walled AM structural parts will have lesser cross-section to bear the imparted loading. Hence, thickness of such structures need to be scaled up during the design stage appropriately to meet the strength requirements. Precise manufacturing of powder particles and optimisation of process parameters are needed to achieve the thin walled AM products with quality.

2.9 Knowledge Gaps and Opportunities

- In this chapter, a detailed literature review has been carried out to study and discuss the range of mechanical, HCF and FCG properties of PBF Ti-6Al-4V. The properties gathered were observed to be dependent on AM processes and process parameters. At the same time, the post processes such as the machining, SP, HTs, HIP etc. were also seen to have varying degree of impact on the mechanical, fatigue and fracture properties. Anisotropy in mechanical and fatigue properties was also seen due to the specific microstructure with columnar PBG which is typically observed in the PBF Ti-6Al-4V. The orientation of LOF voids also seems to be contributing towards causing anisotropy in the mechanical and fatigue properties of AM Ti-6Al-4V.
- The properties presented in Tables 2.6 to Table 2.11 provide information about the extensive research studies performed to explore the mechanical, fatigue and fracture properties of AM Ti-6Al-4V. However, it is important to note that these properties were obtained from the tests carried out at the specimen level and at RT only. The effect of ET on these properties of AM Ti-6Al-4V has not been explored and understood in great details. Since, the aeroengine components will typically operate in ET and will experience vibratory loading environment, it is of significant importance that the effect of ET on mechanical and fatigue properties of AM Ti-6Al-4V is explored in detail. Also, it is important that the fatigue performance (LCF and HCF) of

AM Ti-6Al-4V is explored at RT and ET to use the properties in the AM parts design to ensure sufficient robustness and durability against the operating loadings in an engine environment.

- Furthermore, due to the fact that different thermal histories are experienced by the specimens and components during the AM build process, which could be due to differences in geometry and sizes, the fatigue (LCF and HCF) performances of AM Ti-6Al-4V components are expected to be different than the fatigue behaviour of AM Ti-6Al-4V obtained at specimen level.
- The component design and standardisation for safety critical application, such as aerospace, remains a challenge. Till date, to the author's knowledge, there are no studies which investigate the fatigue performances of AM Ti-6Al-4V components. This creates opportunity to investigate and analyse the AM Ti-6Al-4V component to ensure suitability and certification of component design before the AM component can enter into aeroengine service.
- As studies on component fatigue performances are carried out, the possible mechanisms and features responsible for failure of AM components under cyclic loading need to be investigated so that these can be accounted for at the design and assessment stages in the component design cycle for AM.
- For AM components, the effect of defects, to some extent, is implicit in the material properties collected by fatigue testing of specimens. These properties are then used in the lifing assessment methodologies which are based on the traditional safe life approach utilising the S-N data. However, a FCG life prediction method is still needed to be explored as part of the ongoing efforts to understand the effect of defects on fatigue life of AM components for cases where either the S-N fatigue data availability is limited or where the size of defects in the AM component being assessed fall outside of the statistical bounds of the defects found in the specimens used to collect the fatigue properties.

Based on the identified gaps and opportunities, the main objectives of this research study were set to fulfill the identified gaps and to meet the expectations of the sponsoring industrial body. The main aim and objectives of this research study (see Chapter 1) were based on the customer (R-R) needs and requirements and were in line with the technology strategy of R-R around AM Ti-6Al-4V.

-----x x x x x x x-----

CHAPTER 3

3 Materials and Methods

Since the current research study is based on the range of experimental results observed from the mechanical and fatigue testing of PBF Ti-6Al-4V material at specimen and component levels, it becomes necessary to fully explain the materials, manufacturing methods and machines used to manufacture the test specimens, as has been done in this chapter. Furthermore, in order to investigate the test results and relate them to the mechanical and fatigue performances of the AM Ti-6Al-4V, it was necessary to characterise the PBF Ti-6Al-4V material micro-structure, fracture surface, defects and hardness. Section 3.1 includes the materials that were used for the manufacturing of PBF (EPBF and LPBF Ti-6Al-4V) test specimens and components for the experiments carried out in different phases as discussed below. The methods and microscopy techniques used for various physical characterisations (microstructure, surface roughness, micro-hardness, defects and fracture surfaces) are presented in section 3.2. The manufacturing details, including design dimensions/specifications and build parameters, used to manufacture the EPBF and LPBF test specimens and brackets are described in section 3.3. The details of test matrix, testing methods and specifications and test machines have been included in section 3.4.

Due to the sequence adopted for manufacturing of test specimens, the testing campaign through the duration of this research study was split into three different phases as discussed below:

Phase 1: In this phase, the tensile behaviour of EPBF Ti-6Al-4V material at specimen level at RT and ETs was studied.

Phase 2: This phase covers the following types of testing;

1. Tensile behaviour of LPBF Ti-6Al-4V material at specimen level at RT and ET.
2. LCF behaviour of LPBF Ti-6Al-4V material both at specimen level at RT and ET.
3. HCF behaviour of LPBF Ti-6Al-4V material at specimen level at RT.
4. LCF behaviour of a LPBF Ti-6Al-4V bracket at RT.
5. HCF behaviour of a LPBF Ti-6Al-4V bracket at RT.

Phase 3: This phase covers the following types of testing;

1. HCF behaviour of LPBF Ti-6Al-4V material at ET.
2. LCF behaviour of a LPBF Ti-6Al-4V bracket at ET.

It is to be noted that the mechanical and fatigue testing was performed at room temperature (20 °C) and at elevated temperature (up to 400 °C). The maximum test temperature of 400 °C was decided to test the Ti-6Al-4V to its maximum suggested operating temperature of 400°C [22]. This is because at temperature higher than 400°C, due of the high affinity of titanium to oxygen, formation of a very thin oxygen layer on the surface and a hard and brittle oxygen diffusion zone develops in the underneath substrate due to inward diffusion of oxygen happens. However, the maximum operating temperature of Ti-6Al-4V is often around 350°C for its safe and reliable performances in several general applications [31].

3.1 Materials

3.1.1 EPBF Specimen Manufacturing

To make the EPBF tensile test specimens in Phase 1 of the testing, Ti-6Al-4V (Grade 23) Extra Low Interstitials (ELI) plasma atomised powder, supplied by Arcam, was used. The Ti-6Al-4V alloy powder had the mean chemical composition shown in Table 3.1, which is in line with the ASTM B348 [20] for all elements except for the oxygen content (maximum allowed is 0.13 % wt). The Ti-6Al-4V powder used had a higher oxygen content of 0.195 % wt, which was due to the recycling and blending of the used powder with the fresh powder, and is expected to have a negative impact on material ductility.

Table 3.1. Mean chemical composition of the Ti-6Al-4V powder used in the EPBF process–Phase 1.

Alloying Elements	Ti	Al	V	Fe	O	N	H	C
Mean (% wt)	Balance	6.04	4.02	0.19	0.195	0.022	0.002	0.01095
Standard Deviation (± %)		0.68	0.05	0.00	-	-	-	0.00046

The as received powder particle size distribution is shown in the Table 3.2. Powder particle morphology consisted of 74.56% (vol.) of particles considered as highly spherical, with 94.02% (vol.) particles having an aspect ratio > 0.8.

Table 3.2. Distribution of particle size of the Ti-6Al-4V powder used in the EPBF process – Phase 1.

Parameter	D10 (µm)	D50 (µm)	D90 (µm)	%<45 µm	% > 106 µm
Mean	52.00	72.70	102.00	2.92	7.94
Standard Deviation (± %)	1.13	1.39	1.86	10.96	12.22

3.1.2 LPBF Specimens and Bracket Manufacturing–Phase 2

To make the Phase 2 LPBF test specimens, Ti-6Al-4V (Grade 23) ELI plasma atomised powder (Supplied by LPW Technology, UK) was used. The Ti-6Al-4V alloy powder had the mean chemical composition as shown in Table 3.3, which is in line with the ASTMB 348 [20];

Table 3.3. Mean chemical composition of the Ti-6Al-4V powder used to make the LPBF specimen and bracket – Phase 1.

Alloying Elements	Ti	Al	V	Fe	O	N	H	C
Mean (% wt)	Balance	6.4	4.0	0.19	0.12	0.02	0.002	0.01095

From the data analysis carried out by the supplier, the powder size was distributed between 15 – 45 μm with a mean of 30 μm. This distribution analysis also found that only 3% of powder particles were below 16 μm in size and only 2% of the powder particles were above 45 μm in size.

3.1.3 LPBF Specimens and Bracket Manufacturing–Phase 3

To make the Phase 3 LPBF test specimens, Ti-6Al-4V (Grade 23) Extra Low Interstitials (ELI) plasma atomised powder (Supplied by LPW Technology, UK) was used. The Ti-6Al-4V alloy powder had the mean chemical composition shown in Table 3.4, which again is in line with the ASTMB 348 [20];

Table 3.4. Mean chemical composition of the Ti-6Al-4V powder used to make the LPBF specimen and bracket – Phase 3.

Alloying Elements	Ti	Al	V	Fe	O	N	H	C
Mean (% wt)	Balance	6.53	4.03	<0.05	0.083	0.007	0.0025	0.01

3.2 Physical Characterisation

3.2.1 Material Microstructure

For metallographic characterisation, the sample sections were cut and hot mounted in bakelite resin. The mounted samples were polished first with the SiC papers (p240, 400, 800 and 1200 grit sizes), followed by a fine polish using the plane-cloth (6 μm) and alpha-cloth (1 μm) in diamond suspension, and finally using the chemi-cloth in colloidal silica solution. Only the samples for SEM examination were etched using the Keller's etchant (190 ml of distilled water, 5 ml of nitric acid, 3 ml of hydrochloric acid and 2 ml of hydrofluoric acid) with 20 seconds immersion. A Nikon Eclipse LV100ND microscope was used to carry out optical microscopy for preliminary examination of the microstructure. The SEM examinations were carried out using a Quanta FE600 SEM for microstructural and fracture surface characterisations. Additionally, a JEOL 7100F Field Emission Gun Scanning Electron Microscope (FEG-SEM) was used to perform Electron backscatter diffraction (EBSD) scans for a detailed microstructure characterization. The FEG-SEM is equipped with an Oxford Instruments AZtec HKL Advanced EBSD system (with NordlysMax3) for crystallographic characterization. The EBSD scans were conducted at 15 kV with the scan area and step size chosen as; (i) 90 μm x 90 μm with a step size of 0.50 μm for scans on EPBF samples (Phase 1), (ii) 125 μm x 125 μm with a step size of 0.50 μm for scans on EPBF tensile tested specimen (Phase 1), (iii) 66 μm x 66 μm with a step size of 0.20 μm for scans on LPBF samples associated with the HCF study (Phase 2), and (iv) 150 μm x 150 μm with a step size of 0.25 μm for scans on LPBF samples (from as-built sample, LCF tested specimen and fractured bracket struts) associated with the LCF studies in Phase 2 and Phase 3. The postprocessing software such as HKL channel and AZtec Crystal software were used to analyse the EBSD project data. The grains were identified based on a 10° mis-orientation criteria, i.e. continuous presence of more than 10° boundary was used to distinguish the grains. The AZtec Crystal

software was used to do the Kernel Average Misorientation (KAM) plots using the EBSD results. The KAM plots were built using a 'square' Kernel shape in 3 x 3 size and with a max angle of 7°. The EBSD scans were taken on the samples prepared from the AM Ti-6Al-4V as-built samples, specimens or brackets as follows;

(i) As-built samples taken out from the EPBF Phase 1 build,

(ii) At the cross-section of a fractured tensile specimen from the EPBF Phase 1 build,

(iii) As-built samples taken out from the LPBF Phase 2 and Phase 3 builds,

(iv) At the cross-section of uniaxial specimens from LCF testing at RT and at ET (from fractured and interrupted tests) build in Phase 2,

(v) At the cross-section of the fractured elements of the brackets tested under LCF loading and built in Phase 2 and Phase 3.

3.2.2 Surface Roughness

Surface roughness measurements were carried out using a Zeta 3D optical profiler. The roughness readings were performed on the vertical and horizontal built representative as-built EPBF samples, which were built in the same batch of the EPBF tensile specimens built in Phase 1. Further surface finish measurements were carried out on the gauge portion of a LPBF tensile specimen, which was judged to be representative of the average surface roughness of other LPBF specimens and the LPBF bracket built in Phase 2 and Phase 3. The surface profile, measured across the layer boundaries, contained the surface deviations from a mean profile over the evaluation length. The mean absolute deviation from the mean profile, R_a (μm), was chosen to indicate the surface roughness.

3.2.3 Defect Distribution

The X-ray CT scan technique is used to determine of the internal defects within an AM sample or a part based on the voxel-based volumetric mapping, whereby, during post processing, the reconstruction of 2D images into a rendered 3D volume can show internal surfaces of the defects in 3D [56, 177].

To study the morphology and distribution density of defects, X-ray CT scans were carried out using a ZEISS Xradia 510 Versa X-ray machine. The X-ray scan parameters are listed in the Table 3.5. The CT scans were performed on the vertical and horizontal as-built EPBF samples (Phase 1) and also on a representative LPBF tensile specimen (Phase 2).

For any 3D object if its surface area and volume are known then its Sphericity can be calculated. According to Wadell [178], the sphericity, ψ, of an object is defined as the ratio of the nominal surface area (surface area of a sphere having the same volume as the object) to the actual surface area of the object and can be treated as a measure of how spherical a defect is [178];

$$\text{Sphericity } (\psi) = \frac{A_n}{A} = \frac{\pi^{1/3}(6V)^{2/3}}{A} \quad (3.1)$$

Where, V, A and A_n are the volume, surface area and nominal surface area of a defect, and as the shape of the defect deviates from that of sphere, ψ decreases in magnitude.

Also 'flatness' is defined as the ratio S/I, where S and I are the dimensions perpendicular to the longest dimension of an object, I is the second longest dimension and S is the smallest dimension [179]. The value of flatness ranges from almost zero (very flat) to one (not flat). The X-ray image data set was reconstructed and post processed using the Simpleware ScanIP software to calculate defect statistics in terms of 'Sphericity' and 'Flatness' and were reported in the graphical form.

Table 3.5. X-ray CT scan parameters.

CT Parameter	EPBF (Phase 1) Vertically Built Sample	EPBF (Phase 1) Horizontally Built Sample	LPBF (Phase 2) Vertically Built Sample
X-ray voltage (kV)	140	160	160
Current (μA)	71	63	63
Exposure time (s)	0.7	3	1.4
Voxel resolution (μm)	20	20	20
Number of projections	1018	1017	1018

Furthermore, to study the presence of inclusions and voids, and also to better understand the crack initiation mechanism, the X-ray CT scans were carried out using a Nikon XTH225 Reflection Target X-ray machine on the uniaxial specimens from two interrupted LCF tests in Phase 2. The X-ray scan parameters are listed in the Table 3.6.

Table 3.6. X-ray CT scan parameters for interrupted LCF test specimens.

CT Parameter	Vertically Built Sample
X-ray voltage (kV)	220
Current (μA)	200
Exposure time (s)	0.7
Voxel resolution (μm)	11
Number of projections	3141

3.2.4 Micro-Hardness Mapping

The Vickers Micro-indentation Hardness (VMH) tests were carried out using a Wilson VH3100 automatic hardness testing machine. For the EPBF built, the VMH tests were performed on a representative as-built sample (15 mm x 15 mm square section) and also on a necked-out sample cut from the EPBF tensile specimen (Phase 1) post tensile testing at 400 °C to study the material hardness in the necked region. For LPBF Ti-6Al-4V in Phase 2, the micro-hardness characterization was carried on the as-built samples and also on the samples taken from the LCF tested specimens including from

interrupted tests. The micro-hardness measurements were carried out using a load of 500 gf, applied for 10 s, on a grid spacing of 500 μm x 500 μm.

3.3 Manufacturing Details

3.3.1 Phase 1: EPBF Specimens

An Arcam A2XX EPBF machine, which has a chamber size of 350mm x 350mm x 380mm, was used to build the tensile specimens for this study with standard build parameters used. The temperature of the build chamber was kept at 700 °C, the layer thickness was 70 μm and the hatch spacing, i.e. the parallel distance between the two adjacent scan lines, was 200 μm. The scanning strategy adopted was the 'snake x-y' where, for each successive layer, the scanning direction is rotated by 90° [180, 181]. In the EPBF process, the beam power and speed vary depending upon the scan length, which is the length of the two farthest points in the build along the scanning direction, and the melt pool size is kept constant by choosing the speed function. The build process was carried out in a vacuum with chamber filled with Helium to 4×10^{-3} mbar. This, combined with ETs, minimises residual stress and ensures superior material properties [91]. The beam spot size was kept as 0.2 mm – 1 mm, and the beam power (3000 W max) and scan speed (8000 m/s max.) vary depending upon the scan line length to be covered [18, 182, 183].

For the tensile tests, three types of specimens were prepared: (i) 'vertical as-built', (ii) 'vertical machined' and (iii) 'horizontal machined'. Orientations of these specimens with respect to directions of build and rake movement is shown in Fig. 3.1. The vertical built specimens were aligned to the Z direction (designated as the 'Z' orientation, [184, 185]) and the horizontal built specimens were aligned to the XY orientation (i.e. 'C+45' orientation from the x-axis, [184, 185]) as shown in Fig. 3.1. The vertical built specimens were made cylindrical in shape, whereas the horizontal specimens were made in square cross-section (Fig. 3.1) to avoid the possibility of ovalisation. The 'vertical as-built' specimens were machined only at the two grip ends, whereas the 'vertical machined' and 'horizontal machined' specimens were machined all along the length of the specimen to the final dimensions presented in Fig. 3.2. For the 'vertical machined' and 'horizontal machined' specimens, machining was carried out with cylindrical grinding to 0.4 μm. The vertical and horizontal specimens were made in two separate builds, but with the same build parameters and powder batch.

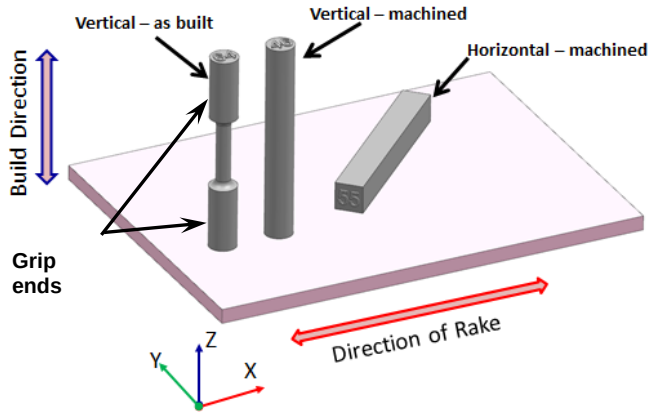


Fig. 3.1. Build orientation of the tensile specimens on the build platform.

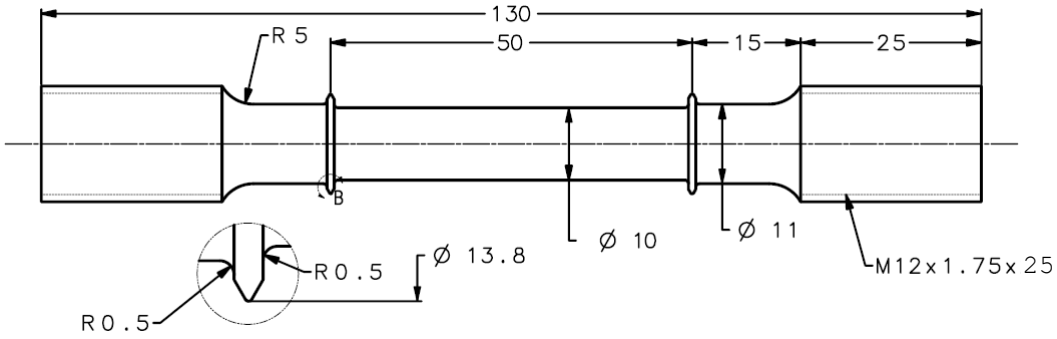


Fig. 3.2. Dimensions (mm) of tensile test specimen.

3.3.2 Phase 2: LPBF Test Specimens and Bracket

The test specimens and brackets were built using a commercially available EOS M280 AM machine, which has a chamber size of 250 mm x 250 mm x 325 mm, in an argon atmosphere on a substrate of Grade 5 Ti-6Al-4V material preheated to 35°C. The build parameters included: laser power = 170 W, laser scan speed = 1250 mm/s, hatch width = 5 mm, hatch distance = 0.1 mm, hatch overlap = 0 mm and table displacement [186] = 30 µm. Post build, the specimens and bracket were removed from the base plate using wire-EDM and aqua blasting was performed to remove the loosely sintered powder. After this, a SRL at 650°C was carried out for 3 hours in argon atmosphere, followed by FC to RT.

3.3.2.1 Dog-Bone Specimens – Tensile Testing

The tensile strength of LPBF Ti-6AL-4V was characterised in air at RT and at ET using tensile specimens built in the vertical direction, i.e. in the Z direction/orientation [184, 185] i.e. perpendicular to the layer deposition direction. The key dimensions of the tensile specimens are shown in Fig. 3.2, where the central gauge section of the specimens was kept as-built and only the threads at the two ends were machined. A total of six specimens were built for tensile testing.

3.3.2.2 Dog-Bone Specimens – LCF Testing

Since the loading of components in an end application can be complex, in this study, the uniaxial cyclic tests were performed to try to accurately establish the material fatigue behaviour and Strain Range (SRE, $\Delta\varepsilon$) dependent cyclic plasticity. For the cyclic LCF tests, cylindrical solid LPBF Ti-6Al-4V fatigue specimens with a gauge diameter of 5 mm and gauge length of 10 mm, shown in Fig. 3.3, were built in the vertical direction to the ISO 12106 standard [187]. A total of eight specimens were built for LCF testing.

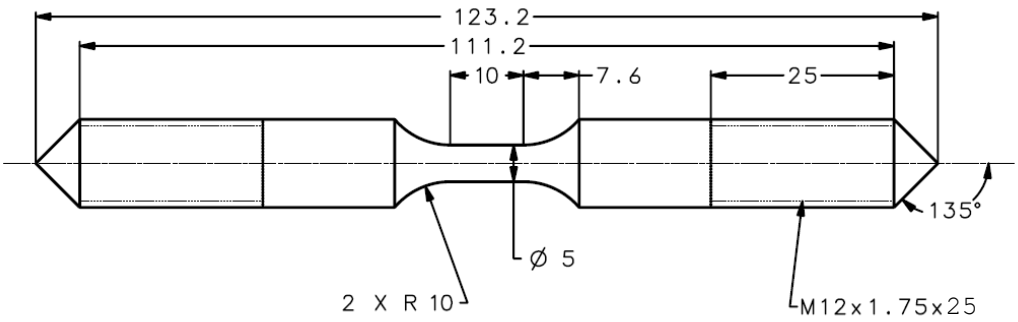


Fig. 3.3. LPBF test specimens (dims in mm) for uniaxial LCF testing.

3.3.2.3 Dog-Bone Specimens – HCF Testing

The HCF strength of LPBF Ti-6Al-4V was characterised using fatigue specimens with the dimensions shown in Fig. 3.4, in accordance with BS EN 6072 [188]. A total of five specimens were built for HCF testing at RT.

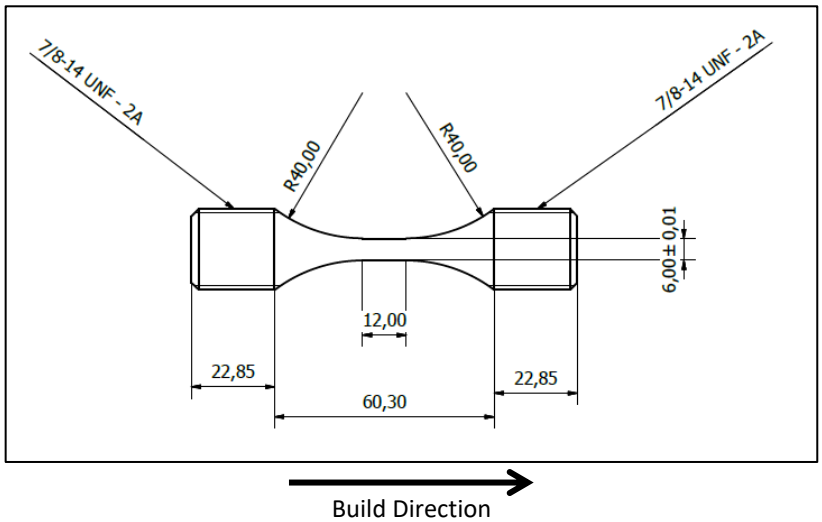


Fig. 3.4. LPBF test specimens (dims in mm) for uniaxial HCF testing.

3.3.2.4 Brackets

For an aeroengine application, the brackets are typically fabricated from sheet metal or made from the conventional machining process, and are designed to achieve strength and stiffness with a minimum amount of material. These brackets in Ti-6Al-4V are typically mounted on the fan-case or core-case of an aeroengine and provide support to the electronic sensors, controls units, harnesses, pipes or an aerostructure assembly. The LPBF bracket in this study was named as the struts and connectors design bracket and its major dimensions are shown in Fig. 3.5. The bracket was designed with main load carrying struts running in the longitudinal direction to support a sensor unit on the engine. The transverse running elements, also called connectors, provide stiffness to the load carrying struts in the lateral direction. Fig. 3.5(c) shows the dimensions of the struts and connectors of the brackets, which ranges from 1.4 mm (diameter of thinnest connectors) to 4.5 mm (diameter of main struts). The LPBF bracket design was optimised for its weight and offered more than 50% weight savings compared to its equivalent sheet metal bracket. The development and optimisation of bracket was an iterative process which was carried out carefully to distribute the mass and stiffness (hence strength) of it such that the design objectives set in relation to its LCF and HCF performances are achieved when tested under the planned conditions.

Two brackets of this design were made in the same build; one for LCF testing at RT and second for HCF testing at RT. After the SRL process, the brackets were GOM scanned to assess the dimensional accuracy against the supplied CAD geometry. A maximum distortion of 0.3 mm (worst case) was observed at and around the bottom mounting locations, as seen in Fig. 3.6, which was deemed low relative to the dimensions of the bracket (Fig. 3.5). Since, this small level of distortion was not expected to cause any significant impact on fit, form and function of the bracket, this level of distortion was deemed as acceptable. The typical distortion values are observed to be much lower.

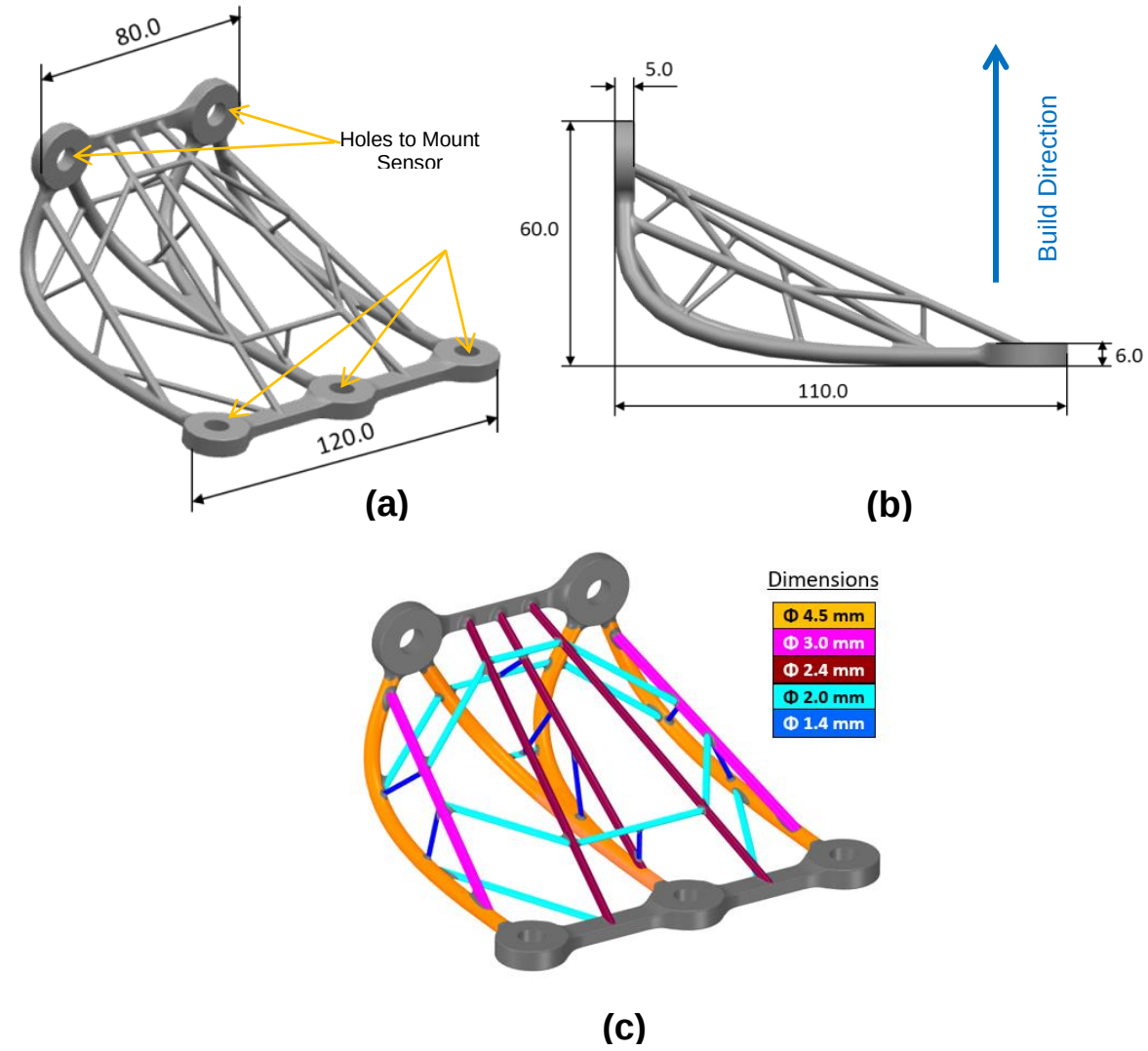


Fig. 3.5. The weight optimised unit mounting bracket geometry in struts and connectors design- Phase 2: (a) isometric view, (b) side view, and (c) dimensions of struts and connectors (dimensions in mm, not to scale).

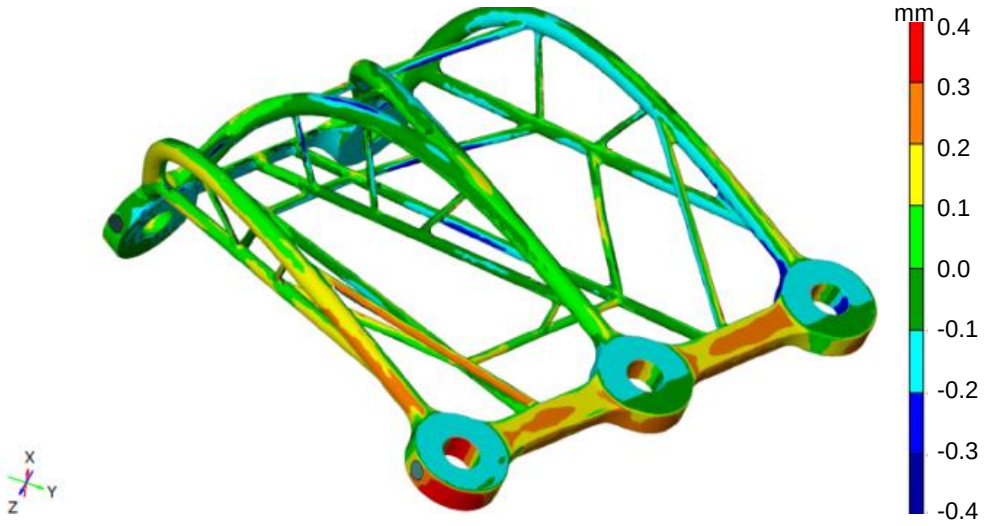


Fig. 3.6. Phase 2 Bracket: GOM scan result - deviations from nominal dimensions.

3.3.3 Phase 3: LPBF Test Specimens and Bracket

In this phase, some additional HCF test specimens in dog-bone shape and a LPBF bracket in strut and connector design was built, using a commercially available EOS M280 AM machine. The build process parameters, post build operations and heat treatment were kept same as discussed in Section 3.3.2.

3.3.3.1 Dog-Bone Specimens

Five specimens in dog-bone shape (see Fig. 3.4 for dimensions) were built for HCF testing at ET.

3.3.3.2 Bracket

One bracket in strut and connector design (see Fig. 3.7 for dimensions) was built for LCF testing at ET. The dimensions of the bracket in Phase 3 were slightly different as compared to the bracket in Phase 2. The bracket dimensions were altered to make it fit within the furnace size for LCF testing at ET. After the SRL process, this bracket was also GOM scanned to assess the dimensional accuracy against the supplied CAD geometry of Phase 3 bracket. A maximum distortion of 0.19 mm (worst case) was observed at top curved portion of the two outer main struts, as seen in Fig. 3.8. This distortion was deemed low relative to the dimensions of the bracket (see Fig. 3.7) and was not expected to cause any significant impact on fit, form and function of the bracket, this level of distortion was deemed as acceptable. The typical distortion values are observed to be much lower.

3.4 Test Matrix and Testing Details

3.4.1 Phase 1: EPBF Tensile Tests

An electric Mayes250 test rig, fitted with a Mayes 250kN load cell (accuracy : ± 0.5%), was used for the tensile tests at RT and ETs and a pair of Linear Variable Differential Transformers (LVDTs) (make: Tinius Olsen, serial number #0582, accuracy : ± 0.5%) were used to measure the strain and control the test Strain Rate (SR). A SF2170B three zone split resistance furnace, with rated voltage of 230 V and power of 1000 Watts, was used to maintain the required temperature. Three ‘type K’ thermocouples, spaced out along the gauge length of the specimen, were used to measure the temperature inside the surface. For the vertical built specimens, the load application was parallel to the build direction, i.e. perpendicular to the layer deposition direction. Whereas, for the horizontal built specimens, the load application was perpendicular to the built direction/ deposited layers (Fig. 3.1).

A total of thirteen tests were performed using the EPBF tensile specimens and the test matrix followed is shown in Table 3.7.

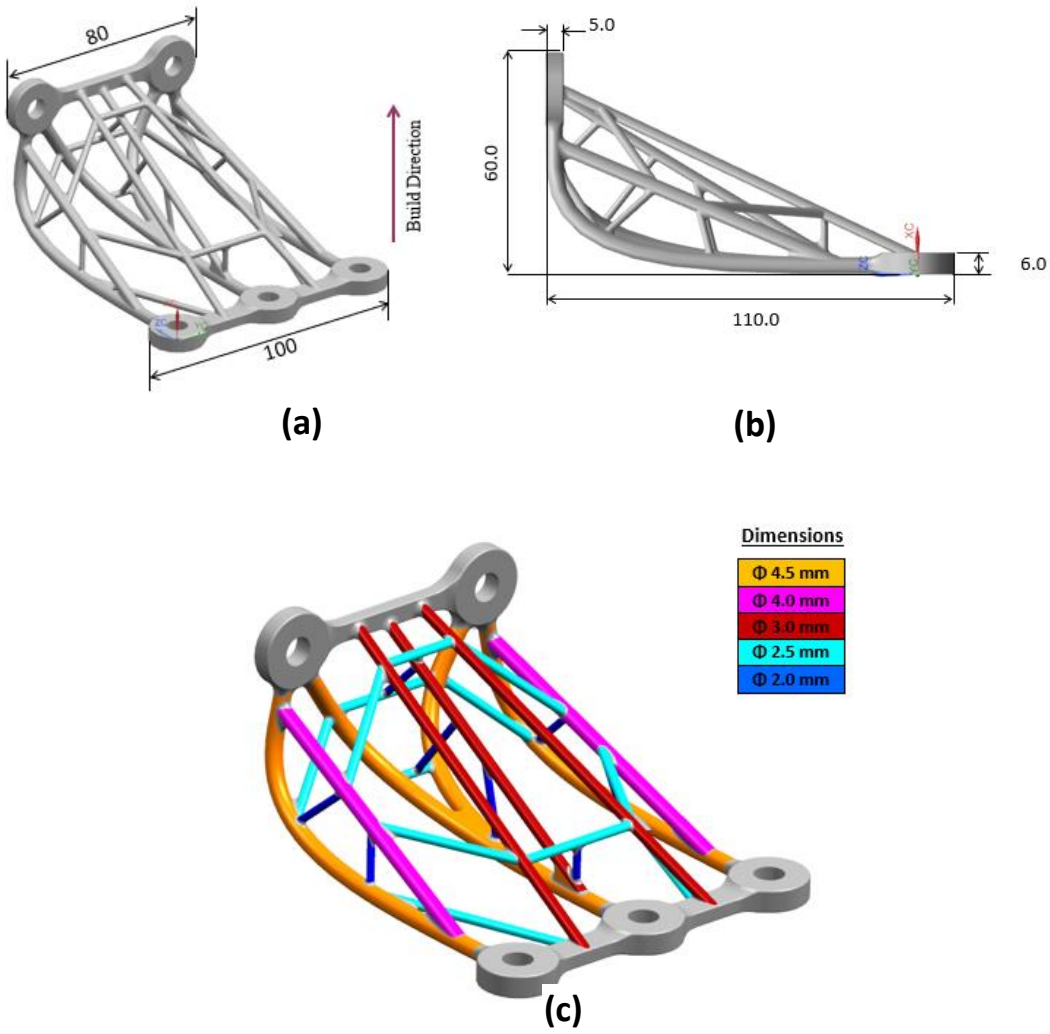


Fig. 3.7. The weight optimised unit mounting bracket geometry in struts and connectors design-Phase 3: (a) isometric view, (b) side view, and (c) dimensions of struts and connectors (dimensions in mm, not to scale).

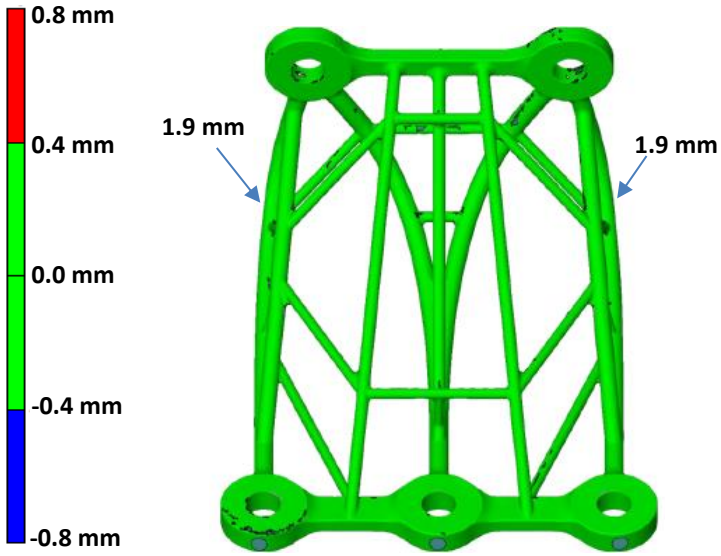


Fig. 3.8. Phase 3 bracket: GOM scan result - deviations from nominal dimensions.

Table 3.7. EPBF tensile test matrix – Phase 1.

Test Identification Number (#)	Build Orientation - Surface Condition	Temperature (°C)	Strain Rate (SR) - $\dot{e}$ (s^{-1})
VM1	Vertical machined	20	0.0002
VM2	Vertical machined	20	0.0265
VM3	Vertical machined	200	0.0002
VM4	Vertical machined	400	0.0002
VM5	Vertical machined	400	0.0265
HM1	Horizontal machined	20	0.0002
HM2	Horizontal machined	20	0.0265
HM3	Horizontal machined	400	0.0002
HM4	Horizontal machined	400	0.0265
VA1	Vertical as-built	200	0.0002
VA2	Vertical as-built	200	0.002
VA3	Vertical as-built	400	0.002
VA4	Vertical as-built	400	0.0265

3.4.2 Phase 2 and Phase 3: LPBF Test Campaign

3.4.2.1 Tensile Tests

Uniaxial tensile tests on the Phase 2 LPBF specimens were done on the same electric Mayes 250 test rig which was used for the tensile testing of Phase 1 EPBF specimens – see description in 3.5.1. A total of six tensile tests were performed using the LPBF tensile specimens and the test matrix followed is shown in Table 3.8.

Table 3.8. LPBF tensile test matrix - Phase 2.

Test Identification Number (#)	Build Orientation - Surface Condition	Temperature (°C)	Strain Rate (SR) - $\dot{e}$ (s^{-1})
TT1	Vertical as-built	20	0.0002
TT2	Vertical as-built	20	0.0265
TT3	Vertical as-built	200	0.0002
TT4	Vertical as-built	200	0.0265
TT5	Vertical as-built	400	0.0002
TT6	Vertical as-built	400	0.0265

3.4.2.2 Low Cycle Fatigue Testing

This section describes the methodology followed for the LCF testing carried out at specimen and at Bracket (i.e. component) levels at RT and ETs.

(a) Uniaxial Dog-Bone Specimen Tests

Fully reversed strain controlled LCF tests (at load ratio of $R = -1$) at RT and ETs with a SR of 0.002 s^{-1} were carried out using the saw-tooth type (SWT) waveform shown in Fig. 3.9 and data was acquired continuously until specimen fracture to investigate the cycles to failure and softening/hardening of LPBF Ti-6Al-4V material under LCF loading. The SWT waveform was chosen for LCF testing at RT to get constant SR throughout the loading and unloading part of the testing, to get optimal test time efficiency and also because any time dependent load dwell effects were judged to be insignificant. The LCF tests were performed at predefined SRE ($\Delta\varepsilon$) of ±0.8% ≤ SRE ≤ ±1.5%, and the LCF test matrix is presented in Table 3.9. The selected temperatures for the LCF tests enveloped the operating temperatures in the intended end application, i.e. for aeroengine externals parts. Furthermore, two interrupted cyclic tests were also carried out at a SRE of ±1.2% and at ET to investigate the microstructural evolution during the progression of cyclic loading. The interrupted tests were planned to be stopped once the intended number of cycles was reached.

The LCF tests were conducted in air on a Tinius Olsen H25KS electromechanical testing system fitted with a Tinius Olsen DSCCTOL 25 kN pancake style load cell and a Severn Thermal Solutions SF2107 split section resistance furnace. The temperature along the gauge length of the specimen was controlled using three thermocouples spaced out along the specimen surface. The load was measured using a Tinius Olsen DSCCTOL 25 kN pancake style load cell and the strain values were controlled and recorded using a side-contact extensometer. The accuracy of load cell, LVDT and extensometer used was ± 0.5% of the respective measurements.

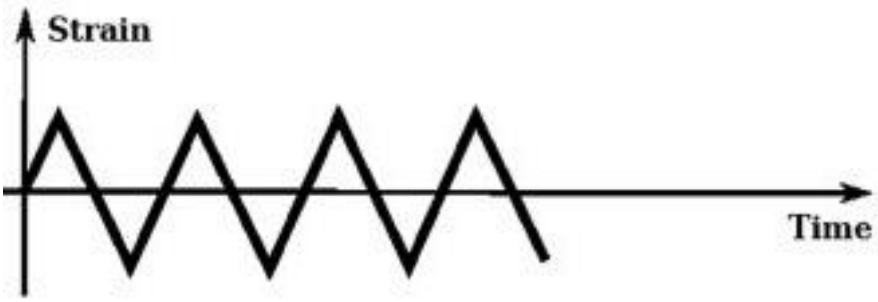


Fig. 3.9. Saw-tooth type waveform used for LCF tests.

Table 3.9. Cyclic strain-controlled uniaxial test matrix – Phase 2

Test No.	Test Identification Number (#)	Description	Temperature °C	Strain Range (SR) (%)
1	L-RT1	Test to fracture	20	± 0.8
2	L-RT2	Test to fracture	20	± 1.2
3	L-RT3	Test to fracture	20	± 1.5
4	L-ET1	Test to fracture	400	± 0.8
5	L-ET2	Test to fracture	400	± 1.2
6	L-ET3	Test to fracture	400	± 1.5
7	L-ET4	First interrupted test	400	± 1.2
8	L-ET5	Second interrupted test	400	± 1.2

(b) Bracket Testing at RT

The set-up for the LCF test on the bracket, also conducted on the Tinius Olsen H25KS electromechanical testing machine, is shown in Fig. 3.10, where the bracket was installed on the test machine via the bolted top and bottom FV566 steel fixtures. The bracket LCF test was again a displacement controlled (load ratio R = −1) test using the SWT waveform. A LVDT (accuracy : ± 0.5%) was used to control and measure the movement (displacement) of the top fixture and therefore the extension of the bracket. Firstly, the bracket was tested at a displacement range of ±1 mm (BT1 at a Displacement Rate (DR) of 0.002 mm/s) with a target of 3000 LCF cycles without failure. In the second test run, the same bracket was tested at ±4 mm displacement range (BT2 test at a DR of 0.008 mm/s) to induce failure in the bracket, with a target of 100 cycles, and to study the failure sequence and mechanism. The displacement range set for the BT1 test was far greater than the loading typically expected on the LPBF bracket during normal engine operation and likewise the applied loading in BT2 test was in the displacement range which could typically be expected in an extreme occurrence experienced by the engine, such as a FBO event. Furthermore, it was also required to show that the bracket has redundancy in the load paths i.e., the bracket does not show a significant drop in its load carrying capacity in the case of a failure of a strut or connector.

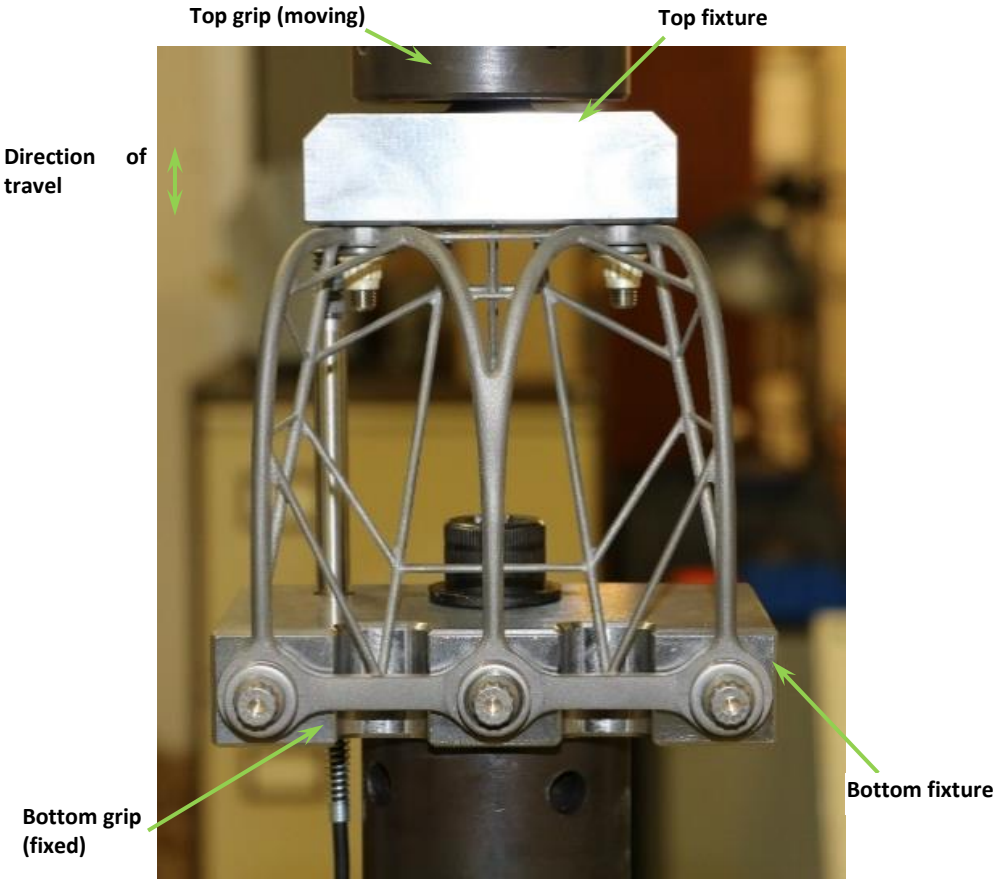


Fig. 3.10. LPBF Ti-6Al-4V bracket in struts and connectors design – test set-up for LCF test at RT.

(c) Bracket Testing at ET

The test configuration and mounting set-up of the bracket assembly for the displacement controlled LCF test is shown in Fig. 3.11. This time again, the LCF testing on the bracket conducted again on a Tinius Olsen H25KS electromechanical testing system fitted with a Tinius Olsen DSCCTOL 25kN load cell and a Severn Thermal Solutions SF2107 furnace. The bracket was installed on the test machine via the bolted top and bottom fixtures. The bottom fixture remained stationary whereas the top fixture travelled by a pre-set distance. A LVDT was used to control and measure the movement of the bracket. The bracket LCF tests were fully reversed displacement controlled LCF tests (i.e. Load ratio R = −1) at 200°C. Firstly, the bracket was tested at a displacement range of ±1 mm (BET1 test) for a target of 3000 LCF cycles without the failure. In the second test run, the same bracket was tested at a displacement range of ±2 mm (BET2) to understand the cycles to failure when it is tested with elasto-plastic strain levels. To optimize the overall testing time, both BET1 and BET2 tests were carried out at a DR of 0.008 mm/s. Again, it was also required to show that the bracket has redundancy in the load path.

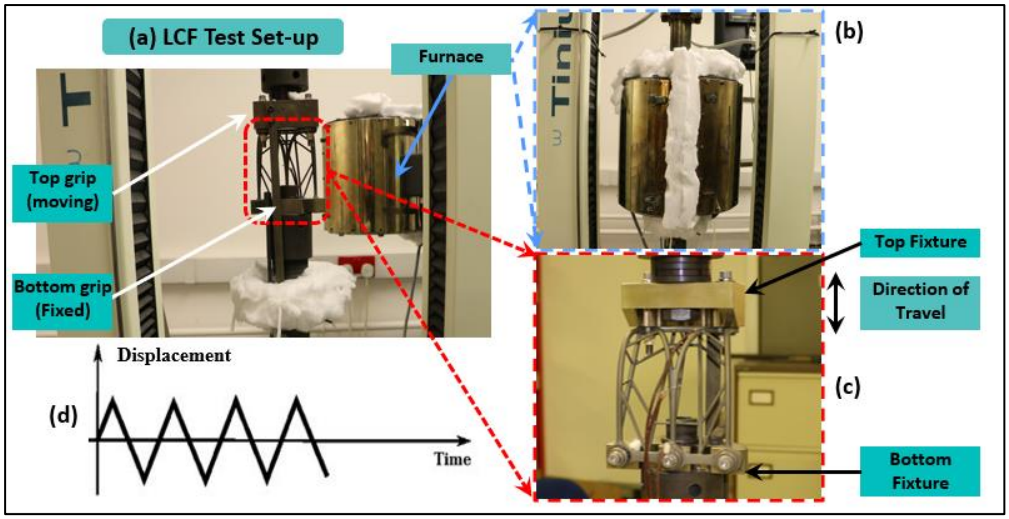


Fig. 3.11. LCF testing on LPBF Ti-6Al-4V bracket: (a) ET test set-up, (b) Furnace enclosure for ET testing, (c) Bracket installation details, and (d) Saw tooth displacement loading

3.4.2.3 High Cycle Fatigue Testing

This section describes the methodology followed for the HCF testing carried out using the dog-bone specimens at RT and ET and on Bracket (component level) at RT only. The HCF tests on the LPBF Ti-6Al-4V dog-bone specimens and bracket were carried out at external test houses. The HCF tests on dog-bone specimens were carried out at Swansea Materials Research & Testing Ltd (SMaRT), Swansea, and the HCF tests on the bracket were performed at Element, Warwick.

(a) Dog-Bone Specimen Tests at RT

Constant amplitude load controlled HCF tests were performed using a fully reversed sinusoidal waveform (i.e. at R = -1) at RT. HCF tests were carried out on a Amsler Vibrophore fatigue test equipment (designated as VB-1, Model: HFP422, Sr. No. 422/528), see Fig. 3.12. The Vibrophore uses a Servocon Analogue Control (Model: SE99-10), which has a load range of 5 – 100 kN with calibration standard of BS EN ISO 7500-1:2018 (Class 5). The testing frequency was around 100 Hz and the objective was to test each specimen until failure for a chosen stress amplitude. In the case of a run-out, the stress amplitude was incremented (in steps of 5 MPa) and the test was repeated until failure.

(b) Dog-Bone Specimen Tests at ET

The required HCF testing was carried out to BS EN 6072. All force controlled HCF tests were carried-out using a fully reversed sinusoidal waveform (i.e. at R = -1) at ET (200 °C). The HCF testing utilized a mechanical test frame designated as VB-2. which were all calibrated by the test house (SMaRT), and the details of the test machine is given below, also see Fig. 3.13;

- Test frame capacity: ±100 kN, calibration: ±100 kN (25V, 16 bit resolution),
- Servo-electric actuator,
- Digital controller (Servocon),
- Type of grip: Threaded both ends,

- Radiant furnace assembly used,
- Estimated axial temperature gradient in parallel length: 3°C,
- N-type thermocouples used for temperature monitoring.

Again, the testing frequency was set as > 60 Hz and the objective was to test each specimen until failure for a chosen stress amplitude. In the case of a run-out, the stress amplitude was incremented (in steps of 5 MPa) and the test was repeated until failure.



Fig. 3.12. Amsler vibrophore (VB-1) used for HCF testing at RT.



Fig. 3.13. Amsler vibrophore (VB-2) used for HCF testing at ET.

(c) Bracket HCF Testing at RT

the LPBF bracket in struts and connectors was required to be optimised to meet three main requirements: (i) the fundamental frequency of the bracket assembly should be outside of the 1st Low Pressure (LP) shaft frequency of 48 Hz to avoid resonance during engine operation, (ii) the bracket assembly should have a minimum g load capability of 20g (response), and (iii) the bracket should have redundancy in the load transfer path, should a strut fail either under normal operation or due to a FBO event. The minimum g load capability of 20g is required to cope with the inertial effects during engine manoeuvres, acoustically driven vibrations or vibrations generated during windmilling post shutting down of the engine due to an extreme event.

The LPBF bracket in struts and connectors design was evaluated for its HCF performance through shaker table testing at RT. Parts of the bracket assembly and mounting fixtures for the shaker table testing are shown in Fig. 3.14. A dummy machined aluminium block, representing the sensor unit, was attached to the bracket using two 0.25" diameter Inconel 718 bolts. The bolts and nuts to assemble the bracket were tightened to 15.2 Nm torque. The total mass of the bracket assembly participating in the dynamic response was 306.7 grammes (Bracket: 91.7 grammes, dummy block: 179 grammes and fasteners (2 off): 36 grammes). A fixture (mass ~4.9 kg) acted as a mounting plate between armature of the shaker and the bracket assembly and was fastened onto the shaker armature using four high strength steel bolts (of M10 size). The fixture and bolting arrangement were designed to be sufficiently rigid to not influence the dynamic characteristics of the bracket assembly. The optimised LPBF bracket with a mass of 91.7 grammes was a significant weight reduction (> 50%) compared to the baseline sheet metal bracket (200 grammes).

As part of the test planning, a modal FE analysis was performed in Ansys Mechanical v19.1 to identify the fundamental vibration mode of the bracket assembly. Quadratic tetrahedral (Tet10) elements were used and the mesh consisted of 410,000 elements (see Fig. 3.15(a)). The boundary conditions were defined to closely mimic the test set-up, where bottom face of the fixture block was given fixed restraint ($U_x = U_y = U_z = R_x = R_y = R_z = 0$) and linear bonded contacts were defined between the mating faces of the interfacing parts (i.e. bracket to fixture, bracket to dummy block). The material properties used in the FE model are given in Table 3.10. The material density for the aluminium block was adjusted to account for missing mass of the bolts, nuts and washers, which were not explicitly included in the FE model (Table 3.9). The fundamental mode of the bracket was predominantly an axial deformation mode, as shown in Fig 3.15(b), at 85.6 Hz.

Table 3.10. FE Model for modal analysis – material properties

Material	Young's modulus E (GPa)	Poisson's ratio ν	density ρ (kg/m³)
Bracket (Ti-6Al-4V) [136]	110	0.31	4429
Fixture (Aluminium) [136]	72.4	0.33	2760
Block (Aluminium) [136]	72.4	0.33	3316*

Note ** Density adjusted for missing mass of bolts, nuts and washers*

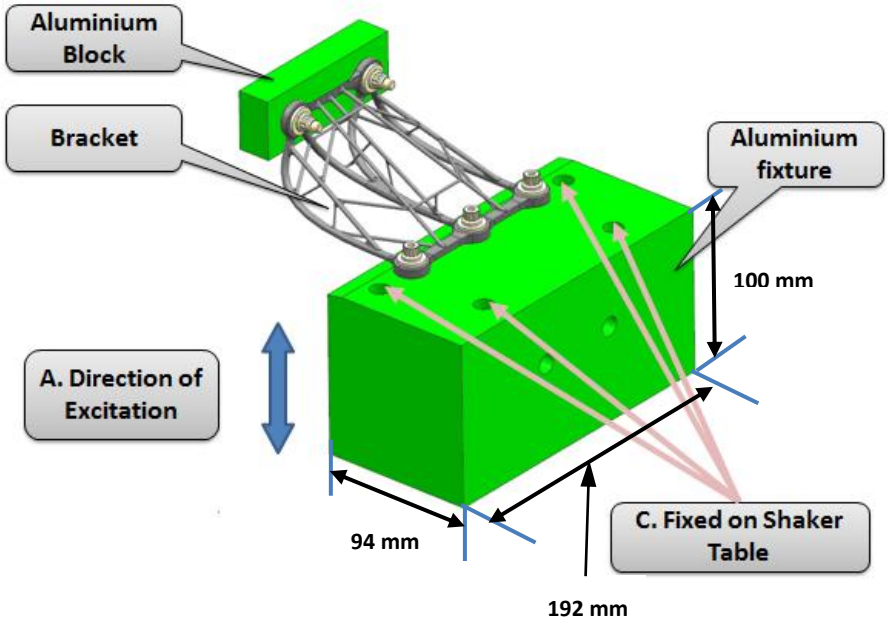
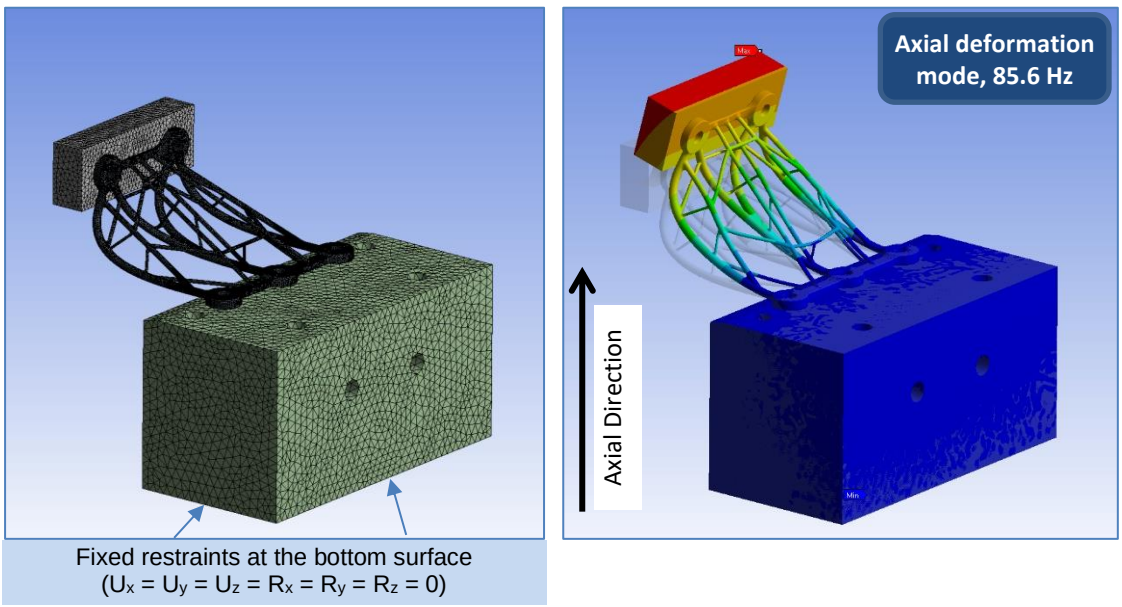


Fig. 3.14. Bracket assembly parts for the shaker table tests.



(a) (b)

Fig. 3.15. (a) A FE model of the AM bracket assembly for modal analysis, (b) FE predicted fundamental vibration mode of the bracket assembly at 85.6 Hz depicting axial deformation mode of the AM bracket.

The vibration tests on the bracket assembly were conducted on a Derritron electromagnetic shaker (model VP1500N) with a maximum payload (sinusoidal) of 75 kN and acceleration (in g units) of 100g, and operates in the frequency range of 20 – 2000 Hz. A 16 channel vibration controller (model - Vibrunner), made by m+p international which is capable of operating in the 3 - 4000 Hz frequency range, was used to control the shaker and collect the dynamic response data from the test specimen and the shaker. Accelerometers (make: Endevco [189]) were used to control the shaker and to capture the input excitation and output response of the bracket. These lightweight (3 grammes) accelerometers were mounted on the brackets with a medium viscosity glue (make : pc24) using lightweight tufnol cubes as mounting blocks. The shaker table test setup, shown in Fig. 3.16, indicates that the excitation to the bracket was in the vertical direction, which is the axial direction of the bracket. As shown in Fig. 3.16, three uniaxial accelerometers, one in each of the axial, radial and tangential directions, were mounted on the dummy block to measure the response of the dummy block/bracket. Again, three uniaxial accelerometers, (one in each of the axial, radial and tangential directions) and a uniaxial accelerometer (axial direction) were mounted on the fixture to control the input to the bracket and a uniaxial accelerometer (axial direction) was mounted on the armature plate to monitor and control the movement of the armature plate/shaker.

First, a resonance search (frequency sweep) test was carried out to identify the fundamental vibration mode of the bracket assembly. The test was performed with the axial response of the bracket controlled at 25g acceleration level (maximum). This control loop was chosen to ensure that the bracket response would not go beyond 25g level, meaning that the system control loop automatically reduces the input level at and around the resonance point.

Subsequently, a series of dwell tests were carried out to establish the g load capability of the bracket. In a dwell test, the bracket was excited at its fundamental frequency at a specific response g level measured at the dummy block (sensor). The first dwell test was at 84 Hz frequency and 30g response level as a trial test to ensure that the bracket assembly, the sensors, the shaker and the data acquisition system were performing as expected. The trial test was stopped after 2050 s (172,239 cycles) and the mounting bolts were checked to ensure that the bolts were still tightened to the specified torque values. The subsequent dwell tests, starting with 40g response level, were performed to establish the brackets g load capability. Each dwell test was referred as a test run where the response g level at the dummy block was kept constant. Upon successful completion of a test run, the response g level in subsequent test run was increased to the next planned level, i.e. first to 60g and then to 80g; a level at which failure of the bracket struts/connectors began. The last test run was at low 20g level to avoid an uncontrolled failure of the entire bracket assembly and therefore limiting any possible damage to the surrounding equipment and sensors.

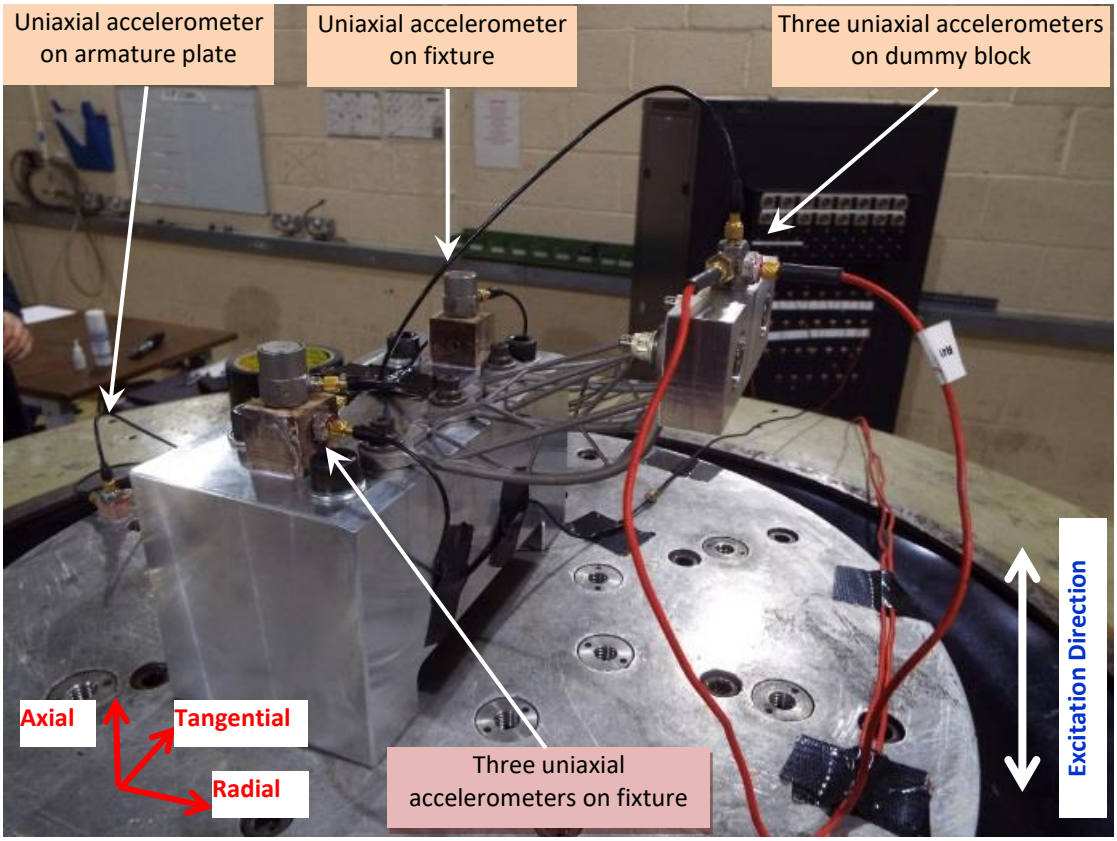


Fig. 3.16. HCF Test setup - bracket assembly and fixture mounted on the shaker table and excitation direction (bracket axial).

-----x x x x x x x-----

CHAPTER 4

4 Tensile Behaviour of EPBF Ti-6Al-4V

In this chapter, the tensile behaviour of the EPBF Ti-6Al-4V material and its dependence on Strain rate (SR), temperature, surface roughness and build orientation has been studied and discussed. Results are analysed in relation to the observations made on the material microstructure, fracture surface and material micro-hardness. Fracture surface characterisation has also been discussed based on the analysis of SEM microscopic images of the fracture surfaces of tensile specimens tested at RT and ETs. The characterisation of defects and its role in relation to the mechanical strength of the EPBF processed Ti-6Al-4V materials have also been presented and discussed in detail.

4.1 Tensile Test Results

From the tensile tests performed, the PS, Ultimate Tensile Strength UTS and material ductility values were derived and are summarised in Table 4.1 for EPBF Ti-6Al-4V. For comparison purpose, the individual test results/curves are grouped and are presented in this section.

From Table 4.1, for EPBF Ti-6Al-4V, the strength values at RT (PS, UTS) are in the similar range but the ductility was slightly lower compared to the values found by the other researchers [93, 94, 113, 114, 115]. The differences in strengths and ductility values between the current and the other published data are due to possible differences in the AM machines used, build parameters, morphology and distribution of defects, HTs and other post processing treatments.

The property results obtained from the tensile stress-strain curves of the 'vertical machined', 'horizontal machined' and 'vertical as-built' specimens, as shown in Fig. 4.1, Fig. 4.2 and Fig. 4.3 respectively, were used to study the effect of temperature and SR. The tensile property results at same temperature were paired to study the effect of SR on tensile properties. The SRs studied differed only by two orders of magnitude for machined specimens and by only one order of magnitude for as-built specimens. From the pairs of data curves at the same temperatures in Fig. 4.1 – Fig. 4.3, the majority of tests (except the VM4 - VM5 pair) showed that the PS and UTS increase but the ductility decreases with increasing SR. The VM4 - VM5 pair indicated a reverse trend, shown in Fig. 4.1, where a decrease in tensile strength but increase in ductility was observed with increasing SR.

Again, the tensile results for same SR in Fig. 4.1 - Fig. 4.3 were paired to study the effect of temperature on tensile properties. It was observed that, with an increase in temperature, the PS and UTS decreased as expected but the ductility increased for machined specimens but decreased for as-built specimens as shown in Figs. 4.1 – Fig. 4.2 and Fig. 4.3, respectively.

The effect of build orientation is shown in Fig. 4.4, where the results were paired by keeping the same temperature and SR, the differences in PS and UTS were observed to be small with a slightly higher PS and UTS observed for the 'vertical machined' specimens; however, a noticeable difference in material ductility was observed where higher ductility was noticed for the horizontal specimens [190].

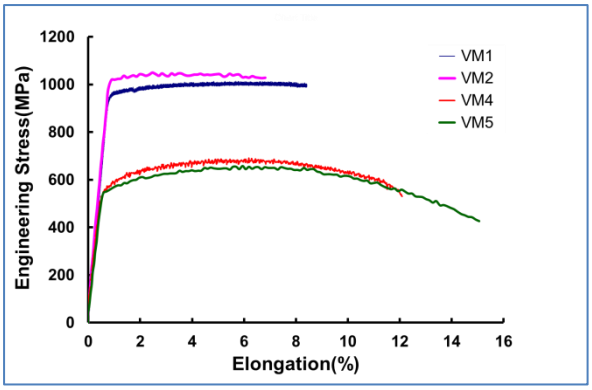


Fig. 4.1. Effect of SR and temperature, 'vertical machined' specimens.
(#VM1: T=20 °C, SR =0.0002 s^{-1}, #VM2: T=20 °C, SR =0.0265 s^{-1}, #VM4: T=400 °C, SR =0.0002 s^{-1}, #VM5: T=400 °C, SR =0.0265 s^{-1}, Where T = Temperature, SR = Strain Rate)

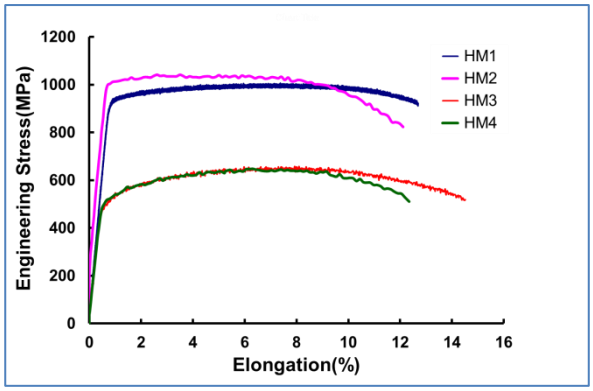


Fig. 4.2. Effect of SR and temperature, 'horizontal machined' specimens.
(#HM1: T=20 °C, SR =0.0002 s^{-1}, #HM2: T=20 °C, SR =0.0265 s^{-1}, #HM3: T=400 °C, SR =0.0002 s^{-1}, #HM4: T=400 °C, SR =0.0265 s^{-1}, Where T = Temperature, SR = Strain Rate)

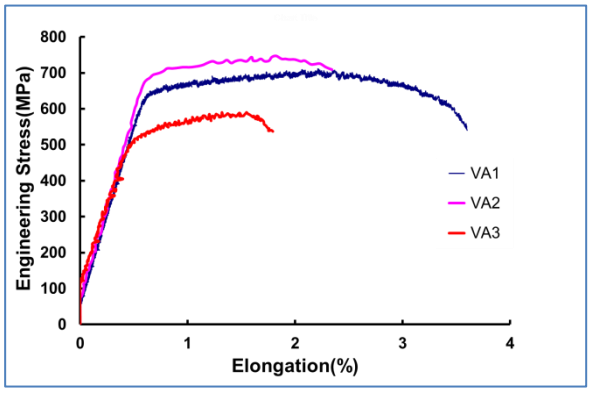


Fig. 4.3. Effect of SR and temperature, 'vertical as-built' specimens.
(#VA1: T=200 °C, SR =0.0002 s^{-1}, #VA2: T=200 °C, SR =0.002 s^{-1}, #VA3: T=400 °C, SR =0.002 s^{-1}, Where T = Temperature, SR = Strain Rate)

Further, in Fig. 4.5, the pairing of tensile results for 'vertical machined' and 'vertical as-built' specimens were done by keeping the temperature and SR the same to study the effect of surface roughness on tensile properties. Significant reductions in PS, UTS and ductility were observed for the as-built specimens.

From the results of machined vertical (VM1) and horizontal (HM1) EPBF specimens presented in Table 4.1, both the PS and UTS values were observed to be higher than the respective values for the conventionally manufactured annealed Ti-6Al-4V bar [136]. The ductility was lower for the vertical machined specimen (VM1) but was higher for the horizontal machined specimen (HM1) than for the conventionally manufactured annealed Ti-6Al-4V bar. From the property values in Table 4.1, the UTS is only marginally higher than the PS indicating a small work hardening rate for EPBF Ti-6Al-4V material beyond the yield point [91].

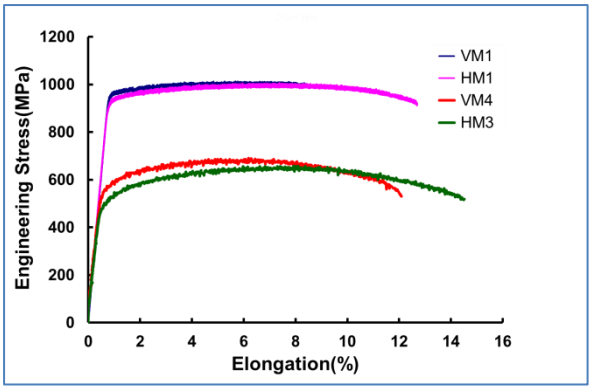


Fig. 4.4. Effect of build orientation, 'vertical machined' and 'horizontal machined' specimens. **(#VM1: T=20 °C, SR =0.0002 s^{-1}, #HM1: T=20 °C, SR =0.0002 s^{-1}, #VM4: T=400 °C, SR =0.0002 s^{-1}, #HM3: T=400 °C, SR =0.0002 s^{-1}, Where T = Temperature, SR = Strain Rate)**

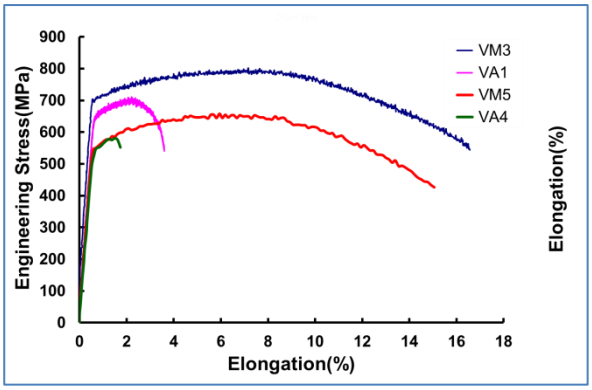


Fig. 4.5. Effect of surface roughness, 'vertical machined' and 'vertical as-built' specimens. **(#VM3: T=200 °C, SR =0.0002 s^{-1}, #VA1: T=200 °C, SR =0.0002 s^{-1}, #VM5: T=400 °C, SR =0.0265 s^{-1}, #VA4: T=400 °C, SR =0.0265 s^{-1}, Where T = Temperature, SR = Strain Rate)**

Table 4.1. Tests parameters and tensile strength properties (PS, UTS and Ductility).

Test Identification Number (#)	Temperature (°C)	Strain Rate (SR) – $\dot{e}$ (s^{-1})	PS (MPa)	UTS (MPa)	Ductility (%)
VM1	20	0.0002	953	1013	8.4
VM2	20	0.0265	1020	1050	6.8
VM3	200	0.0002	708	802	16.6
VM4	400	0.0002	575	691	12.1
VM5	400	0.0265	550	658	15
HM1	20	0.0002	927	1007	12.6
HM2	20	0.0265	1022	1042	12.1
HM3	400	0.0002	506	658	14.5
HM4	400	0.0265	522	648	12.3
VA1	200	0.0002	652	711	3.6
VA2	200	0.002	718	747	2.4
VA3	400	0.002	560	590	1.8
VA4	400	0.0265	547	580	1.7
Annealed Ti-6Al-4V Bar [136]	20	-	861	930	10

In comparison with the results of this study, the tensile strength values for EPBF Ti-6Al-4V alloy reported by Edwards et al. [92] and Rafi et al. [91] are lower, but the values reported by Zhai et al. [94] and Murr et al. [116] are slightly higher. Formanoir et al. [181] observed higher PS but surprisingly lower ductility from their dense and defect free EPBF Ti-6Al-4V specimens than the respective values observed in this study, which they attributed to the excessive oxygen content in the alloy. Hrabe et al. [115] also observed slightly higher tensile strength values but similar ductility values.

4.2 Characterization

4.2.1 Microstructure

The microstructure of Ti-6Al-4V material, comprising of fraction of α and β phases, morphology, size of α laths and size of α colonies all affect its mechanical properties [191, 192, 193]. The front longitudinal section of a vertical built sample containing build direction was scanned by both the optical microscope and the SEM. An optical micrograph (a scanned area of 0.664 mm x 0.6 mm) of the longitudinal section, depicting prior β grains morphology is shown in Fig. 4.6(a). The micrograph in Fig. 4.6(a) shows the columnar lenticular β grains oriented approximately along the build direction [91, 193, 190] and seen to be growing epitaxially across multiple build layers [50, 91, 92]. The width of prior β grain boundaries observed in the micrograph is 70 -100 μm. The width of columnar grains is not related to the cooling rate but is rather dependent upon the residence time of the material at temperatures between the liquidus and β transus temperature of Ti-6Al-4V (995 °C). Overheating of the melt pool by the high energy EB, a narrow liquid/solid phase region, high thermal gradient, heat dissipation along the build direction and high solubility of Al and V elements in the Ti-6Al-4V alloy are the contributing factors to cause epitaxial growth of prior β grains [194].

The SEM scanned images of the longitudinal section and of the transverse section (i.e. perpendicular to the build direction) of EPBF sample are shown in Fig. 4.6(b) and Fig. 4.7, respectively. In both the longitudinal and transverse sections, the α phase is a lamellar morphology with surrounding prior β grain boundaries and this suggests a diffusional transformation of β phase during cooling from high temperature [6, 39, 190, 193]. The presence of α and β phases in the EPBF processed Ti-6Al-4V alloy is the result of the naturally aged condition due to the higher temperature maintained (700 °C) in the chamber during the build process [194].

It can also be seen in Fig. 4.6(b) and Fig. 4.7 that the α lamellae (with average thickness of 1.6 μm) is arranged in a widmanstätten/basket weave structure with different sizes and orientations, and also occasionally the α lamellae colonies are formed within the columnar β grains, [50, 93]. Grain boundary α (α_{GB}) is also seen around the boundaries of the columnar prior β grains. A cooling rate of > 410 °C/s forms the martensitic α' [93, 193], but the formation of α' in Ti-6Al-4V is activated only if the temperature upon fast cooling drops down to be in between the martensite starting temperature (M_s = 575 °C) and martensite finishing temperature (M_f = 400 °C), and in this study the presence of martensitic α' was not noticed [50, 94]. The complex microstructure formation is idealised in Fig. 4.8 where the first stage of the cooling produces fast solidification rates ($10^3 – 10^5$ °C/s) to bring the melt-pool temperature to build temperature in the chamber. Time for this stage lasts only for a few seconds (~2–4 s). In the first stage, formation of β-grains begins during solidification and, upon further cooling, transformation of β happens once the temperature starts to go below the β-transus temperature in a quick span of time. In the second stage, the new layer being deposited re-heats or partially re-melts the previously deposited material depending on process parameters and the temperature variation is only due to the heat transfer from the upper layers causing coarsening of α-laths. In the third and final stage,

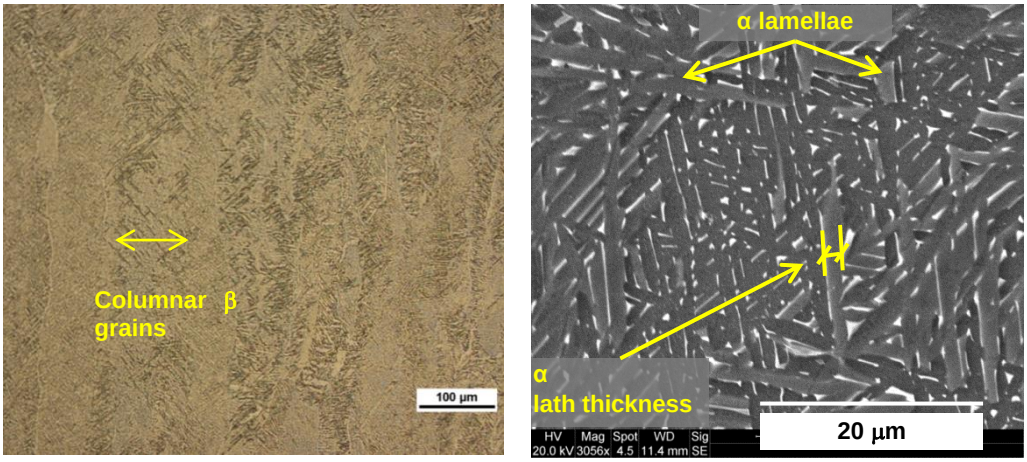
the build chamber temperature goes down to RT after the EPBF process is complete, which lasts longer than the previous stages and promotes the formation of α_{GB} and α platelets. In all these stages, the alloy experiences complex thermal history due to continuous nature of scanning and melting of powder depending upon the shape of the part as shown in Fig. 4.8. The part being built experiences a rapid quench of melt and follow-on in-situ AN within the build chamber maintained at 700 °C [50]. The classical Hall-Petch relationship approximately applies to EPBF Ti-6Al-4V alloy in a way that the PS of the material varies linearly with the inverse of the square root of α-lath thickness (δ_{lath}) [93, 116, 195, 196, 197], as below.

$$P = P_0 + K_y(\delta_{lath})^{-0.5} \quad (4.1)$$

Where, P is PS (or hardness) of EPBF Ti-6Al-4V alloy, P_0 is a constant which represents the PS (or hardness) of a single crystal of the material and K_y is another constant known as a strengthening coefficient [197]. From equation (4.1) the PS decreases with increasing α-lath thickness [41, 91]. This is because the thicker α-lath increases the effective slip length hence reduces PS [41, 91, 93]. The increase in α-lath thickness is also seen due to further post processing HTs, again resulting in a detrimental effect on PS but positive effects on material ductility [93, 181, 191]. For the HT temperatures below 600 °C, the growth of α-lath is usually minimal, therefore the tensile properties remain unchanged [93]. According to Galarraga et al. [93], the Influence of α-lath thickness on UTS is negligible.

4.2.2 Defects

From the optical microscopic images, the defects observed are spherical shape 'pores' and irregular shape 'voids' as illustrated in Fig. 4.9(a) and Fig. 4.9(b). From X-ray CT scan, the defect distribution in a representative vertical built sample of 5 mm diameter is shown in Fig. 4.10(a) where the total defect volume observed is 0.034% (vol). Again, both irregular and spherical shape defects, shown in Fig. 10(b), are observed. The population of pores was found to be high, but their total volume fraction was small. A histogram of the 'sphericity' and 'flatness' of the internal defects in the vertical built sample is shown in Fig. 4.11(a) and Fig. 4.11(b) respectively.



(a) (b)

Fig. 4.6. Longitudinal sections of EPBF sample: (a) Optical image showing columnar β grains running along several layer thicknesses, (b) SEM image showing α lamellae in widmanstätten structure.

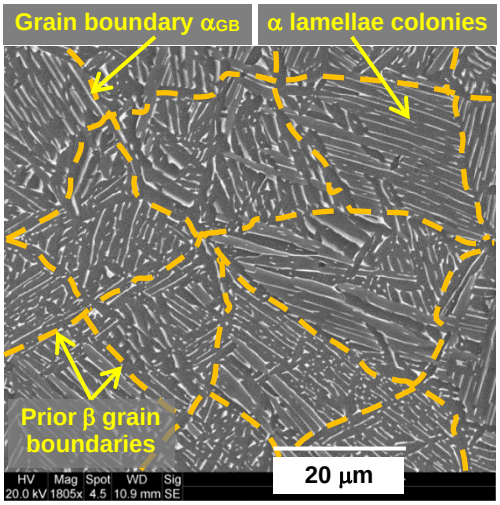


Fig. 4.7. Transverse section of the EPBF sample, SEM image showing lamellar α (white/light grey) surrounded by β (black) phase within prior β grain boundaries.

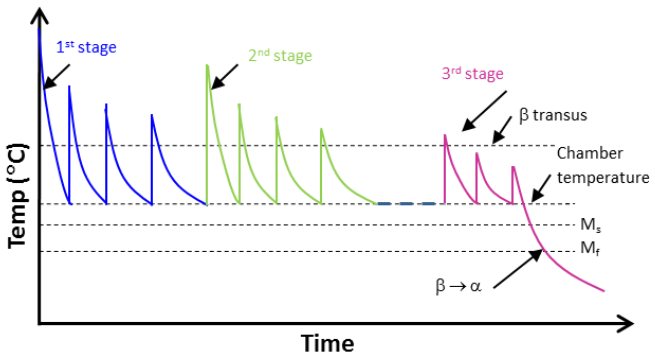


Fig. 4.8. Complex thermal history experienced by the material during the EPBF process.

The smaller size defects, which are large in numbers and are of near spherical shape (pores), are uniformly distributed throughout the internal volume. Whereas the bigger and elongated/flat defects (voids) are fewer in number and can be seen at discreet locations in Figs. 4.10, 4.11(a) and 4.11(b). As seen in Fig. 4.10(b), the axis of elongated voids (due to LOF) fall in the plane of layers and is perpendicular to the loading axis. A horizontal built sample (section size 15 mm x 15 mm) was also CT scanned to study the effect of build orientation on defect characterisation. The 3D rendered horizontal sample with defects characteristics observed from the CT scan analysis are shown in Fig. 4.12. For horizontal built sample, the number of defects and volume fraction (0.07% - vol) was higher than for the vertical built sample. From the histograms of 'sphericity' and 'flatness', shown in Fig. 4.12(b) and Fig. 4.12(c), respectively, majority of defects in the horizontal built sample are small in size and spherical in shape (pores).

From the tests performed, the voids are judged to cause pronounced effects on material ductility for tests at high temperature where, due to volumetric expansion, the collapsed/flat voids open up [198] and cause premature fracture along the section containing a single large size or multiple small size voids under tensile loading. Although these small size pores are comparatively much less damaging [191], a possible coalescence of these small pores, resulting into bigger elongated defects, cannot be ruled out which may be equally damaging as the larger size voids under tensile loading [198, 199].

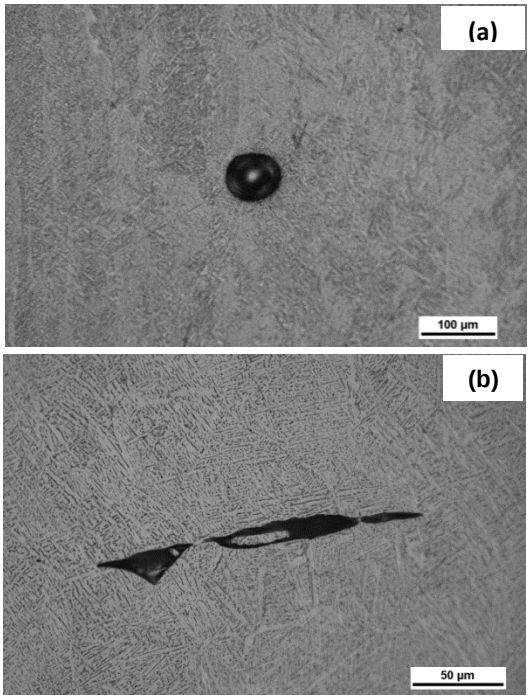


Fig. 4.9. Typical anomalies in EPBF specimens: (a) spherical gas pores (b) void due to unfused powder.

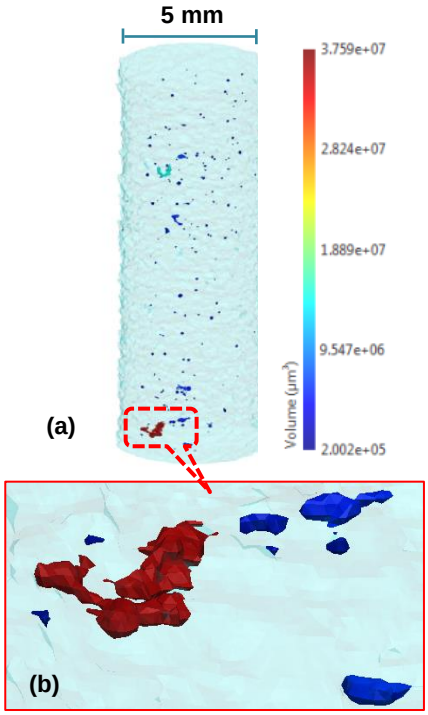


Fig. 4.10. 3D rendered volume of X-ray CT scans: (a) Vertical built sample, (b) zoomed-in view showing large shape flat defects due to LOF.

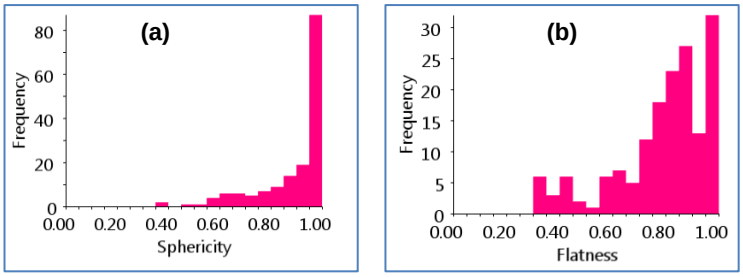


Fig. 4.11. Defects statistics of vertical built EPBF sample: (a) sphericity distribution, (b) flatness distribution.

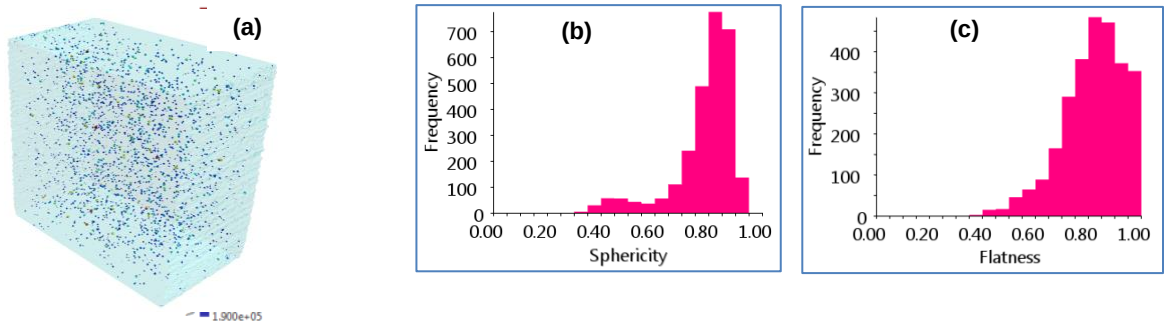


Fig. 4.12. Defect details for horizontal built sample of 15 mm x 15 mm section size: (a) X-ray CT scan, (b) sphericity distribution, (c) flatness distribution.

4.2.3 Fractography

The SEM scanned images of the fractured surface of specimens tested at RT (VM1) and at ET (VM4) are shown in Fig. 4.13 and Fig. 4.14, respectively. The amount of necking observed was lower for the specimen tested at RT than the one tested at ET. The fracture surface of VM1 is a mix of ductile and brittle types of failure where a small shear lip is formed towards the outer region (ductile) and nearly a flat face can be seen in the inner region (brittle) as seen in Fig. 4.13(a). Discrete zones of LOF and gas pores are common, as seen in Fig. 4.13(b) and Fig. 4.14(b) and described in Fig. 4.10, which accelerated the tensile fracture [50]. The micrograph in Fig. 4.13(c) showed the presence of quasi-cleavage facet with shallow and smaller size dimples which confirmed mix of ductile and brittle type of failure in the specimen tested at RT (VM1). A slight flaking-off of the metal is also observed which may be due to the layer peeling-off effect caused by the discrete LOF zones between the layers in the central region.

The fracture surface of the specimen tested at high temperature (VM4), shown in Fig. 4.14(a), was observed to be quite uneven with typical cup-and cone shape type of failure and a significant amount of necking. Much bigger in size and deeper dimples were observed for the specimen tested at high temperature (VM4) – see Fig. 4.14(c).

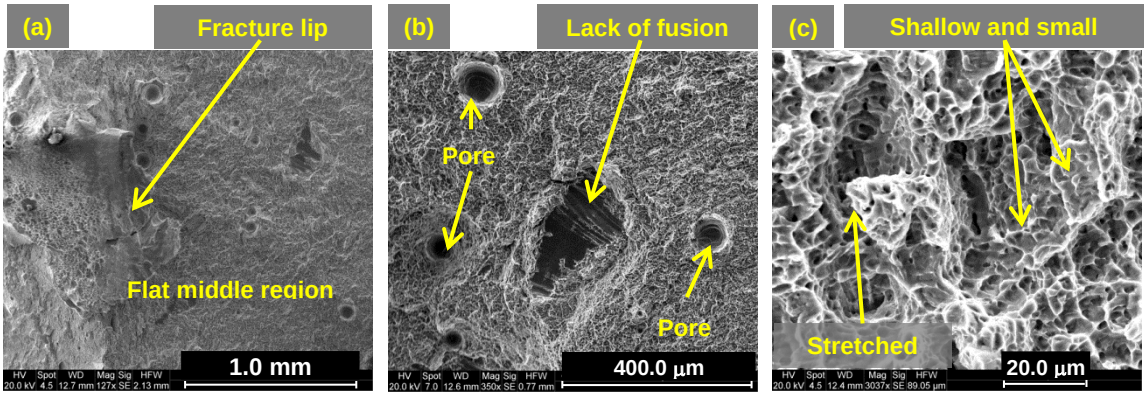


Fig. 4.13. SEM micrographs of the fractured surface (#VM1, test at 20 °C); (a) Shear lip and flat middle region, (b) typical LOF defects and pores, and (c) Shallow and smaller dimples on the fractured surface.

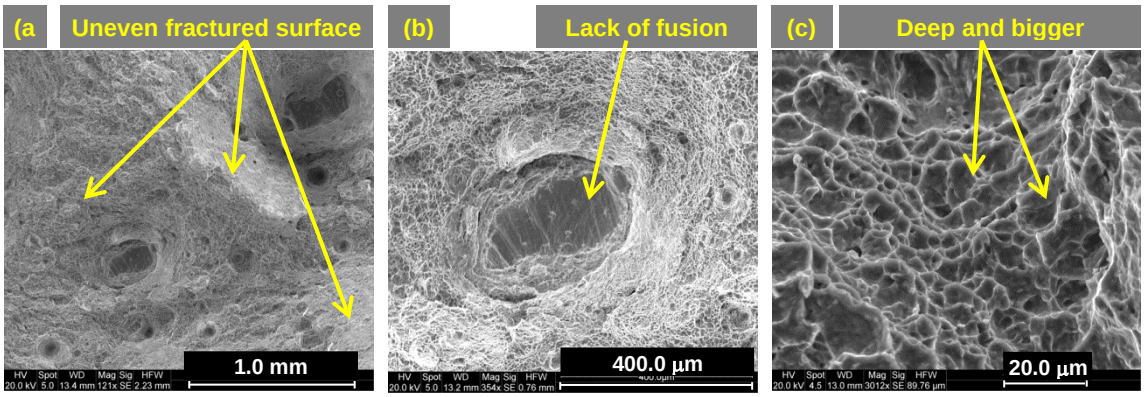


Fig. 4.14. SEM micrographs of the fractured surface (#VM4, test at 400 °C); (a) Uneven fractured surface, (b) typical LOF defect, and (c) deeper and bigger dimples on the fractured surface.

From the micro-examinations, there was no obvious change in surface colour or α-case layers were noticed. The low oxygen content in the powder used (below 0.173% (wt)) and high vacuum environment during the EPBF build process has helped to avoid oxygen contamination in the specimens used in this study [41]. The non-existence of oxide surface layer may also be due to the short duration of tensile tests.

4.2.4 Hardness Mapping

Micro-hardness testing can be an effective method to characterise the local mechanical strength of Ti-6Al-4V AM parts [195]. The VMH tests were carried out to show the spatial variation of micro-hardness in the cross-section of specimens. A 'horizontal as-built' sample in square cross-section was chosen to estimate the micro-hardness variation in the sample and is characterised in Fig. 4.15(a). Furthermore, to characterise the micro-hardness in a necked specimen, a longitudinal section was cut from the fractured HM3 specimen, which was tested at 400°C and showed a ductility of 15%. For the cut sample, the neck region and the region away from it were scanned, and the micro-hardness distributions within

these two regions are shown Fig. 4.15(b) and Fig. 4.15(c) respectively. The range of micro-hardness and the average micro-hardness values obtained for the three scanned regions are listed in Table 4.2.

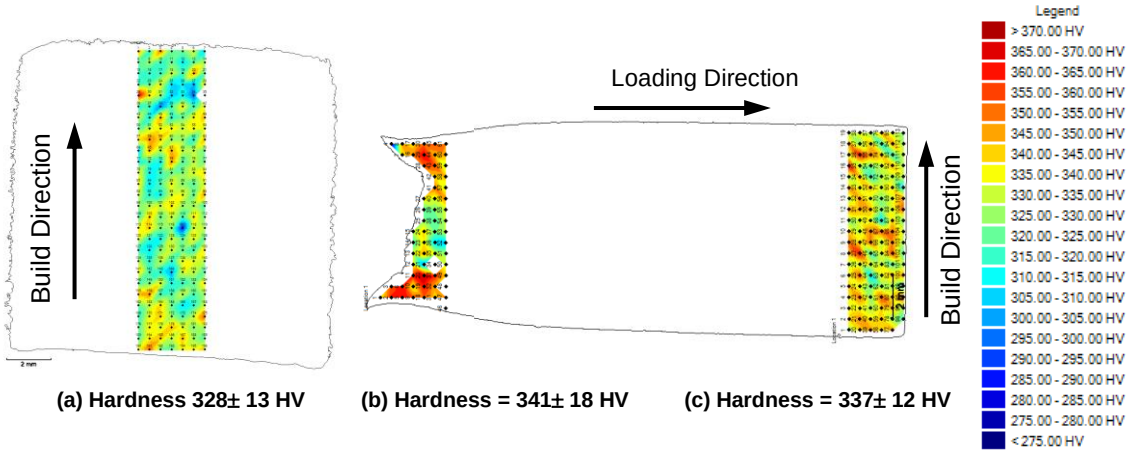


Fig. 4.15. VMH test results with average micro-hardness values in: (a) horizontal as-built sample, (b) HM3 specimen at the neck region, (c) HM3 away from the neck region.

From Fig. 4.15(a), the raw as-built sample did not show any particular pattern of micro-hardness along the width and height of the sample [190]. From Table 4.2, the raw as-built sample shows a higher micro-hardness value (328 HV average measured with a load of 500 gf) as compared to the extruded equiaxed α/β Ti-6Al-4V material (302 HV average measured with a load 1000 gf, [200], suggesting that the as-built EPBF Ti-6Al-4V material is, in general, harder as compared to the conventionally made Ti-6Al-4V material) owing to its finer α laths. Note, a difference in the indentation force applied during the hardness test will also cause some difference in the measured hardness value.

This difference in micro-hardness values between EPBF and wrought Ti-6Al-4V observed could be due to possible differences in the test force used, microstructure with varying shape and size of α grains and different ratio of α and β phases.

For the necked sample of HM3 specimen, shown in Fig. 4.15(b), the necked area shows quite a lot of variation in the micro-hardness value across the fracture line, where the micro-hardness under the shear lip is a bit higher than the central fractured part. From the scanned micro-hardness results, since the material under the shear lip undergoes plastic flow, experiences rapid and significant change in grain structure and therefore gets hardened. The lower micro-hardness in the central region is because the amount of material plastic flow is less and, possibly, some stress relaxation happened in this region post fracture. In the region away from the neck, the observed hardness is higher than that for the raw as-built sample but lower than the neck region, this may be due to small length (25 mm) of the cut sample (from HM3 specimen) which perhaps experienced a level of plastic strain hardening. The micro-hardness value reported by Galarraga et al. [190] and Hrabe et al. [115] (both 368 HV) was higher than the hardness resulted observed in this study and they reported an insignificant variation in micro-hardness value between the vertical and horizontal build orientations. Researchers have reported that

the micro-hardness of EPBF Ti-6Al-4V is related to the α-lath thickness (δ_{lath}), using the Hall-Petch relationship, see equation (4.1) [40, 116, 195, 196].

Table 4.2. Hardness test data for the raw as-built and tested samples.

Zone Studied	Micro-Hardness Range (HV)	Average Micro-Hardness (HV)
As-built sample	368 – 287	328 ± 13
Necked region (HM3)	389 – 278	341 ± 18
Away from neck region (HM3)	366 – 308	337 ± 12
Vickers Micro-Hardness is shown in GPa, where 1 GPa = 100 HV		

4.3 Discussion

4.3.1 Effect of Strain Rate

All the data pairs in Figs. 4.1- Fig. 4.3 with same temperature, except the VM4 - VM5 pair, show that the PS and UTS increase but the ductility decreases with increase in SR, a behaviour also concluded by Giuseppe et al. [180]. The data pair VM4 - VM5 indicated a reverse trend where PS and UTS were lower value but ductility was higher with higher SR. From Fig. 4.14, the fractured surface of VM4 was examined and was found to have relatively large areas of LOF defects causing the VM4 (at SR = 0.0002 s^{-1}) to fail prematurely and thus resulting in lower ductility than for VM5 specimen (at SR = 0.0265 s^{-1}). Although an indicative positive trend of strength properties with change in SR was observed, similar to the observation made by Li et al. [201] and Rodriguez et al. [113] , it is judged that the SRs used in this study are not big enough to cause a significant difference in tensile properties [113]. Therefore, for applications requiring analysis for fast transients, such as the impact loading, it will be prudent to do tests at the required higher SRs to estimate the large gains in PS and UTS and reduction in material ductility. Giuseppe et al. [180] observed a 20% higher plastic flow curve for dynamic SR as compared to the plastic flow curve for static SR for the EPBF Ti-6Al-4V alloy. On the combined effect of SR dependency and anisotropic behaviour, Rodriguez et al. [202] reported a noticeable difference in tensile and compressive strength responses of EPBF Ti-6Al-4V with changing SR, whereas Ladani et al. [203] showed a positive tensile response with increasing SR for vertical build specimens but no SR dependency for specimens build in horizontal direction.

4.3.2 Effect of Temperature

With increase in temperature the migration and annihilation of dislocations are enhanced, therefore the dislocation density will decrease with increasing temperature [201]. A decrease in density of material and multiplication rate of dislocations with increase in temperature results in a loss of resistance to plastic flow (i.e. reduction in strength), and therefore, the material becomes softer and more ductile [201, 204], as observed in Figs. 4.1 and 4.2 for the data pairs of machined specimens. However, for as-built specimens, the effects of surface roughness and internal defects are more

prominent, where the surface nucleating micro-cracks and internal pores experience dimensional growth and cause a significant reduction in ductility with increase in temperature as seen in Fig. 4.3.

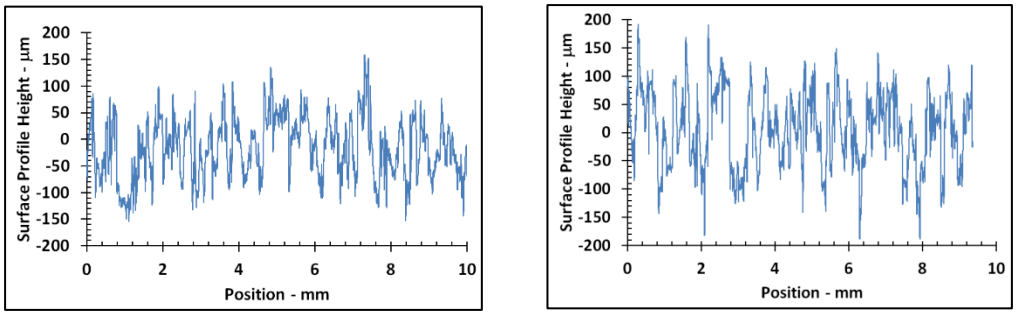
4.3.3 Effect of Build Orientation

The effect of build orientation on mechanical properties was studied using the test results of 'vertical machined' and 'horizontal machined' specimens, i.e. the data pairs were made with same temperature and SR, as shown in Fig. 4.4. For the two temperatures studied, although the difference in PS and UTS was observed to be small, a slightly higher values of PS and UTS were observed for the 'vertical machined' specimens which could be attributed to the torturous crack path along the α_{GB} and through the PBG, running parallel to the loading direction. This results in crack deflections and therefore increases strength [194]. However, a noticeable difference in material ductility was observed, where higher ductility was noticed for the horizontal built specimens than that for the vertical built specimens [190]. The lower ductility for vertical built specimen is attributed to the fact that the layers containing LOF areas become perpendicular to the loading axis and sharp tips of these voids act as the points of stress concentration which leads to premature failure of the specimen with reduced ductility [39, 41, 50, 93, 190]. The thermal history of the AM built parts is an important factor to cause anisotropy in material properties of AM built parts [39, 205]. The vertical and horizontal built parts experience different thermal histories during the build process which, in addition to affecting microstructure, also affects the shape, distribution, and density of defects within it [205]. Furthermore, the deleterious effects of α_{GB}, running along the long axis of columnar β grains, as seen in this study, also cause anisotropy in ductility response of the material. Presence of α_{GB} on PBG boundary serves as a path for cracks. Since PBG boundaries are near-parallel to the build direction, for horizontal specimen the tensile loads acts on the short length of columnar β-grains and α_{GB} acts to separate the adjacent β-grains and attempting to cause failure of mode (I) type of crack opening. Whereas, in the vertical specimen, the long axes of β-grains and α_{GB} are parallel to the tensile load which tends to result in higher ductility value, which is contrary to the observation made in this study. It should be noted that the deleterious effects of α_{GB} on material ductility comes into play only if the LOF voids, which play a dominant role, are totally absent in the specimen [41].

4.3.4 Effect of Surface Roughness

In the EPBF process, the electrons penetrate (and charge) the powder particles and into grains, to allow their kinetic energy converted into the thermal energy and facilitate melting of powder. The bigger spot size of the EB and larger powder particle size causes the powder particles being repelled from each other [42]. Therefore, the main reasons identified for poor surface roughness of EPBF process are; (i) the staircase effect related to the increased layer numbers and thickness, (ii) the adherence of partially melted powder to the external surface, (iii) the existence of open pores and incomplete regions approaching the surface [41, 62]. Therefore, the surface roughness of an EPBF part is typically larger relative to the roughness produced by the laser-based AM processes.

From the two data pairs studied in Fig. 4.5, a significant reduction in PS, UTS and ductility was observed for the as-built specimens. Surface topography and roughness scans were performed on the representative vertical and horizontal as-built test samples. These additional test samples were built together with the tensile specimens in the same AM builds. The scans were run along the build direction i.e. the scans were perpendicular to the deposited layers. Note that, since the horizontal built tensile test specimens were built in a cuboid shape and were machined to the final shape prior to the tests, the roughness scan on the horizontal built sample was only to see if the build orientation has a significant impact on the surface roughness. Multiple scan runs were carried out on both types of sample which indicated a slight variation in overall roughness value for each scan runs, hence only a typical scan reading is presented in Fig. 4.16 for both samples. The arithmetic average of filtered roughness (R_a) is 49 μm and 55 μm for the vertical and horizontal built samples respectively. These readings suggest that the horizontal built sample has a slightly worse surface finish which needs to be considered carefully when deciding the build strategy for an actual part. The average readings obtained are slightly higher than the roughness value reported by Qian et al. [196] (R_a=40 μm) and Galarraga et al. [190] ((R_a = 46 μm), and this difference in roughness observed is due to the possible differences in build process parameters.



(a) (b)

Fig. 4.16. Surface roughness in terms of measured surface profile height (0-max/min): (a) vertical built sample (b) horizontal built sample.

From the optical image of vertical built sample in Fig. 4.17, the surface is characterised by a wavy/very irregular and rough appearance which is typical of an EPBF build. Fig. 4.17 also shows the partially melted/un-sintered powder particles sticking to the outer surface. Since, the build chamber is held at a high temperature, it is likely that the heat diffusing out from the melt pool causes surrounding powder to be partially melted and get stuck onto the solidifying geometry [190, 197]. Examination of the horizontal built sample surface also showed the steps formed by each scan layer thickness [190]. The variation in scan speeds and use of relatively bigger powder size and layer thickness are responsible for poor surface roughness observed in the EPBF built specimens [41, 91, 197]. The stair-step effect is dependent on the track width and the distance between adjacent tracks (hatch spacing), therefore, in the EPBF process, usually a pronounced stair-step effect is observed due to the relatively wider melt pool [41]. The higher scan speed, scan spacing and the bigger powder size make the EPBF production rate faster but at the expense of poor surface finish [91].

As observed in this study, the rough surface of the as-built specimens has influenced the PS and UTS and more significantly the ductility of EPBF Ti-6Al-4V alloy [196]. The surface roughness induces stress concentration and helps to initiate cracks and thereby affect material ductility and its fatigue and fracture strengths [91, 92, 190]. To achieve improved properties, the surface finish of the part is required to be improved by performing post build treatments such as machining, acid etching, surface polishing or Abrasive Fluid Machining (AFM) [196]. From the collected scan data, the maximum peak to valley height (R_{pv}) observed was 312 μm for vertical built sample and 380 μm for horizontal built sample. Hence, a 400 μm surface layer should be machined off to avoid the detrimental effects of poor surface finish. However, depending upon the magnitude of surface roughness observed in an AM part, a much deeper cut may be required. For example, Chern et al. [50] have suggested a machining cut of 725 μm. Machining will increase the cost and the time to make AM part ready for in-service use, therefore, it is suggested that the machining of AM parts is carried out only if necessary and in critical regions only [181]. Additionally, the machining could be a problem for the thin walled parts as it will drastically reduce the load carrying sectional area, hence this factor must be accounted for in the initial design stage where the part is designed to be built thicker to allow for subsequent machining. Furthermore, the intricate areas and locations of geometric discontinuity, where machining/polishing cannot be done easily, must be designed appropriately to tolerate the in-service stresses with its as-built surface conditions. If a part is built with sub-optimal build parameters then it is likely to be full of internal pores and if such a part is machined then it is likely that the internal pores will move to the surface, producing detrimental effects on mechanical and fatigue performances [74].

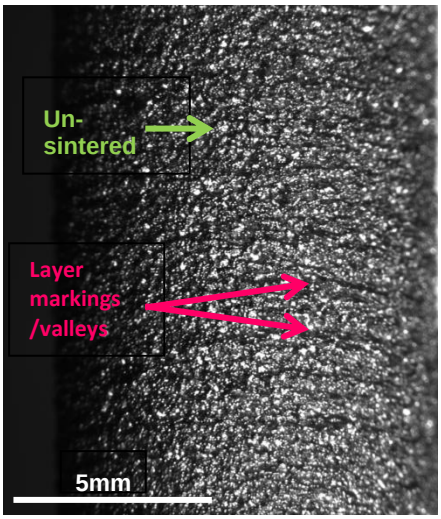


Fig. 4.17. Optical image of vertical built sample.

4.3.5 Role of Defects

Anomalies/defects are common in the EPBF process as found in other research studies and are heavily influenced by the EPBF process parameters [40, 42, 91, 93, 197]. Discontinuities in the hatch lines and

lack of overlap between the hatch lines result in porosity and entrapped powder particles. There are various factors which could aid to produce voids in the EPBF parts. The EPBF process uses a speed function index which is directly proportional to the scan speed to achieve the desired melt pool size. The Arcam system controls the scan speed dynamically according to the max current and powder bed temperature. A higher scan speed increases porosity by creating entrapped un-melted powder particles [42]. Further, the CCF of the Arcam system calculates the Beam Current Value (BCV) for a given scan as a function of the scan line length in a way that the variation required in the input beam power when melting small and large areas is considered [50]. The upper value of the BCV is limited by the MCV of the Arcam system. In case of exceedance of the BCV, the MCV is used by the Arcam system to melt the scan line length instead which then leaves the scan line deprived of sufficient energy for complete melting, thus assisting to develop voids. The Arcam recommended maximum scan length is 100 mm to achieve complete melting [50, 181]. An increase in the LOV (the distance between two hatch lines) and FOV decreases the energy density between the melt lines, which again influences the defect generation [40, 42, 30]. Furthermore, the EB power fluctuations, surface gas flows, thermal history and raw material characteristics are some other contributing factors known to cause development of defects in the EPBF processed parts [42, 93]. According to Gong et al. [40], even the excessive energy density levels could cause the melt pool to become deep and thereby pores and voids to form due to entrapped gases or improper closure of the keyhole.

Based on the findings presented in Section 4.2.2, both the vertical and horizontal built samples have shown different defects characteristics and statistics. In addition to the deleterious effects on mechanical strength caused by the voids and pores, the differences in voids' statistics relate to the anisotropy in material properties as observed in the tensile test results discussed in section 4.3.3.

The higher material ductility for the horizontal built specimens observed in Fig. 4.4 is attributed to the fact that the pores are less influential in comparison to bigger size elongated voids. To further improve the EPBF technology, the relationship between the location on the build platform and porosity should be further investigated and influence of it should be further reduced [190].

Archimedes method according to ASTM B962-17 [59] has been used by the researchers to calculate the density of an AM part with defects [42]. Alternatively, a suitable post processing of X-ray CT scanned data to calculate total volume of defects could be utilised to determine the density of a part as done in this study [199, 206, 207].

4.3.6 Role of Microstructure and Crystallographic Texture

The mechanical properties of a metallic materials are dependent upon its microstructure, which is characterised by the morphology and distribution of constituent phases, typically revealed through the optical, SEM or EBSD micrographs. The structures of grains, phases present, and the interface characteristics are some of the parameters which are characterised through the microstructure examination. However, an extended knowledge about the crystallographic orientation of the constituent grains is also needed to fully understand the material microstructure. The geologists

describe the term texture to indicate a spatial alignment of constituents in the structure and uses the word fabric for the mean crystallographic orientation.

Texture is a statistical concept, if 30-40% of the grains have similar orientations, the material can be said to be strongly textured. The final texture of the material will depend upon the entire thermal and processing history the material has been subjected to, and anisotropy of mechanical properties may be strongly influenced by the texture of the material as much as by any other factors such as the voids, fissures or grain boundaries. In polycrystalline materials, the texture develops due to preferred orientation of the grains and it happens without regard to the spatial location of any particular grain or group of grains. In that sense it is a macroscopic phenomenon and therefore can be termed as the 'macrotexture'. By contrast, the material texture can also have microscopic connotation that may involve the determination of orientation of each grain in a population of grains in a material, as well as the nature and degree of its misorientation with respect to its immediate neighbours and is often referred as the microstructure. For a small targeted cluster of grains, this will give information regarding the orientation of grains in the scanned area and the measured texture here will be termed as the micro-texture [208] as discussed in the following paragraphs. The examination of macro-structure requires different testing techniques and is not in the scope of current study.

Fig. 4.18 shows the EBSD micrographs of EPBF Ti-6Al-4V samples. It shows that the crystallographic grains distribution and the phases present and indicates that the microstructure mainly consists of α phase and a very small amount of β within the prior β grain boundaries. As seen in Fig. 4.18, the crystallographic α grains appear to be finer for the horizontal sample than for the vertical sample suggesting higher mis-orientation of adjacent grains therefore less intense texture of the horizontal sample.

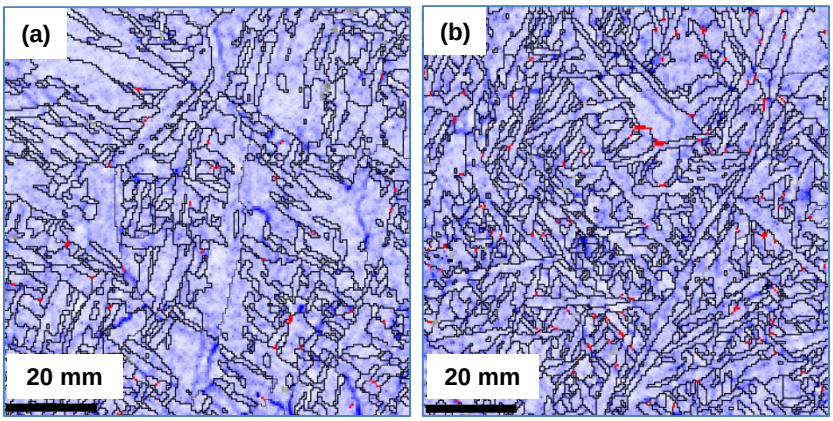


Fig. 4.18. EBSD images showing crystallographic grains and phase distribution in AM Ti-6Al-4V samples, cross-section perpendicular to the build direction, α phase in white/blue and β phase in red: (a) Vertical build sample, (b) Horizontal build sample.

The mechanical properties of crystalline materials depend on the individual properties of its crystals and crystalline texture i.e. preferred orientation of grains. The texture may undergo evolution during the AM process and during the post build heat treatments. When all possible orientations of the crystallites occur with equal frequency, the orientation dependence disappears, and properties are

isotropic on average. Engineering hexagonal materials, such as the EPBF Ti-6Al-4V material, may possess fewer easy glide systems than cubic metals/alloys at RT, causing greater potential for texture strengthening and crystal anisotropy of the mechanical and physical properties [191, 209]. Therefore, a weaker texture is desirable to achieve isotropic properties and better fatigue performance of parts made of titanium alloys for practical applications [191].

The columnar PBGs in an AM fabricated Ti-6Al-4V components have a strong ⟨0 0 1⟩ fibre texture in the build direction. As the volume fraction of β-phase is quite less (at RT, Fig. 4.18), the texture studied is only of the α-phase. EBSD Inverse Pole Figure (IPF) map of the initial microstructure of the vertical and horizontal samples is shown in Fig. 4.19(a) and 4.20(a) respectively. Crystallographic grains in 'red' colour indicate α-laths oriented towards (0001) basal planes. Neither the vertical nor the horizontal sample exhibited an obvious local preferred orientation of the α phase microstructure. The absolute textures of α-phase in the vertical and horizontal samples are shown using the pole figures in Fig. 4.19(b) and 4.20(b), respectively. In Fig. 4.19(b) and 4.20(b), the pole intensity of the basal planes $\{0\ 0\ 0\ 1\}_\alpha$, aligned parallel to the build direction (Z_0 axis in pole figures), showed strongest texture whereas the $\{1\ 0\ \bar{1}\ 0\}_\alpha$ prismatic plane pole figures showed the weakest texture. From Fig. 4.19(b) and 4.20(b), the vertical sample has shown stronger texture (pole intensity) than the corresponding pole intensity of the horizontal sample.

However, from a more macroscopic point of view, the $\{0\ 0\ 0\ 1\}_\alpha$ pole figures obtained by EBSD based texture analyses showed that the c-axis of the HCP-α phase were preferentially aligned approximately at 45° and 90° to the build direction in the as-built vertical and as-built horizontal samples, respectively, as shown in Fig. 4.19(b) and Fig. 4.20(b), respectively. The relationship between the ⟨0 0 1⟩ oriented columnar PBGs and the resulting transformation to α phase that occurs follows the BOR [194];

BOR: $\{1\ 1\ 0\}_\beta \,||\, \{0\ 0\ 0\ 1\}_\alpha$ (parallel planes) and
$\langle 1\ 1\ 1\rangle_\beta \,||\, \langle 1\ 1\ \bar{2}\ 0\rangle_\alpha$ (parallel direction)

During β to α transformation, grains evolve with close-packed planes of HCP-α (basal (0001) planes) parallel to the close-packed planes of BCC-β ((1 1 0) planes). According to the above relationship, three α-variants can be formed from each of the four $\langle 1\ 1\ 1\rangle_\beta$ β directions, giving twelve possible orientations referred to as variants [194]. If several α-laths are formed from the same variant, it gives rise to the α-colonies in the microstructure as observed in the same colour in Fig. 4.19(a) and Fig. 4.20(a).

Since the crystallographic planes $(0\ 0\ 1)_\beta$ and $(1\ 1\ 0)_\beta$ are either 45° or 90°, as per BOR, the $\langle 0\ 0\ 1\rangle_\beta$ direction (parallel to the build direction) would either be inclined at 45° or 90° to the $\langle 0\ 0\ 0\ 1\rangle_\alpha$ direction of the α plates. Any scatter in the preferential orientation of the α grains will be due to the orientation variation of the PBGs during the rapid cooling during the EPBF process. The other poles are aligned at 45-85° from the build direction. It is to be noted that the direction of tensile loading is parallel to the build direction for the vertical sample whereas it is perpendicular to the build direction for the horizontal sample and the obvious differences in texture with respect to the build direction will also contribute towards anisotropy in material strength.

Although the most favoured slip planes vary from metals to metals, for the α phase of Ti-6Al-4V material with *c*/*a* ratio of 1.587, the directions of easy glide is of the type $\langle 1\ 1\ \bar{2}\ 0\rangle$ and therefore is difficult in producing any components of normal strain along the *c*-axis at RT. Twinning usually provides additional deformation, however, for a particular stress direction the twinning can occur only in one particular sense and, therefore, the ease of deformation in these metals will depend on whether the applied stress is tensile or compressive. So, the knowledge of active deformation modes allows to determine the optimum conditions for texture strengthening [209].

The deformation model in HCP crystals is based on the following three distinct slip systems and one twinning system: (i) basal $\{0\ 0\ 0\ 1\}\langle 1\ 1\ \bar{2}\ 0\rangle$; (ii) prismatic $\{1\ 0\ \bar{1}\ 0\}\langle 1\ 1\ \bar{2}\ 0\rangle$; (iii) pyramidal $\{1\ 1\ \bar{2}\ 2\}\langle 1\ 1\ \bar{2}\ \bar{3}\rangle$ and $\{1\ 0\ \bar{1}\ 1\}\langle 1\ 1\ \bar{2}\ 0\rangle$; as well as (iv) twinning $\langle 1\ 0\ \bar{1}\ 0\rangle$ slip on $\{1\ 0\ \bar{1}\ 2\}$. Therefore, the relative contributions from the above four deformation paths will contribute towards developing the deformation texture in HCP α phase of Ti-6Al-4V material [209]. A slip system becomes activated when the critical resolved shear stress (CRSS) exceeds the relevant critical or threshold level. The slip system associated with the lowest CRSS in Ti-6Al-4V is the prismatic $\langle$ a $\rangle$ slip followed by the basal $\langle$ a $\rangle$ slip. The pyramidal $\langle$ c + a $\rangle$ slip is about 2–5 times more difficult to be activated than the basal and prismatic. Basal or prismatic slips do not accommodate the strain along the c-axis. Therefore, twinning and pyramidal $\langle$ c + a $\rangle$ slips are the important mechanisms to cause deformation at RT along the c axis [194]. The $\{1\ 0\ \bar{1}\ 2\}$, $\{1\ 1\ \bar{2}\ 1\}$, and $\{1\ 1\ \bar{2}\ 3\}$ twins (tensile) allow an extension along the c-axis.

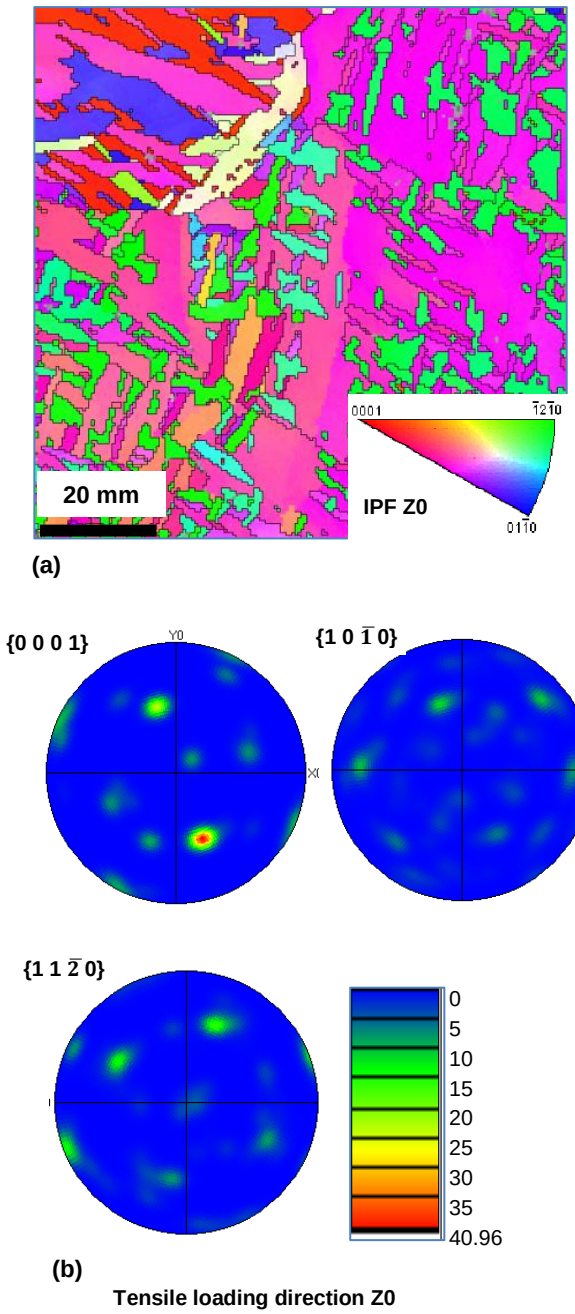


Fig. 4.19. EBSD images of vertical build sample, cross-section perpendicular to the build direction: (a) IPF Z0 map revealing crystallographic orientation (b) Crystallographic texture pole figures.

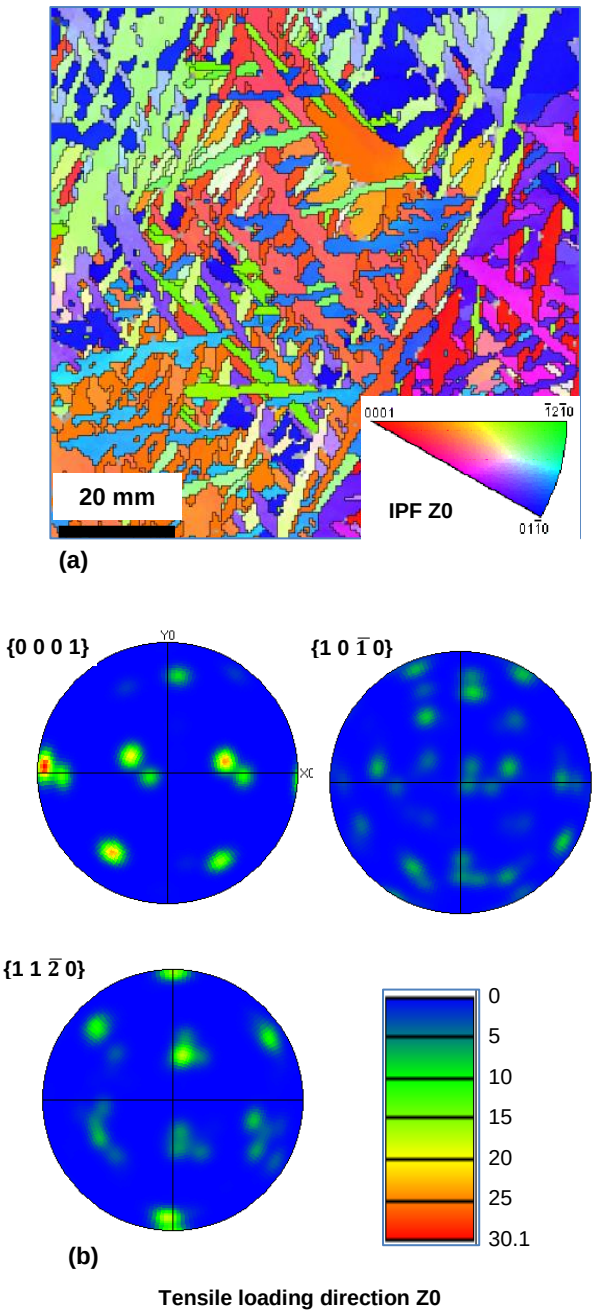


Fig. 4.20. EBSD images of horizontal build sample, cross-section perpendicular to the build direction: (a) IPF Z0 map revealing crystallographic orientation, (b) Crystallographic texture pole figures.

In order to study the crystallographic orientation map of the tensile tested specimen, a longitudinal cut section of the vertical specimen (VM) after the tensile test was scanned using the EBSD technique. Three discrete locations marked as A, B and C in Fig. 4.21 were scanned. Location A is in the vicinity of fracture surface. The IPF crystallographic orientation maps in the loading direction (Z_0 direction) for the three marked locations shown in Fig. 4.21 show that the α grains are stretched in the loading direction suggesting that the plastic strain flows in the tensile loading direction. The crystallographic orientation

for majority of HCP α grains is in the $\langle 0\ 1\ \bar{1}\ 0 \rangle$ direction (blue colour, Location A), which indicates that the grains deformation is caused predominantly by the basal and prismatic slips. As we move slightly away from the neck region, i.e. to location B in Fig. 4.21, the IPF maps indicates the easy glide/deformation of only few α grains participating along the $\langle 0\ 1\ \bar{1}\ 0 \rangle$ slip direction. Further away from the neck region (Location C), the IPF map consists of all the designated colours suggesting that the α grains are randomly oriented and haven't taken part in the necking formation or slipping of grains.

4.4 Further Discussion

A higher energy input increases the size of the melt pool and top temperature of the surface and causes escape of gases to the vacuum atmosphere in the EBM chamber and thereby reduces pore formation. However, a higher energy input could also cause significant loss of Aluminium due to evaporation effects under vacuum atmosphere of the EBM chamber, resulting in non-uniform distribution of Aluminium content within the part [191]. Aluminium being the principal strengthening element of the α-phase of Ti-6Al-4V material causes strength anisotropy. This necessitates the need to achieving the chemical homogeneity under as-built conditions to hone the isotropic behaviour of EBM parts.

As discussed, there are several factors which influence the strength and material ductility of Ti-6Al-4V alloy and many of these factors can be put on an interaction diagram shown in Fig. 4.22. The interaction of these factors can be complex and therefore poses challenges in achieving consistency in material data and performance of parts made using the EBM process. An emphasis should be put to optimise these parameters, in addition to the process parameters, to confidently and repeatedly make the AM parts which can be tested and judged to be reliable and safe for load bearing applications. Each of the influencing factors in Fig. 4.22 should be thoroughly investigated to understand their individual and coupled effects and should be part of the ongoing research in this area.

4.5 Conclusions

- At elevated temperatures, the material density and multiplication rate of dislocation decrease therefore, as expected, a significant decrease in material PS and UTS but increase in material ductility was observed for the tests at higher temperatures on machined specimens.
- The poor surface finish of the as-built specimens significantly reduced the PS and UTS. The material ductility was also lower, especially for the as-built specimens tested at higher temperatures. The surface nucleating micro-cracks and internal defects experience dimensional growth at elevated temperature and thus cause a reduction in material ductility.
- The SRs reported in this study differed only by two orders (max) which was judged to be a small difference to cause any significant difference in the tensile results. Although the current study presented a trend in tensile results variation with changing SR, further tests at higher SRs are suggested to obtain tensile properties for the simulation of dynamic events.
- Defects such as voids and pores were observed in the EPBF tensile specimens. The vertically built specimens had elongated and flattened voids between the build layers with their

longitudinal axis perpendicular to the loading axis, whereas many small size near spherical shape pores were observed in the horizontal build sample. A possible coalescence of these small pores, resulting in larger elongated defects, the presence of which produce deleterious effects on the ductility of EPBF Ti-6Al-4V.

- The torturous crack path along the α_{GB} and through the prior columnar β grains, running parallel to the loading direction, produced a higher strength for the vertical built specimens. The prior β-boundaries in the horizontal built specimens are near-parallel to the build direction meaning that the tensile loading acts perpendicular to the prior β-boundaries and therefore producing a weaker tensile response.
- The vertical and horizontal built parts experience different thermal histories during the build process. The difference in microstructure and orientation of voids with respect to the loading direction cause anisotropy in mechanical strength of EPBF Ti-6Al-4V.

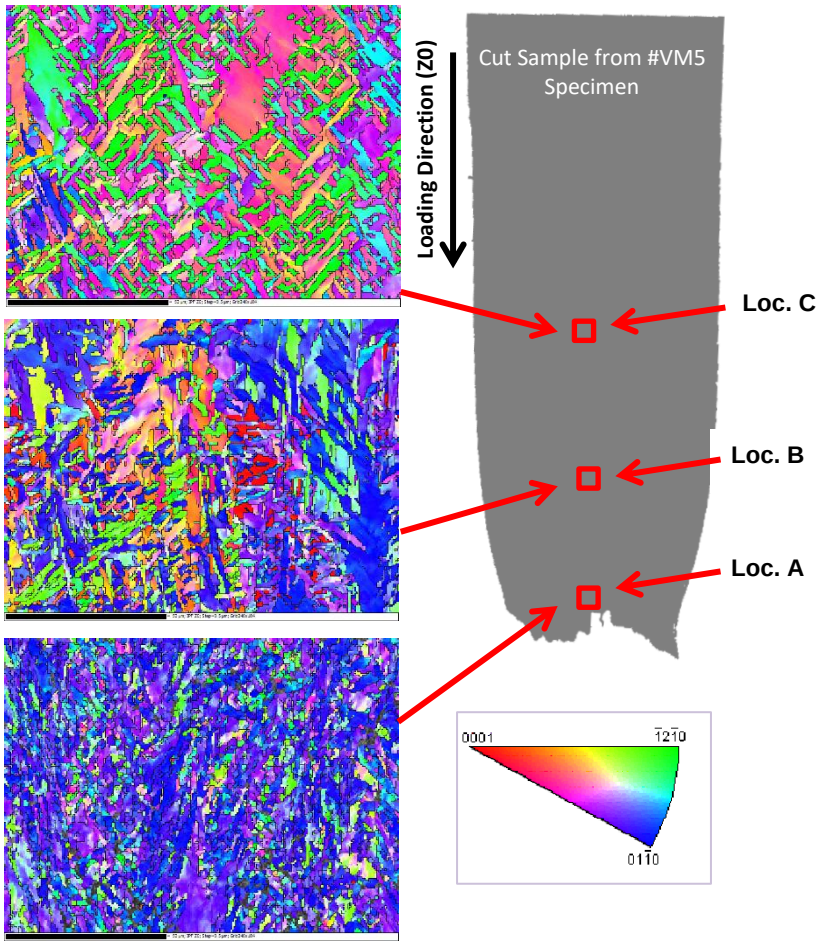


Fig. 4.21. EBSD IPF crystallographic orientation map (loading direction is Z0) of longitudinal section of the vertical specimen (VM5) post tensile test.

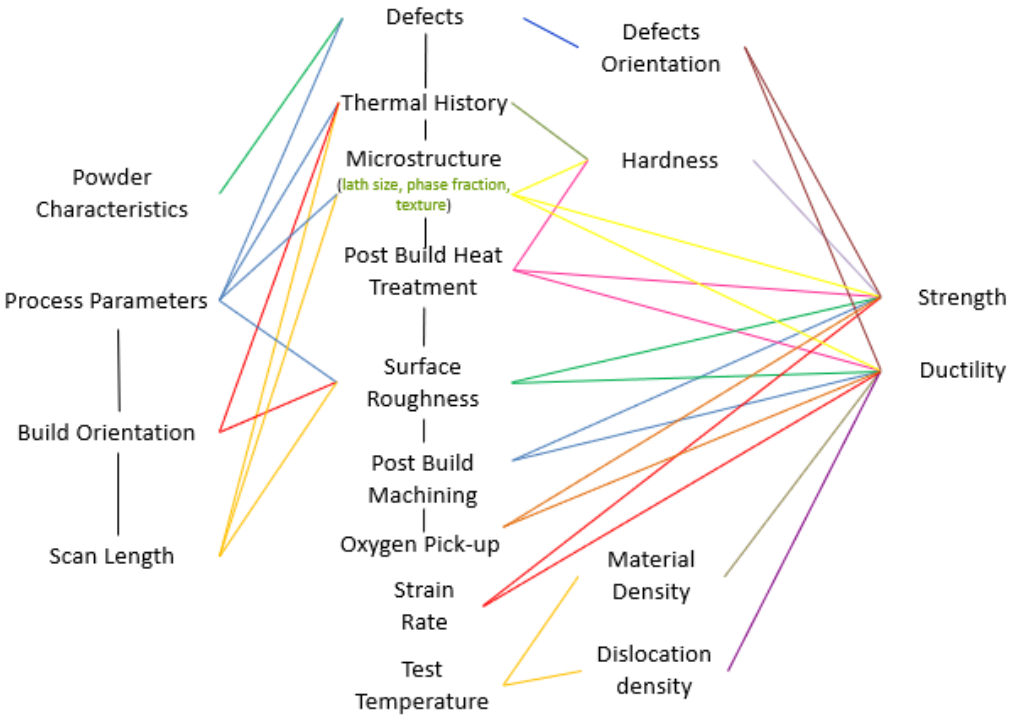


Fig. 4.22. EBSD IPF crystallographic orientation map (loading direction is Z0) of longitudinal section of the vertical specimen (VM5) post tensile test.

-----x x x x x x x-----

CHAPTER 5

5 Tensile Behaviour of LPBF Ti-6Al-4V

In this chapter, the tensile behaviour of LPBF Ti-6Al-4V material and its dependence on Strain rate (SR), temperature and surface roughness has been studied and discussed. Results are analysed in relation to the observations made on the material microstructure, fracture surface and material micro-hardness. Fracture surface characterisation has also been discussed based on the analysis of SEM microscopic images of the fracture surfaces of tensile specimens tested at RT and ETs. The characterisation of defects and its role in relation to the mechanical strength of the LPBF processed Ti-6Al-4V materials have also been presented and discussed in detail.

5.1 Tensile Test Results

The engineering stress-strain curves for LPBF Ti-6Al-4V material from the tensile tests performed at RT and ET (at 200°C and 400°C) are presented in Fig. 5.1. The mechanical properties obtained from the engineering stress-strain curves (Fig. 5.1) are summarised in Table 5.1. From Table 5.1, for LPBF Ti-6Al-4V, the strength values (PS, UTS) at RT are in the similar range but the ductility values are slightly lower as compared to the respective values observed in other research studies [86, 106, 107, 108]. The difference in strengths and ductility values, as compared to the other published data, is due to the possible differences in AM machines, build parameters, morphology and distribution of defects, HTs and other post processing treatments typically used to make the LPBF Ti-6Al-4V test specimens.

From, it can be seen that the PS and UTS values were significantly lower but the material ductility was higher for the ET tests, for both 200°C and 400°C, as compared to the RT test.

The strength values for the LPBF Ti-6Al-4V are also compared with those of the annealed Ti-6Al-4V bar material in Table 5.1, where it can be seen that the PS and UTS values for LPBF Ti-6Al-4V at RT are higher than the corresponding values for the conventionally manufactured annealed Ti-6Al-4V bar.

Table 5.1 also presents the values of strength ratio (STR, where STR = UTS/ PS) for the six tensile results performed. As shown in Table 5.1, for each the tests performed, the STR is less than 1.2, suggesting that some level of cyclic softening can be expected during the cyclic performance of LPBF Ti-6Al-4V [210].

Table 5.1. LPBF Ti-6Al-4V parameters and tensile strength properties (PS, UTS and Ductility).

Test Identification Number (#)	Temperature (°C)	Strain Rate (SR) – $\dot{e}$ (s^{-1})	Young's Modulus (MPa)	PS (MPa)	UTS (MPa)	Ductility (%)	STR
TRT1	20	0.0002	109317	993.6	1114.4	6.4	1.12
TRT2	20	0.0265	113762	1109.0	1170.6	8.7	1.05
TET11	200	0.0002	105001	808.5	904.4	13.8	1.12
TET12	200	0.0265	107373	851.8	934.1	13.1	1.15

TET21	400	0.0002	90423	695.8	826.6	13.2	1.19
TET22	400	0.0265	103686	699.3	803.5	12.2	1.15
Annealed Ti-6Al-4V Bar [136]	20	-	116526	861	930	10	1.08

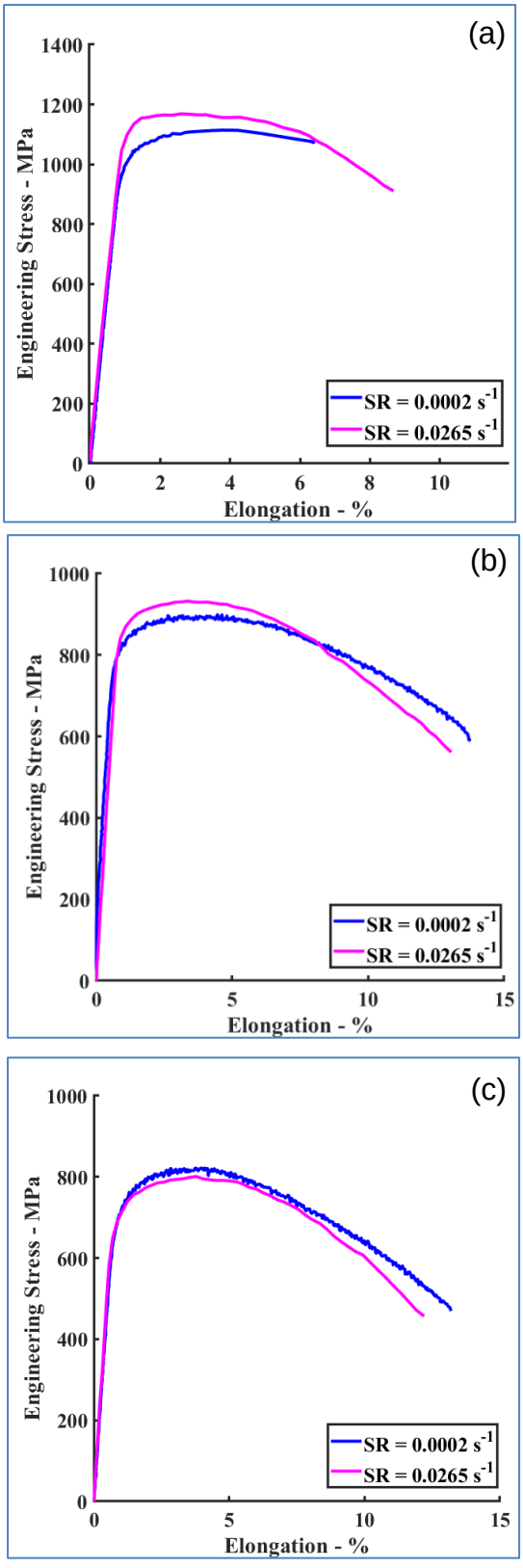


Fig. 5.1. Tensile behaviour of LPBF Ti-6Al-4V, effect of SR and temperature, 'vertical as-built' specimens: (a): T=20 °C, (b): T=200 °C, (c) T=400 °C.

5.2 Characterization

5.2.1 Macrostructure and Microstructure

The optical macrograph of the vertical cut section (along the build direction), scanning an approximate area of 1.3 mm x 1.3 mm, is shown in Fig. 5.2. The macrostructure is characterised by the several PBG with its epitaxial growth running across multiple layers. The average width of prior columnar β grains is between 50 - 100 μm. The macrograph also shows α grains randomly oriented within the prior β grains. The microstructure is then analysed further using the SEM and EBSD micrographs discussed as below.

The SEM micrograph of the section along the build direction in Fig. 5.3(a) shows martensitic acicular α' phase (needle shape) in long length, i.e. with high aspect ratio. In the section transverse to the build direction, the α' needles appear to span within the prior β grain boundaries as seen in Fig. 5.3(b) [211].

The key microstructural features and the phases present in the as-built LPBF Ti-6Al-4V material were studied using EBSD mapping. The EBSD micrograph showing the phases present and grain boundaries in the LPBF material can be seen in Fig. 5.4. Only a small amount of β phase (~0.253%) indicated by red zones in Fig. 5.4 was present. The remaining portion was the martensitic α' phase Indicated by blue/white zones in Fig. 5.4 The β phase improves ductility due to slip transfer at the α'/β interfaces [123], and a limited volume fraction of β phase suggests a relatively low ductility of the stress relieved LPBF Ti-6Al-4V material as observed in the TRT1 tensile test (Table 5.1).

The IPF maps of the α phase (Ti-Hex) are shown in Fig. 5.5. The microstructure of LPBF Ti-6Al-4V is characterised by the columnar prior β grains with acicular α' formed within the prior β grains [211, 212] as seen in Fig. 5.5(a).

The repeated heating and cooling of the molten metal and subsequent rapid cooling in the LPBF process produces a complex microstructure of LPBF Ti-6Al-4V. The melt starts to solidify into the β phase upon cooling from the melting temperature (1670°C) and β grains start to form. Below the β transus temperature (995°C) the β phase transforms into the α' martensitic phase at high cooling rates (>410°C/s) and to the α phase at slow cooling rates (<20°C/s) [212]. In the LPBF process, the cooling rate is high, causing nucleation of the α' martensitic phase through diffusionless/displacive transformation [211, 213]. The α' martensitic needles grow from these locations, both within and at the boundaries of PBGs simultaneously and meet each other to form a basketweave type of microstructure which comes with a high free dislocation density and/or twins [211].

According to the BOR, twelve possible orientations, referred to as 'variants', are formed during β phase (bcc structure) → α' transformation [211-214].

BOR: $\{1\,1\,0\}_\beta \,||\, \{0\,0\,0\,1\}_\alpha$ (parallel planes) and
$\langle 1\,1\,1\rangle_\beta \,||\, \langle 1\,1\,\bar{2}\,0\rangle_\alpha$ (parallel direction)

As the volume fraction of β-phase is small, only the texture of the α' phase was studied using the IPF map shown in Fig. 5.5(b). Crystallographic grains in 'red' indicate that the α' needles are oriented towards (0001) basal planes and there was no obvious local preferred orientation of the α' phase microstructure. The pole intensity of the basal planes $\{0\,0\,0\,1\}_\alpha$, aligned parallel to the build direction

(Z_0 axis in pole figures), showed the strongest absolute textures of the α' phase, whereas the $\{1\ 0\ \bar{1}\ 0\}_\alpha$ prismatic plane pole figures showed the weakest texture.

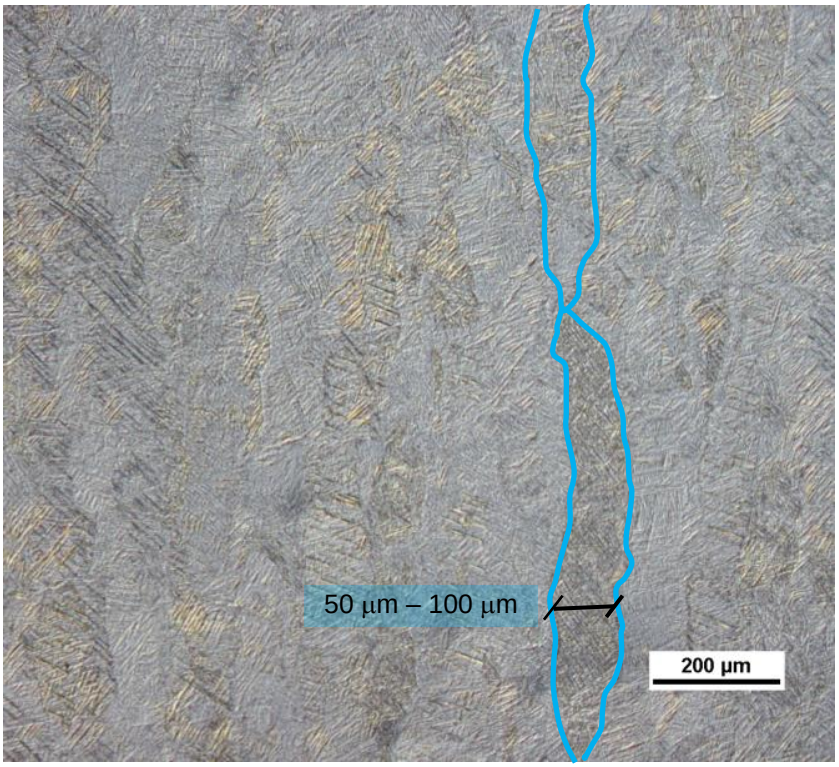


Fig. 5.2. Optical micrograph of the as-built LPBF Ti-6Al-4V material, section along the build direction.

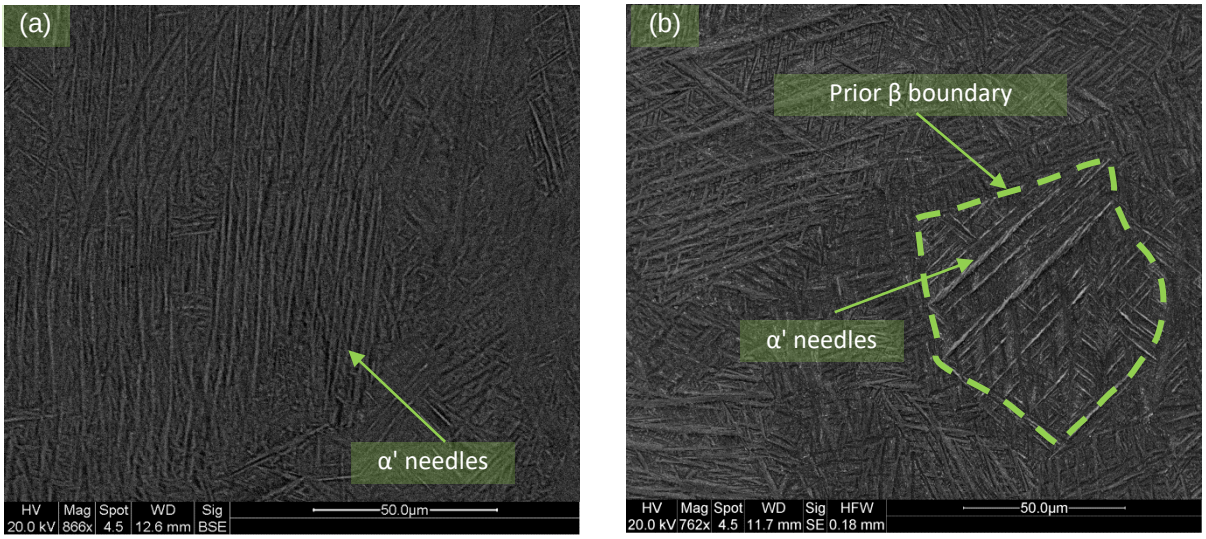


Fig. 5.3. SEM micrographs showing α' needles within the prior β grain boundary: (a) SEM image of the section containing build direction and (b) SEM image of the transverse section.

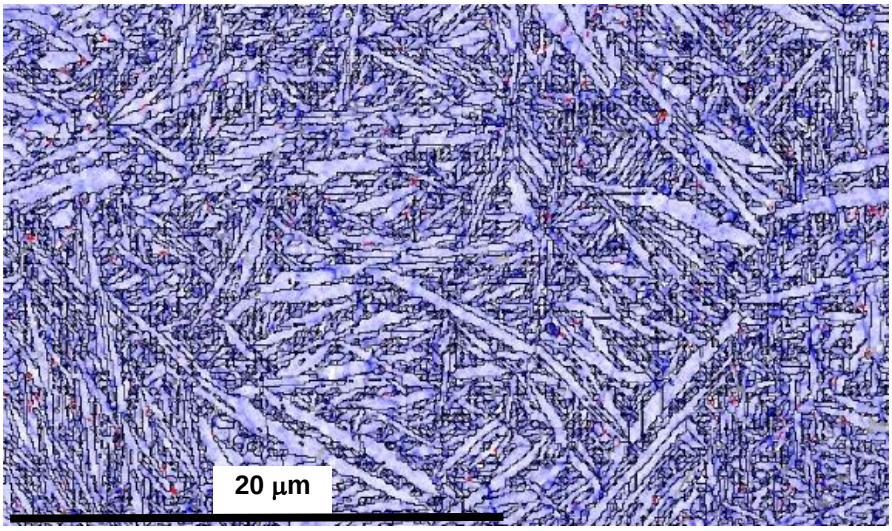


Fig. 5.4. EBSD micrograph of the LPBF Ti-6Al-4V sample longitudinal-section showing grain boundary and phases present (β phase is in red and α' is in blue/white).

5.2.2 Defects

To study the morphology and distribution density of defects, X Ray CT scans were carried out on a tensile specimen. In the scanned volume of LPBF Ti-6Al-4V specimen, shown in Fig. 5.6(a) (diameter = 10 mm, length = 17.8 mm), a total of 200 pores / voids were found with a total pore volume percentage of 0.01%, i.e. the total pore volume was only 0.01% of the scanned volume. The volume of maximum size pore was 2.6×10^{-4} mm^3, which equates to a sphere of diameter 79 μm, typically characterised as a physically small defect [215] (see Fig. 5.6(a)). The mean relative density was found to be greater than 99.9%. A histogram of sphericity of the internal defects is shown in Fig. 5.6(b). The majority of defects observed in the LPBF material were spherical in shape (pores), of small size (~35 μm). A histogram of flatness of the internal pores is shown in Fig. 5.6(c), where it can be seen that the majority of the defects identified (>50%) have a flatness of 1, meaning that these are defects are not flat i.e. are spherical in shape (pores). This is followed by the flat shape pores with a flatness of 0.65 (i.e. < 1) which indicates the presence of some pores/voids which are somewhat elongated but are not fully flat. Since only the small size micro-pores were observed, it suggested that the use of optimum process parameters is essential in LPBF builds to avoid formation of any larger size defects, and to achieve a good fatigue life of LPBF components.

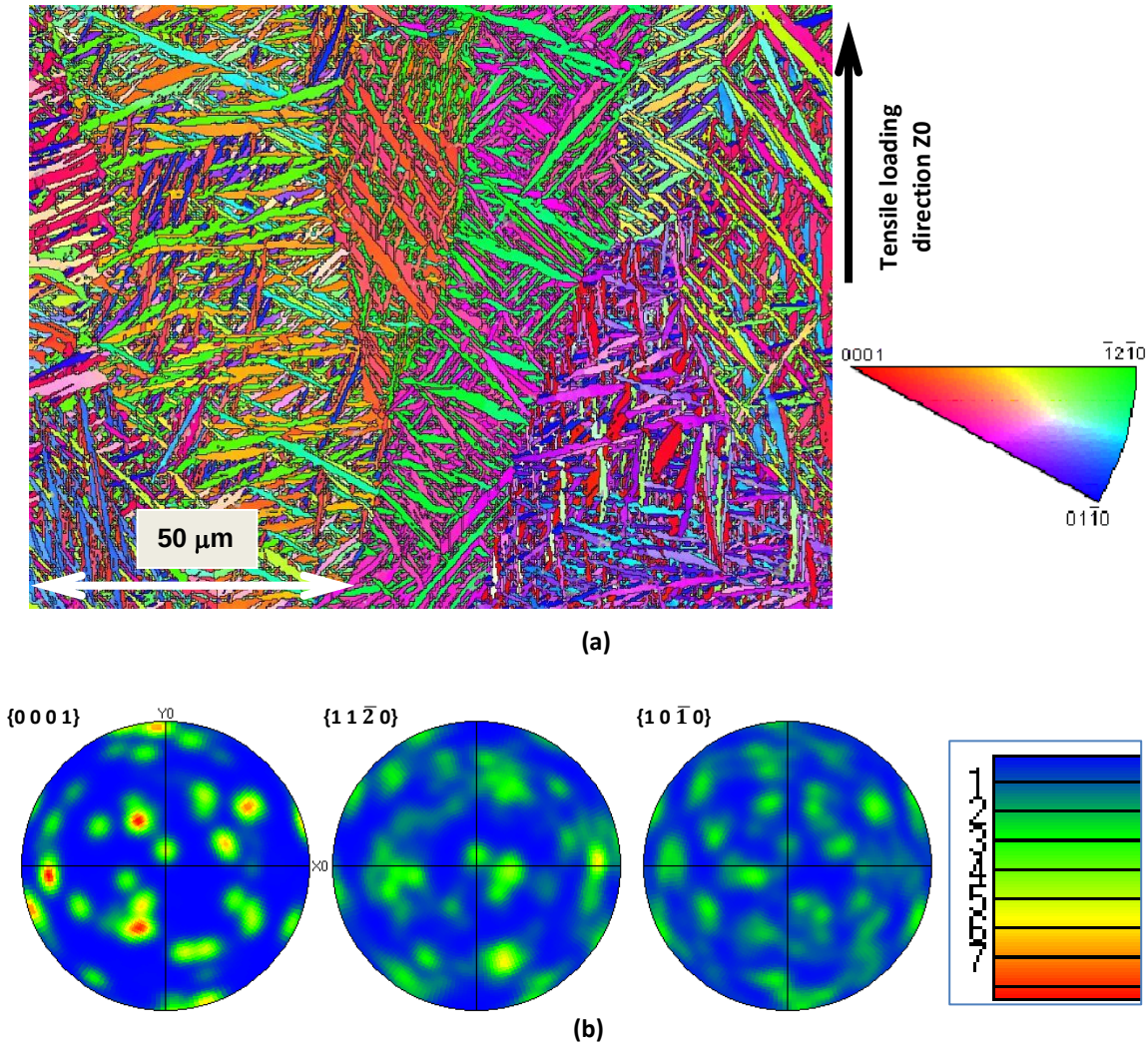


Fig. 5.5. EBSD images of LPBF Ti-6Al-4V sample, cross-section parallel to the build direction: (a) IPF Z0 map revealing crystallographic orientation, and (b) Crystallographic texture pole figures.

5.2.3 Fractography

The TRT1 and TET21 tensile specimens have exhibited a typical cup and cone type failure with their central portion being almost flat, as shown in the SEM images in Fig. 5.7. The fractured surface appears to be rough with shear lips observed in both the fractured specimens (Figs. 5.7(a) and Fig. 5.7(e)). With a smaller central portion, the necking is more prominent in the TET21 specimen which was tested at 400 °C. The cracks have appeared to initiate from the grain boundary α (α_{GB}) and have propagated along the PBG boundary resulting in α - cleavage or lamellar fracture. The PBGs being parallel to the build direction, the fracture along the grain boundary causes deflections of cracks at the PBG boundaries resulting into a torturous crack path and a rougher central portion marked in Fig. 5.7(a) and Fig. 5.7(e) [192, 197, 216].

The flat central portion, seen in Figs 5.7(b) and Fig. 5.7(f), is characterised by the coalescence of micro-voids resulting in a dimpled appearance, cleavage facets, numerous small opened–up pores and formed craters. The ductile tearing associated with the coalescence of pores is much more prominent in the

fractured TET21 specimen. The irregular shaped voids with sharp edges and random orientation are also evident, which are the preferential sites for crack initiation and growth causing tearing of specimens under tensile loading as depicted in fractured TRT1 specimen under Fig. 5.7(c). Furthermore, the TRT1 specimen shows equiaxed shallow dimples appearing on the surface of the terraces as depicted in Fig. 5.7(d). In contrast, as observed in Figs. 5.7(g) and Fig. 5.7(f), the cone shaped craters caused by the larger sized pores and a spongy textured surface with numerous finer and deeper dimples suggests a greater extent of plastic deformation and ductility in the TET21 specimen.

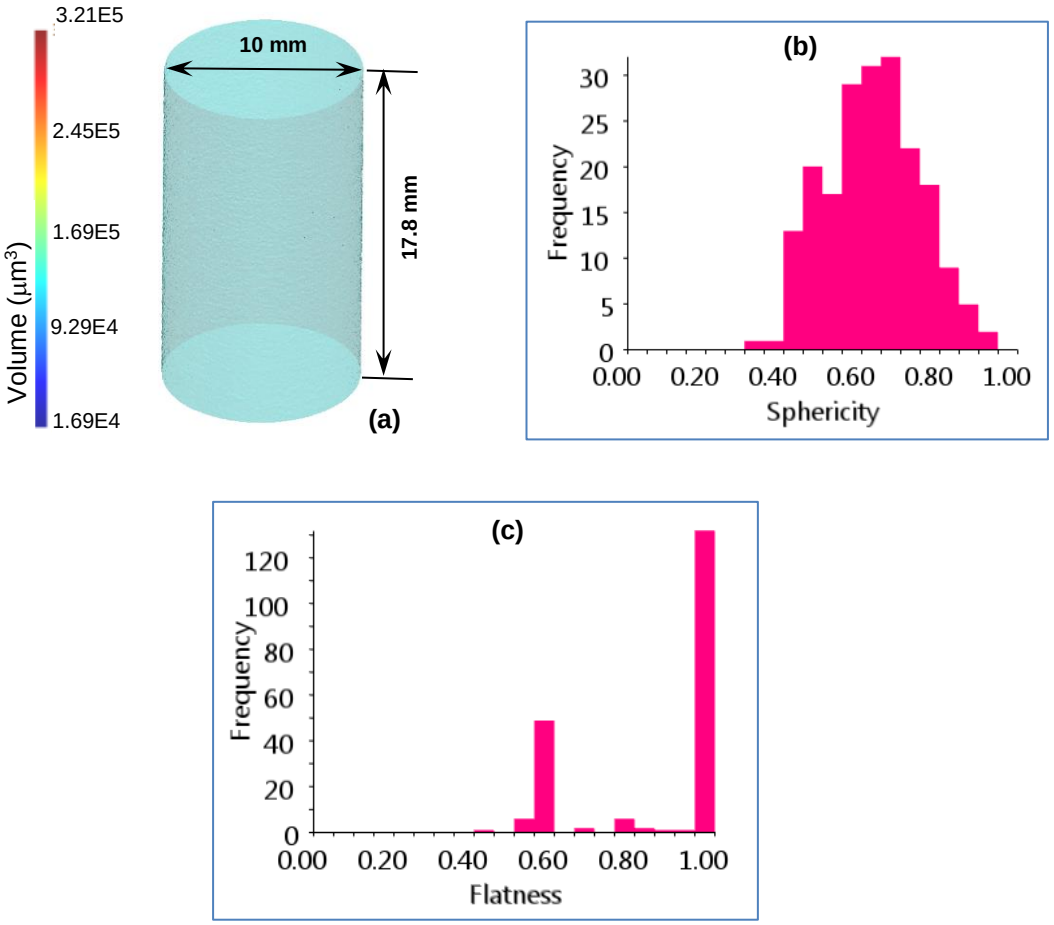


Fig. 5.6. CT scan result of as-built LPBF Ti-6AL-4V material: (a) scanned volume with distribution of defects found, (b) distribution of sphericity (c) distribution flatness of pores.

Additionally, the columnar PBGs, α' grains and grain boundary α (α_{GB}) can also influence the ductility of LPBF Ti-6Al-4V. The α_{GB} is softer than the α' grains and is the prime site for damage accumulation [192]. Upon tensile deformation, the strain mainly localises in α' grains, and those α' grains which are oriented 45° from the loading direction are the prime sites for this localisation. The boundaries of α' grains are particularly prone to interface plasticity to accommodate strain incompatibilities with the surrounding grains / microstructure. Strain localisation results in void formation within the α' grains which subsequently results in final fracture of the material, which is a mixture of ductile and brittle fracture, where the fracture surface contain both dimples and cleavage features, which has also been observed in other studies [192, 197, 209, 216]. Furthermore, the micro-voids appearing between the

layers results in weaker bonding of layers which, under the action of tensile loading, opens-up and subsequently grow and coalesce leading to deterioration of ductility of the LPBF Ti-6Al-4V [209].

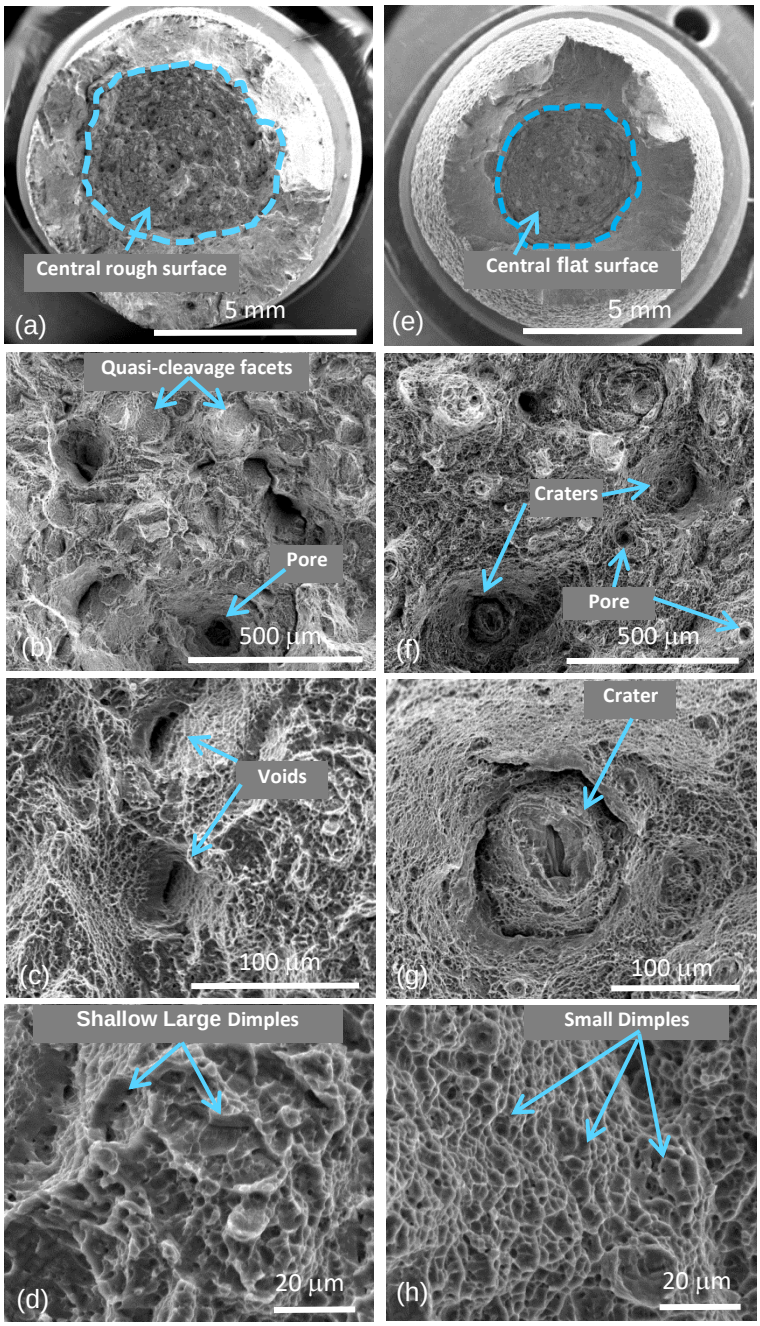


Fig. 5.7. Macro and micrographs of fractures surface of tensile specimens tested at: (a) – (d) 20°C (TRT1) and (e) – (h) at 400°C (TET21).

5.2.4 Hardness Mapping

The micro-hardness is closely related to the microstructure and densification level resulting from the complex thermal history during the LPBF process and indicates resistance to plastic deformation/rupture. The micro-hardness distribution plots of LPBF Ti-6Al-4V samples (longitudinal and transverse sections) are shown in Fig. 5.8. A slightly higher micro-hardness value (383 ± 5.5 HV) was found in the transverse section compared to the longitudinal section (371 ± 7.4 HV), with a

combined average of 377 HV. The average micro-hardness value is similar to the value reported by Hu et al. [177], but is different to the values reported by Vilaro et al. [129] of 354 ± 8.0 HV and Zhang et al. [217] of 390 HV. This difference in micro-hardness values observed is due to the possible differences in the process parameters used and resulting microstructure with varying length of α' grains and different ratio of α' and β phases [218].

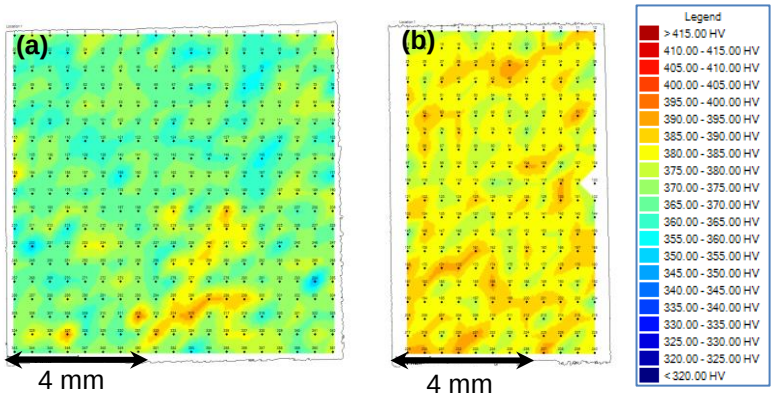


Fig. 5.8. Micro-hardness distribution plot; (a) longitudinal section, (b) transverse section.

5.3 Discussion

With the initial load applied during a tensile test, the stress-strain curves rise rapidly and in elastic manner due to the rapid accumulation of dislocations [219]. When the stress level in the testing exceeds the yield stress, the stress-strain curve starts to become non-linear. In the plastic deformation stage, i.e. beyond the yield stress, the LPBF Ti-6Al-4V material starts to show a softening phenomenon. With further increase in strain levels, the stacking of dislocations happens which causes an uneven distribution of dislocations. When the shear stress exceeds the critical shear stress the necking in the specimen starts to form and the damaging cracks appear at the edge of the specimen. The crack initiate and propagate along a certain angle and the true stress decreases quickly till the specimen breaks.

5.3.1 Effect of Strain Rate

The LPBF Ti-6Al-4V is a SR sensitive material. Fig. 5.1 shows the effect of SR on PS, UTS and ductility of LPBF Ti-6Al-4V for tests at RT and ET (200°C and 400°C). For tests at RT and ET @200°C, the PS and UTS increased with the SR. However, for the test at ET @400°C (TET21), the UTS was found to be slightly lower from the test result at higher SR (TET22). The flow stress increases with the SR for each test temperature. The higher SR increases the deformation storage energy in the metal making a delayed plastic deformation in the deforming material. Besides, with the increase of SR, the increasing range of flow stress is more extensive due to the rise of plastic deformation per unit time, which now requires an higher movement of dislocations [219, 220]. The dislocations are then entangled to form a cut step [221], causing the slip and diffusion of dislocations to be more difficult.

Fig. 5.1 shows the effect of SR on elongation of LPBF Ti-6Al-4V. It was seen that the ductility decreases slightly with the increase in SR at ET (@ both 200°C and 400°C), but increased slightly with increase in

SR at RT. As the SR increases, the dislocation density increases, and the dislocation increment rate increases [222, 223], which decreases the degree of deformation required to reach the maximum stress. Therefore, the increase in SR will reduce the ductility of Ti-6Al-4V alloy in general [219, 222, 223]. A lower value of ductility for the RT test at lower SR could possibly be attributed to the presence of pores in the specimen as shown in Fig. 5.7(b).

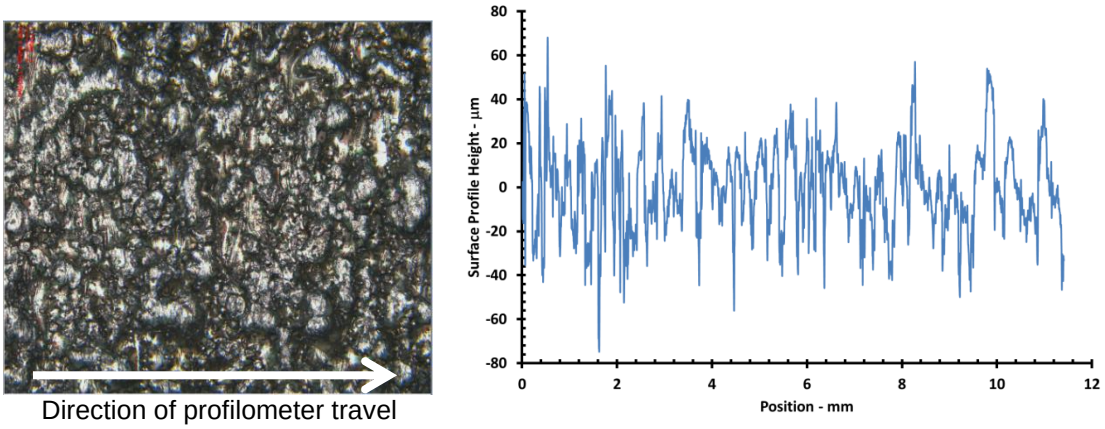
5.3.2 Effect of Temperature

As shown in Fig. 5.1, the flow stress of LPBF Ti-6Al-4V decreases with the increase in deformation temperature at each SR. The strength values in Table 5.1 show the influence of temperature on PS and UTS. The LPBF Ti-6Al-4V is a temperature-sensitive material and the changing trend of PS and UTS with temperature is similar, i.e. both decrease with the increase in temperature.

With increase in temperature, the average absorbed kinetic energy of each atom increases, which causes the amplitude of atomic vibration to increase. Besides, the resistance to the motion of dislocations to cross the energy barrier also reduces with an increase in temperature, which increases the mobility of dislocations, vacancies, and slip systems [201, 204], and therefore reduces the strength of material. The combined effect of these factors reduces the CRSS, resulting in a decrease in the flow stress of the alloy. Fig. 5.1 also shows the effect of test temperature on the elongation. Since the α phase in Ti-6Al-4V alloy is the close-packed hexagonal structure, the number of movable slip systems in the hexagonal lattice will increase with increase in temperature [201, 204]. Under the high-temperature condition, the dislocation slip mechanism dominates the deformation [201, 204], making the deformation easier than the RT condition. Therefore, the increase in test temperature improves the alloy's plasticity and elongation significantly.

5.3.3 Effect of Surface Roughness

The optical image of the scanned surface of the LPBF Ti-6Al-4V used in this study is shown in Fig. 5.9(a) and depicts a wavy surface with the layer thickness distinctly visible. From the typical surface profile reading, shown in Fig. 5.9(b), the average surface roughness, R_a, and the maximum peak to valley height, R_{pv}, are found to be 15.3 μm and 143 μm, respectively. These roughness values are less than, or similar to, the surface roughness values reported in similar studies [64, 65, 74], and indicate a relatively good surface finish for the LPBF test specimens, considering the layer-wise nature of the LPBF process.



(a) (b)

Fig. 5.9. (a) Optical image of the LPBF specimen surface indicating peaks and valleys, (b) Surface profilometer reading indicating the typical surface profile height variation along the specimen length i.e. along the build direction.

Although, a comparison between the mechanical properties of as-built and machined LPBF Ti-6Al-4V specimens has not been performed in this study, it is believed that an improvement in surface finish will improve the material ductility but with insignificant effect on mechanical strength values (PS and UTS). This is because a rougher surface will accelerate the initiation of cracks and their propagation post necking and thus leading to a reduction in material ductility [64].

5.3.4 Role of Defects

According to Voisin et al. [224], although the strength and ductility of LPBF Ti-6Al-4V are dependent on material microstructure, the presence of pores primarily affects the material ductility. The effect of pores on material ductility is dependent on the relationship between the build orientation and loading axis. In the LPBF process, the defects are caused due to higher or lower energy input than the optimum energy required to produce an AM part with minimum defect volume. The defects caused by the insufficient energy are more harmful than those caused by the excessive energy [224]. Haynes [225] has suggested that the effect of porosity on tensile yield strength is negligibly small when the porosity content is <1%. For the LPBF Ti-6Al-4V sample scanned in this study, the total pore volume was only 0.01% of the scanned volume, which suggests that the sample was built with optimal energy input, and the sample is expected to have minimum effect of defects on its mechanical properties. The pores and voids observed in the fracture surfaces of the TRT1 sample (Fig. 5.7(b) and Fig. 5.7(c)) has resulted in lower ductility (6.4%), but still has produced tensile strengths (PS and UTS), higher than the corresponding values for the wrought annealed Ti-6Al-4V bar (see Table 5.1).

5.3.5 Role of Microstructure

LPBF Ti-6Al-4V often contains both α and β microstructural phases at RT and, therefore, the properties of the alloy benefits from: (i) the strength of the α phase (the low temperature allotrope) and (ii) the ductility of the β phase (the high temperature allotrope) [7]. Several α' needles of the same variants

give rise to the colonies of α' in the microstructure as observed in the same colour in Fig. 5.5(a). The columnar PBGs with strong texture of ⟨1 0 0⟩ build direction enhances the material anisotropy with respect to its mechanical strength and fatigue properties. However, the acicular α' needles, with their long axis confined within the PBG boundaries and different variants distributed uniformly (see Fig. 5.5(a)), promotes the material to behave in an isotropic manner [212]. The thickness of α' relies on the processing parameters and resulting thermal history, and the post processing HTs. The reduced thickness of α' grains tends to improve the monotonic strength of LPBF Ti-6Al-4V material, where slip length is essentially the size of a single α' needle, as compared to the wrought Ti-6Al-4V [123, 214]. Hence, typically a finer grain size (α' and β) is desired by the end users to achieve higher mechanical strength of LPBF Ti-6Al-4V [23, 212]. However, the martensitic α' needles offer lower ductility as compared to ductility of fully lamellar microstructure [23, 88, 212].

Post build HT results in the transformation of fine α' into coarse and lamellar α grains in a β matrix, to form an α+β microstructure. This change leads to a reduction in PS and UTS but improvement in ductility. However, significant grain growth at high AN temperatures can significantly reduce the PS below that of the wrought alloy [106]. According to Becker et al. [88], to obtain an optimum balance between tensile strength with ductility of LPBF Ti-6Al-4V, a HT below the β transus temperature is often suggested. According to Xu et al. [110], by doing a careful adjustment of LPBF parameters such as the layer thickness and volume energy, the thermal cycle during the build process can be controlled such that the in-situ decomposition of α' takes place, leading to a more favourable high strength - high ductility combination. Oxygen pickup by titanium is known to be increasing its strength and reducing ductility [111]. Hence, the practicing engineers should be aware of the fact that even a minor oxygen pick-up may lead to variation in the reported mechanical properties.

5.4 Conclusions

A series of tensile tests were performed to evaluate the effect of SR, temperature, build orientation, defects and surface finish on mechanical strength of EPBF Ti-6Al-4V. Additionally, some tensile tests on LPBF Ti-6Al-4V were also performed at RT and ET using as-built specimens which were only built in vertical orientation. Further examinations were carried out on the material microstructure and the scans for X-ray CT, fracture surface, VMH and surface roughness were also performed. The tensile test results were discussed based on the outcome of these examinations.

The key findings from the LPBF tensile test results and discussions, and from comparison of tensile results between LPBF and EPBF Ti-6Al-4V are listed below:

- In general, the tensile strength values (PS and UTS) of LPBF Ti-6Al-4V was higher but the ductility was lower than the EPBF Ti-6Al-4V.
- For LPBF Ti-6Al-4V sample, the pore volume fraction was observed to be < 0.01%, with max pore diameter of 79 μm. Such a small defect size is characterized as the physically small defect. Presence of pores primarily affects the material ductility.

- The microstructure of both LPBF and EPBF Ti-6Al-4V contained only a very small amount β phase. The pore volume fraction was observed to be < 1% for EPBF Ti-6Al-4V. The observed differences in pore volume fraction and β phase present causes difference in material ductility of LPBF and EPBF Ti-6Al-4V.
- The observed higher tensile strength and hardness of LPBF Ti-6Al-4V, as compared to EPBF Ti-6Al-4V, was attributed to its microstructure which contains fine α' needles with high aspect ratio.
- Resistance to the motion of dislocations to cross the energy barrier reduces with increase in temperature, which increases the mobility of dislocations, vacancies and slip systems and thus reduces the material tensile strength (PS and UTS) at ET.
- At ETs, the dislocation slip mechanism dominates the deformation, making the deformation easier at ET than at RT with improved ductility.
- The surface roughness of LPBF Ti-6Al-4V was found to be better than that of EPBF Ti-6Al-4V.

-----x x x x x x-----

CHAPTER 6

6 Low Cycle Behaviour of LPBF Ti-6Al-4V at Specimen Level

The majority of structural failures (> 50%) in the aerospace industry are due to fatigue failure [226], therefore a good understanding of fatigue behaviour of LPBF Ti-6Al-4V is a prerequisite to successfully deploying the alloy processed using this technology in safety critical applications [56]. The poor surface roughness, residual stresses, presence of defects and characteristic microstructure are the influencing parameters which affect the fatigue response of LPBF Ti-6Al-4V material and causes anisotropy in its fatigue response [227]. Furthermore, a high affinity of Ti-6Al-4V alloy to oxygen causes formation of a very thin oxygen layer (OL) on the surface of the alloy even in air at RT [22] which again has deleterious effects on fatigue life of Ti-6Al-4V. To date, several research studies have been performed to develop understanding of fatigue (both LCF and HCF) response of LPBF Ti-6Al-4V; however, the LCF performance, where plasticity and elastic–plastic fracture mechanics play a key role, is relatively unexplored for the LPBF Ti-6Al-4V alloy.

Classical strain-controlled tests are often performed to investigate the cyclic performance of metallic materials under moderate to large plastic strains and at low number of cycles, both at RT and at ET. The softening behaviour observed in the low cyclic response at RT and ET typically involves a combined visco-plasticity and creep-fatigue interactions. Typically, the softening is characterised into 3 distinct stages (see Fig. 6.1); (i) Stage 1 where initial softening occurs with decreasing softening rate, (ii) Stage 2 stabilised softening which uses most of the fatigue life, and (iii) Stage 3 with accelerated softening till failure [228]. Several mechanisms may be responsible for softening in each of these stages which often connect the softening behaviour [228, 229]; (i) to changes in microstructure, (ii) to slip bands and (iii) to the presence of pores and voids. Furthermore, the mechanisms related to microstructural changes that are responsible for cyclic softening are: (i) annihilation of dislocations introduced during martensitic transformation, (ii) change from the original lath structure to equiaxed sub-grains, and (iii) coarsening of precipitates. [210, 230, 231, 232].

The cyclic deformation and softening response of a α+β titanium alloy is strain amplitude dependent [229, 230]. According to Huang et al. [231], the primary α phase (α_p), transformed β phase and embedded fine precipitated secondary α phase in the β matrix (α_s) play critical roles at different strain levels and at different cycling stages to affect the softening behaviour of the alloy. Luquiau et al. [230] revealed that the cyclic softening is due to a decrease in both the isotropic and kinematic components of the stresses. The decrease in kinematic component of stresses (internal softening) is associated with a process of homogenisation of α_p particles, which happens due to yielding through the microstructure, whereas the Isotropic softening or the effective stress softening is due to annihilation of dislocations enhanced by cross slip in the α-phase [230]. The cyclic softening behaviour is microstructure dependent in Ti-6Al-4V [210, 232].

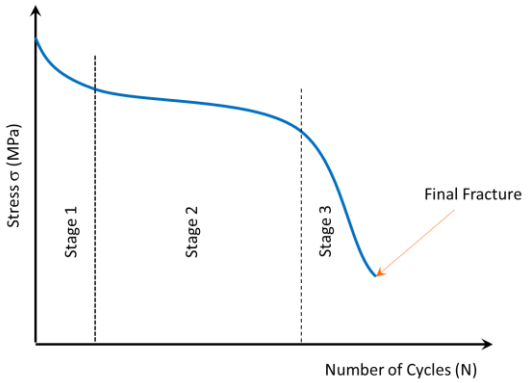


Fig. 6.1. Strain controlled LCF testing: A schematic representation of 3 stages of material cyclic softening [228]

Prasad et al. [210] found that the cyclic softening behaviour in Ti-6Al-4V is due to the rearrangement of dislocations and concluded that the strain accumulation needed to nucleate a crack in the α phase is generally lower than that in the β phase which causes primary α grains (α_p) with large grain boundaries to become the weaker sites for internal crack initiation. According to Han et al. [232], the equiaxed microstructure exhibited the most significant cyclic softening behaviour whilst the Widmanstätten microstructure exhibits the lowest, and the softening behaviour was due to the plasticity of the primary α phase [232]. Prasad et al. [210] also defined a strength parameter 'STR' (= Ultimate Tensile Strength / Proof Strength). If the value of STR is less than 1.2 then this would indicate some level of cyclic softening during LCF testing of LPBF Ti-6Al-4V.

Bressan et al. [228] carried out a study to understand the effect of heat treatment, build orientation and presence of voids on cyclic plastic behaviour of Ti-6Al-4V built using the LPBF process. They found that although the build orientation did not influence the size of the grains or void morphology or density, the effect of build orientation on the cyclic softening and hardening behaviours was noticeable [228]. Also, the HT increased material hardening without significantly affecting its elasto-plastic cyclic behaviour but led to early failure, whereas the voids and pores allowed the micro-cracks to initiate under the initial applied cyclic stress and showed a direct impact on the material softening behaviour [228]. Ren et al. [229] carried out fully reversed strain controlled LCF tests at RT and at different strain amplitudes to study the LCF properties of Laser Solid Formed (LSF) Ti-6Al-4V and suggested that the cyclic softening behaviour was strongly dependent on the strain amplitude, where the cyclic softening was found to increase with increasing strain amplitude. They also suggested a microstructure-based multistage fatigue model which seems to predict LCF life for the LSF Ti-6Al-4V alloy in reasonably good agreement against the experimental data [229].

In this chapter, the LCF behaviour of LPBF Ti-6Al-4V at different SREs was studied through strain controlled tests both at RT (20°C) and at ET (400°C) in air. The study explores the role of microstructure with an aim to identify the prominent mechanisms behind the cyclic softening behaviour in LPBF Ti-6Al-4V. Furthermore, the microstructure evolution was studied by examining the change from the baseline material in grain structure and KAM (representing free dislocation density)

in the samples from interrupted tests at ET, using the EBSD technique. Additionally, the fracture surfaces of failed specimens were characterised and the relationship between the fracture mechanism and role of defects on the LCF behaviour of LPBF Ti-6Al-4V was explored. The characterisation includes the tensile and cyclic stress responses, fatigue life, fracture surface, X-ray CT scan of intermediate stages of the cyclic tests followed by a microstructural investigation of the initial, intermediate (through interrupted tests) and failed stages for fatigue tests at ETs.

6.1 Test Results

In order to illustrate the influence of temperature and SRE on the cyclic response of the LPBF Ti-6Al-4V material, the evolution of the hysteresis loops are discussed in the following sub-sections for the tests carried out at both RT and ET. The hysteresis loops are plotted for the chosen discrete number of fatigue cycle such that the hysteresis loops are spaced out uniformly from start to end which allows to observe a gradual evolution of the shape of hysteresis loops clearly showing a drop in stress. To remove possible undulations in the data points, the loops were smoothened out by using gaussian smoothening filter for 5 - 10 neighbouring points in MATLAB. The LCF fatigue test results are summarised in Table 6.1, where it can be seen that the number of cycles to failure decreases with increasing test SRE for both RT and ET LCF tests.

Table 6.1. Cyclic strain-controlled test results and resulting cycles to failure

Test No.	Test Identification Number (#)	Temperature °C	Strain Range (SRE) (%)	Number of Cycles to Failure	Comment
1	L-RT1	20	± 0.8	1899	Fractured
2	L-RT2	20	± 1.2	294	Fractured
3	L-RT3	20	± 1.5	59	Fractured
4	L-ET1	400	± 0.8	965	Fractured
5	L-ET2	400	± 1.2	319	Fractured
6	L-ET3	400	± 1.5	144	Fractured
7	L-ET4	400	± 1.2		First interrupted test, interrupted at 160 cycles, Unfractured
8	L-ET5	400	± 1.2	189	Second interrupted (planned) test, Specimen fractured prematurely

6.1.1 LCF Tests at RT

The cyclic performance of the LPBF Ti-6Al-4V material at RT is shown in Fig. 6.2(a) – Fig. 6.2(c) with increasing Strain Range (SRE), respectively. The stress – strain hysteresis loops shown in Fig. 6.2(a) –

Fig. 6.2(c) suggest a drop in stress range with increasing number of cycles, i.e. cyclic softening. Also, as we move from Fig. 6.2(a) - Fig. 6.2(c), the hysteresis loops appear to have become increasingly wider due to increase in SRE/ test plasticity level.

Variations in the maximum (max., σ_{max}), minimum (min., σ_{min}) and mean (σ_{mean}) stresses vs cycle number are shown in Fig. 6.2(d) - Fig. 6.2(f). In Fig. 6.2(d) - Fig. 6.2(f), cyclic softening can be seen for each test, and the typical shape of the curves shows three distinct stages: (i) Stage 1 with initial sharp softening, (ii) Stage 2 consisting of stabilised softening and (iii) Stage 3 with an increased softening rate until final fracture. A noticeable difference in the maximum stress in Stage 1 was observed between the L-RT1 and L-RT2 tests, see Fig. 6.2(d) and Fig. 6.2(e), respectively. However, the difference in maximum stress in Stage 1 was much smaller between the L-RT2 and L-RT3 tests, see Fig. 6.2(d) and Fig. 6.2(f), respectively. Also, from Fig. 6.2(d) – Fig. 6.2(f), a slight asymmetry was observed in the cyclic softening response in the tension (σ_{max}) and compressive (σ_{min}) parts for each of the RT cyclic tests.

6.1.2 LCF Tests at ET

The performance from the ET cyclic tests at 3 different SREs are shown in Fig. 6.3. On comparing the softening patterns in Fig. 6.2 and Fig. 6.3, the rate of softening is found to be greater for the ET tests than the RT tests for the corresponding SRE. The hysteresis loops are increasingly wider with increase in SRE, i.e. increase in test plastic strain. Also, the hysteresis loops for ET tests are wider than the hysteresis loops for RT test for each SRE which is due to a reduction in stiffness at ET where a lower PS is compensated by an increase in the level of plasticity. Furthermore, at high number of test cycles, the width of hysteresis loops is bigger in the tension part of the hysteresis loop than in compression, which is clearly evident for L-ET1 and L-ET2 tests (see Fig. 6.3(a) and Fig. 6.3(b)). However, this difference in shape of the tension and compression part of the hysteresis loops is small for L-ET3 test, which perhaps is due to the failure of the L-ET3 test specimen at a lower number of cycles (see Fig. 6.3(c)).

The performance of maximum, minimum and mean stresses for the ET cyclic tests are shown in Fig. 6.3(d) – Fig. 6.3(f). The maximum stress in Stage 1 is higher for L-ET2 tests when compared to the L-ET1 test, whereas the difference in maximum stress in Stage 1 is insignificant for the L-ET2 and L-ET3 tests. It is also observed that most Stage 1 softening happens within the first few cycles (~20 cycles) before arriving at the quasi-saturated state of softening in Stage 2.

From Fig. 6.3(d) – Fig. 6.3(f), the shape of maximum and minimum stress curves shows an asymmetric response and indicates that the amount cyclic softening is higher in tension than in compression for LCF tests at ET. This asymmetric response in tension and compression also affects the mean stress response. The asymmetry of hysteresis loops at ET is believed to be due to the asymmetric material response of LPBF Ti-6Al-4V w.r.t. its PS and Young's modulus in tension and compressive parts of the loading [210].

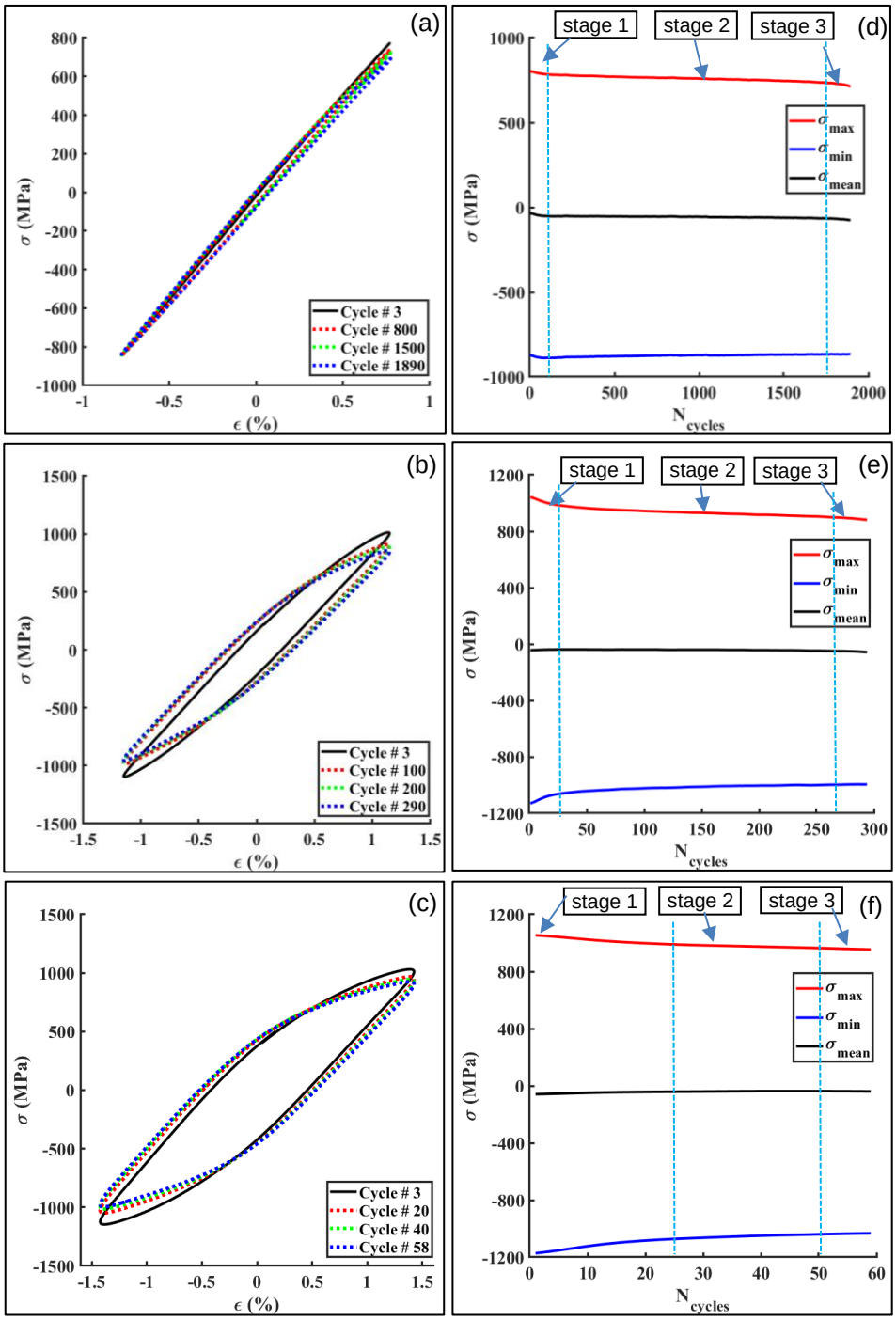


Fig. 6.2. LCF tests at RT: (a) discrete hysteresis loops at SRE = ±0.8% (L-RT1), (b) discrete hysteresis loops at SRE = ±1.2% (L-RT2), (c) discrete hysteresis loops at SRE = ±1.5% (L-RT3), (d) cyclic softening behaviour at SRE = ±0.8% (L-RT1), (e) cyclic softening behaviour at SRE = ±1.2% (L-RT2), and (f) cyclic softening behaviour at SRE = ±1.5% (L-RT3), where RT: Room temperature, SRE: Strain range

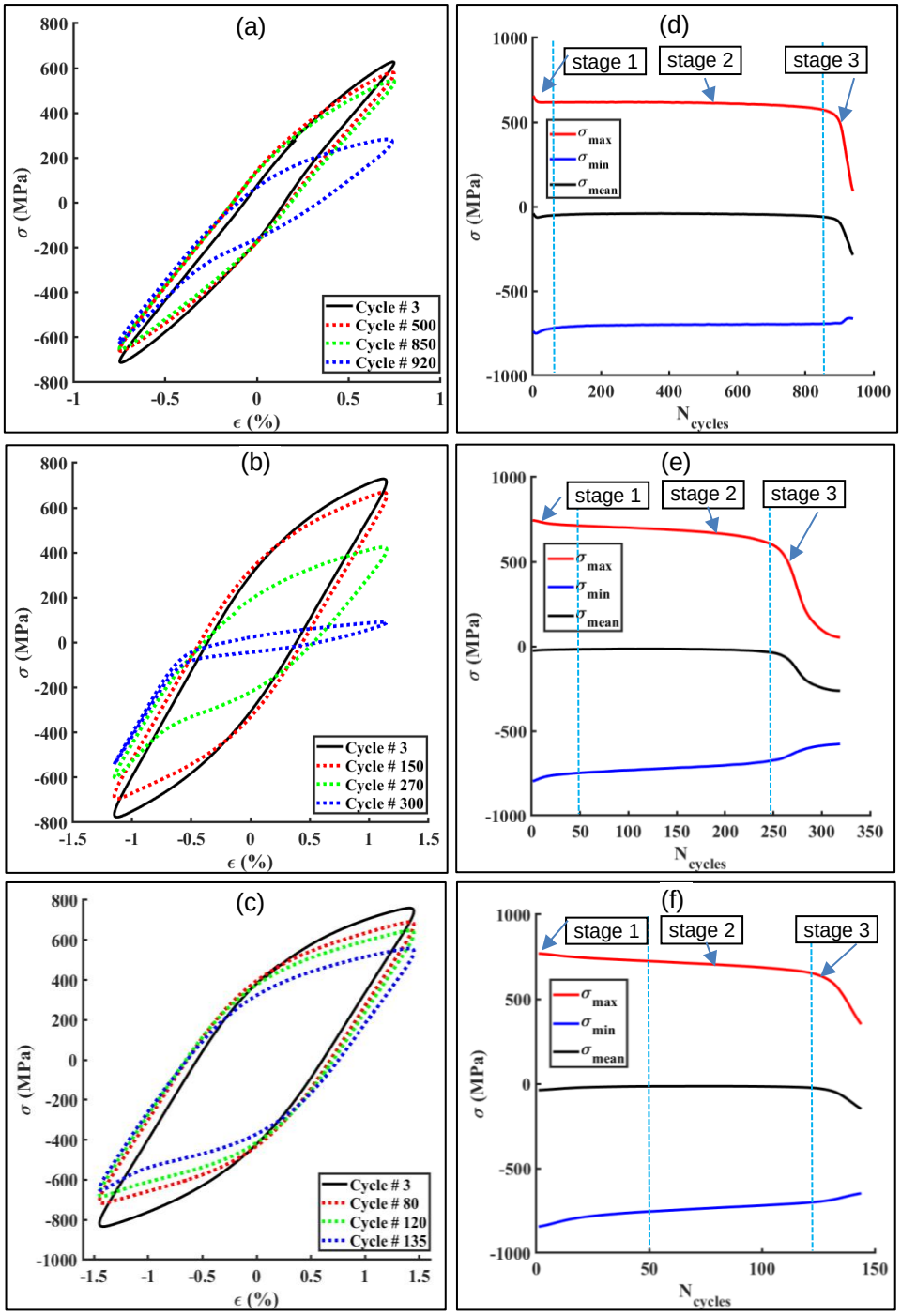


Fig. 6.3. LCF tests at ET: (a) discrete hysteresis loops at SRE = ± 0.8% (L-ET1), (b) discrete hysteresis loops at SRE = ±1.2% (L-ET2), (c) discrete hysteresis loops at SRE = ±1.5% (L-ET3), (d) cyclic softening at SRE = ±0.8% (L-ET1), (e) cyclic softening behaviour at SRE = ±1.2% (L-ET1), and (f) cyclic softening behaviour at SRE = ±1.5% (L-ET1), where ET: Elevated temperature, SRE: Strain range

6.1.3 Cyclic Softening

Wrought Ti-6Al-4V material has been shown to have superior LCF life than that of LPBF Ti-6Al-4V material owing to its fine equiaxed α grains while the reduced material ductility, surface roughness and intrinsic defects are linked to the lower LCF life of the LPBF material [229]. To characterise the LCF behaviour of LPBF Ti-6Al-4V material, the softening behaviour at different SREs is plotted in Fig. 6.4(a) and Fig. 6.4(b) for RT and ET tests, respectively. From Fig. 6.4, the LPBF Ti-6Al-4V material exhibits a lower starting stress amplitude for ET tests than the RT tests. Also, an accelerated and larger amount of softening in Stage 3 was noticed for ET tests which is due to damage localisation, increase in ductility levels and increase in test plastic strains.

As seen in Table 6.1 and in Fig. 6.4, the number of cycles to failure decreases with increase in SRE, but the average softening rate increases, where the average softening rate is defined as:

$$ASR = \frac{(\sigma_{inital} - \sigma_{final})}{N_{final} - 1} \quad (6.1)$$

where, $\sigma_{initial}$ = stress at first cycle, σ_{final} = stress at last cycle, N_{final} = last cycle number.

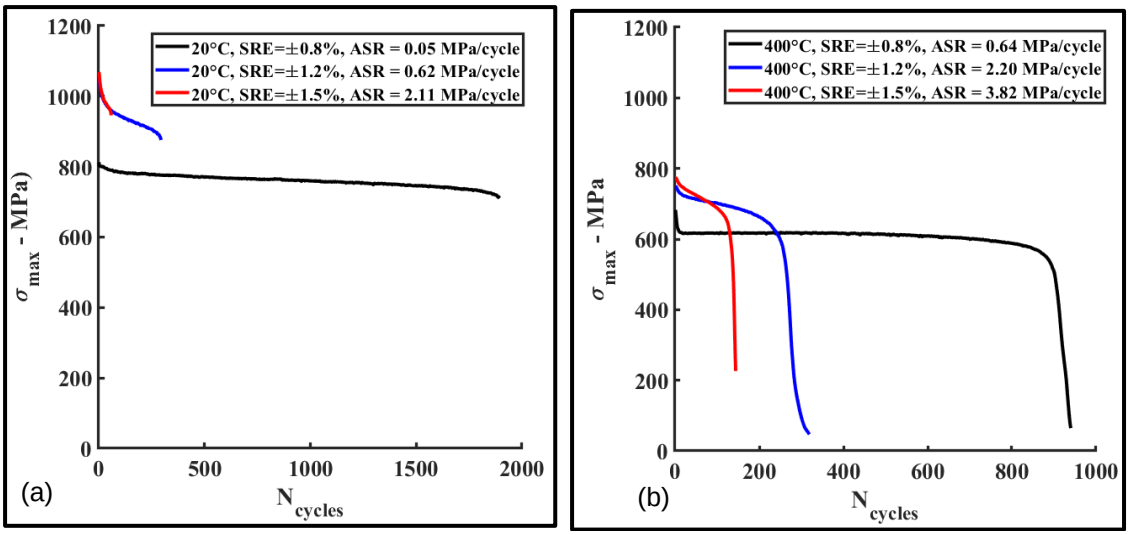


Fig. 6.4. Cyclic softening behaviour of LPBF Ti-6Al-4V material, max stress evolution at different SRE: (a) Tests at RT (20°), and (b) Tests at ET (400°C), where RT: Room temperature, ET: Elevated temperature, and SRE: Strain range.

6.2 Discussion

6.2.1 Fractography

The SEM micrographs of the fractured LCF specimens were taken to analyse the crack initiation sites and area of crack propagation, and to also understand its relationship with the cyclic softening, see Fig. 6.5. The test specimens L-RT3, L-ET3, L-ET2 and L-ET5 were chosen for fracture surface examination and their micrographs are shown in Fig. 6.5(a) – Fig. 6.5(c), Fig. 6.5(d)- Fig. 6.5(f), Fig. 6.5(g) – Fig. 6.5(i) and Fig. 6.5(j) - Fig. 6.5(l), respectively.

A higher SRE in Stage 2 provokes initiation of fatigue crack but with subsequent decrease in stress caused by the cyclic softening in Stage 2 slows down the crack propagation, as depicted in Fig. 6.5(a),

Fig. 6.5(d), Fig. 6.5(g) and Fig. 6.5(j). The crack propagation zone is defined either by a central oval/circular region for the RT test in Fig. 6.5(a) or by a semi-circular region for the ET tests in Fig. 6.5(d), Fig. 6.5(g) and Fig. 6.5(j). The crack initiation is either from the defects present (a pore or a void) located at the surface, observed in Fig. 6.5(b), Fig. 6.5(e) and Fig. 6.5(k), or just inside the surface of the test specimen as observed in Fig. 6.5(h) [228]. A small lump of material around the surface, acting as a stress raising feature, was as well observed in Fig. 6.5(c), which was formed due to incomplete melting during manufacturing. Initiation of secondary micro-cracks from such a feature during cyclic loading cannot be ruled out.

A material subjected to LCF at high SRE has a poorly defined Stage 1 with indications of crack initiation [229], whereas most of the crack growth happens during the Stage 2 stabilised softening region. The fracture surface of LCF specimens does not exhibit ductile dimples or necking because of the cyclic loading and propagating crack. The region of crack propagation shows beach marks, which are typical of cyclic crack growth and are clear for ET test specimens in Fig. 6.5(f), Fig. 6.5(i) and Fig. 6.5(l). The crack propagation region of ET specimens is much rougher and smaller as compared to RT specimen. A rougher surface typically indicates a torturous crack path and greater contribution of the microstructural features (i.e. α lamellae, α_{GB} and PBG boundaries). Hence the observed rougher surface of ET specimens indicates a higher degree of heterogenous deformation in these specimens. In LPBF Ti-6Al-4V, the effective slip length is confined within the single α' grains, therefore the α' grains are the preferential sites for crack initiation during the cyclic loading and the crack propagation is highly dependent on the crystallographic orientation of the α' grains containing the crack tips and number of grain boundaries in the microstructure [123, 211]. In a fine microstructure, the advancing crack tip deviates at the grain boundaries generating predominantly intergranular features because the neighbouring α' grains (or colonies) have multiple distinct crystallographic orientations (i.e weak texture) as reported in this study (see section 5.2.1) [123]. From Fig. 6.5, the observed rougher crack propagation regions in the fracture surfaces in presence of PBG boundaries in the microstructure (as shown in Fig. 5.2) confirm that the primary mode of fatigue fracture is intergranular [233].

Finally, the portion outside of the crack propagation region marked as 'Lip/Final Fracture' is formed during the final fracture stage of the cyclic tests, see Fig. 6.5(a), Fig. 6.5(d), Fig. 6.5(g) and Fig. 6.5(j). The 'Lip' part of the fracture surfaces happens due to an increased stress (under plane stress condition) with reduced cross-sectional area in the final fracture stage and happens at an angle to the crack propagation surface area/loading axis.

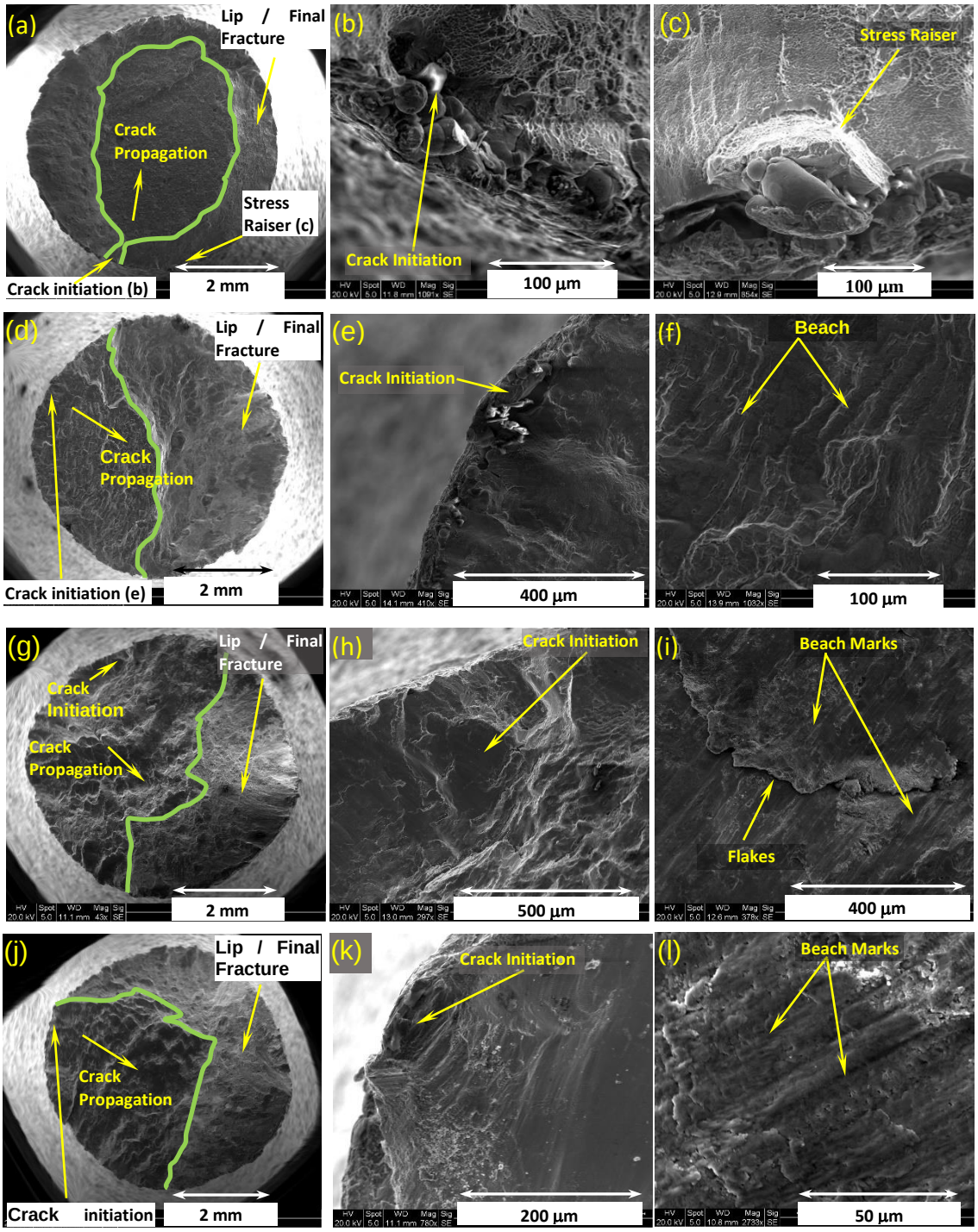


Fig. 6.5. SEM micrographs of fracture surface of LCF specimens: (a) – (c) L-RT3 at temperature = 20°C and SRE = 1.5%, (d)– (f) L-ET3 at temperature = 400°C and SRE = 1.5%, (g) – (i) L-ET2 at temperature = 400°C and SRE = 1.2%, and (j) – (l) L-ET5 second interrupted test at temperature = 400°C and SRE = 1.2%

6.2.2 Evolution of Low Angle Boundaries and Increase in Free Dislocation Density

The softening observed in the strain controlled cyclic tests causes crack growth retardation from the subsequent primary or secondary cracks, often resulting in a better fatigue life as compared to the stress-controlled LCF tests [228]. The dislocation activities, including activation of multiple slip

systems and increase in free dislocation density within the α', grains, play a significant role in the overall cyclic deformation behaviour [231]. The α' needles with high aspect ratio are the soft features in the microstructure where long dislocations mean a free and weaker path in the needles' longitudinal direction. In addition to this, a higher tendency of strain localisation is observed in the colonies of α' needles belonging to the same crystallographic orientation [211]. Moreover, the α' needles with high aspect ratio impedes the growth of subsequently produced α' needles leading to lesser deformability (i.e. an ability to deform under an applied force) but enhanced plasticity and strain localisation in the α' needles. Plastic deformation in Ti-6Al-4V is mostly accommodated by Basal or Prismatic slip system namely (0002) $\langle 11\bar{2}0 \rangle$ and $(11\bar{1}0)\langle 11\bar{2}0 \rangle$ [123].

The distribution of strains within the material microstructure is typically studied using a KAM distribution map which signifies the free dislocation density distribution in a deformed material. In a KAM distribution map of a deformed or strained material, any area with a high KAM number would correspond to an area of high free dislocation density / high local strain [222]. On the contrary, a low KAM value would typically suggest that the primary deformation mechanism is due to grain boundary sliding rather than the sub-grain formation [222].

The cyclic softening was investigated to further understand its dependency on the evolution of grain size and free dislocation density as indicated by the KAM. For this, a comparative study was performed using the results of EBSD scans performed on the longitudinal cut sections of the as-received LPBF Ti-6Al-4V material, and the L-ET2, L-ET4 and L-ET5 tested specimens. The L-ET4 and L-ET5 were the two interrupted tests at ET with a SRE of ±1.2%, see Table 6.1. Firstly, the test points (P1 – P4) for microstructure evolution study are identified on a normalised softening curves in Fig. 6.6. From Fig. 6.6, point P1 is the as-received LPBF Ti-6Al-4V material condition, whereas point P4 is the fracture point of the baseline L-ET2 test. Although the interrupted tests (L-ET4/point P2 and L-ET5 /point P3, see Table 6.1 and Fig. 6.6) were individually planned to be stopped at a predetermined number of cycles without fracture, the second interrupted test specimen (L-ET5) fractured prematurely. Also, the L-ET5 test was observed to have lower starting stress as compared to the baseline L-ET2 test. Therefore, the softening curves were normalised to identify the relative positions of the end points of the two interrupted tests (L-ET4 and L-ET5), and also to relate and ensure that the softening trends of the interrupted tests followed the softening trend of the baseline L-ET2 test. The end of the first interrupted test (L-ET4), which was stopped after 160 cycles, is marked as point P2. This point falls in the stabilised part, i.e. in Stage 2, of the softening curve of the baseline L-ET2 test, see Fig. 6.6. The end of the second interrupted test is denoted as point P3, which falls in Stage 3, representing the accelerated softening part of the softening curve of the baseline L-ET2 test. As shown in Fig. 6.6., both the interrupted test curves seem to closely follow the softening trend of the baseline curve.

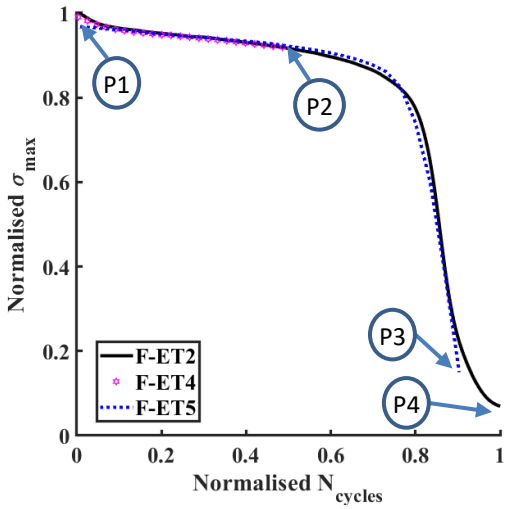


Fig. 6.6. Normalised softening response curves of the interrupted tests (L-ET4 and L-ET5) relative to baseline test (L-ET2). Points P1, P2, P3 and P4 represent the as -built Ti-6Al-4V material, end of the interrupted test L-ET4, end of the interrupted test L-ET5 and end of the baseline L-ET2 test, respectively.

For the points P1 – P4, shown in Fig. 6.6, a comparison of EBSD results between the as-built LPBF Ti-6Al-4V material (point P1) and fatigued samples from the L-ET4 (point P2), L-ET5 (point P3) and L-ET2 (point P4) tests is shown in Fig. 6.7 using the IPF plots (Z0, loading axis) and KAM plots. For the fatigued specimens, two locations were studied where location 1 was 1 mm away from the fractured/cut surface and location 2 was at the fractured/cut surface. The IPF plots in Fig. 6.7 show a continuous refinement of α' grains with fatigue cycles increasing from points P1 to P4. The degree of grains refinement is greater for location 2 (close to the fracture surface) compared to the location 1. Also, as seen in Fig. 6.7, the fatigued samples (P2 -P4) show moderate to high KAM values (shown in green), which increases with an increase in the number of fatigue cycles (P2 to P4) and which are spread throughout the microstructure of the scanned area, as compared to the as-built sample (point P1). The fatigued microstructure is comprised of a uniform distribution of sub-grains and KAM density, i.e. dislocations are homogenously distributed inside the larger α' grains. The average KAM values for each of the scanned area in Fig. 6.7 are listed in Table 6.2, which indicate that the average KAM increases as we move from points P1 to P4 and from locations 1 to 2 (i.e at the fracture surface).

During deformation, evolution of dislocation substructures takes place in LPBF Ti-6Al-4V and this subsequently produces the Low Angle Boundaries (LABs) inside the prior α/α' grains [211, 223]. A misorientation less than 15° between two adjacent entities (grains or sub-grains) in the microstructure usually results from the formation of LABs whereas a misorientation higher than 15° provided information on the well-defined α' grain boundaries. The LABs appear to originate from the interface of α, β phases which do not follow the said BOR between the β and α phases [223]. The generation of LABs is through the formation of dislocation tangles and subsequent recovery leading to rearrangement of dislocations during cyclic loading. The LABs are therefore composed of an array of

dislocations, which can be of edge or screw types; these progressively lead to void nucleation, coalescence, and fracture [222]. Usually, the dislocations do not exist inside the sub-grains.

From the discussion above, the free dislocation density increases with increasing number of LCF cycles, due to a combination of: (i) easing of dislocation annihilation and (ii) recovery of dislocations happening subsequently. Typically, a substructure with distributed dislocation density within the material would undergo plastic deformation through the dislocation motion. Moreover, the cyclic softening occurs due to an increasing dislocation density, decreasing density of obstacles to dislocation motion and increasing the ability of dislocations to overcome these obstacles [234]. Furthermore, an increase in the free dislocation density causes bulk damage, i.e. reduction in resistance of the material to crack initiation, in the material contributing to the LCF fatigue damage in the Ti-6Al-4V material [235].

Table 6.2. A comparison of average KAM values (°) between the as-built sample and LCF tested specimens.

Test Identification Number (#)	Location Description	Test Point Description	Average KAM (°)
-	As-built LPBF Ti-6Al-4V	P1	0.8
L-ET4	Location 1	P2	0.8
L-ET5		P3	0.98
L-ET2		P4	1.15
L-ET4	Location 2	P2	0.87
L-ET5		P3	1.43
L-ET2		P4	1.59

6.2.3 Changes in Micro-hardness

To relate the cyclic softening to the material hardness, micro-hardness tests were performed on a longitudinal section of the as-built LPBF Ti-6Al-4V material (point P1) and of the fatigued samples of L-ET4 (Point 2), L-ET5 (Point P3) and L-ET2 (Point P4) tests. These micro-hardness test results are shown in Fig. 6.8, where it can be seen that the average indicative micro-hardness value appears to increase with increasing number of cycles (from points P1 to P4 of the cyclic tests). In the cyclic LCF tests studied, with increase in number of cycles, the stress amplitude decreases (cyclic softening) because of the increased occurrences of <c + a> slips (in addition to increase in free dislocation density). The increased occurrence of <c + a> slip enhances the interaction of <a> / <c + a> and <c + a> / <c + a> dislocations which then generates latent hardening to counterbalance the cyclic softening to some extent [230]. Here ‘c’ and ‘a’ denote the lattice parameters of an hexagonal closed packed unit cell [213].

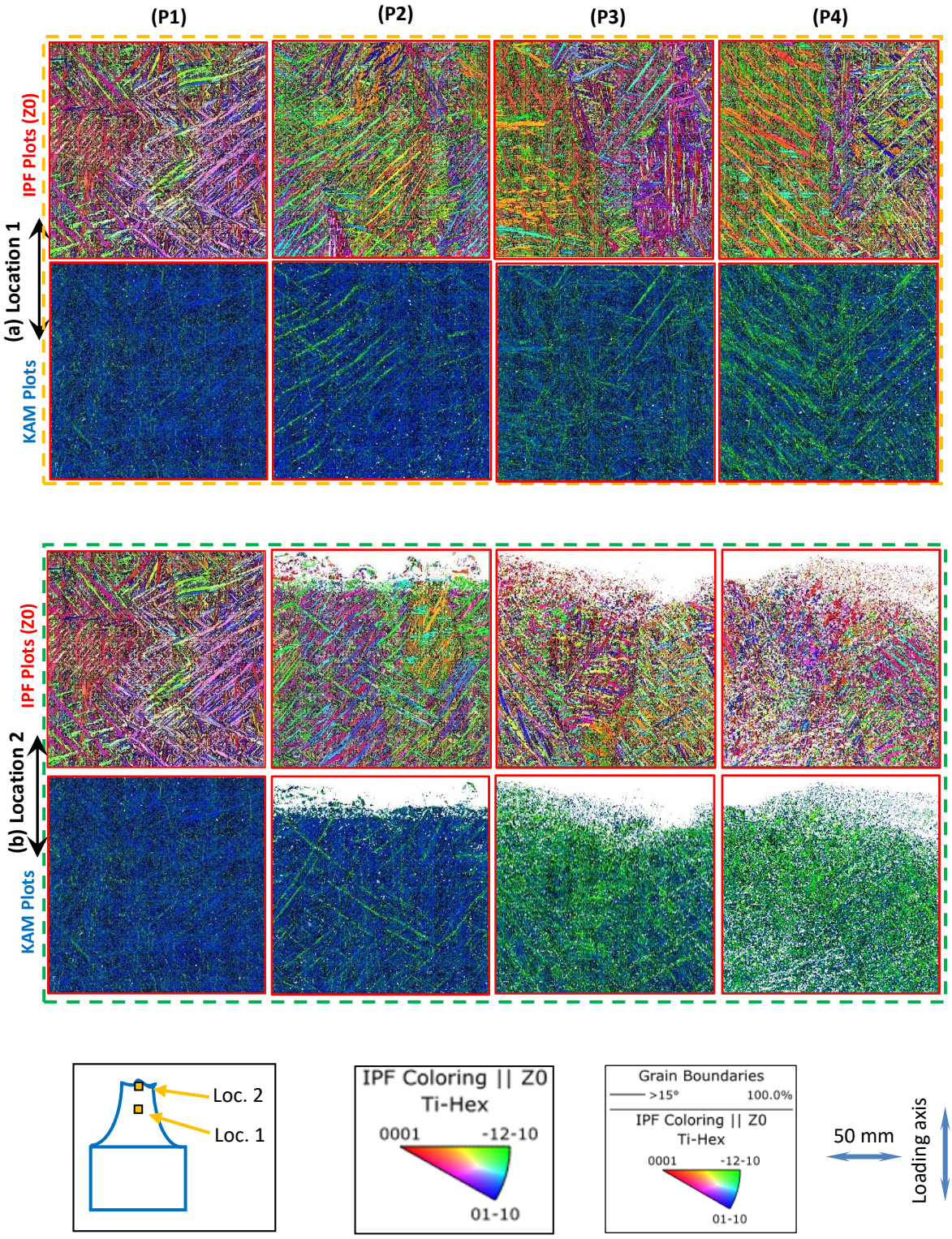


Fig. 6.7. Comparison of EBSD results between the as-built LPBF Ti-6Al-4V material (point P1) and fatigued samples from the L-ET4 (point P2), L-ET5 (point P3) and L-ET2 (point P4) tests with IPF plots and KAM maps. For fatigued specimens, two locations were studied where location 1 is 1 mm away from the fractured / cut surface and location 2 is at the fractured / cut surface.

It is to be noted that the micro-hardness of the as-built LPBF Ti-6Al-4V material shows a higher micro-hardness value (371 HV average measured with a load of 500 gf, Point P1, Fig. 6.8) as compared to the extruded equiaxed α/β Ti-6Al-4V material (302 HV average measured with a load 1000 gf, [200], suggesting that the as-built LPBF Ti-6Al-4V material is, in general, harder as compared to the conventionally made Ti-6Al-4V material) owing to its fine microstructure with α' needles.

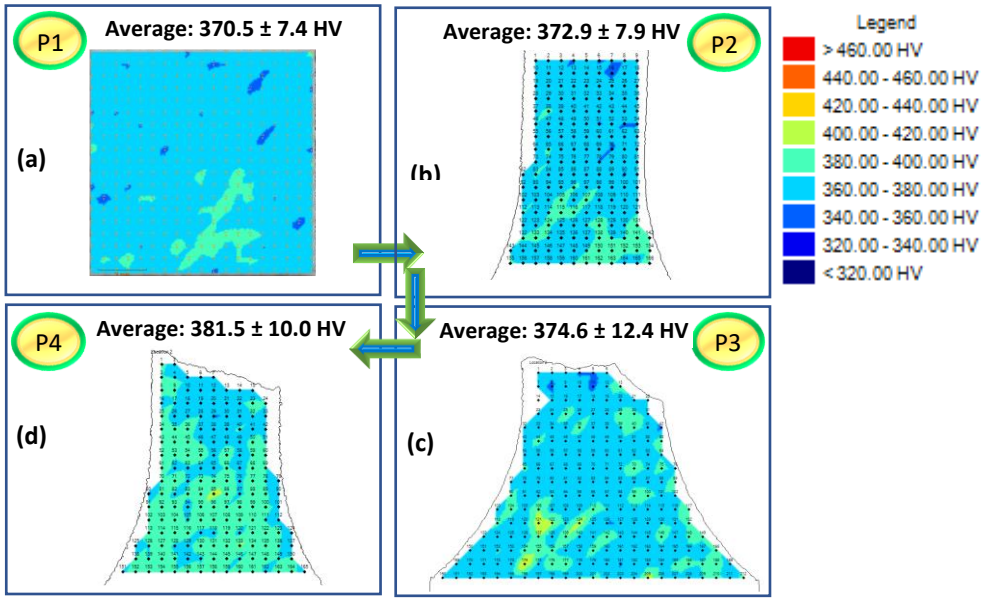


Fig. 6.8. Hardness tests results of: (a) as-built LPBF Ti-6Al-4V alloy (point P1), (b) fatigued sample of L-ET4 test (point P2), (c) fatigued sample of L-ET5 test (point P3), and (d) fatigued sample of L-ET2 test (point P4).

As discussed in Chapter 5, the material ductility of LPBF Ti-6Al-4V increases at ET. Hence, based on the discussion above, the increase in free dislocation density, local strengthening (hardness) and material ductility result in micro-void formation and their coalescence, eventually leading to fracture under the cyclic loading at ET. A schematic representation of the evolution of LABs due to progressive dislocation interaction and formation of voids leading to cyclic fracture is shown in Fig. 6.9 [211].

6.2.4 Effect of Temperature and SRE

Again, the LPBF Ti-6Al-4V material, subjected to cyclic loading at ET, will undergo microstructural evolution and dislocation activity (an increase in both dislocation density and ease of dislocation motion) leading to significant cyclic softening [229]. The effects of SRE and temperature were studied by comparing the IPF and KAM plots of the fatigued samples of L-RT2, L-ET2 and L-ET3 at for their respective location 2 only, as shown in Fig. 6.10. It can be seen that the orientation of grains is homogenous for all three fatigued specimens. The grains of the ET test specimens (L-ET2 and L-ET3) are much finer compared to the grain size observed for the fatigued sample of the RT test (L-RT2), see Fig. 6.10. The distribution of KAM (indicated by green in Fig. 6.10) is much more prominent for the ET

tests as compared to the RT test (L-RT2 vs. L-ET2) and the KAM increases further with increase in test SRE (L-ET2 vs. L-ET3). The average KAM values for the three tests for the scanned area in Fig. 6.10 are also tabulated in Table 6.3. For the tests at ET (see Table 6.3), as expected, the average KAM increases with an increase in SRE and the cycle to failure decreases (L-ET2 vs. L-ET3). However, between the L-RT2 and L-ET2 tests, although the KAM increases with the increase in temperature, the number of cycles to failure decreases. Furthermore, From Fig. 6.3, the hysteresis loops for tests at ET exhibit lower slope in tensile part of the hysteresis loop compared to the slope of compression part, suggesting that the material experiences a faster crack growth under tensile part of the cyclic loading. This confirms a parallel and competing contribution of strain localisation, micro-hardness, micro-voids, coalescence of micro-voids and rate of crack growth towards causing fracture of the specimens.

Table 6.3. Effect of temperature and SRE under cyclic loading: A comparison of average KAM values.

Test Identification Number (#)	Temperature (°C)	Strain Range (SRE) (%)	Average KAM (°)	Cycles to Failure
L-RT2	20	±1.2	1.38	294
L-ET2	400	±1.2	1.59	319
L-ET3	400	±1.5	1.68	144

The cyclic softening intensifies with the increase in SRE as seen in Fig. 6.2 and Fig. 6.3. The increase in plasticity levels helps towards the free dislocation density pile-up and thus accelerates the cyclic softening rate. In addition to dislocation pile-ups at higher SRE, under the cyclic loading at ET, the interaction between the dislocations increases which in-turn reduces the obstacles to dislocation motion and increases the ability of material to overcome these obstacles to dislocation motion, which then results into a significantly higher cyclic softening as compared the RT tests until the fracture is observed.

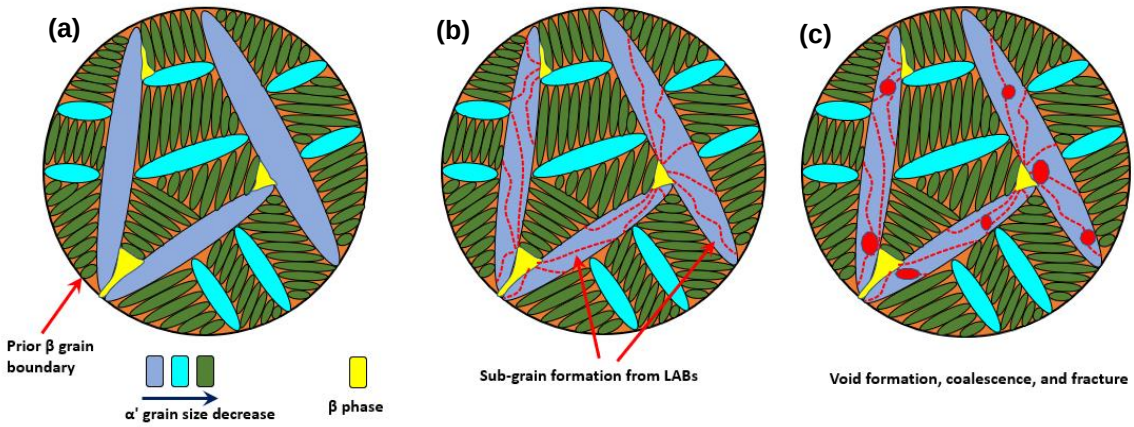


Fig. 6.9. A schematic representation evolution of LABs: (a) α' grains within prior β grain boundaries, (b) formation of sub-grains within α' grains due to dislocation activities and interfacial plasticity, and (c) formation of voids and void coalescence and propagation till fracture under the effect of cyclic loading [211].

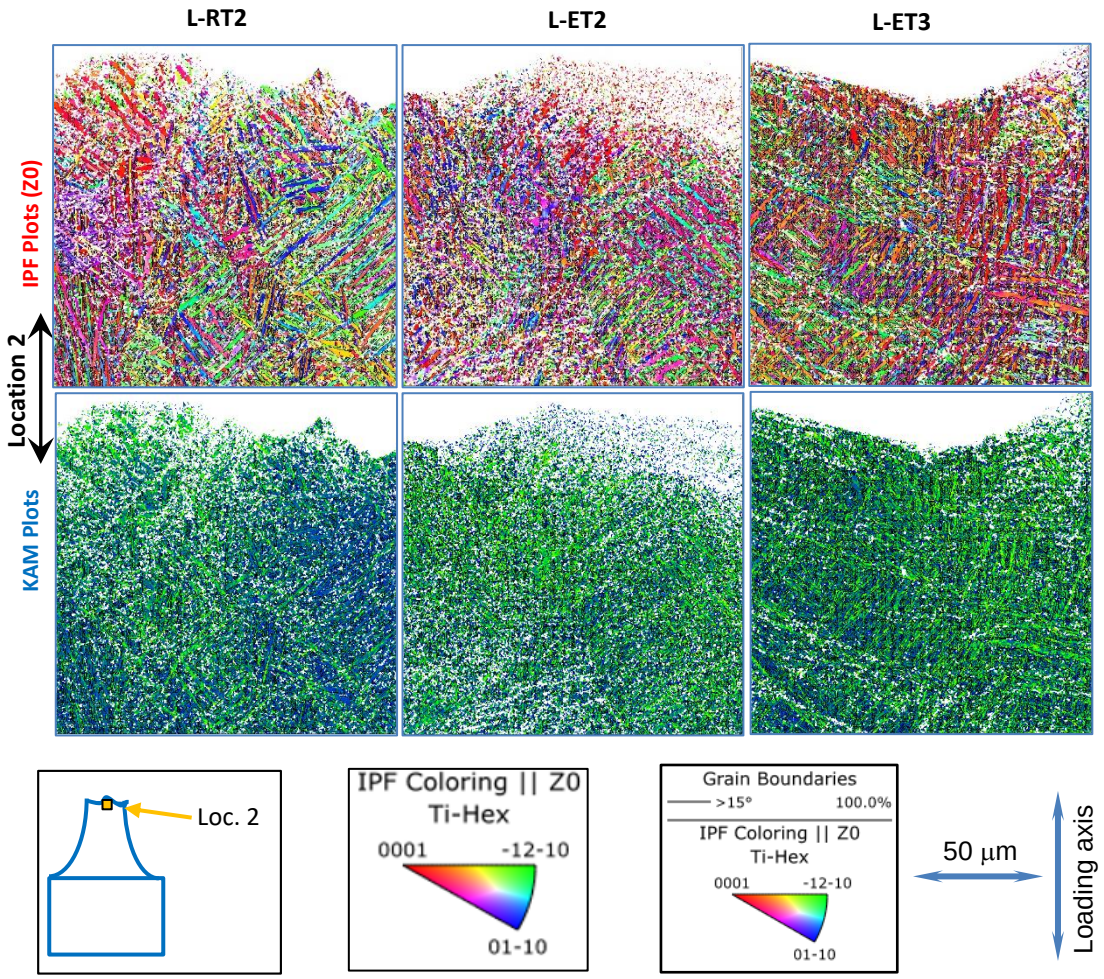


Fig. 6.10. Comparison of EBSD results between the fatigued samples from the L-RT2, L-ET2 and L-ET3 tests with IPF plots and KAM maps. Only the scans at the fractured surface (location 2).

6.2.5 Defects in LCF Tested Samples

Post LCF testing, CT scanning was performed on the L-ET4 and L-ET5 test specimens which were used for the two interrupted tests. The 3D constructed CT images for these two specimens are shown in Fig. 6.11. It can be seen in Fig. 6.11(a) that the L-ET4 specimen consisted of only 4 inclusions with a maximum size of 96 µm. However, the L-ET5 specimen was found with inclusions (maximum 19 µm size), micro-voids (maximum 11 µm size) and surface nucleating cracks (maximum 81 µm deep), as depicted in Fig. 6.11(b). As presented in Fig. 6.5(k) and also discussed in Section 6.2.1, the micro-voids present at the surface of L-ET5 specimen caused the crack initiation, which subsequently propagated and led to final fracture of the specimen under cyclic loading. There are other cracks seen in Fig. 6.11(b) which initiated from the surface of the L-ET5 specimen and propagated within the material, which although did not finally result in a complete fracture but had weakened the material. This suggests that the micro-voids or pores in the LPBF material could lead to its premature failure under cyclic loading.

Hence, the LOF voids or pores present at or near the surface and micro-cracks present at the rough surface are detrimental (compared to the buried defects in the bulk of the material), and typically act as the crack initiation points which propagate to cause fracture of the LPBF specimens/components under the LCF loading (see Fig. 6.5).

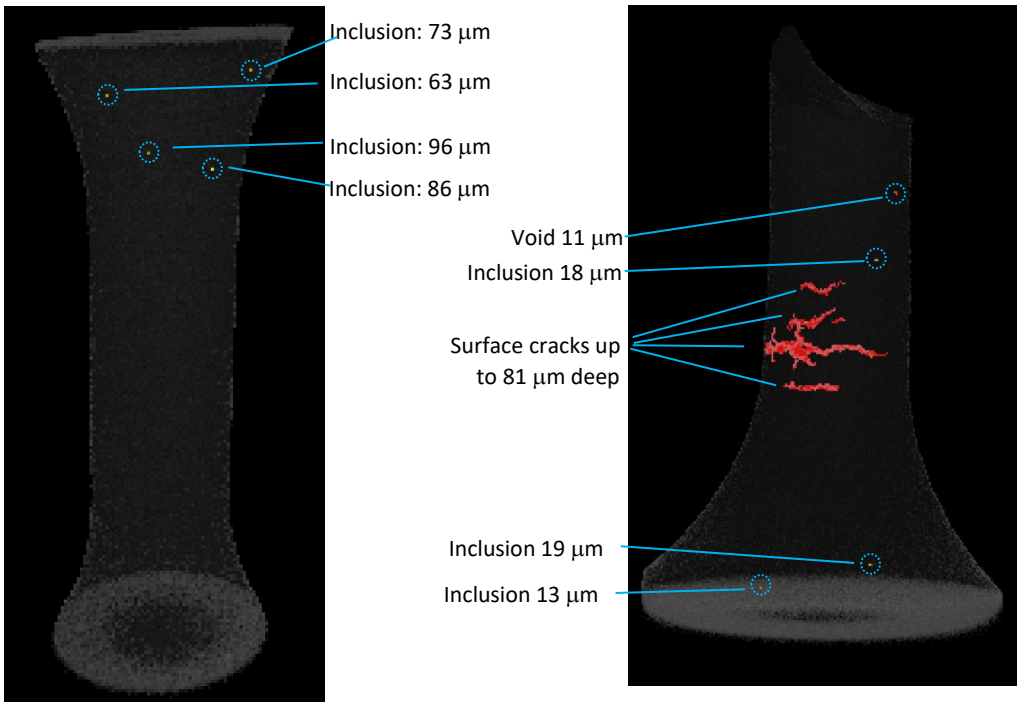


Fig. 6.11. CT scanning of LCF tested specimens (a) L-ET4 specimen showing presence of inclusions, and (b) L-ET5 specimen showing inclusions, micro-voids and propagating cracks.

6.2.6 Additional Considerations

To improve fatigue life of LPBF Ti-6Al-4V, the attempt should be to reduce the occurrence of these micro-voids and also their sizes, using the optimal build parameters and also by using the HIP process. Additionally, the use of post-build machining to improve the surface roughness, which thereby removes the surface nucleating micro-cracks, pores and voids, will improve the fatigue life of the LPBF parts [83, 236]. However, the machining and the HIP processes both are expensive and at the same time negatively impact the lead time for LPBF parts to reach to the customer [83, 236]. Therefore, practicing design and manufacturing engineers should put their efforts into optimising the product design and manufacturing with optimal build parameters, so that the end use of LPBF Ti-6Al-4V parts come without these costly additional processes. Based on the discussion above, the influence of various different parameters on LCF performance of LPBF Ti-6Al-4V, including cyclic softening and crack growth, is summarised on the interaction diagram shown in Fig. 6.12.

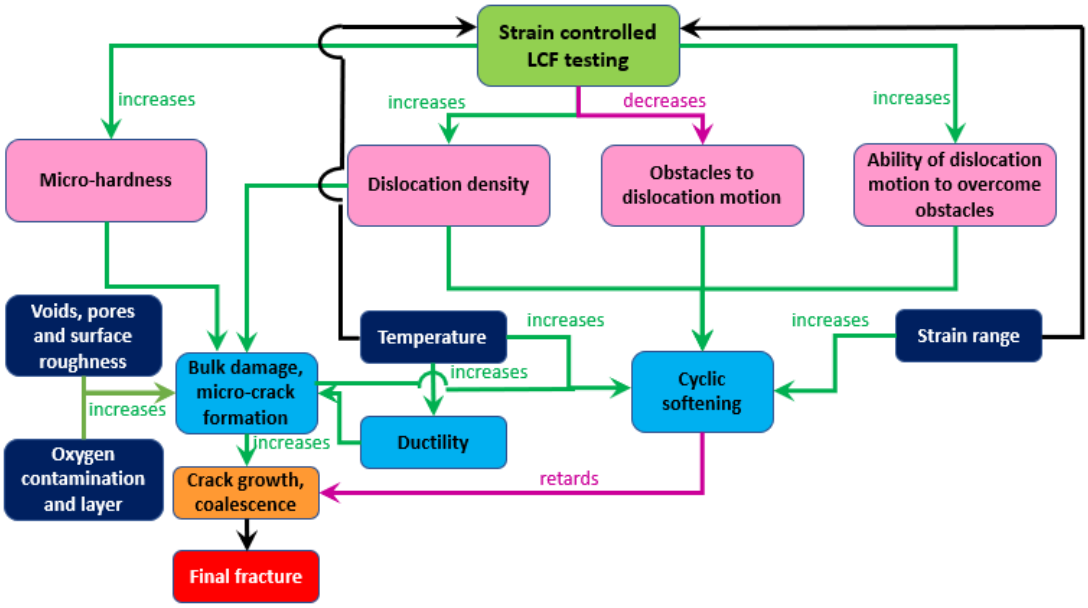


Fig. 6.12. Strain controlled LCF test performance of Ti-6Al-4V - A diagram illustrating complex interaction of various parameters.

6.3 Conclusions

To evaluate the LCF performance of the LPBF Ti-6AL-4V, strain controlled LCF tests at different strain ranges were carried out at RT (20°C) and ET (400°C). The following conclusions can be made based on this study:

- Crack initiation in the uniaxial LCF tested specimens happens at LOF voids or geometric irregularities, due to incomplete melting, which act as the stress raising features under cyclic loading. The number of cycles to failure decreases but the average softening rate increases with an increase in SRE cyclic tests.
- Cyclic softening was observed in each of the LCF tests and RT and ET. For cyclic tests at ET, the LPBF Ti-6Al-4V exhibited higher cyclic softening, compared to cyclic tests at RT, which was due to higher interaction of dislocations and faster crack growth under tensile part of the cyclic loading in cyclic tests at ET.
- Additionally, for tests at ET, the material experiences faster crack growth under tensile part of the cyclic loading.
- During cyclic deformation, evolution of dislocation substructures takes place to subsequently produce LABs inside the prior α' grains. The LABs progressively lead to nucleation and coalescence of voids with fatigue cycles, eventually leading to fracture.
- With an increase in fatigue cycles, an ease of dislocation annihilation and subsequent recovery of dislocations happens, which causes the free dislocation density to increase resulting into cyclic softening of LPBF Ti-6Al-4V. Also, with higher test SRE, the free dislocation density increases.

-----X X X X X X-----

CHAPTER 7

7 LCF Performance of LPBF Ti-6Al-4V Aeroengine Bracket at RT

On an aeroengine, brackets are used to support the sensors, controls units, harnesses and pipes. These brackets, typically fabricated from sheet metal or conventional machining process, are designed to achieve strength and stiffness with a minimum amount of material [237] and must meet the stringent certification requirements of the EASA as detailed in CS-E 650 [238]; however, often these designs are non-optimised and heavier than the initial weight target, therefore contributing to increased Specific Fuel Consumption (SFC) and emissions [239].

To date, studies on the fatigue performance of complex AM brackets are very limited [124], the available studies (see section 2.7) only discuss the performance of AM parts loaded within the material elastic limit and cannot be claimed to be fully understood. From the authors' literature searches, the studies providing analysis and investigations on LCF performance of AM parts at strain levels at or beyond the material elastic limit were not found.

While the brackets used in aero-engine applications will typically see loads resulting in stresses in the elastic regime of the material, they may experience some localised plastic strains around some geometric features; furthermore, in certain extreme loading conditions, it is likely that the brackets may experience plastic strains for small number of LCF loading cycles (e.g. < 100 cycles). To meet certification requirements, it needs to be demonstrated that the brackets have sufficient strength to withstand these extreme loading conditions and the brackets need to be checked under various load cases, including fatigue, to ensure compliance against the certification rules of the EASA. Furthermore, for a bracket under flight loading, it is desirable to have redundancy in the load transfer path of the bracket to ensure functionality of the component / part mounted on top of the bracket.

The LCF performance of a weight optimised bracket in the struts and connectors design, made using the LPBF process in Ti-6Al-4V material, was explored through the displacement controlled LCF testing at RT. The LPBF bracket design was intended to replace its equivalent aeroengine sheet metal bracket. The LCF test results together with its failure sequence are discussed in relation to the design cycles targets set for the LCF performance in an aeroengine application. The loading levels for the LCF tests on the bracket were established based on the findings from the cyclic test performance of the LPBF Ti-6Al-4V material via the specimen testing. Furthermore, the observations made on the characterisation of material microstructure around fracture surface and of fracture surface, are also presented as supporting evidence and discussed to characterise the failure mechanism. Although, the brackets installed on aeroengines will typically experience ETs, but in certain flight operating conditions, depending upon the (mounting location and environmental temperature, the bracket may experience temperatures close to RT.

7.1 Test Results

The displacement range of the BT1 test was chosen so that the LPBF bracket was loaded at or close to the elastic limit. This was approximated by visually examining the first hysteresis loop which had a small width, before continuing with the full BT1 test for the targeted number of 3000 cycles. The small width of initial hysteresis loops from BT1 test indicated small level of plasticity possibly at and around the geometric stress concentrations of the bracket. The BT1 test was stopped after 3280 cycles with no failure observed in any of the struts or connectors of the LPBF bracket. The hysteresis loops for the 1st and last cycles of the BT1 test are shown in Fig. 7.1, where it can be seen that the maximum force in the last cycle is slightly higher than the maximum force in the first cycle which was due to a slight calibration error in the test machine. It can be seen that the maximum force in tension appears to be higher than the force in compression, suggesting an asymmetric stiffness of the bracket. This was because of the reason that the thin struts and connectors of the bracket have tendency to flex with increasing compressive loading, thus lowering down the overall stiffness, and leading to a lower peak compressive load for the same displacement magnitude.

In the BT2 test run, using the same bracket, the displacement range was increased to ±4 mm to allow the bracket to undergo cyclic fatigue with a larger degree of plastic strain, which was confirmed by looking at the width of hysteresis loops from the BT2 test.

The bracket failed progressively in the BT2 test run with a total of seven failure incidences recorded, each at different locations in the bracket as shown in Fig. 7.2(a). The failure occurred at a different discrete LCF cycle, where each failure was identified with a drop in force, see Fig. 7.2(b) and Table 7.1. As shown in Fig. 7.2(b) and in Table 7.1, the bracket showed a good residual tensile strength (47%) even after the 5th failure, which indicates that the bracket design has good redundancy in its load transfer path and that the component will not completely collapse if there is an initial failure.

Table 7.1. Details of failure points under BT2 test.

Failure Number	Cycle Number	Residual Load Carrying Capacity (%)
1	211	83
2	230	75
3	255	66
4	560	64
5	579	47
6 & 7	616	8

The hysteresis loops around each of the failure points in the BT2 test are compared in Fig. 7.3. As seen in Fig. 7.3, the width of hysteresis loops appears to be wider which indicated that the bracket was cycling with increased levels of plastic strains in its structural elements.

Also, the drop in loading carrying capability was increasing with each subsequent failure in the bracket, due to lesser number of bracket elements available to take the loading, i.e. the bracket continued to become flexible with each failure as expected.

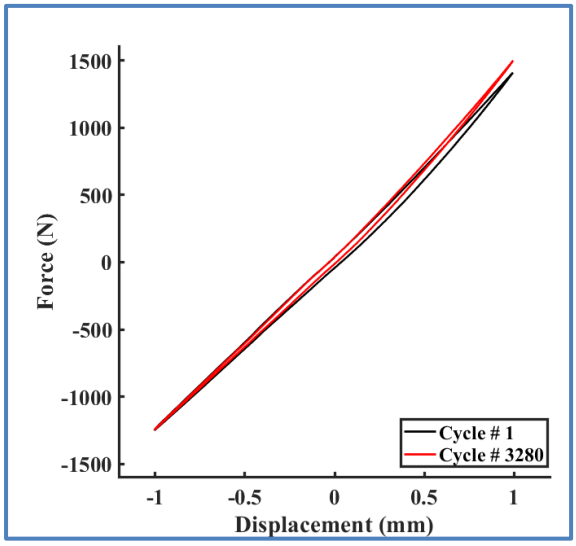


Fig. 7.1. Cyclic performance of LPBF bracket: first and last hysteresis loops under ±1 mm displacement range (BT1 test).

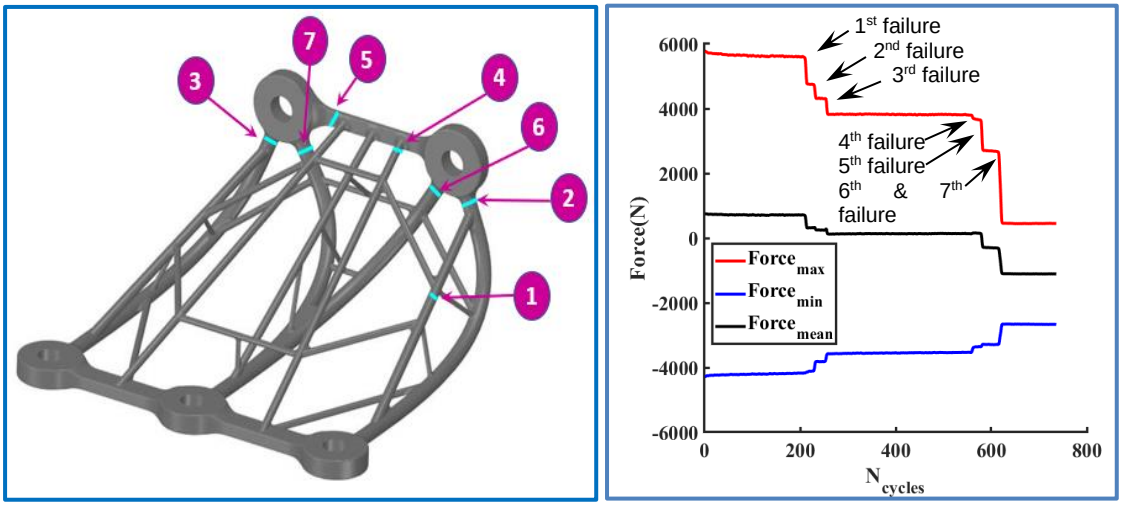


Fig. 7.2. Cyclic performance of LPBF bracket under ±4 mm displacement range (BT2 test): (a) locations and marked sequence of bracket failure, and (b) drop in loading with sequential failure of elements of the bracket.

From Fig. 7.3(b), some cyclic softening was observed in the bracket in the BT2 test, similar to the softening behaviour observed in the uniaxial LCF test results shown in Fig. 6.2. This and the

asymmetric response of the bracket during the BT2 test suggested a higher level of plastic stain (damage) accumulation occurring in the bracket elements in tensile loading part the BT2 test, than the compressive loading part. The first 5 fractured locations observed in the bracket are also shown in Fig. 7.4.

7.2 Discussion

7.2.1 Fractography

The first three failure locations on the bracket (see Fig. 7.4) were analysed using SEM to study the crack initiation and propagation mechanisms and are shown in Fig. 7.5. Similar to the LCF test specimens, the fracture surfaces are characterised by an initiation site/point, a central circular region representing the crack propagation zone and finally an outer shear lip zone, as seen in the overview Fig. 7.5(a), Fig. 7.5(d) and Fig. 7.5(g) for locations 1, 2 and 3, respectively. The crack initiation was either from pores or LOF voids, acting as stress raising features on the surface of the struts. The effective size of these defects can be characterised and compared using the d value [240]:

$$d = \sqrt{A_{eff}}$$

Where A_{eff} is the effective area of the pore. The fracture surface of location 1 depicts the initiation from an area marked with a pore (d = 61 μm) present in vicinity of an irregular geometric feature on the surface of the strut, see Fig. 7.5(b). In Fig. 7.5(b), beach marks can also be seen next to the initiation site. One small LOF void in the outer shear lip, shown in Fig. 7.5(c), was also present at location 1 (d = 57 μm), but it did not participate in crack initiation or growth. For the locations 2 and 3, the initiation was from the LOF voids found near the surface of the struts, shown in Fig. 7.5(e) and Fig. 7.5(h), with d = 117 μm and 90 μm for locations 2 and 3, respectively. The size of LOF voids observed at these locations were larger than the one observed at location 1. From Fig. 7.5(f), a secondary crack initiation from another LOF void (d = 72 μm) present at the surface was also seen at location 2 and the propagation of this caused coalescence with the primary crack to cause fracture earlier than at location 3. Beach marks denoting the crack growth direction and progression were also visible at location 3, as seen in Fig. 7.5(i).

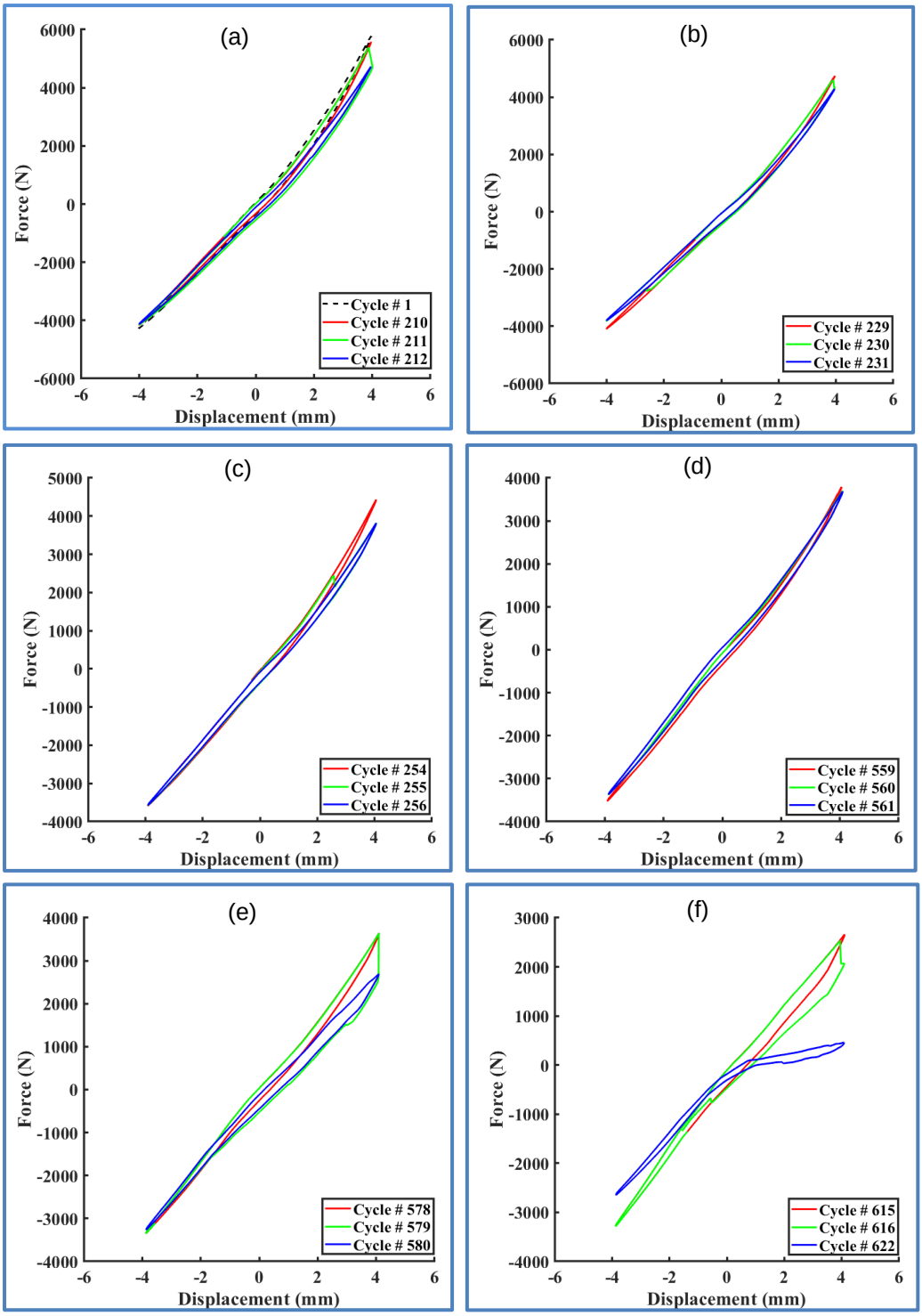


Fig. 7.3. BT2 LCF test on the LPBF bracket, hysteresis loops at each failure point: (a) 1st failure at 211th cycle, (b) 2nd failure at 230th cycle, (c) 3rd failure at 255th cycle, (d) 4th failure at 560th cycle, (e) 5th failure at 579th cycle, and (f) 6th and 7th failures at 616th cycle.

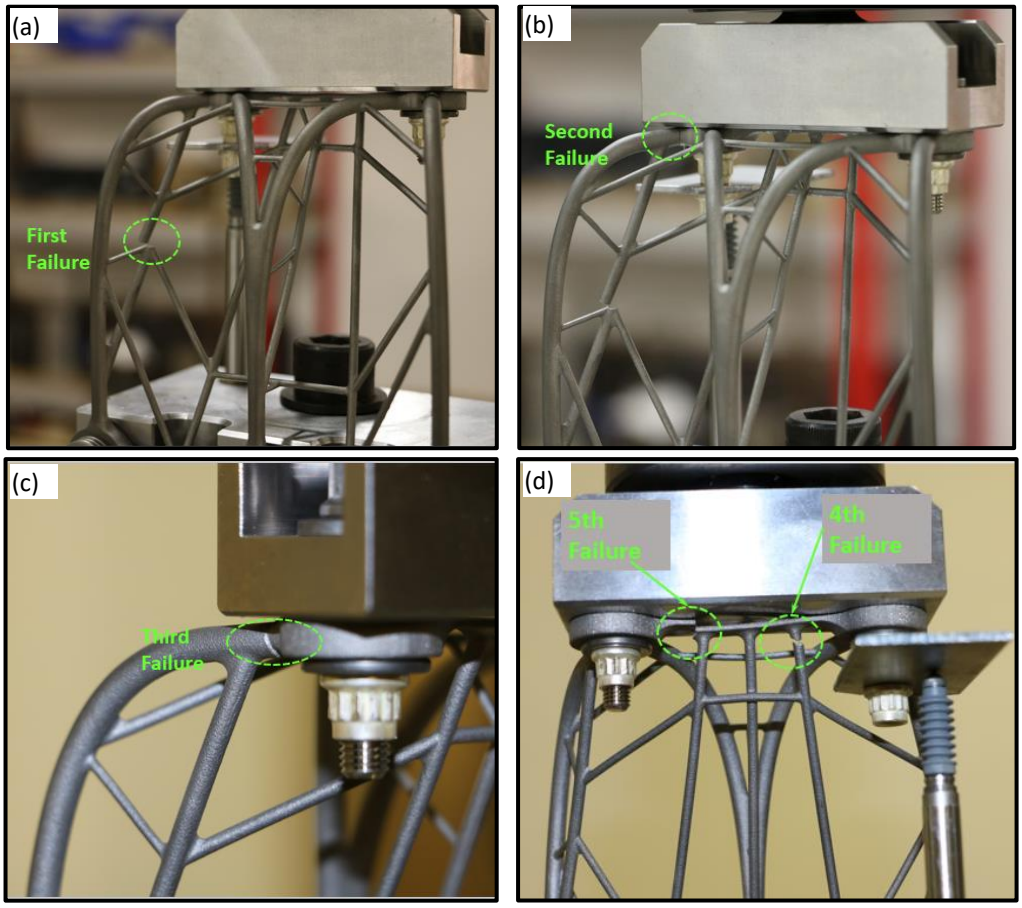


Fig. 7.4. Pictures of bracket in installed condition with marked first five failure locations from BT2 test: (a) 1st failure, (b) 2nd failure, (c) 3rd failure, and (d) 4th and 5th failures.

The fracture surface characteristics examined in Fig. 7.5 are similar to the ones observed for the uniaxial LCF tested specimens shown in Fig. 6.5. Furthermore, the features of fracture surface observed for the other remaining fractured locations of the bracket were similar to the features discussed here for the first three fractured locations.

The failure sequence in the bracket (see Fig. 7.2(a) and Fig. 7.4), depends upon the combination of stress magnitude and the size of the defect (flaw) present at the location. The defects which vary in shape and size (as seen in Fig. 5.6) occur on the surface of the LPBF part or within it and act as the crack initiation sites under fatigue loading. The larger size defect and higher stress magnitude accelerate the crack propagation and shorten the fatigue life. The progressive failure of the bracket with good observed residual strength to withstand the operating load was as expected in terms of overall fatigue performance of the bracket and load drop with each failure. This expectation in bracket performance was due to its peculiar shape in struts and connectors design, and was one of the main considerations during initial design stage of the bracket.

7.2.2 KAM Distribution Plots

For the first failure location of the bracket (location 1), the KAM plots obtained from the EBSD scans are shown in Fig. 7.6. For EBSD scans of location 1, two areas were chosen; (i) an area slightly away

from the fracture surface (see Fig. 7.6(a)) and (ii) an area at the fracture surface (see Fig. 7.6(b)). In Fig. 7.6, the KAM distribution is overlayed on top of the grain boundaries to see the variation in KAM density and grain size.

The KAM plots in Fig. 7.6 show a refinement of α' grains with fatigue cycles where the α' grains have become fine at the fracture surface with a corresponding high average KAM value shown in green (see Fig. 7.6(b)). The fracture surface (location 1), with higher free distributed dislocation density, experiences plastic deformation which subsequently causes cyclic softening and bulk damage / crack initiation in the material. In the area away from the fracture surface (see Fig. 7.6(a)) the grains sizes aren't altered and the KAM distribution, shown in green, remains low which indicates no free dislocation density built up with fatigue cycles in the area away from the fracture surface.

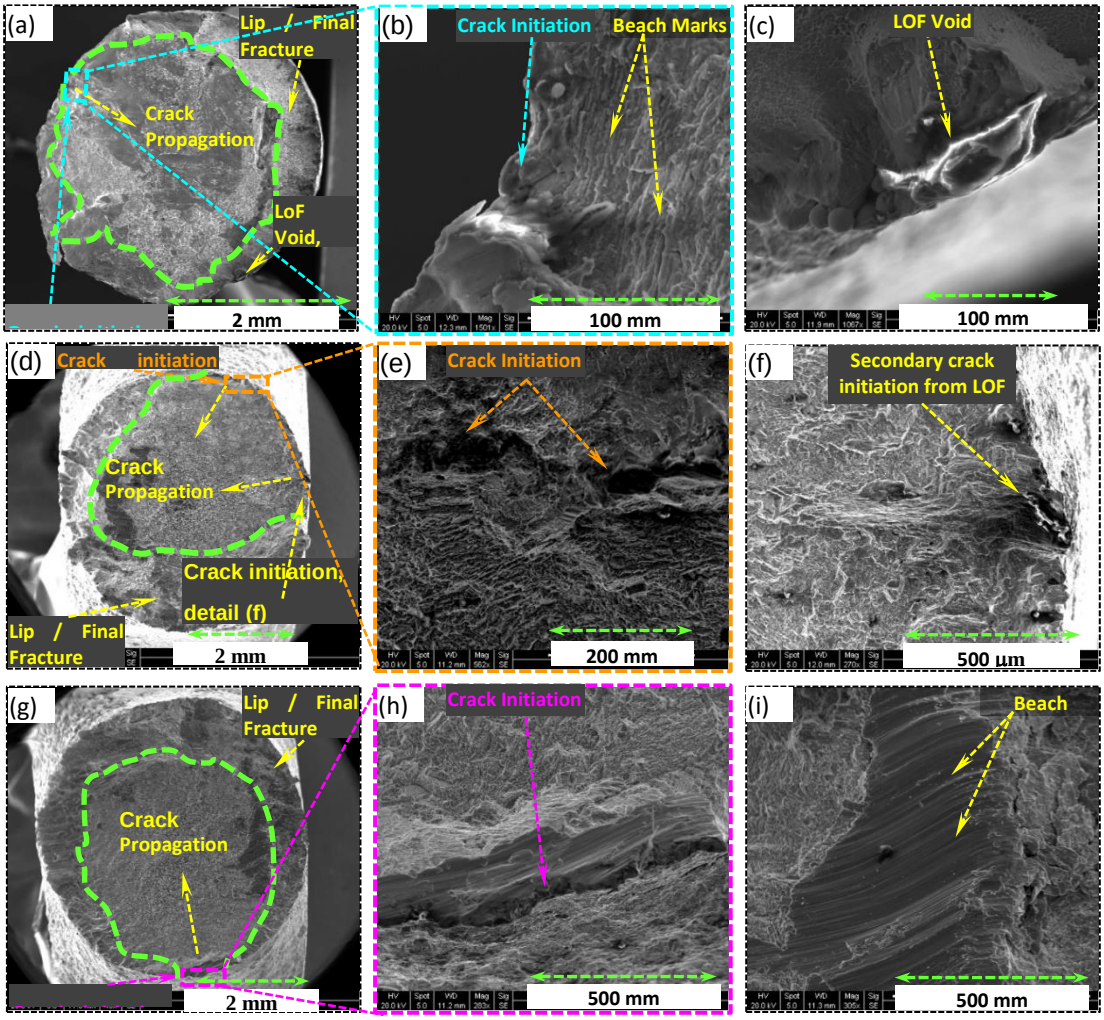


Fig. 7.5. SEM micrographs of fracture surfaces of first three failed struts of the bracket: (a) – (c) fractured strut - location 1, (d)– (f) fractured strut - location 2, and (g) – (i) fractured strut - location 3.

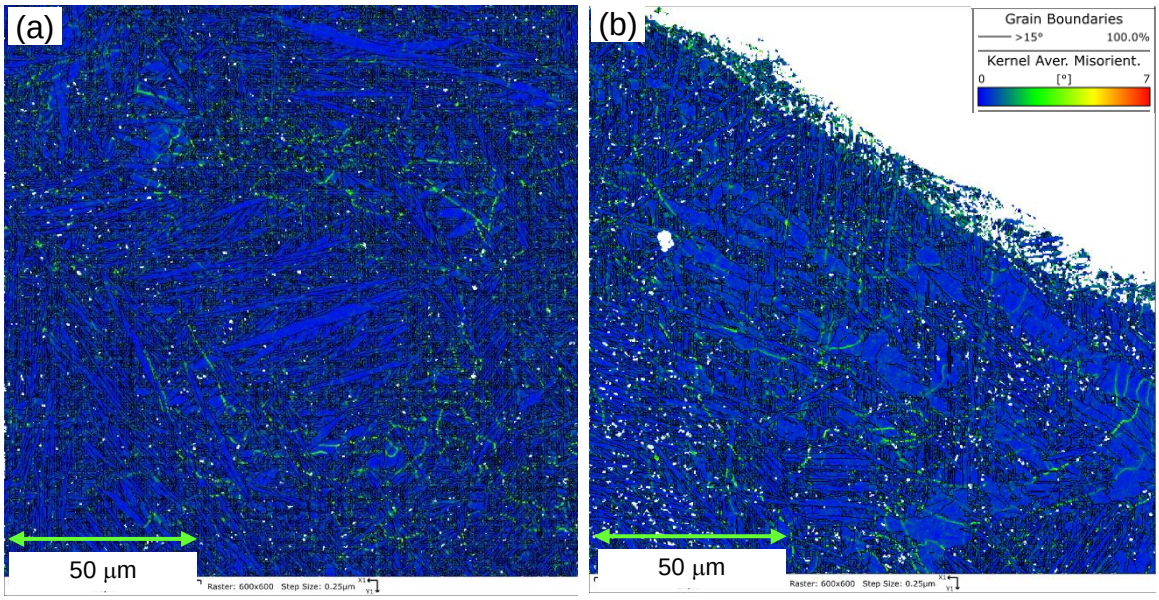


Fig. 7.6. EBSD micrographs showing KAM plot of LPBF Ti-6Al-4V bracket tested under LCF loading at RT: (a) scan away from the fracture line, (b) scan at the fracture line of fracture location 1.

7.3 Conclusions

In this chapter, the LCF behaviour of LPBF Ti-6Al-4V bracket in struts and connectors design at RT has been studied. The key findings from this study are summarized as below:

- The LPBF bracket in the struts and connectors design met the LCF design targets, as demonstrated through the cyclic testing at RT.
- The LPBF bracket successfully exceeded the intended 3000 cycles without experiencing any failure in the first cyclic test (BT1), where the applied loading on the bracket was close to the elastic limit of the material. In real applications, the LCF loads on the brackets during normal operation of the engine/aircraft are significantly less than the loading applied under BT1 test conditions.
- The failures in the bracket were observed only under the extreme loading condition (BT2 test). The failure in the bracket was progressive in nature and happened at increasing number of discrete cycles at different locations. Even after the first 5 failures, the LPBF bracket had 47% residual load carrying capacity in the tensile part of the hysteresis loop, indicating a good redundancy in its load transfer path.
- It has been shown that the surface locations where LOF voids or pores are present in the bracket struts were the likely sites for crack initiation if they coincide with high stress locations.

-----x x x x x x-----

CHAPTER 8

8 LCF Performance of LPBF Ti-6Al-4V Aeroengine Bracket at ET

The brackets installed on aeroengines will typically experience ET. The LCF performance of a weight optimised LPBF Ti-6Al-4V bracket in the struts and connectors design, was explored through the displacement controlled LCF testing at 200°C temperature. This is a typical temperature experienced by the bracket installations on aero-engines. The results of LCF test at ET together with its failure sequence are discussed in relation to the design cycles targets set for the LCF performance in an aeroengine application. Additionally, the observations made on the characterisation of material microstructure and fracture surface are also presented as supporting evidence and are discussed in detail.

8.1 Test Results

The displacement controlled LCF tests on the bracket at ET were performed in two separate runs. In the first run, the cyclic test (BET1) was performed on the bracket with a displacement range of ± 1 mm which was chosen so that the plastic strains in the bracket elements are not significant i.e. total strain is close to the elastic limit. This was confirmed by reviewing the width of the first few cyclic loops before continuing to proceed to the full BET1 test. The cyclic test loops for the 1st and the last cycles of the BET1 test are shown in Fig. 8.1(a), and the cyclic softening effects on the max, mean and min stresses are shown in Fig. 8.1(b).

The BET1 test was performed for a total of 3439 cycles with no failure observed in any of the struts or connectors of the bracket. As seen in Fig. 8.1(a), the maximum loading force in the last cycle is lower than the maximum force in the first cycle which indicates a small level of cyclic softening at this level of cyclic loading. From Fig. 8.1(b) the cyclic softening is more evident only in the tensile part of the loading with no softening in the compressive part of the loading.

In the second test run (BET2 test), the displacement range was increased to ±2 mm to increase the amount of plasticity. The BET2 test was to load the bracket such that it simulates the elasto-plastic strain loading level which could happen under an extreme design event of an aeroengine and to study the performance of the bracket at these displacement levels. In the BET2 test, the bracket experienced the 1st local failure at the top of the right most main strut at the 15th cyclic when a sudden drop in loading was observed, as shown in Figs. 8.2(a) and Fig. 8.2(b). The BET2 test was continued after the 1st failure, and subsequently the 2nd failure was noticed at the top of the left most main strut at the 286th cycle, presented in Fig. 8.2(c) and Fig. 8.2(d). The history of the bracket during the BET2 test is shown in Fig. 8.2(e) which indicates that:

- The bracket has significant residual strength (up to 65% of tensile loading) even after first two failures in the bracket.

- The bracket has asymmetric stiffness where the loading in tension and compression are different. This asymmetric behaviour is due to the thin struts and connectors of the bracket having subtle difference in their behaviour under compression and tension loading.
- Cyclic softening was observed during the bracket LCF test.

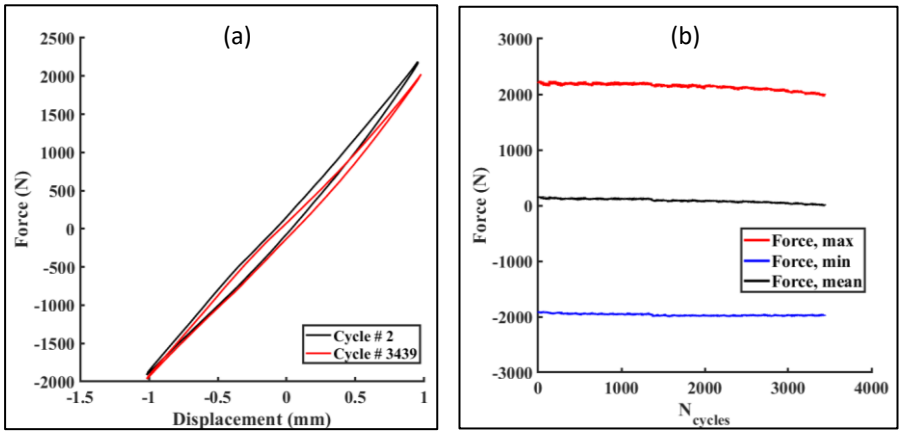


Fig. 8.1. Bracket LCF test (BET1) results: (a) shape of the second and the last loops, and (b) cyclic softening effects on max, mean and min stresses during BET1 test.

8.2 Discussion

8.2.1 Microstructure Characterization

The SEM micrographs of LPBF Ti-6Al-4V built in Phase 3 is shown in Fig. 8.3, where the SEM scan of vertical and horizontal cut sections are shown individually in Fig. 8.3(a) and Fig. 8.3(b), respectively. The microstructure is characterised by the columnar prior β grains spanning across multiple built layers (see Fig. 8.3(a)) and having a width of prior β grains in the range of 50 -100 μm (see Fig. 8.3(a) and Fig. 8.3(b)). The EBSD scan of LPBF Ti-6Al-4V shows a very small presence of β phase (Fig. 8.4(b)). The microstructure is composed of martensitic α' grains (in majority) which are in elongated needle shape and are arranged in the basketweave type of structure (Fig. 8.4(b)). A uniform distribution of colouring in the IPF map in Fig. 8.4(b) shows that the behaviour of LPBF Ti-6Al-4V will predominantly be isotropic. The microstructure of LPBF Ti-6Al-4V, shown in Fig. 8.4(a) and Fig. 8.4(b), is similar to the microstructure observed for LPBF Ti-6Al-4V material built in Phase 2 which is characterised and discussed in detail in section 5.2.1.

8.2.2 Fractography

The SEM micrographs of fracture surfaces of the two cracked locations in the bracket are shown in Fig. 8.5. For the first cracked location (i.e. location 1, see Fig. 8.2(a)), the fracture surface is split into two zones: (i) zone of crack initiation and crack propagation, and (ii) zone of fast fracture forming a lip as shown in Fig. 8.5(a). From Fig. 8.5(b), the crack initiation zone is identified as the LOF void and the beach marks, indicating cyclic crack propagation at location 1. The LOF voids are evident both at the surface (see Fig. 8.5(b) and Fig. 8.5(c)) and also internally into the bulk material (see Fig. 8.5(a)). For the second cracked location (i.e. location 2, see Fig. 8.2(c)), the fracture surface details are shown in

Fig. 8.5(d). In Fig. 8.5(d), the lip indicating final part of the fracture could not be identified. Again, the crack initiation happens at the LOF void present at the surface (see Fig. 8.5(E). The LOF void at location 2 appears to be smaller (see Fig. 8.5(e)) than the one found at location 1 (see Fig. 8.5(b)). Other secondary geometry features, resulting due to LOF void (see Fig 8.5(f)) with associated beach marks are also seen at the surface, suggesting initiation and propagation of secondary cracks which subsequently coalesced with the propagating primary crack to accelerate the propagation at the location 2.

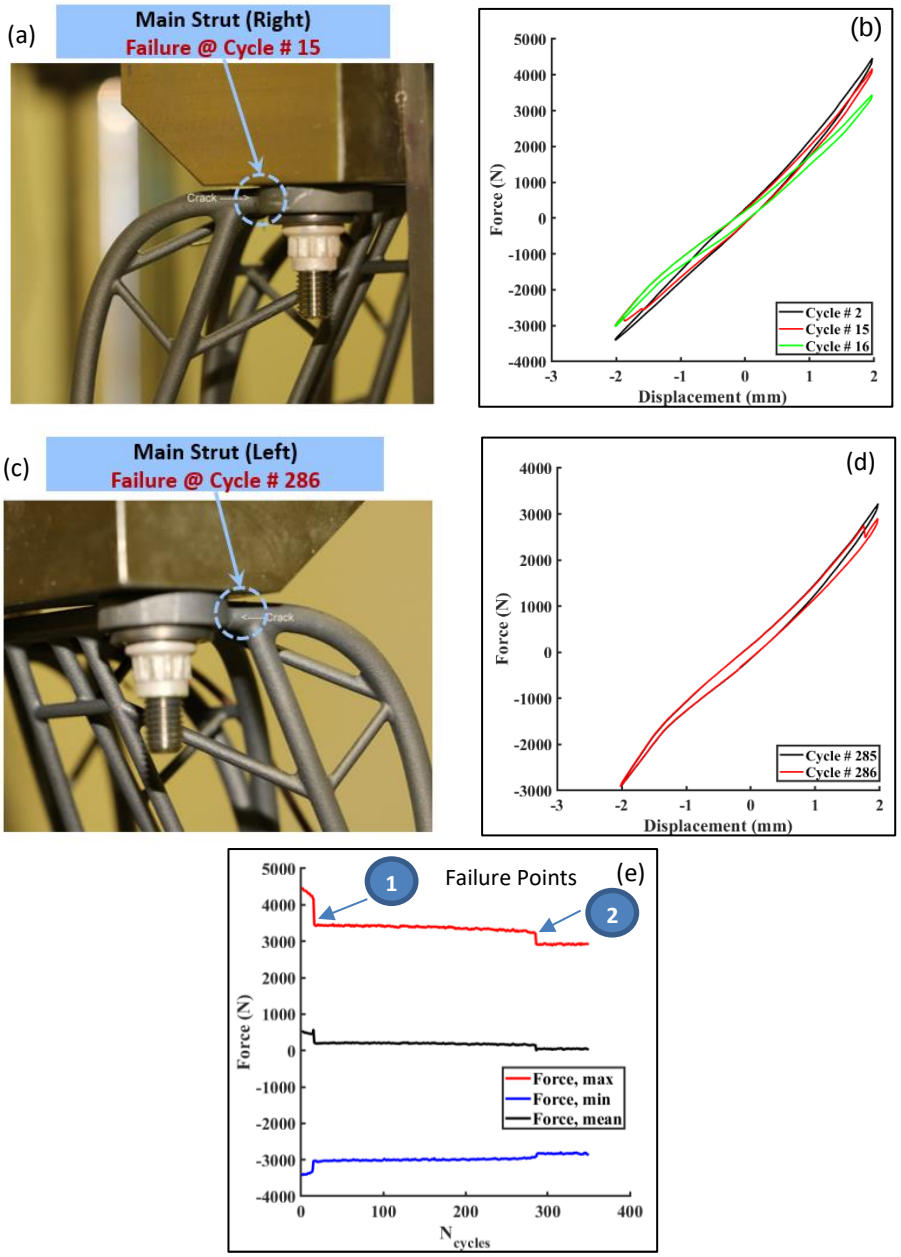


Fig. 8.2. Bracket LCF test (BET2) results: (a) first crack location in top of the right main strut, (b) cyclic loops at first failure point, (c) second crack location in top of the left main strut, (d) cyclic loops at second failure point, and (e) the load history of max, mean and min forces.

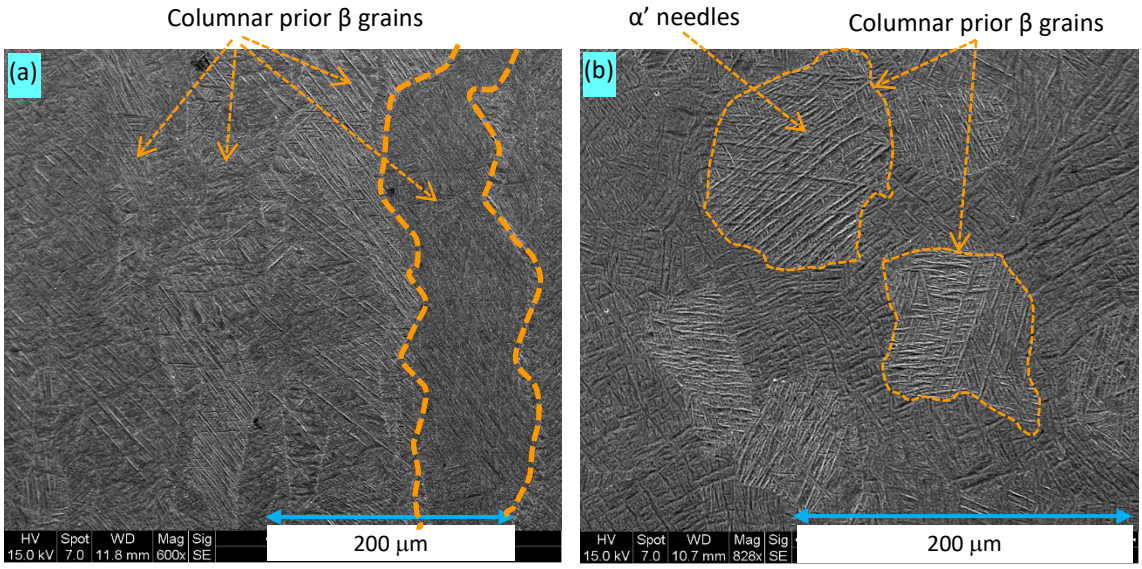


Fig. 8.3. SEM micrographs showing microstructure of LPBF Ti-6Al-4V- Phase 3: (a) vertical section, (b) horizontal section.

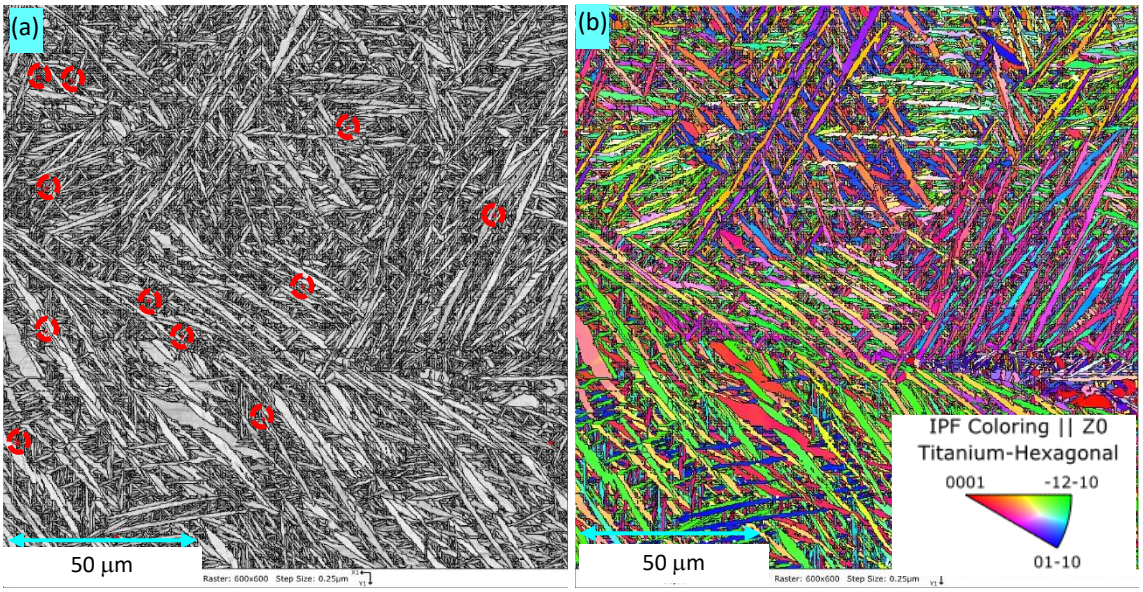


Fig. 8.4. EBSD micrographs showing as-built LPBF Ti-6Al-4V - Phase 3: (a) Phases present: white - α phase, red – β phase, (b) IPF plot showing that the orientation of α grains is equally distributed.

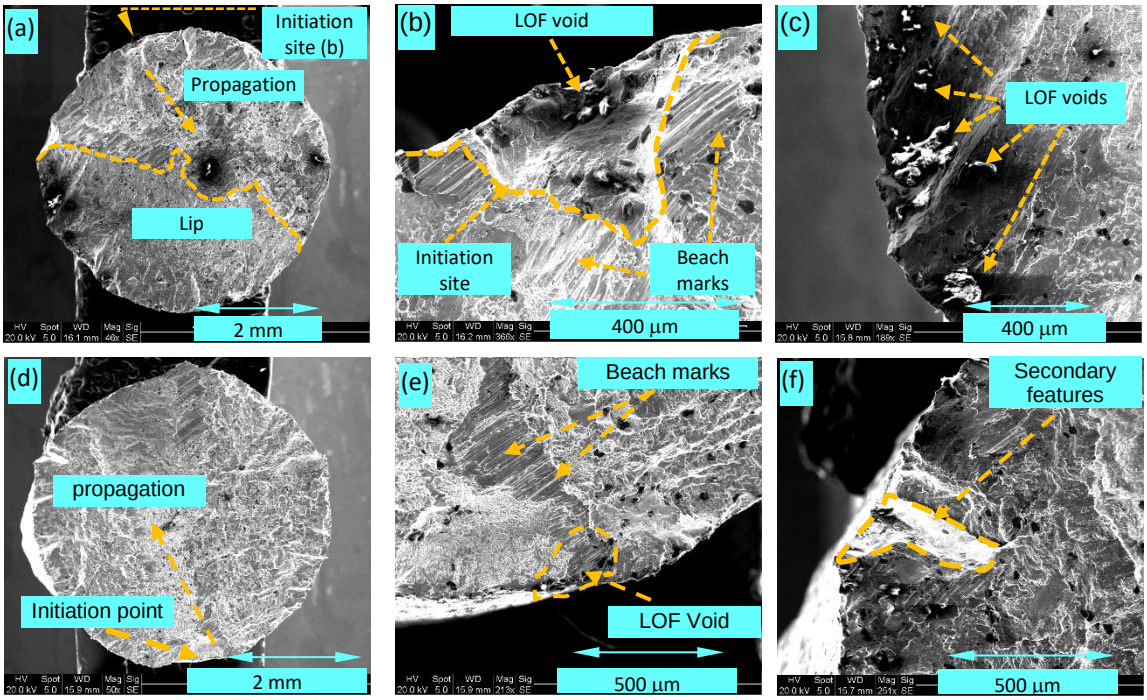


Fig. 8.5. SEM micrographs of fracture surfaces of bracket from ET LCF test: (a) – (c) fracture surface at location 1 showing zones of initiation and propagation and fast fracture (lip) zone, (d) – (f) fracture surface at location 2 showing zones of initiation point and propagation and secondary features causing secondary crack initiation.

8.2.3 KAM Distribution Plots

For the failure location 1 of the bracket tested under LCF loading at ET, the KAM plots obtained from the EBSD scans are shown in Fig. 8.6. Again, two areas were chosen for the EBSD scans; (i) an area slightly away from the fracture surface (see Fig. 8.6(a)) and (ii) an area at the fracture surface (see Fig. 8.6(b)). Again, the KAM distribution is overlayed on top of the grain boundaries to see the variation in KAM density and grain size in the microstructure to do a comparative study between the two scanned areas. At the fracture surface (see Fig. 8.6(b)) a refinement of α' grains was seen indicated by the average KAM value shown in green. A high average KAM value at location 1, was a result of high free distributed dislocation density, which was built-up due to cyclic plastic deformation which subsequently also caused cyclic softening and bulk damage / crack initiation in the material. In the area away from the fracture surface (see Fig. 8.6(a) the grains sizes aren't altered and the KAM distribution, shown in green, remains low which indicates that the free dislocation density did not build-up with fatigue cycles i.e. the stresses at this location were predominantly elastic in nature.

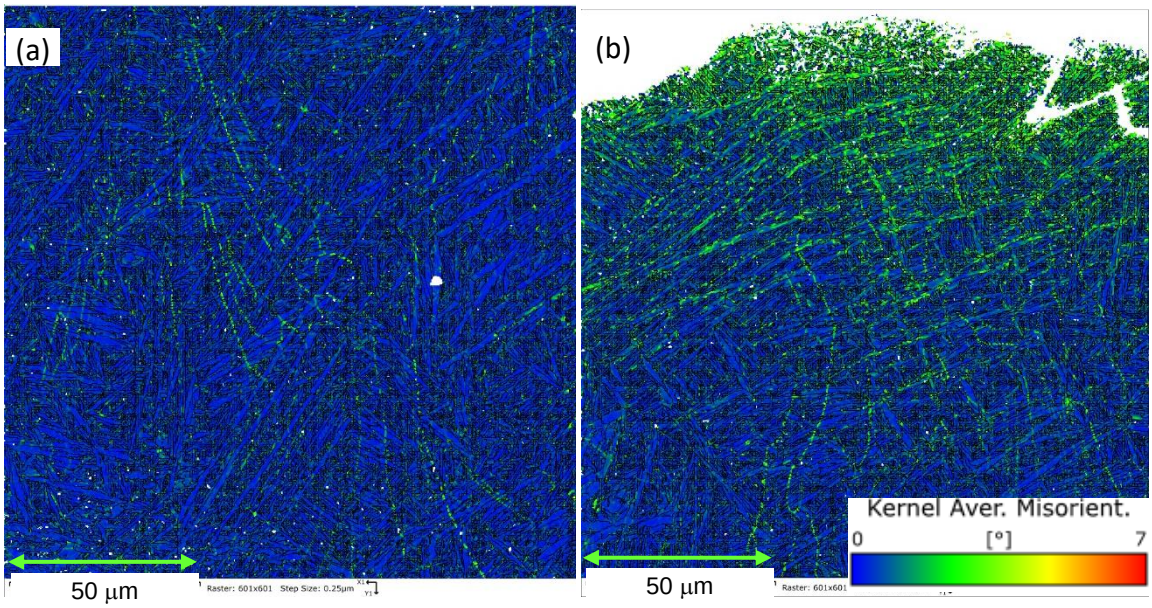


Fig. 8.6. EBSD micrographs showing KAM plot of LPBF Ti-6Al-4V bracket tested under LCF loading at ET: (a) scan away from the fracture line, (b) scan at the fracture line of fracture location 1.

8.2.4 Additional Considerations

The influence of various different parameters which affect the LCF performance of LPBF parts in Ti-6Al-4V, including cyclic softening and crack growth, is summarised in the interaction diagram shown in Fig. 8.7. The parameters included in the interaction diagram are key to establish a strong and validated relationship between the properties of LPBF Ti-6Al-4V and performance of LPBF Ti-6Al-4V parts under mechanical and cyclic loading.

Other factors such as the powder specification and the use of recycled powder, post-build heat and surface treatments, the melt pool dimensions, thermal history experienced during the build, geometry of parts etc. can cause differences between the property and structural performance of the LPBF parts [241, 242]. Additionally, if attempts are made to maintain a similar thermal history between the laboratory specimens and the critical location of the part by altering the process parameters, it may be possible to achieve similar mechanical and fatigue performance between the laboratory specimens and the LPBF part [241, 242].

Furthermore, the use of optimal build parameters and post LPBF build HIPing can reduce, but not fully remove, the internal and near surface gas pores and voids. Improvement in surface finish to remove the surface nucleating micro-cracks through machining will also help to improve the fatigue life of LPBF parts. However, these post build processes can be expensive and could also increase the lead time for the LPBF parts to reach to the end customers [236].

8.3 Conclusions

In this chapter, the LCF behaviour of LPBF Ti-6Al-4V bracket in struts and connectors design at ET has been studied. The key findings from this study are summarized as below:

- From the LCF testing at ET, the LPBF bracket in struts and connectors design successfully exceeded the intended 3000 cycles under the applied loading which was close to the elastic limit of the material. In real applications, the brackets are designed to experience much lower cyclic loading as compared to the cyclic loadings defined for the BET1 tests. The failures in the bracket were observed only under the cyclic tests at extreme loading condition. The failure observed in the bracket was progressive in nature and happened at increasing number of discrete cycles at different locations.
- From the cyclic tests at ET, the sequential failures of the bracket elements, exhibited a distinct design feature of the bracket where it demonstrated redundancies in the load path due to its particular design with multiple load-carrying struts.
- It has been shown that the surface locations, where LOF voids or pores are present in the bracket struts, were the likely sites for crack initiation if they coincide with high stress locations.
- To establish and evaluate the property-structure-performance relationship it is important that the results of cyclic laboratory tests performed on LPBF Ti-6Al-4V specimens are used to obtain information needed to set the loading level of component and sub-component level cyclic testing. The efforts to better understand the relationship between properties and component test performance must continue to minimise expensive component testing in future to produce certifiable and flightworthy aero-engine components.
- This carefully designed weight optimized bracket has shown good fatigue performance, which was very much needed to build the confidence of practicing engineers for successful deployment of the LPBF technology for safety critical load bearing applications.

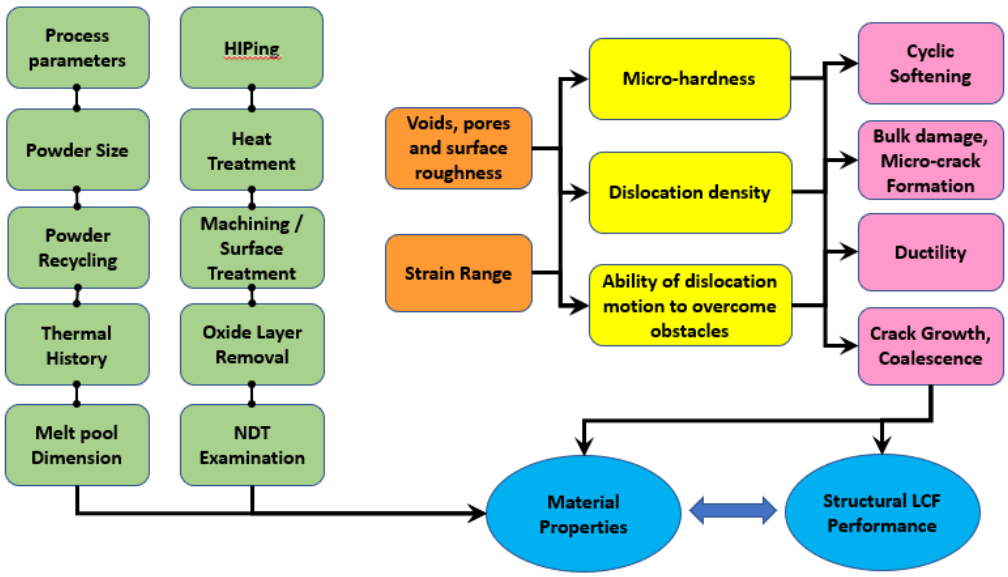


Fig. 8.7. Property-structural performance evaluation: A diagram illustrating complex interaction of various parameters affecting strain controlled LCF test performance of LPBF Ti-6Al-4V material.

-----X X X X X X-----

CHAPTER 9

9 High Cycle Behaviour of LPBF Ti-6Al-4V

Components on an aeroengine experience vibration loading during engine operation and the vibration levels continue to increase as the engine gets older due to expected degradation in the bearings and blades performances. Majority of component failures in aviation industry are due to fatigue caused by the vibration loading [243]. Brackets are used on an engine to support the externals accessories such as the sensor/controls unit, electrical harness or pipe. These brackets are typically made of sheet metal or from machining and are designed to withstand engine driven mechanical vibrations (due to shaft Out of Balance (OoB)) to meet the CS-E 650 certification requirement set-out by the EASA [238]. Because of the mounting locations of brackets on fan-case of the engine, the engine excitations in the Low Pressure shaft frequency range are found to be the most critical for the brackets. Additionally, as per CS-E 810, it needs to be demonstrated that no complete detachment of the bracket, leading to a hazardous situation, will occur in an extreme event such as FBO [238]. Although the primary aim of an engineering design is to achieve the desired strength and stiffness with a minimum amount of material [237], due to the stringent certification requirements and complex engine operating environment, conventional bracket designs are often not optimised and are often heavier than the initially targeted weight. A lower overall engine weight is desired to reduce the SFC [239] during engine operation.

Fatigue cracks are most likely to initiate at a free surface, due to the presence of many micro-cracks and stress raising features, which can negatively impact the HCF strength of LPBF Ti-6Al-4V parts [64, 65]. In the absence of significant surface roughness, defects would dominate to deteriorate the fatigue properties [72]. According to Vayssette et al. [244], the as-built surface roughness can reduce the fatigue strength by a factor of 2 for the LPBF Ti-6Al-4V with HIP treatment. An Equivalent Initial Flaw Size (EIFS) approach to estimate total fatigue life was suggested by Greitemeier et al. [65]. The EIFS, described by a semi-elliptical surface crack, is back extrapolated from the S-N data and was linked to the experimentally determined surface roughness value; however, their proposed linear elastic fracture mechanics (LEFM) based approach ignored the effects of small cracks and also the initiation period. Murakami [240] had suggested the $\sqrt{area}$ approach to determine the size of defects in metals and components, which indicates the square root of the projected area of defect on a plane normal to the loading axis. This $\sqrt{area}$ approach was developed based on a thorough consideration of the fracture mechanics, i.e. the intrinsic strength of the microstructure and the crack closure tendency [68]. Other researchers [240, 245] have discussed a method to evaluate the effect of surface roughness, but these methods do not fully provide details of the link between the surface roughness and material mechanical strength and fatigue properties. According to Nakatani et al. [245], the $\sqrt{area}$ parameter model does not fit with the experimental results, and Masuo et al. [68] reported that the $\sqrt{area}$ parameter does not accurately predict the actual fatigue strength of Ti-6Al-4V. In

addition, according to Le et al. [246], the effect of the spatial position of LOF defects in the material cannot be adequately predicted by the classical Murakami approach. The rough surface of as-built LPBF material often comes with complex 3D morphology with mostly irregular defects, therefore, the size of a defect determined by $\sqrt{area}$ does not reflect the true effect of defects [68]. Accordingly, Masuo et al. [68] suggested that the method to estimate the effective defect size should instead be expressed using the effective defect size, $\sqrt{area_{eff}}$, which is bigger than the real defect size ($\sqrt{area}$) for various possible shapes of defects, and needs to be considered to accurately obtain the fatigue limit of as-built LPBF Ti-6Al-4V [68, 240]. Furthermore, to account for surface roughness alone, an evaluation method of equivalent defect size for roughness represented by $\sqrt{area_R}$ was also proposed by Murakami [240] which considered the dimensional parameters associated with a periodic roughness profile [240, 245]. However, this approach does not interact with the presence of defects or stress raising features at or near the surface, and therefore has limited validation.

The structural integrity of an AM component can be defined as when the component is sound and unimpaired such that it can provide the desired level of structural safety, performance and durability [247]. The fatigue performance of an AM component remains dependent on the microstructure, porosity/voids, surface finish and residual stress levels [74, 123, 133, 248], and this complex relationship is yet to be understood for AM components designed to operate in a complex loading environment [5]. A premature failure of an AM part could cause adverse impact on the ongoing efforts to successfully implement the AM technology in safety-critical applications [243].

Although the HCF performance of LPBF Ti-6Al-4V has been studied widely at specimen level [74, 75, 237, 239, 249], studies on the HCF performance of geometrically complex AM parts are non-existent [124]. In this chapter, first the typical fatigue limit (at R = -1 and 10^7 cycles) of LPBF Ti-6Al-4V at RT and ET are evaluated from the results HCF testing at specimen level. Subsequently, the fatigue performance of a weight optimised Ti-6Al-4V LPBF bracket in struts and connectors design has been studied. The bracket was designed to support an electronic sensor on an aeroengine and aimed to have a minimum g load capability which was set based on the typical worst vibration level that the sensor and the bracket could experience during in-service operation of the engine. The modal and fatigue performances of the bracket were evaluated through shaker table tests at RT and the minimum g load capability (fatigue) was established by recording the response g level and failure sequence of the bracket struts. The results and performance of the bracket are discussed further based on the observations on the characterisation of the fracture surfaces. A relationship between the material fatigue limit and micro-hardness is discussed to understand the fatigue strength reduction due to the combined effects of surface roughness and surface breaking voids in the as-built LPBF Ti-6Al-4V material. A safe-life regime, which links the stress levels with size of defects, is also established and has been recommended to support the property-performance relationship for LPBF component design.

9.1 HCF Test Results

9.1.1 Uniaxial HCF Tests at RT

The results of HCF test at RT are plotted in Fig. 9.1, which presents the run-out and failure points for all the HCF test specimens. Three HCF specimens showed a run-out at 10^7 cycles. From the curve fitting, the typical fatigue limit (at R = -1 and 10^7 cycles) is 210MPa and the lower bound of the fatigue life is identified as 200 MPa.

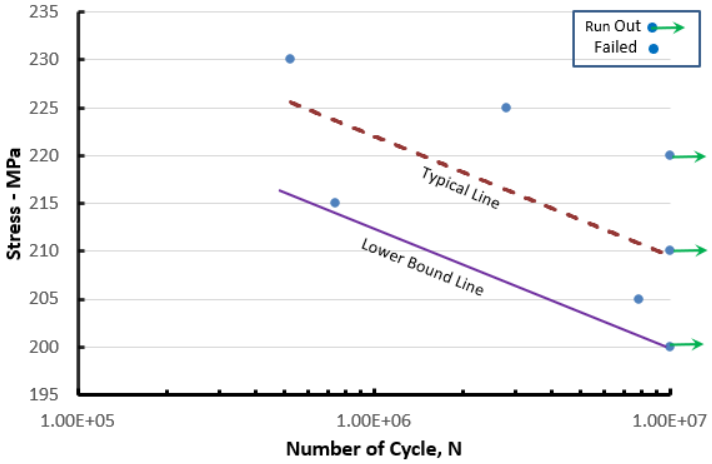


Fig. 9.1. HCF life of LPBF Ti-6Al-4V at RT.

The scatter observed in the fatigue endurance data at 10^7 cycles was as expected due to the nature of the LPBF processes i.e. due to the varying effect of defects (size, location, distribution etc.), roughness etc. and has also been reported in other studies [250].

Although, a limited number of specimens have been used for HCF testing, the derived HCF endurance strength of LPBF Ti-6Al-4V material has subsequently been used to develop a safe life curve for the bracket in view of the presence of defects due to the LPBF process. Further testing is suggested to build a larger data set, with minimum and typical endurance strengths derived based on statistical approaches, if the endurance strength data is to be used for certification purposes in real applications.

9.1.2 Uniaxial HCF Tests at ET

The test results of HCF testing at ET (200°C) are plotted in Fig. 9.2, which presents the run-out and failure points for all the HCF test specimens. Three HCF specimens showed a run-out at 10^7 cycles. From the curve fitting, the typical fatigue limit (at R = -1 and 10^7 cycles) is 226MPa and the lower bound of the fatigue life is identified as 210 MPa.

The typical and the lower bound values of the fatigue endurance values at 10^7 cycles at ET (both typical and lower bound) was observed to be higher than the fatigue endurance values at 10^7 cycles at RT. Although, the specimens for HCF tests at RT and ET were prepared in two different builds, no obvious difference was spotted in the material microstructure of LPBF Ti-6Al-4V from these two separate builds (Fig. 5.2, Fig. 5.3 and Fig. 8.3). Possible changes in the distribution of defects and / or

surface roughness could potential cause this difference in fatigue endurance strength at ET and RT which should be investigated as part of the future studies.

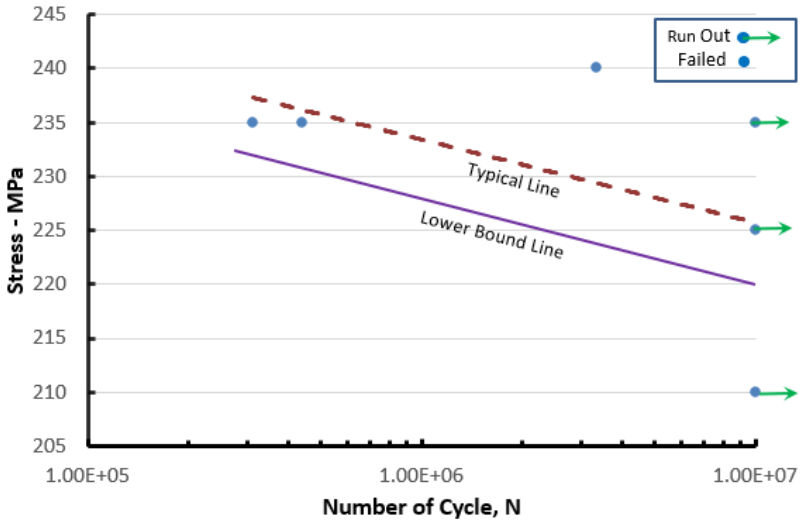


Fig. 9.2. HCF life of LPBF Ti-6Al-4V at ET.

9.1.3 Shaker Table Tests at RT

From the resonance search (frequency sweep) test, the Frequency Response Curve (FRC) in the axial and tangential directions (see Fig. 3.16) are shown in Fig. 9.3(a) and Fig. 9.3(b), respectively. The fundamental vibration mode was observed at 84 Hz, which was the dominant axial bending mode of the bracket. The observed fundamental frequency of 84 Hz does not coincide with the 1st LP rotor speed (48 Hz) and thus the bracket meets the first design requirement. The amplification factor observed was 73, meaning a low damping ratio of 0.68% for the fundamental mode of the bracket assembly.

The second vibration mode, a less responsive mode, observed was at 183 Hz which is the tangential mode of the bracket assembly. Since the excitation given was in the axial direction, but the measured response was in the tangential direction, the inference of damping from the response amplification for the second mode could not be justified.

The subsequent dwell test runs of the bracket with their corresponding acceleration (g) response levels, accrued number of cycles until failure and associated observations are listed in Table 9.1. The marked sequence of failure (numbers 1-5) in the bracket is shown in Fig. 9.4(a).

Based on the observations presented in Table 9.1, the bracket survived for 10^6 cycles at 60g acceleration level without any failure observed in any of the struts or connectors. However, during the test run at 60g, there was an increase in input excitation level observed after 635,866 cycles. The test was stopped at this point and a resonance search test was carried out which indicated a slight drop (of 3 Hz) in fundamental modal frequency of the assembly. A careful visual examination at this point did not show cracking of any of the struts or connectors.

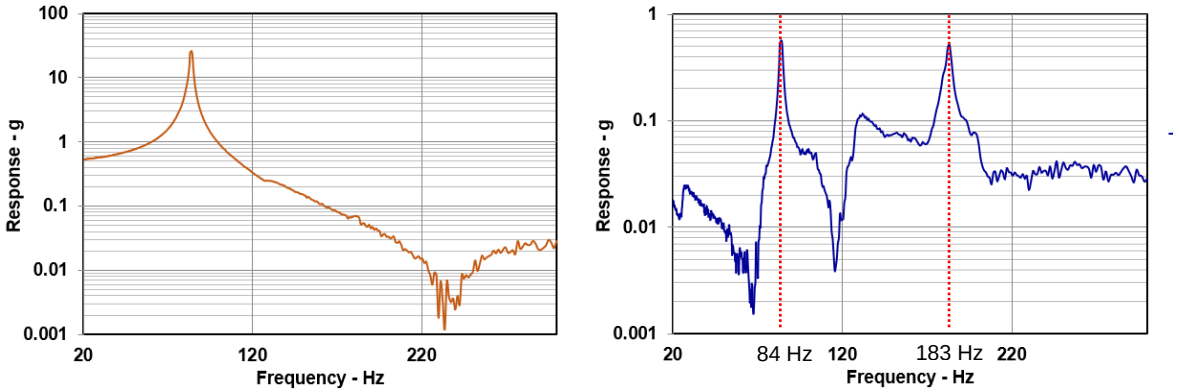


Fig. 9.3. Frequency response curves; (a) FRC in the axial direction showing the fundamental vibration mode at 84 Hz, (b) FRC in the tangential direction with distinct peaks at 84 Hz and 183 Hz (second vibration mode).

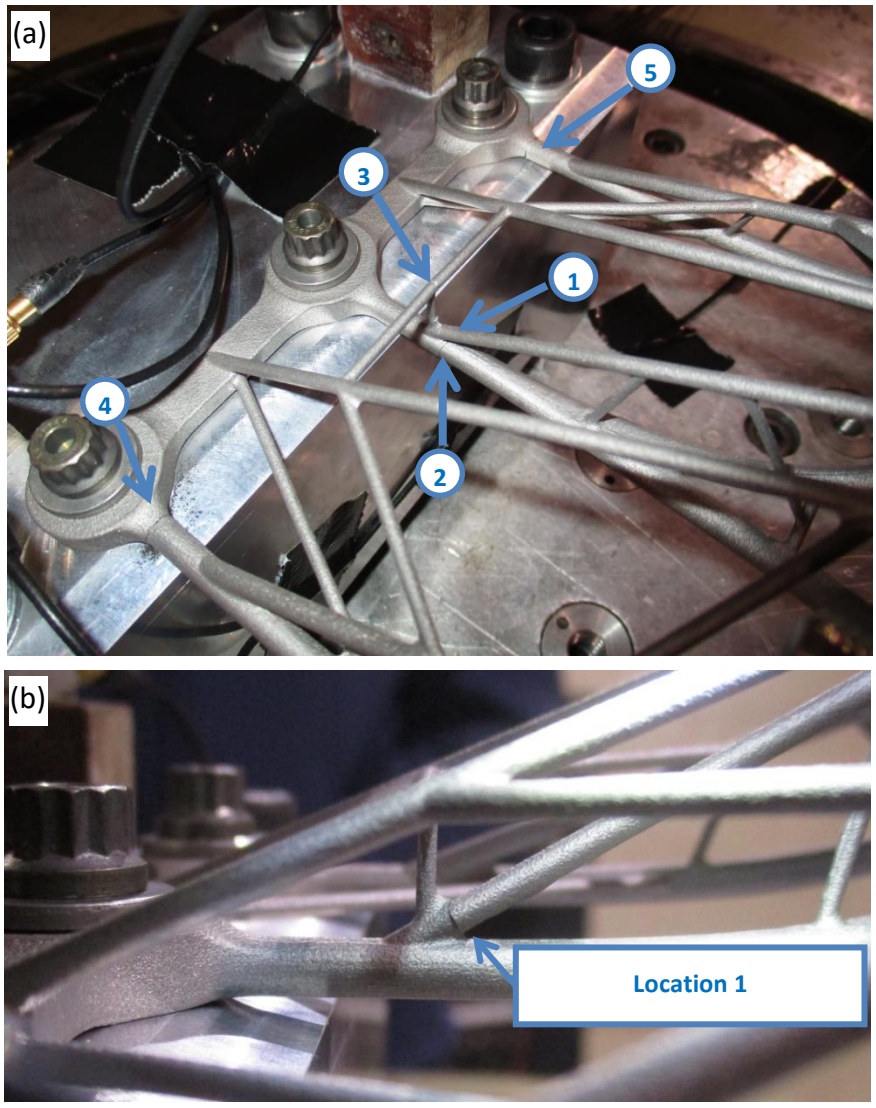


Fig. 9.4. Fracture locations in the bracket: (a) 5 distinctive fractured locations with numbers indicating the sequence of failure, (b) magnified view of first fracture location in the middle diagonal strut.

The dwell test was continued at 81 Hz frequency to complete 1 x 10^6 cycles at 60g. Upon completion of this test run, a detailed inspection was carried out which again did not report any cracks or fractures in any of the struts. In the subsequent test run at 80g, a sequential failure of bracket struts/connectors was observed as listed in Table 9.1 and shown in Fig. 9.4(a). The first failure was in the middle diagonal strut which was found fractured after 2315 cycles at 80g, see Fig. 9.4(b).

Table 9.1. Dwell test runs and corresponding number of cycles to failure

Dwell Test Sequence	Dwell Test Runs Details		Number of Cycles	Observation
	Response Level (g)	Frequency (Hz)		
1	30g	84	172,239	This dwell test was stopped, and the bracket mounting bolts were retightened. No integrity issues were observed.
2	40g	84	1,000,000	No integrity issues were observed.
3	60g	84	635,866	A slight drop in fundamental frequency (to 81Hz) but no cracks/integrity issues were observed.
4	60g	81	364,134	Test was continued to complete 1E6 cycles at 60g dwell. Total cycles at 60g dwell = 1,000,000. No struts were observed to be cracked or fractured.
5	80g	81	2,315	Middle diagonal strut fractured (Location 1, Fig. 9.4(a) and 9.4(b)).
6	80g	79	16,225	Middle main strut fractured (Location 2, Fig. 9.4(a)).
7	80g	77	24,110	Cross connector fractured (Location 3, Fig. 9.4(a)).
8	80g	68	8,269	Right main strut fractured (Location 4, Fig. 9.4(a)). Total cycles at 80g dwell = 50,919 cycles.
9	20g	60	17258	Left main strut fractured (Location 5, Fig. 9.4(a)).

9.2 Discussion

9.2.1 Fractography of Failed Bracket Struts

To understand the failure mechanisms, an analysis of the fracture surfaces of the failed struts was performed, Fig. 9.5(a), Fig. 9.5(c) and Fig. 9.5(e) show the SEM micrographs of fracture surfaces of the three failed strut locations 1, 4 and 5, respectively, depicting the crack initiation sites. Whereas, Fig.

9.5(b), Fig. 9.5(d) and Fig.9.5(f) show the magnified view of fracture surface in the crack propagation sites of locations 1, 4 and 5, respectively. For each of these locations, the cracks seem to have initiated from the surface at a geometric discontinuity feature. At location 1, shown in Fig. 9.5(a), the crack initiation site was characterised by a LOF void. A combination of high stress and the presence of a stress raising feature due to LOF void was the reason for location 1 to become the location of the first failure under HCF loading. With the crack advancement under HCF up to a certain length, the crack propagated faster with every vibration cycle, which is evidenced by the beach marks seen in Fig. 9.5(b). The initiation sites of locations 4 and 5 are shown in Fig. 9.5(c) and Fig. 9.5(e), respectively, where the fracture happened in quick succession at the 80g loading level. As seen in Fig. 9.5(c), micro-cracks at the strut surface were the crack initiation sites at location 4. Under cyclic loading, these initial micro-cracks started to propagate and coalesced with some developing internal cracks, which were mostly of intergranular type, to cause faster fracture in the strut, as seen in Fig. 9.5(d). From Fig. 9.5(e), the multiple initiation sites, due to the small LOF voids at location 5, were found nearer to the surface which, upon crack front advancement, coalesced to cause faster crack advancement in the presence of increasingly higher stresses due to the failure of other struts. Figs 9.5(d) and Fig. 9.5(f) seem to suggest that the higher stresses generated due to the failure of other struts and connectors caused fast fracture and therefore left distinct beach marks at these respective propagation sites. The crack front advancement also caused some delamination or a peeling-off effect in the material at locations 4 and 5, as seen in Fig. 9.5(d) and Fig. 9.5(f), respectively, which continued to make the material weaker with advancing fatigue loading cycles. On applying the $\sqrt{area}$ concept [240] on the defect boundaries identified in Fig. 9.5(a), Fig. 9.5(c) and Fig. 9.5(e), the equivalent defect size was calculated to be 190 μm, 156 μm and 181 μm for location 1, 4 and 5, respectively.

9.2.2 g Load Capability and Compliance against the Design Target

If an excitation happens at 84 Hz, i.e. at the observed fundamental frequency of LPBF bracket, then this could cause high stresses and maximum fatigue damage to the LPBF bracket. But, because the fundamental vibration mode of the LPBF bracket fell outside of the 1st LP shaft speed (48 Hz) of the target engine, the LPBF bracket will not experience engine forcing due to the LP shaft OoB during normal engine operation. The bracket successfully passed the dwell test at 60g level with no integrity issues observed. However, during the test run at the 60g level, there was a slight drop in modal frequency of the bracket assembly at 635,866 cycles. From this observation, it can be assumed that a crack may have initiated in the middle diagonal strut (location 1, Fig. 9.5(b)) during this test run, which later resulted in a fracture during the test run at 80g after 2315 cycles. Therefore, it can safely be inferred that the LPBF bracket has a g load capability of at least 40g for 10^6 cycles. Furthermore, a sequential fracture of bracket struts or connectors with a significant number of cycles between each failure proved that the struts and connectors design LPBF bracket has enough redundancy in the load transfer path, thus meeting the second design requirement. It should also be noted that with every strut or connector failure, the modal frequency of the bracket assembly continued to drop (Table 9.1),

and therefor making it less susceptible to the excitation frequency which caused the fracture due to first resonance/excitation force.

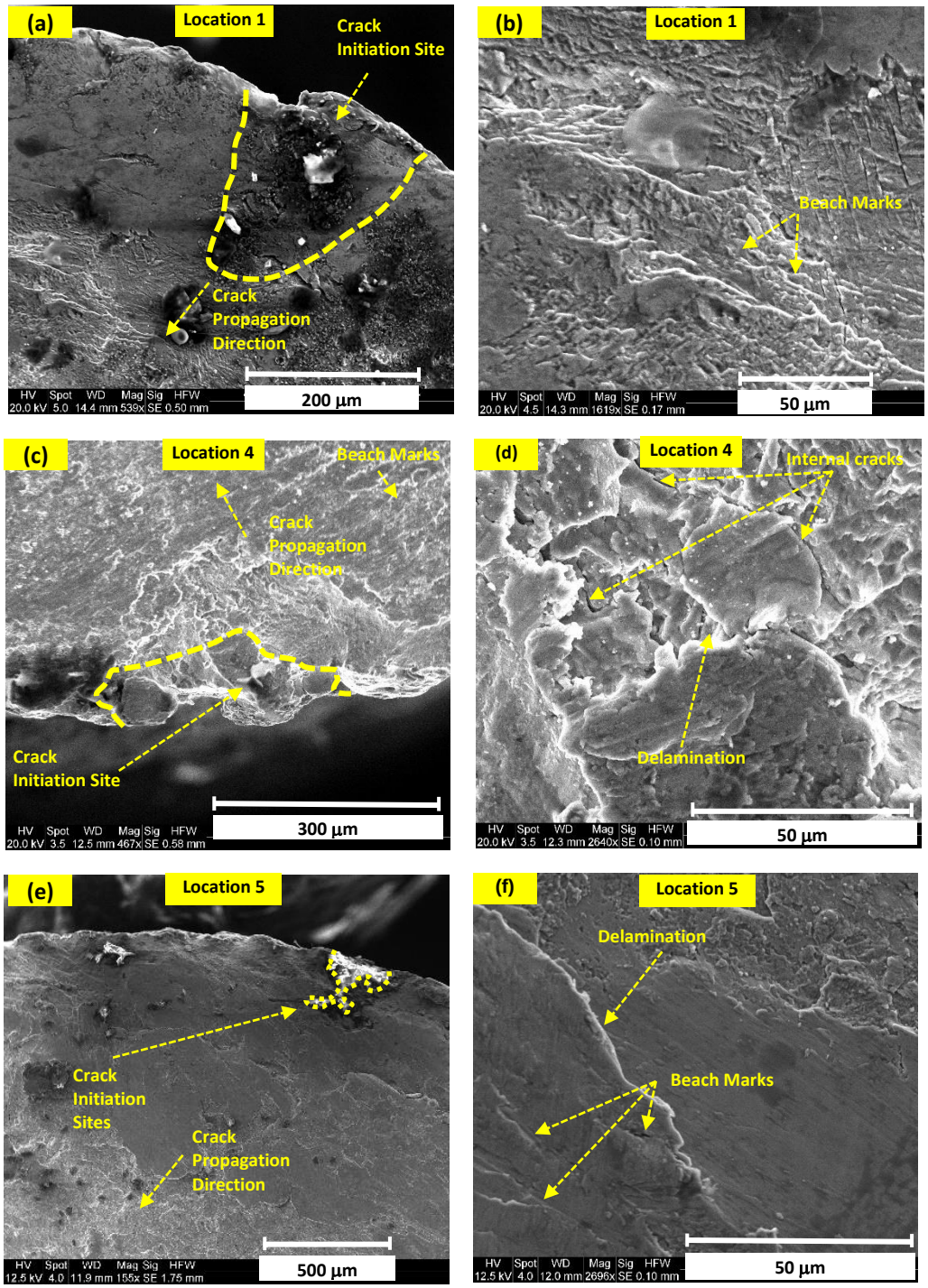


Fig. 9.5. SEM micrographs of the fracture surfaces in the bracket: a) crack initiation site of location 1, b) crack propagation zone of location 1, c) crack initiation site of location 4, d) crack propagation zone of location 4, e) crack initiation site of location 5, and f) crack propagation zone of location 5 (Failure locations in the bracket are shown in Fig. 9.3(a)).

In aeroengine component design, the fatigue endurance limit is typically defined at 10^7 cycles. Since the bracket safely did 635,866 cycles at 60g level before a possible crack initiation point, the g load capability at 10^7 cycles can be estimated using the Miner-Palmgren hypothesis, which includes a fatigue-based power relationship to relate exposure time (cycles) and amplitude and is given by [251]:

$$\frac{t_2}{t_1} = \left[\frac{S_1}{S_2}\right]^m \tag{9.1}$$

Where t_1 is the equivalent test time (635,866 cycles), t_2 is the time at endurance (10^7 cycles), S_1it the capability/severity at test condition (60g), S_2 is the capability/severity at endurance and m is a value based on the slope of the S-N fatigue curve and can be taken as 6 for harmonic excitation [251]. Using equation (9.1), the g load capability (i.e. endurance limit) at 10^7 cycles has been determined as 37.9g.

In summary, the subject bracket demonstrated a very good HCF performance against the target value of 20g despite of a low damping observed for the first mode. More fatigue tests at specimen level and component fatigue tests of this type should be performed in the future to prove the maturity and establish scatter in the fatigue performance of LPBF components. A consistency in the anomalies produced (number, size and distribution) and the link to appropriate NDT techniques to prove this will be required to support the successful implementation of LPBF technology in safety critical applications, it has been shown that the current study is a positive step in this direction.

9.2.3 Micro-Hardness and Fatigue Limit Relationship

The relationship between the micro-hardness and fatigue limit for metals was introduced by Murakami [240], as:

$$\sigma_e = \frac{C\,(VMH+120)}{(\sqrt{area})^{1/6}} \tag{9.2}$$

where VMH is Vickers Micro-Hardness (HV), σ_e is the fatigue limit for R = -1 [177, 240]. The parameter C is the location factor which is taken as either 1.41, 1.43 or 1.56 for surface, sub-surface or internal defects, respectively.

Equation (9.2) holds good for many different conventionally manufactured alloys [177] but the application of it to AM materials has not yet been completely established. In this study, a Strength Knock-Down factor (KDR) is introduced to account for the additional knock-down effect on the fatigue life of LPBF Ti-6Al-4V due to micro-notches at the rough as-built surface and the coalescing effects of propagating multiple cracks from the defects and micro-notches. The modified equation is:

$$\sigma_e = \frac{C\,(VMH+120)\,KDR}{(\sqrt{area})^{1/6}} \tag{9.3}$$

The typical fatigue limit established in this study (at RT) is 208 MPa (Fig. 9.1) and the maximum defect size in a typical LPBF sample, represented by $\sqrt{area}$, is 79 μm (section 5.2.2). Considering this to be a surface defect, for an average micro-hardness of 377 HV (from section 5.2.4), equation (9.3) gives the value of *KDR* = 0.61. Le et al. [246] have reported a similar value for *KDR* of 0.70. This reported value

of *KDR* suggests that the fatigue limit of as-built LPBF Ti-6Al-4V can be 30 – 40 % lower compared to that of fully machined LPBF Ti-6Al-4V.

Because of its detrimental effects on fatigue strength, it is of practical importance to reduce the surface roughness by chemical etching, polishing, machining or SP at least at the critical locations in a LPBF part [68, 245]; however, the loss of material due to a machining operation would reduce the load bearing cross-sectional area, which should be considered in the initial part design. While the combination of surface machining and HIP could improve the fatigue performance by up to 3 times [68], both these operations increase the cost of the end product which, for some end applications, could make the LPBF process unattractive for the manufacture of complex parts in large numbers.

9.2.4 Safe Life Design Curve

The Kitagawa-Takahashi (KT) diagram is a widely adopted mechanism to combine fatigue strength with fracture mechanics [177]. The KT diagram relates the material fatigue limit and threshold SIF range to the defect size and can be used to determine the safe life regime for LPBF Ti-6Al-4V components. The original KT diagram is defined by the region under the two solid orange lines in Fig. 9.6 [177].

The horizontal orange line represents the fatigue limit range (endurance strength) for materials with no or very small sized defects. Based on the data in Fig. 9.1, the minimum fatigue limit, σ_w at 10^7 cycles for R = -1 is 200 MPa. To develop a KT diagram for R = 0.1, the maximum stress fatigue limit at R = 0.1, $Ds_{th,R=0.1}$ can be estimated by:

$$Ds_{th,R=0.1} = \sigma_w \left(\frac{1-R}{2}\right)^{-\eta} \quad (9.4)$$

For Ti-6Al-4V, the exponent η = 0.28 is used for *R* ranging from -0.5 to 0.5 [227]. By using equation (9.4), $Ds_{th,R=0.1}$ = 250 MPa, which is taken as $\Delta\sigma_{th}$ to define the horizontal line in the original KT diagram in Fig. 9.6. The slanting line of the original KT diagram is represented by Ds_{th} (i.e. $\Delta\sigma_{th}$ for the slanting line) as a function of defect or crack size, a, using:

$$Ds_{th} = \frac{DK_{th,L}}{Y\sqrt{\pi(a+a_0)}} \quad (9.5)$$

Where, $DK_{th,L}$ is the SIF range for long cracks, and the value of $DK_{th,L}$ = 3.9 MPa$\sqrt{m}$ (at R = 0.1) from the work of Hu et al. [177] was used. This is acceptable as Hu et al. [177] used the same machine as in this study and had similar powder characteristics to produce their LPBF Ti-6Al-4V samples. *Y* is taken as 0.65 for surface defects and 0.5 for the sub-surface defects [177]. a_0 denotes a fictitious intrinsic crack length below which no effect of defect occurs.

a_0 can be calculated using:

$$a_0 = \frac{1}{\pi}\left(\frac{DK_{th,L}}{Y\,Ds_{th,R=0.1}}\right)^2 \quad (9.6)$$

Given that surface defects have a stronger detrimental effect on the fatigue strength than sub-surface ones, only an original KT diagram for surface defects has been plotted in Fig. 9.6 to get a conservative estimate. The original KT diagram in Fig. 9.6, indicates a defect size of 183 μm as the intersection point of horizontal and slanted orange lines. From the original KT diagram in Fig. 9.6, defects with a size less than 183 μm are not expected to have a detrimental impact on the fatigue life of LPBF Ti-6Al-4V components, but after this size, the fatigue strength reduces with increasing defect size. Conventionally, it is expected that specimens with surface defects with sizes below a threshold value and therefore falling inside KT diagram would have an infinite life.

However, it has been reported that the original KT diagram may be optimistic if used for component design purposes as the original KT diagram is based on the long crack growth behaviour and fails to consider the growth of short cracks. It is well known that short cracks don't experience the plasticity induced closure effects and grow faster than the long cracks [215], and therefore the failure data points could possibly fall inside the original KT diagram in a range of defect sizes [177]. With an increase in crack size, the threshold SIF range increases from an intrinsic DK_{th_eff} to that representative of a long crack $DK_{th,L}$. Chapetti [252] proposed a model which involves the growth of both physically short and long cracks. In the Chapetti formulation, the modified endurance strength $Ds'_{th,R=0.1}$ is determined using equation (9.7) to equation (9.10) [177, 252]:

$$DK_{th,eff} = \chi 10^{-2} E \tag{9.7}$$

$$k = \frac{DK_{th,eff}}{4\, a_{eff} \left(DK_{th,L} - DK_{th,eff}\right)} \tag{9.8}$$

$$a_{eff} = \frac{1}{\pi} \left(\frac{DK_{th,eff}}{Y\, Ds_{th,R=0.1}}\right)^2 \tag{9.9}$$

$$Ds'_{th,R=0.1} = \frac{DK_{th,eff} + \left(DK_{th,L} - DK_{th,eff}\right) * \left[1 - e^{-k\left(a - a_{eff}\right)}\right]}{Y\sqrt{\pi a}} \tag{9.10}$$

where, $DK_{th,eff}$ is the intrinsic threshold SIF, χ is the correction factor and is taken as 1.64 for *E* (Young's modulus) ranging between 25 GPa and 250 GPa [177]. From the tensile test results in this research work, the value of *E* used is 105 GPa. *M* is the microstructural characteristic dimension and is taken as 10 μm for Ti-6Al-4V [252].

The variation of $Ds'_{th,R=0.1}$ as a function of a is denoted by the blue curved line in Fig. 9.6, where it can be seen that the Chapetti curve modifies the original KT diagram only in a specific range of defect size. By merging the Chappeti curve into the original KT diagram at its two extremes, the area under the modified curve represents the safe life regime, defined by the arrows. The safe life regime from the Chapetti curve indicates that the safe defect size has decreased from 183 μm (from original KT diagram) to 36 μm, which is believed to be a more realistic safe life considering the effect of growth of both short and long cracks.

This safe life regime can effectively be used to verify the design of a LPBF Ti-6Al-4V component if the information on defect size (from a CT scan) and stress levels (from a FE analysis) at different locations is known. For example, from Fig. 9.5, the defects size for failure locations 1, 4 and 5 of the bracket are 190, 156 and 181 µm, respectively. Therefore, to avoid the possibility of crack propagation, it must be ensured that the stress range at each of these locations is such that these location points fall inside the safe life regime of Fig. 9.6.

Aeroengine LPBF brackets are expected to operate at ETs, therefore the HCF performances of LPBF brackets should also be investigated at ET as part of future research.

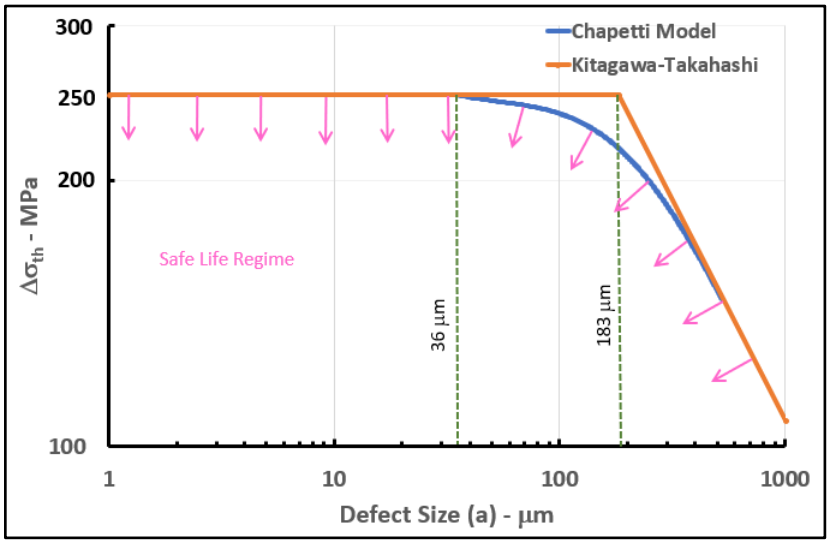


Fig. 9.6. Comparison of original Kitagawa-Takahashi and Chapetti approaches.

9.3 Conclusions

The fatigue performance of a weight optimised LPBF Ti-6Al-4V bracket in the struts and connectors design was studied through shaker table tests and its performance was discussed. The key findings of this study are summarised as below:

- The fundamental vibration mode (84 Hz) of the bracket assembly was remote from the 1st LP shaft speed (48 Hz) of the target aeroengine, meaning that the LPBF bracket would not resonate under LP shaft excitation during engine operation. A low damping of 0.68 % was observed for the fundamental vibration mode of the bracket.
- The g load capability of the bracket of 37.9g was greater than the target value of 20g.
- The bracket was also demonstrated to have enough redundancy in the structural load path. The freedom to design complex shapes with added redundancies in LPBF parts is a reason to adopt LPBF technology in the safety critical load bearing applications.
- LOF voids and micro-cracks present on or near the as-built rough surface can cause significant reduction, up to 40%, in the HCF strength compared to the machined LPBF Ti-6Al-4V equivalent.

- The expected debits in mechanical and fatigue performances of LPBF parts can be overcome through a careful selection of process parameters and by carrying out the design optimisation trade studies for weight reduction opportunities and to uniformly spread the loads in the structural members of the LPBF part.
- The KT diagram, modified using the Chapatti curve, provides a useful link between the material HCF properties and performance of LPBF parts with intrinsic defects.

-----x x x x x x-----

CHAPTER 10

10 Simulation of Fatigue Small Crack Growth

10.1 Introduction

The study of Fatigue Crack Growth (FCG) has received considerable interest for Ti-6Al-4V AM parts [253, 254]; however, understanding and prediction of FCG behaviour in the presence of inherent surface and internal defects still remains a challenge [255].

For parts made of conventional methods of manufacturing, several theoretical methods of predicting fatigue and crack growth have been applied with confidence. But this isn't true for AM parts where the fatigue and fracture studies of AM parts until now are mostly experimentally based and theoretical studies are relatively limited [256]. In a theoretical study by Zhan et al. [256], a Continuum Damage Mechanics (CDM) based method has been proposed to predict the fatigue life of AM parts. In the proposed method a concept of Relative Volumetric Energy Density was introduced which takes into account the laser power, scan speed, hatch spacing and powder layer thickness. Although the material parameters were calibrated using the experimental results, this approach still has shortfalls in the sense that it does not address the effect of specific variations in material microstructure and anisotropic behaviour associated with build direction. In another study by Jones et al. [253], it is suggested that the Hartman-Schijve variant of NASGRO crack growth equation can be utilised to predict the crack growth of AM parts irrespective of specific AM process, power levels and build direction. The calculated crack growth rate (da/dN) vs SIF range (ΔK) curves showed a reasonably good match against the experimentally obtained crack growth curves from various studies. In their calculations, Jones et al. [253] adjusted the values of Effective Lower Fatigue Threshold and Cyclic Fracture Toughness parameters to achieve a good fit against the experimental data. The physical meaning of Effective Lower Fatigue Threshold is not clear, and the values of both these parameters could be different from those obtained from the experiments. Moreover, in both the studies [253, 256] the effect of size, shape and distribution of defects in AM parts have not explicitly been discussed, and therefore use of these two theoretical methods for practical applications is judged to be limited.

From a recently publication, Fomin et al. [257] in their research have proposed a fatigue life assessment model which considers the effects of small cracks for laser welded Ti-6Al-4V butt joints in HCF regime. Their proposed small crack growth model considered the 'cyclic R-curve' as a mean to reflect the reduced threshold value and the crack length dependent $\Delta K_{th}(a)$ for small cracks. They suggested that by using the 'cyclic R-curve', the small crack effects can be analysed by introducing the dependence $\Delta K_{th}(a)$ in the crack growth equation. The construction of 'cyclic R-curve' comes with challenges and, as suggested by Fomin et al. [257] in their simple approach to construct the 'cyclic R-curve' for internal cracks, it requires the knowledge of the *Intrinsic effective threshold SIF* $((\Delta K_{eff})_{th})$ for small cracks, the fatigue endurance limit of the material and the threshold SIF for the long cracks

(ΔK_{th_LC}). Furthermore, to construct a 'cyclic R–curve' there are other approaches outlined by Zerbst et al. [258, 259], which includes the experiment based techniques and also the approaches utilising the KT diagram [260] and the Murakami' model of square root of the area of small surface cracks [240]. All these approaches to construct the 'cyclic R-curves' require extensive test and validation program for AM materials. Due to lack of sufficient test data to develop the 'cyclic R-curve' specific to AM Ti-6Al-4V material it makes the adoption of 'cyclic R-curve' based approach in the small crack growth predictive tools and methods quite challenging.

A crack growth life prediction method for AM parts, which effectively considers the small crack growth behaviour, has been proposed in this chapter. This method includes a detailed FE based crack growth simulation using the ANSYS Separating Morphing and Adaptive Remeshing Technology (SMART) fracture technology. The lifing calculations utilise the modified NASGRO equation and small crack growth data for AM Ti-6AL-4V material reported by Zhai et al. [261]. The predicted *Stress vs Number of cycles* curves are compared against the experimental fatigue test results reported by Gong et al. [254]. Three different test cases were studied and details of analysis together with results, discussion, conclusions and some recommendations are presented.

10.2 Small Crack Growth Behaviour and Modified NASGRO Equation

Cracks are categorised based on the relationship between their dimensions, as shown in Fig. 10.1, such as length (a) and width (w), length of shielding zone (l_s), characteristic microstructural size (m_s) and the plastic zone radius (r_p) [144, 258, 262-264]. A physically small crack (hereafter referred as small crack) is defined as a crack of length in the range between 20 μm – 1 mm [259] and is generally smaller than the typical Non Destructive Testing (NDT) detection limit (< 1 mm) [263, 265-267]. For long cracks, the concept of crack closure was introduced by Elber in 1970 [268]. Closure in the wake of a long crack reduces the effectiveness of the applied crack tip stress intensity, thus retards the crack growth process [258, 267, 269]. For long cracks, the effect of the plastic zone in the applicable 'da/dN vs ΔK' curve is implicit in the SIF dominated stress field [258]. Researchers have studied the closure levels in the small and long crack regimes and suggested that the developing crack wake in small cracks is generally less well developed than in long cracks and therefore the overall plasticity induced crack closure effect is negligible in small crack growth rate [253, 261, 263, 268, 270-271]. As a result, the effective stress ranges for small cracks are greater than that for long cracks under the same applied (far-field, nominal) stress ranges and the crack growth rates of small cracks can be significantly greater than the corresponding rate of the long cracks when characterised in terms of the same driving force or ΔK levels [261, 263, 267-268, 270-271]. The local interaction of cracks with microstructural features, chemical activity at the crack tip and the closure effects at the wake are some of the factors which make the growth behaviour of small and long cracks different, as depicted schematically in the da/dN vs ΔK shown in Fig. 10.2. Furthermore, in the analysis of small crack growth, the use of long crack growth data may lead to overestimates [253, 263]. The analysis of small crack growth remains challenging and complex [261, 263-264, 267, 272], and therefore, a more

detailed understanding of small crack growth behaviour is required, particularly for components fabricated by one of the AM processes [253, 261].

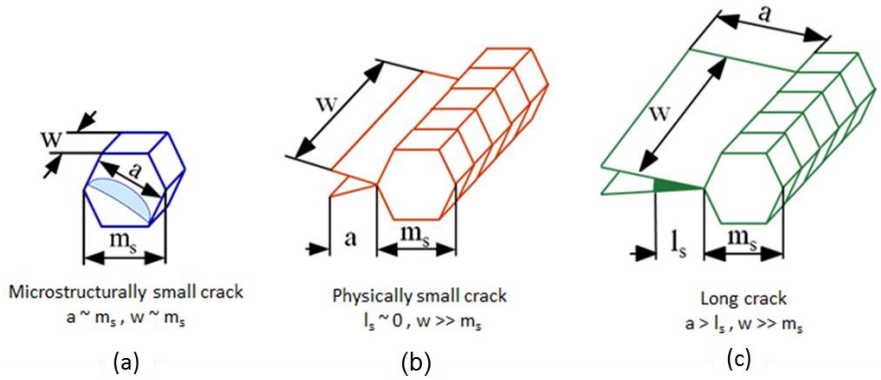


Fig. 10.1. Categorisation of (a) microstructurally small crack, (b) physically small crack, and (c) long crack [261].

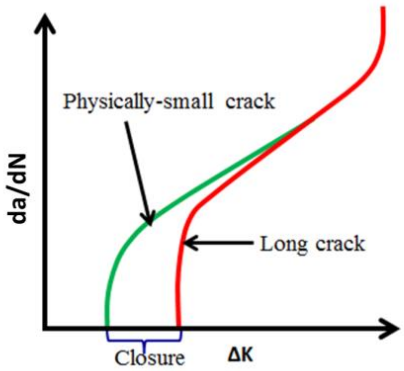


Fig. 10.2. A qualitative comparison of physically small and long crack growth behaviours [261].

The life prediction method for small cracks proposed by Zhang et al. [273] avoids the complex crack growth analysis, and the fatigue life is calculated by directly integrating the crack growth model from the initial crack size (a_i) to the critical crack size (a_c). The method starts with the crack growth equation in the NASGRO code–

$$\frac{da}{dN} = C_1\left(\Delta K_{eff}\right)^{C_2} \frac{\left(1-\frac{\Delta K_{th}}{\Delta K}\right)^{p}}{\left(1-\frac{K_{max}}{K_c}\right)^{q}} \tag{10.1}$$

where, $\frac{da}{dN}$ is the FCG rate, ΔK_{th} is the threshold SIF range, ΔK is the SIF range, K_{max} is the maximum SIF, ΔK_{eff} is the SIF range for small crack, K_c is the critical SIF, and C_1, C_2, p and q are empirically determined materials constants. ΔK_{eff} can be written as a function of the U factor, used to get the equivalent SIF range for small cracks from the SIF range for long cracks, and ΔK:

$$\Delta K_{eff} = U\Delta K \tag{10.2}$$

Also Zhang et al. [273] considered the crack closure effect and introduced the concept of "Intrinsic effective threshold SIF" $(\Delta K_{eff})_{th}$ and treated this as a material property, independent of the stress ratios or experimental techniques. Therefore, the NASGRO equation was modified as below;

$$\frac{da}{dN} = C_1\left(\Delta K_{eff}\right)^{C_2} \frac{\left(1-\frac{\left(\Delta K_{eff}\right)_{th}}{\Delta K_{eff}}\right)^{p}}{\left(1-\frac{Kmax}{K_c}\right)^{q}} \tag{10.3}$$

Since during the fast crack propagation stage, only a very small part of the fatigue life is consumed, equation (10.3) can be simplified to:

$$\frac{da}{dN} = C_1\left(\Delta K_{eff}\right)^{C_2} \left(1-\frac{\left(\Delta K_{eff}\right)_{th}}{\Delta K_{eff}}\right)^{p} \tag{10.4}$$

And then the fatigue life can be calculated as:

$$N = \int_{a_1}^{a_c} \frac{1}{C_1\left(\Delta K_{eff}\right)^{C_2}\left(1-\frac{\left(\Delta K_{eff}\right)_{th}}{\Delta K_{eff}}\right)^{p}} da \tag{10.5}$$

where, the value of *p* is typically assumed to take a value of 2 [253, 274]. ΔK_{eff} is the SIF range for small cracks, and $(\Delta K_{eff})_{th}$ is the threshold SIF range for small cracks.

10.3 FE Based Crack Growth Simulation and Lifing Calculation

The crack growth assessment of an AM part with inherent defects can be carried out using a FE based simulation approach. The previously existing FE simulation approaches for crack growth were found to be quite complicated and required manual meshing and re-meshing to calculate crack growth. Engineers had to continuously tweak the mesh involving 'hexahedron' and 'wedge' elements to capture the crack front, thus a simulation consumed a great amount of time (up to several days). Furthermore, an ideal mesh using only hexahedron (hereafter referred as Hex) elements was often not possible and required simplification of the geometry of the crack to fit a Hex-only mesh pattern, resulting in loss of fidelity in the crack growth analysis [275].

The crack growth simulation in this study was carried out using the ANSYS SMART fracture technology which was recently integrated within the ANSYS package v19.1. The SMART simulation of crack propagation was based on Paris' Law using all-Tetrahedral (Tet) mesh for the crack fronts, where the mesh was updated automatically as the crack front changed due to crack growth. This achieves the same high-fidelity results as from a simulation with the ideal Hex mesh configuration and the rate of crack growth and the number of cycles to failure under fatigue loading are predicted [275]. The Ansys SMART crack growth simulation technology enables automatic remeshing of the crack tip regions during a crack tip extension simulation and is used to predict the SIFs using computational methods. The determination of crack growth is based on contour integration, which allows the evaluation of integrals along certain paths, to obtain fracture mechanics parameters such as the J Integral (J) and then the stress intensity factor (K). The Ansys SMART crack growth technology allows the calculation of such integrals along paths encircling a crack front [275].

10.3.1 Source of Material, Additive Process and Experimental Data

For the purpose of the current study, the test results reported by Gong et al. [254] were used. The material used to build the specimens was EOS Ti-6Al-4V, the max impurity concentration of the powder was as per ASTM F1472 [276]. The particle size of the powder was normally distributed with a mean of 38 µm and ranged from 25 µm to 53 µm [254]. The test specimens were built with their longitudinal axis aligned vertically using the EOS M270 DMLS. The processing parameters included; Laser power 170 W, scan speed 1250 mm/s, hatch spacing 100 µm and layer thickness 30 µm.

The test results for the following two types of specimens were considered in this study:

- **Type 1**: No internal designed defect,
- **Type 2**: With internal designed defect of cylindrical shape

The CAD file for specimen with an internal designed defect contained an internal void of cylindrical shape, as shown in Fig. 10.3 [254].

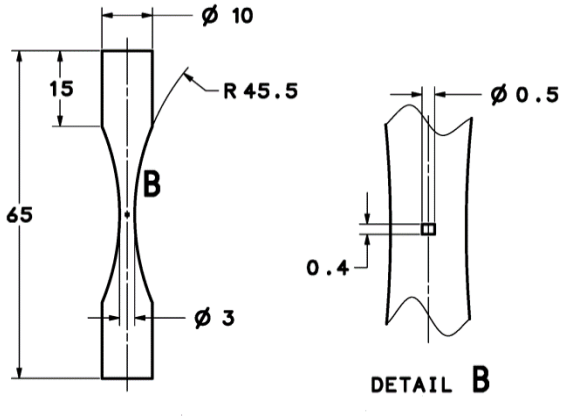


Fig. 10.3. Fatigue specimen dimensions (mm) and designed cylindrical defect in the specimen in detail B [254].

For the purpose of this study, the following 3 analysis cases were studied (Fig. 10.4):

Case A: No internal designed defect: Crack initiating at the surface

Case B: With internal designed defect of cylindrical shape: Crack initiating at the surface

Case C: With internal designed defect of cylindrical shape: Crack initiating at the cylindrical defect

Both Type 1 and Type 2 specimens were stress relieved using HT at 650 °C for 4 hours in an argon environment followed by the FC to RT. Light SB was used to remove the adhered powder particles from the surface of the specimens. The fatigue tests were carried out using the sinusoidal load at R ratio of 0.1, with a frequency of 50 Hz and at different stress levels [254].

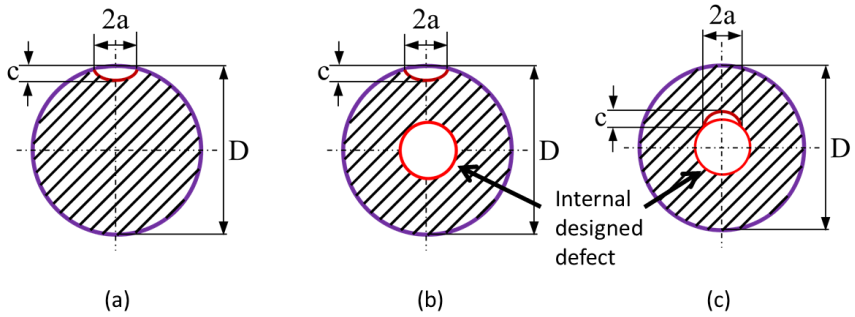


Fig. 10.4. Ansys SMART crack analysis: (a) analysis Case A, (b) analysis Case B and (c) analysis Case C, an illustration (not to scale) [261].

10.3.2 Small Crack Growth Data

Crack closure is a major mechanism at the near threshold part of the crack growth curve [253, 263, 264, 267]; therefore, reliable closure free crack growth data is needed to accurately predict small crack growth [269]. ASTM E647-15 [277] introduced the Adjusted Compliance Ratio (ACR) method to determine the closure free da/dN vs ΔK relationship [261, 274], and Donald et al. [269] provided the detailed steps to determine ACR. Furthermore, the fatigue crack propagation threshold, ΔK_{th}, is a crucial parameter in the framework of a damage tolerant analysis and design [258, 267, 272]. As illustrated in Fig. 10.2, small fatigue cracks grow at a SIF range below the long crack fatigue threshold [144, 261, 263, 267, 270-271] and the fatigue crack propagation threshold (ΔK_{th}) associated with small cracks is less than that for long cracks [253, 263].

Small crack growth data, corrected for crack closure effects from long crack growth data, for Ti-6AL-4V AM material specimens, manufactured using Laser Engineering Net Shaping (LENS) from the work of Zhai et al. [261] was used in this work. While there are possible differences between LENS and DMLS AM, both processes use a laser heat source and a similar build environment and, therefore, the assumption is made that the specimens are likely to have similar microstructure and defect distributions for the purpose of this work.

The test specimens from Zhai et al. [261] were built using the low and high-power levels and both as-built and heat-treated specimens were tested. The long crack growth data from the Low Power Heat Treated Vertical (LPHT-V) propagation specimen was used in the SMART crack growth analysis. The use of LPHT-H data was ruled out due to weakening effects of LOF and irregular shaped defects which are highly possible at low power and low energy density [40, 42]. Zhai et al. [261] also provided the crack growth data for small cracks, which was produced after applying the ACR technique on the long crack growth data [269].

In order to obtain the *U* factor (equation (10.2)), the Paris' parameters and threshold SIF values (ΔK_{th}) for long and small FCG rates, presented in Table 10.1, were used to first determine the idealised *da/dN vs* ΔK FCG curves for small and long cracks, as shown in Fig. 10.5(a), and then the *U vs* ΔK curve

was calculated using equation (10.2) for each value of ΔK, Fig. 10.5(b). In equation (10.2), ΔK_{eff} is the maximum SIF range for a small crack.

Table 10.1. Long and Small crack growth Data (@Low Power + Heat Treatment) - LPHT-V [261].

Parameters	Long Crack Growth Data	Small Crack Growth Data
ΔK_{th} (MPa$\sqrt{m}$)	2.9	2.4
ΔK_{FT} (MPa$\sqrt{m}$)	46.7	-
C_1 (m/(cycle $\times$ (MPa$\sqrt{m}$)^{C_2}))	1.4×10^{-12}	2.6×10^{-12}
C_2	4.0	3.9

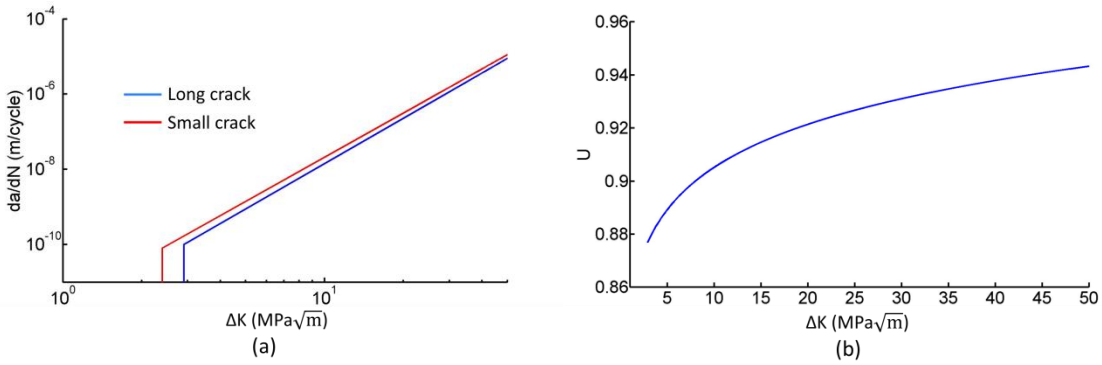


Fig. 10.5. (a) Idealised long and small and FCG curves, (b) U vs ΔK curve.

10.3.3 FE Based Crack Growth Simulation

Crack growth simulations were carried out using the geometry of fatigue specimens shown in Fig. 10.3. To reduce the overall size of the FE model, to improve computational efficiency, only the uniform cylindrical section was used for the simulation and two different types of defect geometry were considered.

Type 1: With no internal designed defect (for analysis Case A) and

Type 2: With internally designed defect of cylindrical shape (for analysis Cases B and C).

The Young's modulus and Poisson's ratio for Ti-6Al-4V were taken as 110 GPa and 0.3, respectively [278].

The FE mesh was generated using the 'Tet' elements on the cylindrical sub-scale model. Within the ANSYS SMART fracture tool, a semi-elliptical crack of the desired size was inserted on the surface (for analysis Cases A (Fig. 10.4(a)) and B (Fig. 10.4(b)) or on the surface of the cylindrical defect (for analysis Case C (Fig. 10.4(c)). A typical body controlled coarse mesh size of ~0.5 mm was assigned to the main body of the sub-scale model. The mesh was refined at the inserted crack front, which is typically five times finer than the mesh in the main body of the specimen. The mesh sensitivity study has shown that such a mesh size ensures contour independence of calculated J-integral. The mesh

contour number for J-integral calculation is set to 5 for all simulations. This is very important to avoid analysis errors and to obtain accurate fracture predictions. A typical mesh is shown in Fig. 10.6.

The ANSYS SMART crack growth analyses were run at a load ratio (R) of 0.1, in accordance with the experimental testing [254], with one end of the specimen assumed as fixed and the cyclic load applied at the other end, see Fig. 10.7. Analyses were run with different initial crack sizes and under different load levels for each of the analysis cases studied. Even though the initial crack size assumed was the size of a small crack, the simulation was run using the LEFM approach using the crack growth parameters for long crack.

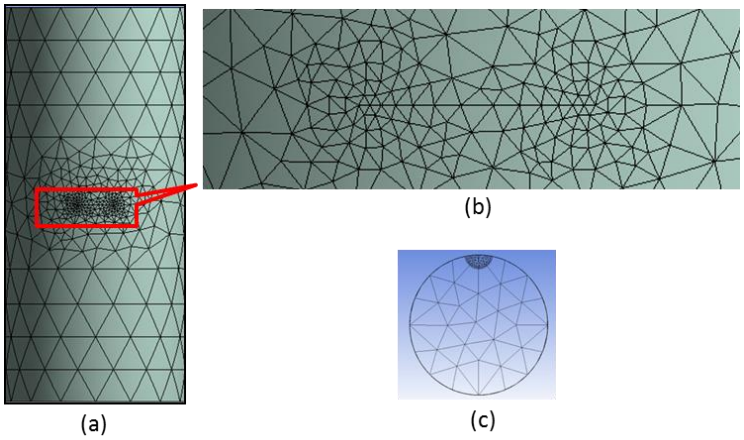


Fig. 10.6. Finite element mesh and inserted surface crack (Case A): (a) FE mesh and inserted surface crack, (b) Front view, (c) Top view.

For the three cases studied, the SMART crack growth analyses were run for different initial defect sizes (2a) as shown in Table 10.2. This was due to the fact that defect size could vary from between specimen to specimen. For each of the initial crack sizes, the SMART crack growth analyses were run for multiple sub-steps until fracture.

Table 10.2. Initial Defect Sizes Assumed for Three Analysis Cases

Analysis Case	Initial Defect Sizes - 2a (mm)
Case A	0.046, 0.07, 0.1, 0.17
Case B	0.1, 0.17
Case C	0.04, 0.06

From the SMART crack growth analysis, the results of LEFM ΔK *(SIF range)* and *da (crack extension)* against the *time steps* were extracted for different initial crack sizes and loads. Using these results, the corrected small crack growth life from AM specimens was then calculated.



Fig. 10.7. SMART crack growth analysis, boundary condition and loading application.

10.3.4 Small Crack Growth Lifing Calculation

An overview of the methodology for the lifing calculation is presented in Fig. 10.8.

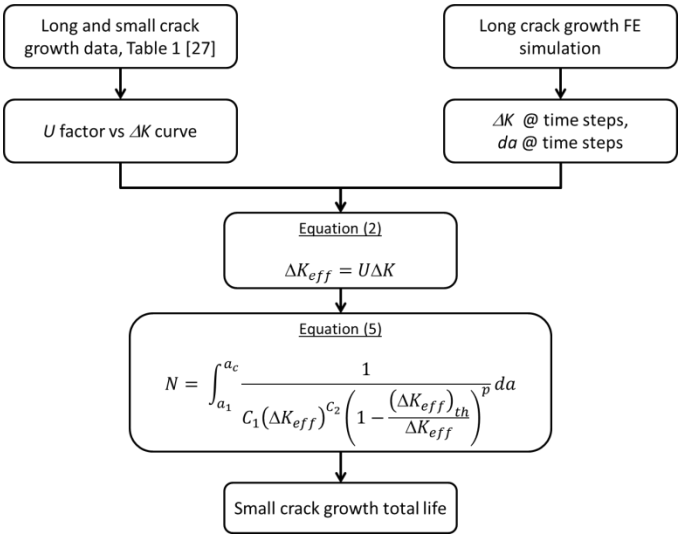


Fig. 10.8. Small crack lifing calculation steps.

The steps followed to calculate the total life from a small crack to fracture can be summarised as follows:

i. Run the LEFM analysis using the SMART simulation using the crack growth data for long crack and for different crack sizes and cyclic load values chosen for the SMART crack growth analysis.

ii. The idealised crack propagation rates for long and small cracks were generated using the fracture data in Table 10.1. These idealised FCG curves are shown in Fig. 10.5(a).

iii. The *U* factor was obtained against increasing values of ΔK using the idealised FCG curves for long and small cracks (see Fig. 10.5(a)) and using the equation below;

$$U = \frac{\Delta K_{eff}}{\Delta K}$$

where ΔK and ΔK_{eff} are the SIF range for long crack and small cracks respectively. The *U* vs ΔK curve was obtained as shown in Fig. 10.5(b). A polynomial regression line and associated fitting parameters were obtained for the subsequent life cycle calculations.

iv. For each time step, using the predicted SIF range (Δ*K*) and crack extension values (*da*) from the SMART simulation (from Step (i)), the crack growth data presented in Table 10.1 and *U* factors (from step iii) as input to equation (10.5), the total number of cycles to fast fracture were calculated.

v. Analysis calculations were repeated for different initial crack sizes and different applied load values and graphs of *Stress vs Number of Cycles* were plotted for each of the analysis cases.

10.4 Results and Discussion

Predicted analysis results (i.e *Stress vs Number of Cycles*) for each of the analysis cases were compared against the fatigue test data presented by Gong et al. [254].

10.4.1 Case A: No Internal Designed Defect, Crack Initiating at the Surface

As shown in Table 10.2, for Case A, the SMART crack growth analyses were run for the initial defect sizes (2a) of 0.046 mm, 0.07 mm, 0.1 mm and 0.170 mm. From the analysis with 0.1 mm initial crack size, the plots of maximum stress intensity at sub-steps 1, 10 and 25 are illustrated in Fig. 10.9, which illustrates a propagating crack and corresponding change in maximum stress intensity.

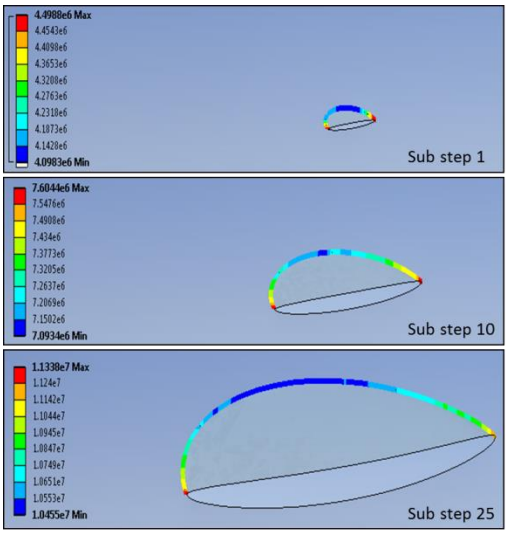


Fig. 10.9. Small crack lifing calculation steps.

Fig. 10.10 shows predicted crack sizes for sub-steps 1, 10 and 25. During the simulation, auto-refinement of the mesh around and at the crack front takes place at each incremental sub-step (see Fig. 10.10). Fig. 10.11 shows the deformation at the final sub-step of the crack growth and corresponding maximum SIF approaching the fracture toughness.

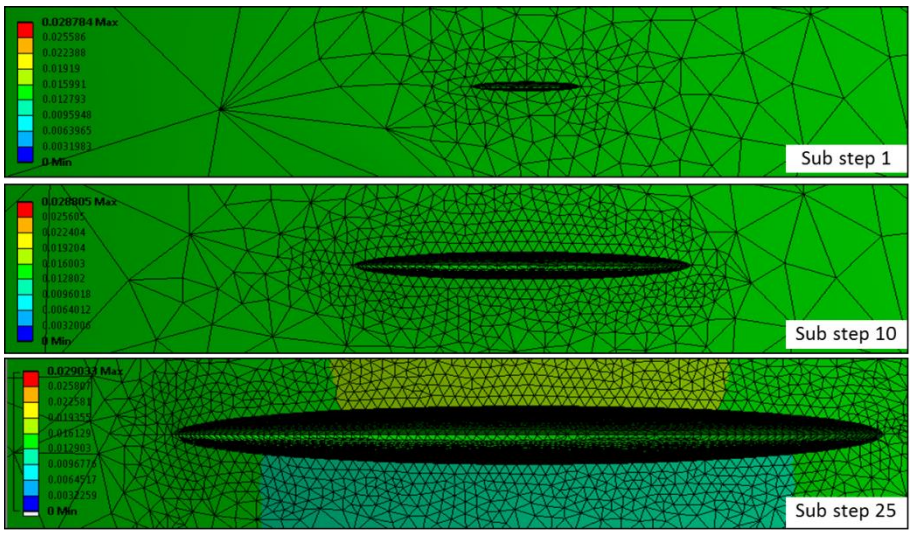


Fig. 10.10. Crack propagation and auto mesh refinement around the propagating crack.

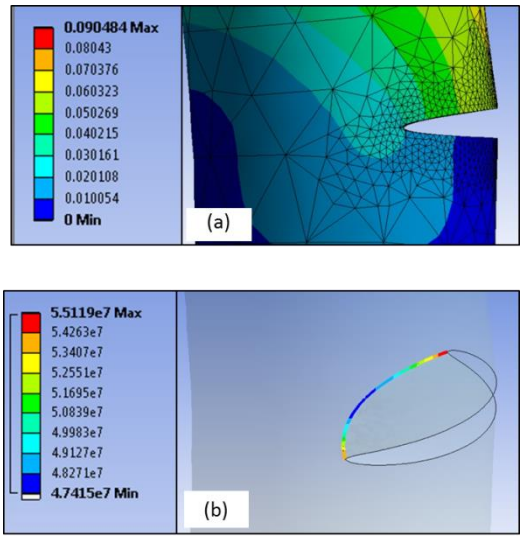


Fig. 10.11. Contour plots: (a) total deformation (mm) and (b) maximum SIF (Pa.√m) at final sub-step.

The predicted lifing curves for small crack growth calculations were compared against the fatigue test data of [254], see Fig. 10.12. Though the predicted lifing curve for 0.1 mm initial defect size appears to be following the three failure points observed in experiments [254], it can be seen that all the experimentally observed failure points fall between the predicted curves for the initial defect of 0.1 mm and 0.170 mm in size.

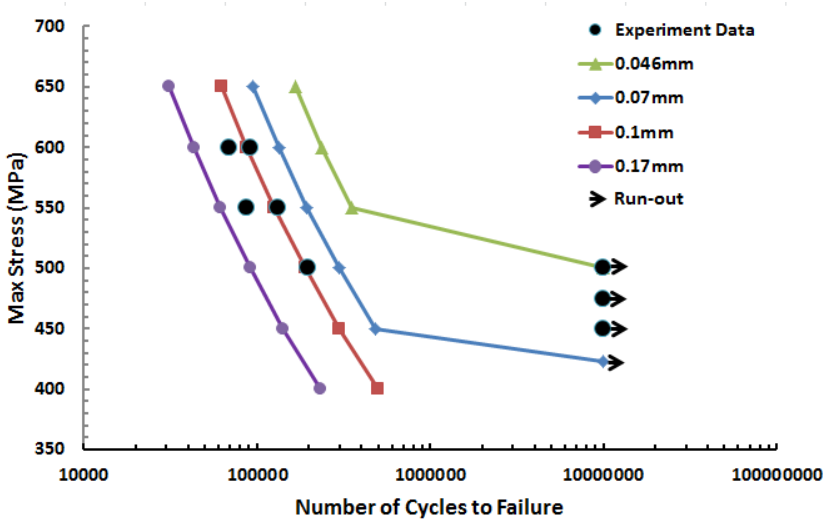


Fig. 10.12. SMART crack growth analysis predictions vs experimental results - Case A.

The rough surface of the as-built gauge section is an ideal site for the stress raising features which adversely affect the fatigue life of the specimen [254]. Cracks usually initiate at one of the sites with highest stress concentration from the surface, then propagate through the section before final fracture occurs. The fractographic image from the experiments for Case A [254], see Fig. 10.13, was reviewed which suggested that the initial size of the defect (2a) was ~0.124 mm.

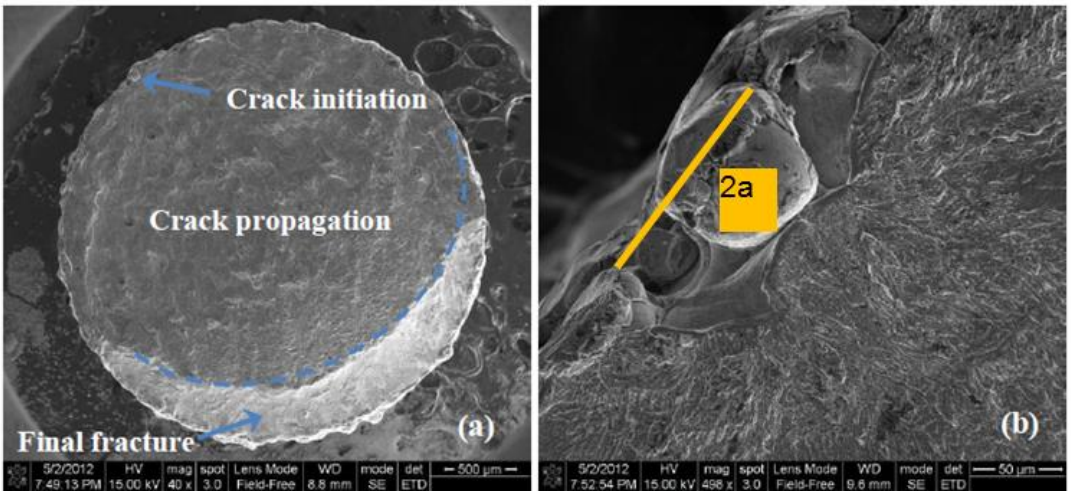


Fig. 10.13. Fractographic images from experiments - Case A [254].

Since the defect size of 0.124 mm comes from a single specimen, the value of 0.124 mm can be treated as an indicative value of the initial defect size on the surface of the specimen. Also, one can

expect a reasonable amount of variation in initial defect size if the fractographic measurements were taken on more than one specimen and the defect size from the fractographic image is an estimation only and not a precise measurement. The small crack growth analysis results for the initial defect sizes of 0.1 mm and 0.170 mm, and its comparison with the test results for the cracks initiating from the surface of the specimens [254] suggest that the analysis predictions are in good agreement with the experimental results, and experimental data is bounded by the crack growth predictions for 0.1 - 0.17 mm initial defects sizes.

For the test points indicating run-outs, no images of the fracture surface were provided by Gong et al. [254]; however, since these specimens did not fail, it can be assumed that the initial defects would have been of size less than 0.1 mm. The runout test points are well bounded by the predicted curves for the defect sizes of 0.046 mm and 0.07 mm (Fig. 10.12).

10.4.2 Case B: With Internal Designed Defect of Cylindrical Shape, Crack Initiating at the Surface

As discussed previously in Table 10.2, for analysis Case B, the small crack growth lifing calculations were performed for initial defect sizes of 0.1 mm and 0.17 mm at various stress levels until final fracture. The results were compared against the experimental results in Fig. 10.14. The predicted lifing curve with an initial defect size of 0.17 mm size follows the test failure points [254]. The analysis for an initial defect size of 0.1 mm predicted a greater number of cycles until fracture against all four experimentally observed failure points.

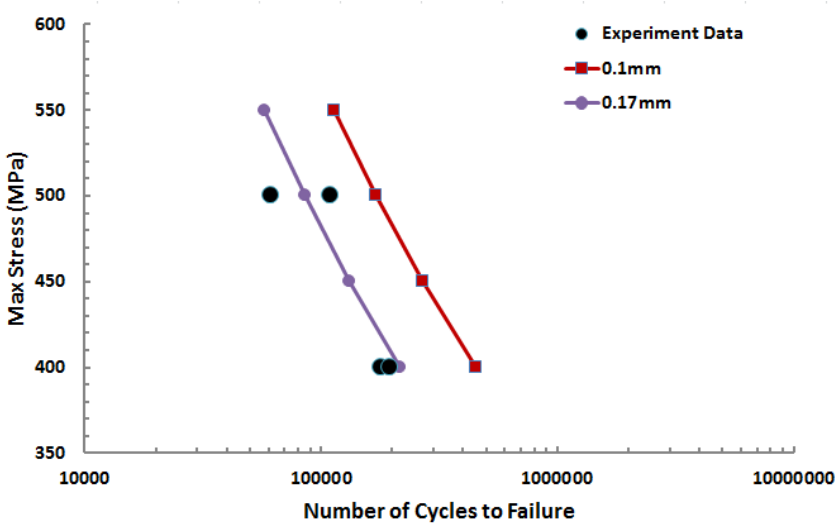


Fig. 10.14. SMART crack growth analysis predictions vs experimental results - Case B.

Fractographic images were not provided by Gong et al. [254] for the tests corresponding to analysis Case B, so the best estimate of size of a surface defect comes from Fig. 10.13, which indicates the surface defect of 0.124 mm size, which is within the bounds of 0.1 mm and 0.17 mm for initial defect

size, analysed for Case B. Also, the four data points are limited in number and may not represent the whole population of specimens with regards to their surface roughness and size of the initial defect.

Furthermore, in the specimens with an internal designed defect, it is likely that a crack may also simultaneously initiate from the internal designed defect, propagate in the direction opposite to the propagating crack, which was initiated from the surface, and subsequently the two cracks merge into each other. If this happens then it will result in a reduction in the life to fracture and may provide a better match between the predictions for an initial defect size of 0.1 mm and the test data; however, at this point, this remains a hypothesis only without any supporting evidence. Also, a simulation of simultaneously propagating multiple cracks is not possible within the current Ansys SMART simulation.

10.4.3 Case C: With Internal Designed Defect of Cylindrical Shape, Crack Initiating at the Cylindrical Defect

For analysis Case C, crack initiation from the surface of the internal designed defect boundaries was simulated. The stress concentrations around the internal defect and rough surface of the designed defect were assumed to be the cause of crack initiation. It is expected that the designed cylindrical defect would have a detrimental effect on the fatigue life of the specimen because the applied stress will be increased in vicinity of the defect [254]. From the fractographic image of the fracture surface shown in Fig. 10.15, the initial defect size was approximated as ~0.046 mm.

The small crack growth analysis was performed for the initial defect sizes of 0.04 mm and 0.06 mm at stress levels ranging from 400 MPa to 550 MPa until final fracture and the analysis results were compared against the test results [254] for Case C in Fig. 10.16. The predicted *Stress vs Number of Cycles* curve with an initial defect size of 0.04 mm is in good agreement with experimental results. The differences between predictions and test results at 400 MPa and 500 MPa could be due to the possible variation in the size of defects in different specimens tested. As it can be seen in Fig. 10.16, the small crack growth is very sensitive to the initial defect size, where a small change in initial defect size significantly affects the total crack growth life. It is due to the stress concentration effect of internally designed defect.

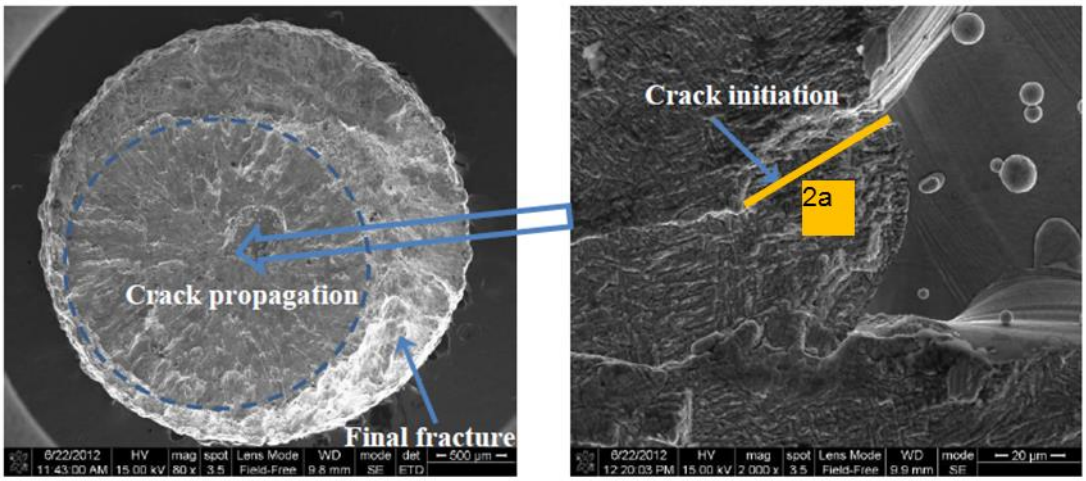


Fig. 10.15. Fractographic surface of specimens with internal designed defect of cylindrical shape [254] (Crack initiated from cylindrical defect).

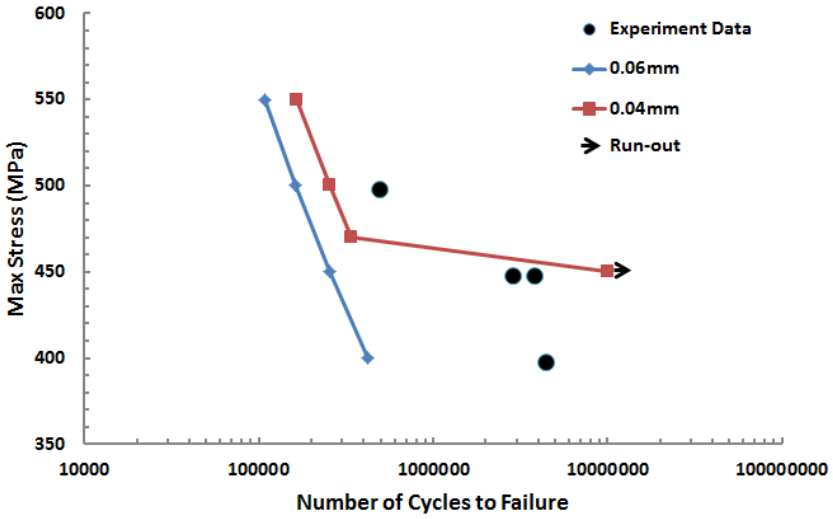


Fig. 10.16. SMART crack growth analysis predictions vs experimental results - Case C.

For the three cases studied in this paper, the small crack growth model used has shown a reasonably good comparison against the test data. The observed differences between the predictions and experimental results could be attributed to;

- In the short crack model introduced in this study although the factor U changes with increasing ΔK, the value of the threshold SIF range for small cracks $(\Delta K_{eff})_{th}$ used in this study was obtained using the ACR correction method in [261] and used as a constant value in the current study i.e. doesn't vary with increasing crack length. Based on the conclusions

made by Fomin et al. [257], their proposed small crack growth model takes into account the varying $(\Delta K_{eff})_{th}$ as a function of crack length '2a' and seems to be more accurate.

- For AM Ti-6AL-4V model we haven't got the sufficient test data to develop the 'cyclic R-curve' and it should be looked into as part of the future research study. This will require a carefully planned extensive and sophisticated test program to study the parameters which affect the small crack growth behaviour of AM Ti-6Al-4V.
- The p value used in equation (10.4) was read across from other similar studies [253, 274]. A more accurate p value is required via the HCF tests on AM Ti-6Al-4V material. Fomin et al. [257] have derived the p value by performing a regression analysis on the weld fatigue test data in HCF regime. This is expected to improve the fatigue life predictions in the HCF regime [257].
- The size of initial defect assumed has a direct impact on the small crack growth life predictions and a precise measurement of the defects' size in an AM material remains a challenge. The more advanced scanning techniques, such as X-Ray CT scan, and post processing techniques should be used to characterise the defect sizes which need to be considered to assess the life of the AM part using the predictive models for small crack growth behaviour.

10.5 Conclusions

The small crack growth life prediction method proposed in this chapter includes a detailed FE based crack growth simulation and lifing calculations using the modified NASGRO equation and small crack growth data.

The small crack growth predictions for the three cases analysed are in reasonably good agreement with the test results [254] for Laser AM specimens made of Ti-6Al-4V material. This suggests that the proposed method can be used to predict the FCG life of AM parts with small defects present.

The difference between the predicted *Stress vs Number of Cycle* curves and the test data points can be attributed to; (i) lack of a precise measurement of defects' size in the test specimen, and (ii) the expected variation in FCG properties due to AM processes, build parameters and build orientations.

The small defects in an AM part operating in cyclic loading environment can start to propagate immediately as soon as the crack driving force (ΔK) is big enough at the applied stress levels, ignoring the initiation life.

The correlation between the predictions and test results gives confidence that the modified NASGRO equation can be used to assess the small crack growth life of an AM parts for aerospace applications where the fatigue effects of cyclic loading can be quite significant.

For an accurate simulation and prediction of defect tolerant life of AM parts the followings important considerations need to be understood and applied in the analysis:

- Size, shape, density and distribution of defects together with AM process and microstructure specific small crack growth data are the key parameters needed to be understood in detail.

- For the small crack growth lifing calculations, although the long crack growth data corrected using the ACR approach can be used but the emphasis should also be to build a robust dataset of small crack growth rates for various materials and load conditions. Furthermore, the fatigue and crack growth experimental dataset for AM built materials is required to develop the AM material specific 'cyclic R-curve' to use in the small crack growth model.
- Accuracy of FCG simulation i.e. crack geometry, location, boundary condition, loading and material property are other important factors which should be measured and defined accurately in the analysis simulation. A robust training plan and standardisation of analysis method will be required to achieve consistent and accurate results.

-----x x x x x x-----

CHAPTER 11

11 Conclusions and Future Work

11.1 Conclusions

Based on the different studies presented in Chapter 4 to Chapter 10, the following are key conclusions:

- For EPBF Ti-6Al-4V, the tensile strength values were observed to be higher than for the conventionally manufactured annealed Ti-6Al-4V bar [136], owing to its microstructure with α laths in prior β boundaries.
- The surface finish and presence of defects reduce the material ductility of as-built EPBF Ti-6Al-4V at ETs. Orientation of defects and columnar β grains in the microstructure of PBF Ti-6Al-4V cause anisotropy in material properties. The difference in microstructure (α_{GB} and prior columnar β grains) and orientation of voids with respect to the loading direction are responsible to cause anisotropy in mechanical strength of EPBF Ti-6Al-4V alloy.
- The tensile strength values of LPBF Ti-6Al-4V were higher, owing to its fine microstructure with α' needles in high aspect ratio, but the ductility was lower than the ductility of conventionally manufactured annealed Ti-6Al-4V bar [136].
- The microstructure of both LPBF and EPBF Ti-6Al-4V contained only a very small amount β phase. The pore volume fraction was observed to be < 1% for EPBF Ti-6Al-4V and < < 0.01% for LPBF Ti-6Al-4V. The observed differences in pore volume fraction and β phase present causes difference in material ductility between EPBF and LPBF Ti-6Al-4V.
- Resistance to the motion of dislocations to cross the energy barrier reduces with increase in temperature, which increases the mobility of dislocations, vacancies and slip systems and thus reducing the material tensile strengths at ETs. At ETs, the dislocation slip mechanism dominates the deformation, making the deformation easier at ET than at RT and thereby improving ductility.
- Due to the lower powder size/lower layer thickness used in the LPBF process, the surface roughness of LPBF Ti-6Al-4V was found to be better than that of EPBF Ti-6Al-4V.
- The material softening under cyclic loading was observed for LPBF Ti-6Al-4V, and amount of softening was higher at ET which was due to higher interaction of dislocations and faster crack growth seen under tensile part of the cyclic loading under cyclic tests at ET.
- During cyclic deformation, evolution of dislocation substructures takes place to subsequently produce LABs inside the prior α' grains. The LABs progressively lead to nucleation and coalescence of voids with fatigue cycles, eventually leading to fracture. An ease of dislocation annihilation and subsequent recovery of dislocations happens, which causes the free dislocation density to increase, resulting into cyclic softening. Also, with higher test SRE, the free dislocation density increases.

- The LPBF bracket in struts and connectors design successfully exceeded the intended 3000 cycles. The failures in the bracket were observed only under the cyclic tests at extreme loading condition. The failure observed in the bracket was progressive in nature and happened at increasing number of discrete cycles and at different locations.
- From the observed modal responses, the bracket successfully avoided the 1st LP shaft speed of the target aeroengine. The predicted g load capability of the bracket was 37.9g which was greater than the targeted capability value of 20g.
- The bracket demonstrated redundancies in the load path under both LCF and HCF tests due to its particular design with multiple load-carrying struts. The surface locations where LOF voids, pores or micro-cracks are present in the bracket struts were the likely sites for crack initiation if they coincide with high stress locations.
- The KT diagram, modified using the Chapatti curve, provides a useful link between the material HCF properties and performance of LPBF parts with intrinsic defects.
- The small defects in an AM part operating in cyclic loading environment can start to propagate immediately as soon as the crack driving force (ΔK) is big enough at the applied stress levels, ignoring the initiation life, needing a fracture mechanics based life prediction method to assess the effect of critical defect.
- The proposed method to predict crack growth life which considers the small crack growth behaviour includes a Finite Element based crack growth simulation and uses the modified NASGRO equation together with small crack growth data.
- A satisfactory correlation was achieved between the predictions and test results which gave the confidence that the modified NASGRO equation can be used to assess the life of AM parts with inherent small defects in it for aerospace applications where the effect of cyclic loading can be quite significant.

A patent has been filed to claim the peculiar design of the AM bracket in struts and connectors design discussed under this research study for its LCF and HCF performances.

11.2 Future Work

The present research work has discussed in detail the mechanical properties and fatigue performance of PBF Ti-6Al-4V. The current ALM strategy of R-R is towards exploring and adopting the LPBF technology for its future engine components. To support R-R with their strategic direction on ALM technology, although the initially mechanical testing was performed on EBPF Ti-6Al-4V material, the main focus of this research study has been to explore mechanical and fatigue performances of LPBF Ti-6Al-4V at specimen and at component levels. Since, the ALM technology is still being developed to produce parts with quality and repeatability, and the AM components for aeroengine application have to be designed and verified to the stringent certification requirements, a detailed understanding of different parameters which affect the mechanical and fatigue performances of aeroengine components is a must.

Future efforts should be to build a robust design dataset of physical, mechanical and fatigue properties of typical material types used on aeroengine. This robust design dataset shall be utilized for the lifing assessment of aeroengine AM components with confidence or at least with known quantifiable risks. The design dataset should be aimed to cover a range of temperatures in the engine operating and extreme running conditions, and to also account for effect of notch, surface roughness, defect and build orientation. The residual stresses in the as-built LPBF part will be dependent upon the build thermal environment and also on the thermal history experienced by the AM part during the build process. In the as-built part, which hasn't gone through a HT process, the efforts should be put in to get an estimate of residual stresses in each AM component type to be produced and at each of the critical stress locations. The estimated residual stresses will then be considered in the stress assessments to get a more accurate prediction on AM component life.

Standardization of analysis and lifing methods for AM components is a key to ensure the robustness of analysis predictions. Like the materials database, the analysis rules, tools and methods need to be evaluated, developed and standardized for AM applications. This will bring the much needed consistency, quality and robustness in the predictions of analysis of AM parts.

In this research work, the LCF and HCF testing on a carefully designed weight optimized LPBF Ti-6Al-4V bracket has shown good performance, which improves confidence towards a successful deployment of the LPBF technology for safety critical load bearing applications. The efforts to better understand the relationship between properties and component test performance must be continued to minimize expensive component testing in future to produce certifiable and flightworthy aero-engine components. Future studies are required to understand the structural mechanics behaviour of the load bearing AM parts in lattice construction. AM parts in lattice construction could offer higher damping with better performance against the impact loading which are beneficial in vibration and impact critical loading environments.

The expected debits in mechanical and fatigue performances of AM parts can be overcome by a careful selection of process parameters and also by carrying out the design optimization trade studies for any weight reduction opportunities and also to uniformly spread the loads and reduce overall magnitude of stresses in the structural elements of an AM part. The rules and techniques for structural optimization and designing for AM also needs attention to maximize the benefits of ALM technology. The aerospace sectors is putting constant efforts to reduce carbon emission to support the net zero strategy of UK government, and ALM technology can be a key contributor to achieve net zero.

The crack geometry and its location, boundary condition, loading and material property are the key factors to accurately predict the crack growth life of AM parts, which should be measured and defined accurately in the analysis simulation.

In the future, studies are needed to be performed to assess the effect of defects in actual AM build parts which experience anisotropic material behaviour and multi-axial state of loading. Many studies have highlighted the need to acquire the small crack growth data to judge the effectiveness of

different AM processes with regards to their resistance to small crack growth [253]. Since it is hard to get the small crack growth data [258, 262, 269, 274] due to experimental difficulties, better testing techniques are required to build the material database of small crack growth rate with various materials, loading ratios, AM processes, build parameters, post build HTs and build direction dependent anisotropy. Furthermore, experimental studies are recommended to understand the behaviour of simultaneously propagating small cracks in AM specimens, and at the same time, the simulation capability for such cases is required to be developed.

This research was focussed on to explore the property and structural behaviour of PBF Ti-6Al-4V. The structural behaviour of AM parts built in other key materials, such as stainless steel, nickel based superalloys etc. should also be explored to achieve a widespread use of ALM technology in aeroengine application. A better understanding and development of material models for various other AM materials for ET and including other loading conditions needs to be explored as part of the future studies. These material models should be explored to include the effect of damage mechanics at microstructural levels and should cover the phenomenon such as fatigue, fracture, creep and creep-fatigue interactions.

-----x x x x x x-----

References

[1] ASTM International, F2792-12a - Standard Terminology for Additive Manufacturing Technologies, Rapid Manuf. Assoc. (2013) 10–12. https://doi.org/10.1520/F2792-12A.2.

[2] A press release, Wohlers Associates, Inc., (2021) https://wohlersassociates.com/press83.html

[3] T.D. Ngo, A. Kashani, G. Imbalzano, K.T.Q. Nguyen, D. Hui, Additive manufacturing (3D printing): A review of materials , methods , applications and challenges, Compos. Part B. 143 (2018) 172–196. https://doi.org/10.1016/j.compositesb.2018.02.012.

[4] H. Bikas, P. Stavropoulos, G. Chryssolouris, Additive manufacturing methods and modeling approaches: A critical review, Int. J. Adv. Manuf. Technol. 83 (2016) 389–405. https://doi.org/10.1007/s00170-015-7576-2.

[5] S.R. Daniewicz, N. Shamsaei, An introduction to the fatigue and fracture behavior of additive manufactured parts, Int. J. Fatigue. 94 (2017) 167. https://doi.org/10.1016/j.ijfatigue.2016.07.007.

[6] G. Lütjering, Influence of processing on microstructure and mechanical properties of (α+β) titanium alloys, Mater. Sci. Eng. A. 243 (1998) 32–45. https://doi.org/10.1016/S0921-5093(97)00778-8.

[7] R.R. Boyer, An overview on the use of titanium in the aerospace industry, Mater. Sci. Eng. A. 213 (1996) 103–114. https://doi.org/10.1016/0921-5093(96)10233-1.

[8] M.B. Kumar, P. Sathiya, Thin-Walled Structures Methods and materials for additive manufacturing : A critical review on advancements and challenges, Thin-Walled Struct. 159 (2021) 107228. https://doi.org/10.1016/j.tws.2020.107228.

[9] P. Singh, H. Pungotra, N.S. Kalsi, On the characteristics of titanium alloys for the aircraft applications, Mater. Today Proc. 4 (2017) 8971–8982. https://doi.org/10.1016/j.matpr.2017.07.249.

[10] ISO/ASTM International, ASTM52900:2015, Standard terminology for Additive Manufacturing — General principles — Terminology, (2015) 1–9. https://doi.org/10.1520/ISOASTM52900-15.

[11] J. Hiemenz, Additive Manufacturing Trends in Aerospace, Stratasys Inc. (2020) https://www.sys-uk.com/wp-content/uploads/2020/07/White-Paper-Additive-Manufacturing-Trends-in-Aerospace-Leading-the-W....pdf

[12] AM_Special_Interest_Group, Shaping our national competency in additive manufacturing, T.S. Board, Editor. 2012, UK Governmen. https://reevesinsight.com/wp-content/uploads/2020/02/26-2012-Natioanl-strategy.pdf

[13] B. Blakey-Milner, P. Gradl, G. Snedden, M. Brooks, J. Pitot, E. Lopez, M. Leary, F. Berto, A. du Plessis, Metal additive manufacturing in aerospace: A review, Mater. Des. 209 (2021) 110008. https://doi.org/10.1016/j.matdes.2021.110008.

[14] C.Y. Yap, C.K. Chua, Z.L. Dong, Z.H. Liu, D.Q. Zhang, L.E. Loh, S.L. Sing, Review of selective laser melting : Materials and applications Review of selective laser melting : Materials and applications, 041101 (2015). https://doi.org/10.1063/1.4935926.

[15] Technical Description EOSINT M280, (2010). https://webbuilder5.asiannet.com/ftp/2684/TD_M280_en_2011-03-29.pdf

[16] X. Gong, T. Anderson, K. Chou, Review on powder-based electron beam additive manufacturing Technology, Manuf. Rev. 1 (2014). https://doi.org/10.1051/mfreview/2014001.

[17] A. Mohammadhosseini, S.H. Masood, D. Fraser, M. Jahedi, Dynamic compressive behaviour of Ti-6Al-4V alloy processed by electron beam melting under high strain rate loading, Adv. Manuf. 3 (2015) 232–243. https://doi.org/10.1007/s40436-015-0119-0.

[18] Arcam EBM, Welcome to Manufacturing Unbound, (2017) 1–20. http://www.arcam.com/wp-content/uploads/arcamebm-corp.pdf

[19] M.J. Donachie, Titanium: A Technical Guide. ASM International, The Minerals Information Society, 2000.

[20] ASTM B348/B348M – 19, Standard Specification for Titanium and Titanium Alloy Bars and Billets, ASTM International (2019) 1–9. https://doi.org/10.1520/B0348_B0348M-19.

[21] G. Lütjering, and J. Williams, Titanium (Engineering Materials and Processes), Berlin Heidelberg: Springer (2007).

[22] H. Guleryuz, H. Cimenoglu, Oxidation of Ti-6Al-4V alloy, J. Alloys Compd. 472 (2009) 241–246. https://doi.org/10.1016/j.jallcom.2008.04.024.

[23] M. Simonelli, Microstructure Evolution and Mechanical Properties of Selective Laser Melted Ti-6Al-4V, A Doctoral Thesis, Loughbrough University, (2014). https://hdl.handle.net/2134/15070.

[24] R. Pederson, Microstructure and Phase Transformation of Ti-6Al-4V alloy, A doctoral thesis, Luley University of Technology, (2002). https://www.diva-portal.org/smash/get/diva2:991369/FULLTEXT01.pdf

[25] T. Ahmed, H.J. Rack, Phase transformations during cooling in α+β titanium alloys, Mater. Sci. Eng. A. 243 (1998) 206–211. https://doi.org/10.1016/S0921-5093(97)00802-2.

[26] Y. Chong, T. Bhattacharjee, N. Tsuji, Bi-lamellar microstructure in Ti – 6Al – 4V : Microstructure evolution and mechanical properties, Mater. Sci. Eng. A. 762 (2019) 138077. https://doi.org/10.1016/j.msea.2019.138077.

[27] R.H. Buzolin, D. Weiß, A. Krumphals, M. Lasnik, M.C. Poletti, Modelling the competitive growth of primary, allotriomorphic, and secondary alpha in Ti-6Al-4V, Metall. Mater. Trans. A 51A (2020) 3967–3980. https://doi.org/10.1007/s11661-020-05810-4.

[28] Z.C. Cordero, H.M. Meyer, P. Nandwana, R.R. Dehoff, Powder bed charging during electron-beam additive manufacturing, Acta Mater. 124 (2017) 437–445. https://doi.org/10.1016/j.actamat.2016.11.012.

[29] M. Sigl, S. Lutzmann, M.F. Zäh, Transient physical effects in electron beam sintering, Solid Freeform Fabrication Symposium Proceedings, Austin, TX, (2006) 397-405.

[30] H. Guleryuz, H. Cimenoglu, Oxidation of Ti-6Al-4V alloy, J. Alloys Compd. 472 (2009) 241–246. https://doi.org/10.1016/j.jallcom.2008.04.024.

[31] R. Gaddam, B. Sefer, R. Pederson, M. Antti, Study of alpha-case depth in Ti-6Al-2Sn-4Zr-2Mo and Ti-6Al-4V, 7th EEIGM International Conference on Advanced Materials Research, IOP Conf. Series: Materials Science and Engineering, 48 (2013) 1–9.

https://doi.org/10.1088/1757-899X/48/1/012002.

[32] E. Engblom, Effect of oxygen concentration in build chamber during laser metal deposition of Ti-64 wire, Degree Project in Materials Design and Engineering, KTH Royal institute of Technology (2018).

[33] M. Yan, W. Xu, M.S. Dargusch, H.P. Tang, M. Brandt, M. Qian, Review of effect of oxygen on room temperature ductility of titanium and titanium alloys, 5899 (2014). https://doi.org/10.1179/1743290114Y.0000000108.

[34] R. Gaddam, B. Sefer, R. Pederson, M. Antti, Materials Characterization Oxidation and alpha-case formation in Ti – 6Al – 2Sn – 4Zr – 2Mo alloy, Mater. Charact. 99 (2015) 166–174. https://doi.org/10.1016/j.matchar.2014.11.023.

[35] K. Dietrich, J. Diller, S.D. Go, D. Bauer, P. Forêt, The influence of oxygen on the chemical composition and mechanical properties of Ti-6Al-4V during laser powder bed fusion (L-PBF), 32 (2020). https://doi.org/10.1016/j.addma.2019.100980.

[36] C. Pauzon, K. Dietrich, P. For, S.D. Goff, E. Hryha, G. Witt, Control of residual oxygen of the process atmosphere during laser-powder bed fusion processing of Ti-6Al-4V, 38 (2021). https://doi.org/10.1016/j.addma.2020.101765.

[37] ASTM International, ASTM F3001-14, Standard specification for Additive Manufacturing Titanium-6 Aluminium-4 Vanadium ELI (Extra Low Interstitial) with Powder Bed Fusion. (2021) 1–6. https://doi.org/10.1520/F3001-14.

[38] SAE International, AMS4999A, Titanium alloy direct deposited products 6Al - 4V annealed, Aerospace Materials Specifications, (2016). https://www.sae.org/standards/content/ams4999a/

[39] A. Yadollahi, N. Shamsaei, S.M. Thompson, A. Elwany, L. Bian, Effects of building orientation and heat treatment on fatigue behavior of selective laser melted 17-4 PH stainless steel, Int. J. Fatigue. 94 (2017) 218–235. https://doi.org/10.1016/j.ijfatigue.2016.03.014.

[40] H. Gong, K. Rafi, H. Gu, G.D. Janaki Ram, T. Starr, B. Stucker, Influence of defects on mechanical properties of Ti-6Al-4V components produced by selective laser melting and electron beam melting, Mater. Des. 86 (2015) 545–554. https://doi.org/10.1016/j.matdes.2015.07.147.

[41] S. Liu, Y.C. Shin, Additive manufacturing of Ti6Al4V alloy: A review, Mater. Des. 164 (2019) 107552. https://doi.org/10.1016/j.matdes.2018.107552.

[42] H. Gong, K. Rafi, H. Gu, T. Starr, B. Stucker, Analysis of defect generation in Ti-6Al-4V parts made using powder bed fusion additive manufacturing processes, Addit. Manuf. 1 (2014) 87–98. https://doi.org/10.1016/j.addma.2014.08.002.

[43] L. Thijs, F. Verhaeghe, T. Craeghs, J. Van Humbeeck, J.P. Kruth, A study of the microstructural evolution during selective laser melting of Ti-6Al-4V, Acta Mater. 58 (2010) 3303–3312. https://doi.org/10.1016/j.actamat.2010.02.004.

[44] N. Sanaei, A. Fatemi, N. Phan, Defect characteristics and analysis of their variability in metal L-PBF additive manufacturing, Mater. Des. 182 (2019) 108091. https://doi.org/10.1016/j.matdes.2019.108091.

[45] G. Kasperovich, J. Haubrich, J. Gussone, G. Requena, Correlation between porosity and processing parameters in TiAl6V4 produced by selective laser melting, Mater. Des. 105 (2016) 160–170. https://doi.org/10.1016/j.matdes.2016.05.070.

[46] M. Saunders, How process parameters drive successful metal AM part production, Metal AM 4-2, (2018), https://www.metal-am.com/articles/70927-2/

[47] N. Sanaei, A. Fatemi, Progress in Materials Science Defects in additive manufactured metals and their effect on fatigue performance : A state-of-the-art review, (2020). https://doi.org/10.1016/j.pmatsci.2020.100724.

[48] H. yu Chen, D. dong Gu, Q. Ge, X. yu Shi, H. mei Zhang, R. Wang, H. Zhang, K. Kosiba, Role of laser scan strategies in defect control, microstructural evolution and mechanical properties of steel matrix composites prepared by laser additive manufacturing, Int. J. Miner. Metall. Mater. 28 (2021) 462–474. https://doi.org/10.1007/s12613-020-2133-x.

[49] C. Qiu, C. Panwisawas, M. Ward, H.C. Basoalto, J.W. Brooks, M.M. Attallah, On the role of melt flow into the surface structure and porosity development during selective laser melting, Acta Mater. 96 (2015) 72–79. https://doi.org/10.1016/j.actamat.2015.06.004.

[50] A.H. Chern, P. Nandwana, R. McDaniels, R.R. Dehoff, P.K. Liaw, R. Tryon, C.E. Duty, Build orientation, surface roughness, and scan path influence on the microstructure, mechanical properties, and flexural fatigue behavior of Ti–6Al–4V fabricated by electron beam melting, Mater. Sci. Eng. A. 772 (2020) 138740. https://doi.org/10.1016/j.msea.2019.138740.

[51] S. Tammas-Williams, H. Zhao, F. Léonard, F. Derguti, I. Todd, P.B. Prangnell, XCT analysis of the influence of melt strategies on defect population in Ti-6Al-4V components manufactured by Selective Electron Beam Melting, Mater. Charact. 102 (2015) 47–61. https://doi.org/10.1016/j.matchar.2015.02.008.

[52] F. Cao, P. Kumar, M. Koopman, C. Lin, Z.Z. Fang, K.S.R. Chandran, Understanding competing fatigue mechanisms in powder metallurgy Ti-6Al-4V alloy: Role of crack initiation and duality of fatigue response, Mater. Sci. Eng. A. 630 (2015) 139–145. https://doi.org/10.1016/j.msea.2015.02.028.

[53] J.H. Zuo, Z.G. Wang, E.H. Han, Effect of microstructure on ultra-high cycle fatigue behavior of Ti-6Al-4V, Mater. Sci. Eng. A. 473 (2008) 147–152. https://doi.org/10.1016/j.msea.2007.04.062.

[54] H. V Atkinson, S. Davies, Fundamental Aspects of Hot Isostatic Pressing: An Overview, Metallurgical and Mechanical Transactions A 31A (2000), 2981 - 3000.

[55] S. Tammas-williams, P.J. Withers, I. Todd, P.B. Prangnell, The Effectiveness of Hot Isostatic Pressing for Closing Porosity in Selective Electron Beam Melting, Metall. Mater. Trans. A. 47 (2016) 1939–1946. https://doi.org/10.1007/s11661-016-3429-3.

[56] Y.N. Hu, S.C. Wu, P.J. Withers, J. Zhang, H.Y.X. Bao, Y.N. Fu, G.Z. Kang, The effect of manufacturing defects on the fatigue life of selective laser melted Ti-6Al-4V structures, Mater. Des. 192 (2020). https://doi.org/10.1016/j.matdes.2020.108708.

[57] M Roudnicka, K Mertova, and D Vojtech, Influence of hot isostatic pressing on mechanical response of as-built SLM titanium alloy, The 2nd International Conference on Material Strength and Applied Mechanics, Materials Science and Engineering 629 (2019). https://doi.org/10.1088/1757-899X/629/1/012034.

[58] Z. Xu, J.W. Murray, C.J. Hyde, A.T. Clare, Effect of post processing on the creep performance of laser powder bed fused Inconel 718, Addit. Manuf. 24 (2018) 486–497. https://doi.org/10.1016/j.addma.2018.10.027.

[59] ASTM B962-17, Standard Test Methods for Density of Compacted or Sintered Powder Metallurgy (PM) Products Using Archimedes' Principle, ASTM International, West Conshohocken, PA, 2017, DOI: 10.1520/B0962-17

[60] S. Siddique, M. Imran, M. Rauer, M. Kaloudis, E. Wycisk, C. Emmelmann, F. Walther, Computed tomography for characterization of fatigue performance of selective laser melted parts, Mater. Des. 83 (2015) 661–669. https://doi.org/10.1016/j.matdes.2015.06.063.

[61] N. Sanaei, A. Greitemeier, Analysis of the effect of surface roughness on fatigue performance of powder bed fusion additive manufactured metals, Theor. Appl. Fract. Mech. 108 (2020) 102638. https://doi.org/10.1016/j.tafmec.2020.102638.

[62] A. Yadollahi, N. Shamsaei, Additive manufacturing of fatigue resistant materials: Challenges and opportunities, Int. J. Fatigue. 98 (2017) 14–31.

https://doi.org/10.1016/j.ijfatigue.2017.01.001.

[63] W.E. Frazier, Metal additive manufacturing: A review, J. Mater. Eng. Perform. 23 (2014) 1917–1928. https://doi.org/10.1007/s11665-014-0958-z.

[64] J. Pegues, M. Roach, R.S. Williamson, N. Shamsaei, Surface roughness effects on the fatigue strength of additively manufactured, Int. J. Fatigue. 116 (2018) 543–552. https://doi.org/10.1016/j.ijfatigue.2018.07.013.

[65] D. Greitemeier, C. Dalle Donne, F. Syassen, J. Eufinger, T. Melz, Effect of surface roughness on fatigue performance of additive manufactured Ti–6Al–4V, Mater. Sci. Technol. (United Kingdom). 32 (2016) 629–634. https://doi.org/10.1179/1743284715Y.0000000053.

[66] M. Heinl, M. Heinl, S. Greiner, K. Wudy, C. Pobel, M. Rasch, M. Rasch, F. Huber, F. Huber, T. Papke, M. Merklein, M. Schmidt, M. Schmidt, C. Körner, D. Drummer, T. Hausotte, Measuring procedures for surface evaluation of additively manufactured powder bed-based polymer and metal parts, Meas. Sci. Technol. 31 (2020). https://doi.org/10.1088/1361-6501/ab89e2.

[67] H. Masuo, Y. Tanaka, S. Morokoshi, H. Yagura, T. Uchida, Y. Yamamoto, Y. Murakami, Effects of Defects, Surface Roughness and HIP on Fatigue Strength of Ti-6Al-4V manufactured by Additive Manufacturing, Procedia Struct. Integr. 7 (2017) 19–26. https://doi.org/10.1016/j.prostr.2017.11.055.

[68] H. Masuo, Y. Tanaka, S. Morokoshi, H. Yagura, T. Uchida, Influence of defects, surface roughness and HIP on the fatigue strength of Ti- 6Al-4V manufactured by additive manufacturing, Int. J. Fatigue. 117 (2018) 163–179. https://doi.org/10.1016/j.ijfatigue.2018.07.020.

[69] A. Fatemi, R. Molaei, S. Sharifimehr, N. Shamsaei, N. Phan, Torsional fatigue behavior of wrought and additive manufactured Ti-6Al-4V by powder bed fusion including surface finish effect, 99 (2017) 187–201. https://doi.org/10.1016/j.ijfatigue.2017.03.002.

[70] J. Zhang, A. Fatemi, Surface roughness effect on multiaxial fatigue behavior of additive manufactured metals and its modeling, Theor. Appl. Fract. Mech. 103 (2019) 102260. https://doi.org/10.1016/j.tafmec.2019.102260.

[71] R. Molaei, A. Fatemi, Crack paths in additive manufactured metallic materials subjected to multiaxial cyclic loads including surface roughness, HIP, and notch effects, 124 (2019) 558–570. https://doi.org/10.1016/j.ijfatigue.2019.03.007.

[72] D. Greitemeier, F. Palm, F. Syassen, T. Melz, Fatigue performance of additive manufactured TiAl6V4 using electron and laser beam melting, Int. J. Fatigue. 94 (2017) 211–217. https://doi.org/10.1016/j.ijfatigue.2016.05.001.

[73] M. Kahlin, H. Ansell, J.J. Moverare, Fatigue behaviour of notched additive manufactured Ti6Al4V with as-built surfaces, Int. J. Fatigue. 101 (2017) 51–60. https://doi.org/10.1016/j.ijfatigue.2017.04.009.

[74] P. Edwards, M. Ramulu, Fatigue performance evaluation of selective laser melted Ti-6Al-4V, Mater. Sci. Eng. A. 598 (2014) 327–337. https://doi.org/10.1016/j.msea.2014.01.041.

[75] A. Fatemi, R. Molaei, S. Sharifimehr, N. Phan, N. Shamsaei, Multiaxial fatigue behavior of wrought and additive manufactured Ti-6Al-4V including surface finish effect, Int. J. Fatigue. 100 (2017) 347–366. https://doi.org/10.1016/j.ijfatigue.2017.03.044.

[76] M. Benedetti, V. Fontanari, M. Bandini, F. Zanini, S. Carmignato, Low- and high-cycle fatigue resistance of Ti-6Al-4V ELI additively manufactured via selective laser melting: Mean stress and defect sensitivity, Int. J. Fatigue. 107 (2018) 96–109. https://doi.org/10.1016/j.ijfatigue.2017.10.021.

[77] S. Bagehorn, J. Wehr, H.J. Maier, Application of mechanical surface finishing processes for roughness reduction and fatigue improvement of additively manufactured Ti-6Al-4V parts, Int. J. Fatigue. 102 (2017) 135–142. https://doi.org/10.1016/j.ijfatigue.2017.05.008.

[78] H. Zhang, R. Chiang, H. Qin, Z. Ren, X. Hou, D. Lin, G.L. Doll, V.K. Vasudevan, Y. Dong, C. Ye, The effects of ultrasonic nanocrystal surface modification on the fatigue performance of 3D-printed Ti64, Int. J. Fatigue. 103 (2017) 136–146. https://doi.org/10.1016/j.ijfatigue.2017.05.019.

[79] P.E. Carrion, A. Soltani-Tehrani, N. Phan, N. Shamsaei, Powder Recycling Effects on the Tensile and Fatigue Behavior of Additively Manufactured Ti-6Al-4V Parts, Jom. 71 (2019) 963–973. https://doi.org/10.1007/s11837-018-3248-7.

[80] T.M. Mower, M.J. Long, Mechanical behavior of additive manufactured, powder-bed laser-fused materials, Mater. Sci. Eng. A. 651 (2016) 198–213. https://doi.org/10.1016/j.msea.2015.10.068.

[81] P. Mercelis, J.P. Kruth, Residual stresses in selective laser sintering and selective laser melting, Rapid Prototype. J. 12 (2006) 254–265. https://doi.org/10.1108/13552540610707013.

[82] L.S. Anderson, A.M. Venter, B. Vrancken, D. Marais, J. Van Humbeeck, Investigating the Residual Stress Distribution in Selective Laser Melting Produced Ti-6Al-4V using Neutron Diffraction, Mech. Stress Eval. by Neutron Synchrotron Radiat. 4 (2018) 73–78. https://doi.org/10.21741/9781945291678-11.

[83] T.H. Becker, P. Kumar, U. Ramamurty, Fracture and fatigue in additively manufactured metals, Acta Mater. 219 (2021) 117240. https://doi.org/10.1016/j.actamat.2021.117240.

[84] T. Mukherjee, W. Zhang, T. DebRoy, An improved prediction of residual stresses and distortion in additive manufacturing, Comput. Mater. Sci. 126 (2017) 360–372. https://doi.org/10.1016/j.commatsci.2016.10.003.

[85] L.D. Bobbio, S. Qin, A. Dunbar, P. Michaleris, A.M. Beese, Characterization of the strength of support structures used in powder bed fusion additive manufacturing of Ti-6Al-4V, Addit. Manuf. 14 (2017) 60–68. https://doi.org/10.1016/j.addma.2017.01.002.

[86] P. Kumar, O. Prakash, U. Ramamurty, Micro-and meso-structures and their influence on mechanical properties of selectively laser melted Ti-6Al-4V, Acta Mater. 154 (2018) 246–260. https://doi.org/10.1016/j.actamat.2018.05.044.

[87] M. Seifi, A. Salem, D. Satko, J. Shaffer, J.J. Lewandowski, Defect distribution and microstructure heterogeneity effects on fracture resistance and fatigue behavior of EBM Ti–6Al–4V, Int. J. Fatigue. 94 (2017) 263–287. https://doi.org/10.1016/j.ijfatigue.2016.06.001.

[88] T.H. Becker, M. Beck, C. Scheffer, Microstructure and mechanical properties of direct metal laser sintered Ti-6Al-4V, South African Journal of Industrial Engineering, 26 (2015) 1-10.

[89] B. Vrancken, S. Buls , J.P. Kruth, J. Van Humbeeck, Influence of preheating and oxygen content on selective laser melting of Ti6Al4V, Proceeding of 16th RAP- DASA Conference, 2015 . https://lirias.kuleuven.be/1748568?limo=0

[90] X. Tan, Y. Kok, Y.J. Tan, M. Descoins, D. Mangelinck, S.B. Tor, K.F. Leong, C.K. Chua, Graded microstructure and mechanical properties of additive manufactured Ti-6Al-4V via electron beam melting, Acta Mater. 97 (2015) 1–16. https://doi.org/10.1016/j.actamat.2015.06.036.

[91] H.K. Rafi, N. V. Karthik, H. Gong, T.L. Starr, B.E. Stucker, Microstructures and mechanical properties of Ti6Al4V parts fabricated by selective laser melting and electron beam melting, J. Mater. Eng. Perform. 22 (2013) 3872–3883. https://doi.org/10.1007/s11665-013-0658-0.

[92] P. Edwards, A. O'Conner, M. Ramulu, Electron beam additive manufacturing of titanium components: Properties and performance, J. Manuf. Sci. Eng. Trans. ASME. 135 (2013). https://doi.org/10.1115/1.4025773.

[93] H. Galarraga, R.J. Warren, D.A. Lados, R.R. Dehoff, M.M. Kirka, P. Nandwana, Effects of heat treatments on microstructure and properties of Ti-6Al-4V ELI alloy fabricated by electron beam melting (EBM), Mater. Sci. Eng. A. 685 (2017) 417–428. https://doi.org/10.1016/j.msea.2017.01.019.

[94] Y. Zhai, H. Galarraga, D.A. Lados, Microstructure Evolution, Tensile Properties, and Fatigue Damage Mechanisms in Ti-6Al-4V Alloys Fabricated by Two Additive Manufacturing Techniques, Procedia Eng. 114 (2015) 658–666. https://doi.org/10.1016/j.proeng.2015.08.007.

[95] S. Raghavan, M.L.S. Nai, P. Wang, W.J. Sin, T. Li, J. Wei, Heat treatment of electron beam melted (EBM) Ti-6Al-4V: microstructure to mechanical property correlations, Rapid Prototyp. J. 24 (2018) 774–783. https://doi.org/10.1108/RPJ-05-2016-0070.

[96] J. Yang, H. Yu, J. Yin, M. Gao, Z. Wang, X. Zeng, Formation and control of martensite in Ti-6Al-4V alloy produced by selective laser melting, JMADE. 108 (2016) 308–318. https://doi.org/10.1016/j.matdes.2016.06.117.

[97] P. Kumar, U. Ramamurty, Microstructural optimization through heat treatment for enhancing the fracture toughness and fatigue crack growth resistance of selective laser melted Ti-6Al-4V alloy, Acta Mater. 169 (2019) 45–59. https://doi.org/10.1016/j.actamat.2019.03.003.

[98] G.M. Ter Haar, T.H. Becker, The influence of microstructural texture and prior beta grain recrystallisation on the deformation behaviour of laser powder bed fusion produced Ti–6Al–4V, Mater. Sci. Eng. A. 814 (2021) 141185. https://doi.org/10.1016/j.msea.2021.141185.

[99] N. Sridharan, A. Chaudhary, P. Nandwana, S.S. Babu, Texture Evolution During Laser Direct Metal Deposition of Ti-6Al-4V, 68 (2016) 772–777. https://doi.org/10.1007/s11837-015-1797-6.

[100] G.M. Ter Haar, T.H. Becker, Low temperature stress relief and martensitic decomposition in selective laser melting produced Ti6Al4V, Mater. Des. Process. Commun. 3 (2021) 2–7. https://doi.org/10.1002/mdp2.138.

[101] C. de Formanoir, G. Martin, F. Prima, S.Y.P. Allain, T. Dessolier, F. Sun, S. Vivès, B. Hary, Y. Bréchet, S. Godet, Micromechanical behavior and thermal stability of a dual-phase α+α' titanium alloy produced by additive manufacturing, Acta Mater. 162 (2019) 149–162. https://doi.org/10.1016/j.actamat.2018.09.050.

[102] S. Tammas-Williams, P.J. Withers, I. Todd, P.B. Prangnell, Porosity regrowth during heat treatment of hot isostatically pressed additively manufactured titanium components, Scr. Mater. 122 (2016) 72–76. https://doi.org/10.1016/j.scriptamat.2016.05.002.

[103] R. Cunningham, A. Nicolas, J. Madsen, E. Fodran, M.D. Sangid, A.D. Rollett, R. Cunningham, A. Nicolas, J. Madsen, E. Fodran, Analyzing the effects of powder and post-processing on porosity and properties of electron beam melted Ti-6Al-4V Analyzing the effects of powder and post-processing on porosity and properties of electron beam melted Ti-6Al-4V, Mater. Res. Lett. 0 (2017) 1–10. https://doi.org/10.1080/21663831.2017.1340911.

[104] J. Yang, H. Yu, Z. Wang, X. Zeng, Effect of crystallographic orientation on mechanical anisotropy of selective laser melted Ti-6Al-4V alloy, Mater. Charact. 127 (2017) 137–145. https://doi.org/10.1016/j.matchar.2017.01.014.

[105] K. Chang, X. Wang, E. Liang, R. Zhang, On the texture and mechanical property anisotropy of Ti6Al4V alloy fabricated by powder-bed based laser additive manufacturing, Vacuum. 181 (2020) 2–6. https://doi.org/10.1016/j.vacuum.2020.109732.

[106] M. Tarik Hasib, H.E. Ostergaard, X. Li, J.J. Kruzic, Fatigue crack growth behavior of laser powder bed fusion additive manufactured Ti-6Al-4V: Roles of post heat treatment and build orientation, Int. J. Fatigue. 142 (2021) 105955. https://doi.org/10.1016/j.ijfatigue.2020.105955.

[107] E. Wycisk, S. Siddique, D. Herzog, F. Walther, C. Emmelmann, Fatigue performance of laser additive manufactured Ti–6Al–4V in very high cycle fatigue regime up to 109 cycles, Front. Mater. 2 (2015) 2–9. https://doi.org/10.3389/fmats.2015.00072.

[108] J. Gao, X. Zhao, J. Yue, M. Qi, D. Zhang, Microstructure and Mechanical Properties of Ti-6Al-4V Alloy Samples Fabricated by Selective Laser Melting, 770 (2018) 179–186. https://doi.org/10.4028/www.scientific.net/KEM.770.179.

[109] G.M. Ter Haar, T.H. Becker, Selective laser melting produced Ti-6Al-4V: Post-process heat treatments to achieve superior tensile properties, Materials (Basel). 11 (2018). https://doi.org/10.3390/ma11010146.

[110] W. Xu, M. Brandt, S. Sun, J. Elambasseril, Q. Liu, K. Latham, K. Xia, M. Qian, Additive manufacturing of strong and ductile Ti-6Al-4V by selective laser melting via in situ martensite decomposition, Acta Mater. 85 (2015) 74–84. https://doi.org/10.1016/j.actamat.2014.11.028.

[111] O.A. Quintana, W. Tong, Effects of Oxygen Content on Tensile and Fatigue Performance of Ti-6Al-4 V Manufactured by Selective Laser Melting, JOM. 69 (2017) 2693–2697. https://doi.org/10.1007/s11837-017-2590-5.

[112] S.L. Lu, H.P. Tang, Y.P. Ning, N. Liu, D.H. StJohn, M. Qian, Microstructure and Mechanical Properties of Long Ti-6Al-4V Rods Additively Manufactured by Selective Electron Beam Melting Out of a Deep Powder Bed and the Effect of Subsequent Hot Isostatic Pressing, Metall. Mater. Trans. A Phys. Metall. Mater. Sci. 46 (2015) 3824–3834. https://doi.org/10.1007/s11661-015-2976-3.

[113] O.L. Rodriguez, P.G. Allison, W.R. Whittington, D.K. Francis, O.G. Rivera, K. Chou, X. Gong, T.M. Butler, J.F. Burroughs, Dynamic tensile behavior of electron beam additive manufactured Ti6Al4V, Mater. Sci. Eng. A. 641 (2015) 323–327. https://doi.org/10.1016/j.msea.2015.06.069.

[114] A. Mohammadhosseini, D. Fraser, S.H. Masood, M. Jahedi, Microstructure and mechanical properties of Ti-6Al-4V manufactured by electron beam melting process, Mater. Res. Innov. 17 (2013). https://doi.org/10.1179/1432891713Z.000000000302.

[115] N. Hrabe, T. Quinn, Effects of processing on microstructure and mechanical properties of a titanium alloy (Ti-6Al-4V) fabricated using electron beam melting (EBM), Part 2: Energy input, orientation, and location, Mater. Sci. Eng. A. 573 (2013) 271–277. https://doi.org/10.1016/j.msea.2013.02.065.

[116] L.E. Murr, E. V. Esquivel, S.A. Quinones, S.M. Gaytan, M.I. Lopez, E.Y. Martinez, F. Medina, D.H. Hernandez, E. Martinez, J.L. Martinez, S.W. Stafford, D.K. Brown, T. Hoppe, W. Meyers, U. Lindhe, R.B. Wicker, Microstructures and mechanical properties of electron beam-rapid manufactured Ti-6Al-4V biomedical prototypes compared to wrought Ti-6Al-4V, Mater. Charact. 60 (2009) 96–105. https://doi.org/10.1016/j.matchar.2008.07.006.

[117] L. Facchini, E. Magalini, P. Robotti, A. Molinari, Microstructure and mechanical properties of Ti-6Al-4V produced by electron beam melting of pre-alloyed powders, Rapid Prototyp. J. 15 (2009) 171–178. https://doi.org/10.1108/13552540910960262.

[118] M. Koike, K. Martinez, L. Guo, G. Chahine, R. Kovacevic, T. Okabe, Evaluation of titanium alloy fabricated using electron beam melting system for dental applications, J. Mater. Process. Technol. 211 (2011) 1400–1408. https://doi.org/10.1016/j.jmatprotec.2011.03.013.

[119] T. McLouth, Y.-W. Chang, J. Wooten, J.-M. Yang, The Effects of Electron Beam Melting on the Microstructure and Mechanical Properties of Ti-6Al-4V and Gamma-TiAl, Microsc. Microanal. 21 (2015) 1177–1178. https://doi.org/10.1017/s1431927615006674.

[120] V. Cain, L. Thijs, J. Van Humbeeck, B. Van Hooreweder, R. Knutsen, Crack propagation and fracture toughness of Ti6Al4V alloy produced by selective laser melting, Addit. Manuf. 5 (2015) 68–76. https://doi.org/10.1016/j.addma.2014.12.006.

[121] G. Kasperovich, J. Hausmann, Improvement of fatigue resistance and ductility of TiAl6V4 processed by selective laser melting, J. Mater. Process. Technol. 220 (2015) 202–214. https://doi.org/10.1016/j.jmatprotec.2015.01.025.

[122] S. Leuders, T. Lieneke, S. Lammers, T. Tröster, T. Niendorf, On the fatigue properties of metals manufactured by selective laser melting - The role of ductility, J. Mater. Res. 29 (2014) 1911–1919. https://doi.org/10.1557/jmr.2014.157.

[123] M. Simonelli, Y.Y. Tse, C. Tuck, Effect of the build orientation on the mechanical properties and fracture modes of SLM Ti-6Al-4V, Mater. Sci. Eng. A. 616 (2014) 1–11. https://doi.org/10.1016/j.msea.2014.07.086.

[124] S. Leuders, M. Thöne, A. Riemer, T. Niendorf, T. Tröster, H.A. Richard, H.J. Maier, On the mechanical behaviour of titanium alloy TiAl6V4 manufactured by selective laser melting : Fatigue resistance and crack growth performance, Int. J. Fatigue. 48 (2013) 300–307. https://doi.org/10.1016/j.ijfatigue.2012.11.011.

[125] M. Simonelli, Y.Y. Tse, C. Tuck, The formation of α + β microstructure in as-fabricated selective laser melting of Ti-6Al-4V, J. Mater. Res. 29 (2014) 2028–2035. https://doi.org/10.1557/jmr.2014.166.

[126] B. Vrancken, L. Thijs, J.P. Kruth, J. Van Humbeeck, Heat treatment of Ti6Al4V produced by Selective Laser Melting: Microstructure and mechanical properties, J. Alloys Compd. 541 (2012) 177–185. https://doi.org/10.1016/j.jallcom.2012.07.022.

[127] L. Facchini, E. Magalini, P. Robotti, A. Molinari, S. Höges, K. Wissenbach, Ductility of a Ti-6Al-4V alloy produced by selective laser melting of prealloyed powders, Rapid Prototyp. J. 16 (2010) 450–459. https://doi.org/10.1108/13552541011083371.

[128] L.E. Murr, S.A. Quinones, S.M. Gaytan, M.I. Lopez, A. Rodela, E.Y. Martinez, D.H. Hernandez, E. Martinez, F. Medina, R.B. Wicker, Microstructure and mechanical behavior of Ti-6Al-4V produced by rapid-layer manufacturing, for biomedical applications, J. Mech. Behav. Biomed. Mater. 2 (2009) 20–32. https://doi.org/10.1016/j.jmbbm.2008.05.004.

[129] T. Vilaro, C. Colin, J.D. Bartout, As-fabricated and heat-treated microstructures of the Ti-6Al-4V alloy processed by selective laser melting, Metall. Mater. Trans. A Phys. Metall. Mater. Sci. 42 (2011) 3190–3199. https://doi.org/10.1007/s11661-011-0731-y.

[130] B. Vandenbroucke, J.P. Kruth, Selective laser melting of biocompatible metals for rapid manufacturing of medical parts, Rapid Prototyp. J. 13 (2007) 196–203. https://doi.org/10.1108/13552540710776142.

[131] A. Mertens, S. Reginster, H. Paydas, Q. Contrepois, T. Dormal, O. Lemaire, J. Lecomte-Beckers, Mechanical properties of alloy Ti-6Al-4V and of stainless steel 316L processed by selective laser melting: Influence of out-of-equilibrium microstructures, Powder Metall. 57 (2014) 184–189. https://doi.org/10.1179/1743290114Y.0000000092.

[132] D.A. Hollander, M. Von Walter, T. Wirtz, R. Sellei, B. Schmidt-Rohlfing, O. Paar, H.J. Erli, Structural, mechanical and in vitro characterization of individually structured Ti-6Al-4V produced by direct laser forming, Biomaterials. 27 (2006) 955–963. https://doi.org/10.1016/j.biomaterials.2005.07.041.

[133] C. Qiu, N.J.E. Adkins, M.M. Attallah, Microstructure and tensile properties of selectively laser-melted and of HIPed laser-melted Ti-6Al-4V, Mater. Sci. Eng. A. 578 (2013) 230–239. https://doi.org/10.1016/j.msea.2013.04.099.

[134] L. Thijs, M. Luz, M. Sistiaga, R. Wauthle, Q. Xie, J. Kruth, J. Van Humbeeck, Strong morphological and crystallographic texture and resulting yield strength anisotropy in selective laser melted tantalum, Acta Mater. 61 (2013) 4657–4668. https://doi.org/10.1016/j.actamat.2013.04.036.

[135] A. Gupta, C.J. Bennett, W. Sun, Fatigue response of selective laser melted Ti-6Al-4V bracket: an experimental study, Procedia Struct. Integr. 31 (2021) 15–21. https://doi.org/10.1016/j.prostr.2021.03.004.

[136] MMPDS-15, Metallic Materials Properties Development and Standardization, Federal Aviation Administration: Battelle Memorial Institute (2020).

[137] E. Wycisk, A. Solbach, S. Siddique, D. Herzog, F. Walther, C. Emmelmann, Effects of defects in laser additive manufactured Ti-6Al-4V on fatigue properties, Phys. Procedia. 56 (2014) 371–378. https://doi.org/10.1016/j.phpro.2014.08.120.

[138] S. Kikuchi, S. Heinz, D. Eifler, Y. Nakamura, A. Ueno, Evaluation of very high cycle fatigue properties of low temperature nitrided Ti-6Al-4V alloy using ultrasonic testing technology, Key Eng. Mater. 664 (2016) 118–127. https://doi.org/10.4028/www.scientific.net/KEM.664.118.

[139] K. Mertova, J. Dzugan and M. Roudnicka, Fatigue properties of SLM-produced Ti6Al4V with various post-processing processes, 5th International Conference - Recent Trends in Structural Materials, Materials Science and Engineering, 461 (2019) 012052, https://doi.org/10.1088/1757-899X/461/1/012052.

[140] P. Kumar, U. Ramamurty, High cycle fatigue in selective laser melted Ti-6Al-4V, Acta Mater. 194 (2020) 305–320. https://doi.org/10.1016/j.actamat.2020.05.041.

[141] J. Günther, D. Krewerth, T. Lippmann, S. Leuders, T. Tröster, A. Weidner, H. Biermann, Fatigue life of additively manufactured Ti–6Al–4V in the very high cycle fatigue regime, 94 (2017) 236–245. https://doi.org/10.1016/j.ijfatigue.2016.05.018.

[142] H. Soyama, Y. Okura, The use of various peening methods to improve the fatigue strength of titanium alloy Ti6Al4V manufactured by electron beam melting, AIMS Materials Science, 5 (2018) 1000–1015. https://doi.org/10.3934/matersci.2018.5.1000.

[143] Y. Zhai, H. Galarraga, D.A. Lados, Microstructure, static properties, and fatigue crack growth mechanisms in Ti-6Al-4V fabricated by additive manufacturing: LENS and EBM, Eng. Fail. Anal. 69 (2016) 3–14. https://doi.org/10.1016/j.engfailanal.2016.05.036.

[144] R. Pippan, A. Hohenwarter, Fatigue crack closure: a review of the physical phenomena, Fatigue Fract. Eng. Mater. Struct. 40 (2017) 471–495. https://doi.org/10.1111/ffe.12578.

[145] T.H. Becker, N.M. Dhansay, G.M.T. Haar, K. Vanmeensel, Near-threshold fatigue crack growth rates of laser powder bed fusion produced Ti-6Al-4V, Acta Materialia, 197 (2020) 269–282. https://doi.org/10.1016/j.actamat.2020.07.049.

[146] K.S. Ravichandran, A.K. Vasudevan, Fracture resistance of structural alloys, Fatigue and Fracture. 19 (2018) 381–392. https://doi.org/10.31399/asm.hb.v19.a0002379

[147] N. Macallister, K. Vanmeensel, T. Hermann, Fatigue crack growth parameters of Laser Powder Bed Fusion produced Linear elastic Fracture Mechanics, Int. J. Fatigue. 145 (2021) 106100. https://doi.org/10.1016/j.ijfatigue.2020.106100.

[148] R.K. Nalla, B.L. Boyce, J.P. Campbell, J.O. Peters, R.O. Ritchie, Influence of Microstructure on High-Cycle Fatigue of Ti-6Al-4V: Bimodal vs. Lamellar Structures, Metall. Mater. Trans. A Phys. Metall. Mater. Sci. 33 (2002) 899–918. https://doi.org/10.1007/s11661-002-1023-3.

[149] R.O. Ritchie, The conflicts between strength and toughness, Nat. Publ. Gr. 10 (2011) 817–822. https://doi.org/10.1038/nmat3115.

[150] H. Galarraga, R.J. Warren, D.A. Lados, R.R. Dehoff, M.M. Kirka, Fatigue crack growth mechanisms at the microstructure scale in as-fabricated and heat treated Ti-6Al-4V ELI manufactured by electron beam melting (EBM), Eng. Fract. Mech. 176 (2017) 263–280. https://doi.org/10.1016/j.engfracmech.2017.03.024.

[151] M. Seifi, M. Dahar, R. Aman, O. Harrysson, J. Beuth, J.J. Lewandowski, Evaluation of Orientation Dependence of Fracture Toughness and Fatigue Crack Propagation Behavior of As-Deposited ARCAM EBM Ti-6Al-4V, Jom. 67 (2015) 597–607. https://doi.org/10.1007/s11837-015-1298-7.

[152] A. Iliopoulos, R. Jones, J. Michopoulos, N. Phan, R. K. S. Raman, Crack Growth in a Range of Additively Manufactured, Aerospace 5, 118 (2018) 1–19. https://doi.org/10.3390/aerospace5040118.

[153] P. Edwards, M. Ramulu, Effect of build direction on the fracture toughness and fatigue crack growth in selective laser melted Ti-6Al-4 V, (2015) 1228–1236. https://doi.org/10.1111/ffe.12303.

[154] B. Van Hooreweder, D. Moens, R. Boonen, J.P. Kruth, P. Sas, Analysis of fracture toughness and crack propagation of Ti6Al4V produced by selective laser melting, Adv. Eng. Mater. 14 (2012) 92–97. https://doi.org/10.1002/adem.201100233.

[155] O. Sigmund, K. Maute, Topology optimization approaches A comparative review, (2013) 1031–1055. https://doi.org/10.1007/s00158-013-0978-6.

[156] J. Liu, A.T. Gaynor, S. Chen, Z. Kang, K. Suresh, A. Takezawa, L. Li, J. Kato, J. Tang, C.C.L. Wang, L. Cheng, X. Liang, A.C. To, Current and future trends in topology optimization for additive manufacturing, (2018) 2457–2483. https://doi.org/10.1007/s00158-018-1994-3

[157] B. Blakey-Milner, P. Gradl, G. Snedden, M. Brooks, J. Pitot, E. Lopez, M. Leary, F. Berto, A. du Plessis, Metal additive manufacturing in aerospace: A review, Mater. Des. 209 (2021) 110008. https://doi.org/10.1016/j.matdes.2021.110008.

[158] J. Kranz, D. Herzog, C. Emmelmann, Design guidelines for laser additive manufacturing of lightweight structures in TiAl6V4, J. Laser Appl. 27 (2015) S14001. https://doi.org/10.2351/1.4885235.

[159] C. Emmelmann, P. Sander, J. Kranz, E. Wycisk, Laser additive manufacturing and bionics: Redefining lightweight design, Phys. Procedia. 12 (2011) 364–368. https://doi.org/10.1016/j.phpro.2011.03.046.

[160] S. Donath, 3D printing a rocket engine (2019). https://www.etmmonline.com/3d-printing-a-rocket-engine-a-886960/.

[161] General Electric - Additive, LEAP engine Fuel nozzle, https://www.ge.com/additive/stories/new-manufacturing-milestone-30000-additive-fuel-nozzles (accessed Feb. 02, 2021).

[162] K.V. Fetisov, P V Maksimov, Topology optimization and laser additive manufacturing in design process of efficiency lightweight aerospace parts, IOP Conf. Series: Journal of Physics: Conf. Series 1015 (2018) 052006 doi:10.1088/1742-6596/1015/5/052006

[163] J. Plocher, A. Panesar, Review on design and structural optimisation in additive manufacturing : Towards next-generation lightweight structures, 183 (2019). https://doi.org/10.1016/j.matdes.2019.108164.

[164] Z. Xiao, Y. Yang, D. Wang, C. Song, Y. Bai, Structural optimization design for antenna bracket manufactured by selective laser melting, 3 (2018) 539–547. https://doi.org/10.1108/RPJ-05-2017-0084.

[165] M. Tomlin, J. Meyer, Topology Optimization of an additive layer manufactured (ALM) aerospace part, 7th Altair CAE Technol. Conf. 2011. (2011) 1–9.

[166] S.C. Altıparmak, B. Xiao, A market assessment of additive manufacturing potential for the aerospace industry, J. Manuf. Process. 68 (2021) 728–738. https://doi.org/10.1016/j.jmapro.2021.05.072.

[167] A. Dagkolu, I. Gokdag, O. Yilmaz, Design and additive manufacturing of a fatigue-critical aerospace part using topology optimization and L-PBF process, Procedia Manuf. 54 (2020) 238–243. https://doi.org/10.1016/j.promfg.2021.07.037.

[168] E. Brusa, R. Sesana, E. Ossola, Numerical modelling and testing of mechanical behavior of AM Titanium alloy bracket for aerospace applications, Procedia Struct. Integr. 5 (2017) 753–760. https://doi.org/10.1016/j.prostr.2017.07.166.

[169] S. Leuders, S. Meiners, L. Wu, A. Taube, T. Tröster, T. Niendorf, Structural components manufactured by Selective Laser Melting and Investment Casting—Impact of the process route on the damage mechanism under cyclic loading, J. Mater. Process. Technol. 248 (2017) 130–142. https://doi.org/10.1016/j.jmatprotec.2017.04.026.

[170] J. Mardaras, P. Emile, A. Santgerma, Airbus approach for F&DT stress justification of Additive Manufacturing parts, Procedia Struct. Integr. 7 (2017) 109–115. https://doi.org/10.1016/j.prostr.2017.11.067.

[171] F. Lasagni, J. Vilanova, A. Periñán, A. Zorrilla, S. Tudela, V. Gómez-Molinero, Getting confidence for flying additive manufactured hardware, Prog. Addit. Manuf. 1 (2016) 129–139. https://doi.org/10.1007/s40964-016-0014-7.

[172] S. Singamneni, Y. Lv, A. Hewitt, R. Chalk, W. Thomas, D. Jordison, Additive manufacturing for the aircraft industry : A Review, Journal of Aeronautics & Aerospace 8:1 (2019). https://doi.org/10.4172/2329-6542.1000214.

[173] Market Research Future, “Global Aerospace Additive Manufacturing Market Research Report–Forecast 2016-2021,” 2019. https://www.cagrmarketresearchfuture.com/reports/aerospace-additive-manufacturing-market-1551.

[174] Additive manufacturing - applications in aerospace, Aerospace Technical Institute, Insight 08 (2018). https://www.ati.org.uk/publications-tools/publications/

[175] Global Aerospace Materials Industry, A market report by the global industry analysts (2021) ID: 5797793. https://www.reportlinker.com/p05797793/Global-Aerospace-Materials-Industry.html?utm_source=GNW

[176] AIA additive manufacturing group, Recommended guidance for certification of AM components, Aerospace Industry Association (2020).

[177] Y.N. Hu, S.C. Wu, Z.K. Wu, X.L. Zhong, S. Ahmed, S. Karabal, X.H. Xiao, H.O. Zhang, P.J. Withers, A new approach to correlate the defect population with the fatigue life of selective laser melted Ti-6Al-4V alloy, Int. J. Fatigue. 136 (2020). https://doi.org/10.1016/j.ijfatigue.2020.105584.

[178] H. Wadell, Volume, Shape, and Roundness of Quartz Particles, J. Geol. 43 (1935) 250–280. https://doi.org/10.1086/624298.

[179] S.J. Blott, K. Pye, Particle shape : a review and new methods of characterization and classification, Sedimentology, (2007) 31–63. 143. https://doi.org/10.1111/j.1365-3091.2007.00892.x.

[180] M. Giuseppe, B. Raffaele, G. Fabio, D.B. Simone, Analysis and modelling of tensile and torsional behaviour at different strain rates of Ti6Al4V alloy additive manufactured by electron beam melting (EBM), Mater. Sci. Eng. A. 793 (2020). https://doi.org/10.1016/j.msea.2020.139916.

[181] C. De Formanoir, S. Michotte, O. Rigo, L. Germain, Materials Science & Engineering A Electron beam melted Ti – 6Al – 4V : Microstructure , texture and mechanical behavior of the as-built and heat-treated material, Mater. Sci. Eng. A. 652 (2016) 105–119. https://doi.org/10.1016/j.msea.2015.11.052.

[182] M. Galati, L. Iuliano, A literature review of powder-based electron beam melting focusing on numerical simulations, Addit. Manuf. 19 (2018) 1–20. https://doi.org/10.1016/j.addma.2017.11.001.

[183] L.C. Zhang, Y. Liu, S. Li, Y. Hao, Additive Manufacturing of Titanium Alloys by Electron Beam Melting: A Review, Adv. Eng. Mater. 20 (2018). https://doi.org/10.1002/adem.201700842.

[184] ASTM F2971-13, Standard Practice for Reporting Data for Test Specimens Prepared by Additive Manufacturing, ASTM International (2013) 1-4. https://doi.org/10.1520/F2971-13

[185] ISO/ASTM 52921-13, Standard Terminology for Additive Manufacturing - Coordinate Systems and Test Methodologies. ASTM International, (2019). 1–14. https://doi.org/10.1520/ISOASTM52921-13R19

[186] R.D.M. Nobre, D.L.R. Ju, Comparing Spherical and Irregularly Shaped Powders in Laser Powder Bed Fusion of Nb47Ti Alloy, 30 (2021) 6557–6567. https://doi.org/10.1007/s11665-021-05916-9.

[187] BS ISO 12106:2017, Metallic materials — Fatigue testing — Axial-strain controlled method, British Standard, BSI Standards Publication, ISBN 9780580902611 (2017).

[188] BS EN 6072: 2010, Aerospace series — Metallic materials — Test methods — Constant amplitude fatigue testing, British Standards Institution (2010).

[189] Endevco product catalogue (2019) http://endevco.com/contentStore/MktgContent/Endevco/uploads/2019/08/EDV-Catalog_Lowres.pdf

[190] H. Galarraga, D.A. Lados, R.R. Dehoff, M.M. Kirka, P. Nandwana, Effects of the microstructure and porosity on properties of Ti-6Al-4V ELI alloy fabricated by electron beam melting (EBM), Addit. Manuf. 10 (2016) 47–57. https://doi.org/10.1016/j.addma.2016.02.003.

[191] X. Shui, K. Yamanaka, M. Mori, Y. Nagata, K. Kurita, A. Chiba, Effects of post-processing on cyclic fatigue response of a titanium alloy additively manufactured by electron beam melting, Mater. Sci. Eng. A. 680 (2017) 239–248. https://doi.org/10.1016/j.msea.2016.10.059.

[192] A. Dehghan-Manshadi, M.H. Reid, R.J. Dippenaar, Effect of microstructural morphology on the mechanical properties of titanium alloys, J. Phys. Conf. Ser. 240 (2010).

https://doi.org/10.1088/1742-6596/240/1/012022.

[193] J. Xu, J. Zhu, J. Fan, Q. Zhou, Y. Peng, S. Guo, Microstructure and mechanical properties of Ti–6Al–4V alloy fabricated using electron beam freeform fabrication, Vacuum. 167 (2019) 364–373. https://doi.org/10.1016/j.vacuum.2019.06.030.

[194] C. Dharmendra, A. Hadadzadeh, B.S. Amirkhiz, A. Lloyd, M. Mohammadi, Deformation mechanisms and fracture of electron beam melted Ti–6Al–4V, Mater. Sci. Eng. A. 771 (2020) 138652. https://doi.org/10.1016/j.msea.2019.138652.

[195] Y. Kok, X.P. Tan, P. Wang, M.L.S. Nai, N.H. Loh, E. Liu, S.B. Tor, Anisotropy and heterogeneity of microstructure and mechanical properties in metal additive manufacturing: A critical review, Mater. Des. 139 (2018) 565–586. https://doi.org/10.1016/j.matdes.2017.11.021.

[196] M. Qian, W. Xu, M. Brandt, H.P. Tang, Additive manufacturing and postprocessing of Ti-6Al-4V for superior mechanical properties, MRS Bull. 41 (2016) 775–784. https://doi.org/10.1557/mrs.2016.215.

[197] X. Zhao, S. Li, M. Zhang, Y. Liu, T.B. Sercombe, S. Wang, Y. Hao, R. Yang, L.E. Murr, Comparison of the microstructures and mechanical properties of Ti-6Al-4V fabricated by selective laser melting and electron beam melting, Mater. Des. 95 (2016) 21–31. https://doi.org/10.1016/j.matdes.2015.12.135.

[198] J. Bao, S. Wu, P.J. Withers, Z. Wu, F. Li, Y. Fu, W. Sun, Defect evolution during high temperature tension-tension fatigue of SLM AlSi10Mg alloy by synchrotron tomography, Mater. Sci. Eng. A. 792 (2020). https://doi.org/10.1016/j.msea.2020.139809.

[199] S.C. Wu, T.Q. Xiao, P.J. Withers, The imaging of failure in structural materials by synchrotron radiation X-ray microtomography, Eng. Fract. Mech. 182 (2017) 127–156. https://doi.org/10.1016/j.engfracmech.2017.07.027.

[200] A.O. Abdalla, A. Amrin, S. Muhammad, Effect of heat treatment parameters on the microstructure and microhardness of Ti-6Al-4V alloy Effect of Heat treatment Parameters on The Microstructure and Microhardness of Ti-6Al-4V Alloy, AIP Conference Proceedings 1865, 030001 (2017). https://doi.org/10.1063/1.4993335.

[201] P. Li, W. Guo, W. Huang, Y. Su, X. Lin, K. Yuan, Thermomechanical response of 3D laser-deposited Ti – 6Al – 4V alloy over a wide range of strain rates and temperatures, Mater. Sci. Eng. A. 647 (2015) 34–42. https://doi.org/10.1016/j.msea.2015.08.043.

[202] O.L. Rodriguez, P.G. Allison, W.R. Whittington, H. El Kadiri, O.G. Rivera, M.E. Barkey, Strain rate effect on the tension and compression stress-state asymmetry for electron beam additive manufactured Ti6Al4V, Mater. Sci. Eng. A. 713 (2018) 125–133. https://doi.org/10.1016/j.msea.2017.12.062.

[203] L. Ladani, J. Razmi, S.F. Choudhury, Mechanical Anisotropy and Strain Rate Dependency Behavior of Ti6Al4V Produced Using E-Beam Additive Fabrication, 136 (2014) 1–7. https://doi.org/10.1115/1.4027729.

[204] W.S. Lee, C.F. Lin, High-temperature deformation behaviour of Ti6A14V alloy evaluated by high strain-rate compression tests, J. Mater. Process. Technol. 75 (1998) 127–136. https://doi.org/10.1016/S0924-0136(97)00302-6.

[205] R. Molaei, A. Fatemi, Fatigue Design with Additive Manufactured Metals: Issues to Consider and Perspective for Future Research, Procedia Eng. 213 (2018) 5–16. https://doi.org/10.1016/j.proeng.2018.02.002.

[206] S.C. Wu, C. Yu, P.S. Yu, J.Y. Buf, L. Helfen, Y.N. Fu, Corner fatigue cracking behavior of hybrid laser AA7020 welds by synchrotron X-ray computed microtomography, Mater. Sci. Eng. A. 651 (2016) 604–614. `
https://doi.org/10.1016/j.msea.2015.11.011.

[207] S.C. Wu, Z. Song, G.Z. Kang, Y.N. Hu, Y.N. Fu, The Kitagawa-Takahashi fatigue diagram to hybrid welded AA7050 joints via synchrotron X-ray tomography, Int. J. Fatigue. 125 (2019) 210–221. https://doi.org/10.1016/j.ijfatigue.2019.04.002.

[208] S. Suwas, R. K. Ray, Crystallographic texture of materials, Engineering materials and processes series, Springer London (2014). https://doi.org/10.1007/978-1-4471-6314-5.

[209] Y.N. Wang, J.C. Huang, Texture analysis in hexagonal materials, Mater. Chem. Phys. 81 (2003) 11–26.
https://doi.org/10.1016/S0254-0584(03)00168-8.

[210] K. Prasad, V. Kumar, Isothermal and thermomechanical fatigue behaviour of Ti – 6Al – 4V titanium alloy, Mater. Sci. Eng. A. 528 (2011) 6263–6270. https://doi.org/10.1016/j.msea.2011.04.085.

[211] A. Moridi, A.G. Demir, L. Caprio, A.J. Hart, B. Previtali, B.M. Colosimo, Deformation and failure mechanisms of Ti–6Al–4V as built by selective laser melting, Mater. Sci. Eng. A. 768 (2019). https://doi.org/10.1016/j.msea.2019.138456.

[212] Y. Yang, Y.J. liu, J. Chen, H.L. Wang, Z.Q. Zhang, Y.J. Lu, S.Q. Wu, J.X. Lin, Crystallographic features of α variants and β phase for Ti-6Al-4V alloy fabricated by selective laser melting, Mater. Sci. Eng. A. 707 (2017) 548–558.
https://doi.org/10.1016/j.msea.2017.09.068.

[213] H. Beladi, Q. Chao, G.S. Rohrer, Variant selection and intervariant crystallographic planes distribution in martensite in a Ti-6Al-4V alloy, Acta Mater. 80 (2014) 478–489. https://doi.org/10.1016/j.actamat.2014.06.064.

[214] D. Agius, K.I. Kourousis, C. Wallbrink, T. Song, Cyclic plasticity and microstructure of as-built SLM Ti-6Al-4V: The effect of build orientation, Mater. Sci. Eng. A. 701 (2017) 85–100. https://doi.org/10.1016/j.msea.2017.06.069.

[215] A. Gupta, W. Sun, C.J. Bennett, Simulation of fatigue small crack growth in additive manufactured Ti–6Al–4V material, Contin. Mech. Thermodyn. 32 (2020) 1745–1761. https://doi.org/10.1007/s00161-020-00878-0.

[216] B.E. Carroll, T.A. Palmer, A.M. Beese, Anisotropic tensile behavior of Ti-6Al-4V components fabricated with directed energy deposition additive manufacturing, Acta Mater. 87 (2015) 309–320.
https://doi.org/10.1016/j.actamat.2014.12.054.

[217] X.Y. Zhang, G. Fang, S. Leeflang, A.J. Böttger, A. A. Zadpoor, J. Zhou, Effect of subtransus heat treatment on the microstructure and mechanical properties of additively manufactured Ti-6Al-4V alloy, J. Alloys Compd. 735 (2018) 1562–1575.
https://doi.org/10.1016/j.jallcom.2017.11.263.

[218] A.M. Khorasani, I. Gibson, U.S. Awan, A. Ghaderi, The effect of SLM process parameters on density, hardness, tensile strength and surface quality of Ti-6Al-4V, Addit. Manuf. 25 (2019) 176–186.
https://doi.org/10.1016/j.addma.2018.09.002.

[219] S. Gao, T. He, Q. Li, Y. Sun, Y. Sang, Y. Wu, L. Ying, Anisotropic behavior and mechanical properties of Ti-6Al-4V alloy in high temperature deformation, J. Mater. Sci. 57 (2022) 651–670.
https://doi.org/10.1007/s10853-021-06569-8.

[220] W. Guo, S. Nemat-nasser, Flow stress of Nitronic-50 stainless steel over a wide range of strain rates and temperatures, 38 (2006) 1090–1103.
https://doi.org/10.1016/j.mechmat.2006.01.004.

[221] M. Stricker, D. Weygand, Dislocation multiplication mechanisms – Glissile junctions and their role on the plastic deformation at the microscale, Acta Mater. 99 (2015) 130–139. https://doi.org/10.1016/j.actamat.2015.07.073.

[222] S. Roy, A. Sarkar, S. Suwas, On characterization of deformation microstructure in Boron modified Ti-6Al-4V alloy, Mater. Sci. Eng. A. 528 (2010) 449–458. https://doi.org/10.1016/j.msea.2010.09.026.

[223] J.S. Jha, S. Dhala, S.P. Toppo, R. Singh, A. Tewari, S.K. Mishra, B. Jayabalan, Effect of strain amplitude on low cycle fatigue and microstructure evolution in Ti-6Al-4V: A TKD and TEM characterization, Mater. Charact. 155 (2019) 109829. https://doi.org/10.1016/j.matchar.2019.109829.

[224] T. Voisin, N.P. Calta, S.A. Khairallah, J. Forien, L. Balogh, R.W. Cunningham, A.D. Rollett, Y.M. Wang, Defects-dictated tensile properties of selective laser melted Ti-6Al-4V, Mater. Des. 158 (2018) 113–126. https://doi.org/10.1016/j.matdes.2018.08.004.

[225] R. Haynes, Effect of porosity content on tensile strength of porous materials, Powder Metall. 14 (27) (1971) 64–70. https://doi.org/10.1179/pom.1971.14.27.004

[226] S.J. Findlay, N.D. Harrison, Why aircraft fail, Mater. Today. 5 (2002) 18–25. https://doi.org/10.1016/S1369-7021(02)01138-0.

[227] R. Molaei, A. Fatemi, N. Sanaei, J. Pegues, N. Shamsaei, S. Shao, P. Li, D.H. Warner, N. Phan, Fatigue of additive manufactured Ti-6Al-4V , Part II : The relationship between microstructure , material cyclic properties , and component performance Theory of Critical Distance, 132 (2020). https://doi.org/10.1016/j.ijfatigue.2019.105363.

[228] S. Bressan, F. Ogawa, T. Itoh, F. Berto, Cyclic plastic behavior of additively manufactured Ti-6Al-4V under uniaxial and multiaxial non-proportional loading, Int. J. Fatigue. 126 (2019) 155–164. https://doi.org/10.1016/j.ijfatigue.2019.05.003.

[229] Y.M. Ren, X. Lin, P.F. Guo, H.O. Yang, H. Tan, J. Chen, J. Li, Y.Y. Zhang, Low cycle fatigue properties of Ti-6Al-4V alloy fabricated by high-power laser directed energy deposition : Experimental and prediction, 127 (2019) 58–73. https://doi.org/10.1016/j.ijfatigue.2019.05.035.

[230] D. Luquiau, X. Feaugas, M. Clavel, Cyclic softening of the Ti-10V-2Fe-3Al titanium alloy, Mater. Sci. Eng. A. 224 (1997) 146–156. https://doi.org/10.1016/s0921-5093(96)10531-1.

[231] J. Huang, Z. Wang, K. Xue, Cyclic deformation response and micro-mechanisms of Ti alloy Ti-5Al-5V-5Mo-3Cr-0.5Fe, Mater. Sci. Eng. A. 528 (2011) 8723–8732. https://doi.org/10.1016/j.msea.2011.08.045.

[232] F. Han, B. Tang, H. Kou, J. Li, Y. Deng, Y. Feng, Cyclic softening behavior of Ti–6Al–4V alloy at macro and micro-scale, Mater. Lett. 185 (2016) 115–118. https://doi.org/10.1016/j.matlet.2016.08.119.

[233] M. Simonelli, Y.Y. Tse, C. Tuck, On the texture formation of selective laser melted Ti-6Al-4V, Metall. Mater. Trans. A Phys. Metall. Mater. Sci. 45 (2014) 2863–2872. https://doi.org/10.1007/s11661-014-2218-0.

[234] J. Bao, Z. Wu, S. Wu, P.J. Withers, F. Li, S. Ahmed, A. Benaarbia, W. Sun, Hot dwell-fatigue behaviour of additively manufactured AlSi10Mg alloy : Relaxation , cyclic softening and fracture mechanisms, Int. J. Fatigue. 151 (2021) 106408. https://doi.org/10.1016/j.ijfatigue.2021.106408.

[235] M. Kamaya, Influence of bulk damage on crack initiation in low-cycle fatigue of 316 stainless steel, Fatigue Fract. Eng. Mater. Struct. 33 (2010) 94–104. https://doi.org/10.1111/j.1460-2695.2009.01420.x.

[236] A. Gupta, C.J. Bennett, W. Sun, The Role of Defects and Characterisation of Tensile Behaviour of EBM Additive Manufactured Ti-6Al-4V : An Experimental Study at Elevated Temperature, Eng. Fail. Anal. (2020) 105115. https://doi.org/10.1016/j.engfailanal.2020.105115.

[237] Z. Doubrovski, J.C. Verlinden, J.M.P. Geraedts, Optimal Design for Additive Manufacturing: Opportunities and Challenges, Proceedings of the ASME 2011 International Design Engineering Technical Conferences & Computers and Information in Engineering Conference/23rd International Conference on Design Theory and Methodology; 16th Design for Manufacturing and the Life Cycle Conference, 9 (2011) 635-646. https://doi.org/10.1115/DETC2011-48131

[238] European Union Aviation Safety Agency: Certification Specifications and Acceptable Means of Compliance for Engines CS-E, Amendment 5, (2018).

[239] P. Han, Additive design and manufacturing of jet engine parts, Engineering. 3 (2017) 648-652. https://doi.org/10.1016/J.ENG.2017.05.017

[240] Y. Murakami, Metal fatigue: effects of small defects and non-metallic inclusions. Academic Press, (2019).

[241] A. Soltani-Tehrani, R. Shrestha, N. Phan, M. Seifi, N. Shamsaei, Establishing specimen property to part performance relationships for laser beam powder bed fusion additive manufacturing, Int. J. Fatigue. 151 (2021) 106384. https://doi.org/10.1016/j.ijfatigue.2021.106384.

[242] R. Shrestha, N. Shamsaei, M. Seifi, N. Phan, An investigation into specimen property to part performance relationships for laser beam powder bed fusion additive manufacturing, Addit. Manuf. 29 (2019). https://doi.org/10.1016/j.addma.2019.100807.

[243] M. Gorelik, Additive manufacturing in the context of structural integrity, Int. J. Fatigue. 94 (2017) 168–177. https://doi.org/10.1016/j.ijfatigue.2016.07.005.

[244] B. Vayssette, N. Saintier, C. Brugger, M. El May, Surface roughness effect of SLM and EBM Ti-6Al-4V on multiaxial high cycle fatigue, Theor. Appl. Fract. Mech. 108 (2020) 102581. https://doi.org/10.1016/j.tafmec.2020.102581.

[245] M. Nakatani, H. Masuo, Y. Tanaka, Y. Murakami, Effect of Surface Roughness on Fatigue Strength of Ti-6Al-4V Alloy Manufactured by Additive Manufacturing, Procedia Struct. Integr. 19 (2019) 294–301. https://doi.org/10.1016/j.prostr.2019.12.032.

[246] V.D. Le, E. Pessard, F. Morel, S. Prigent, Fatigue behaviour of additively manufactured Ti-6Al-4V alloy: The role of defects on scatter and statistical size effect, Int. J. Fatigue. 140 (2020) 105811. https://doi.org/10.1016/j.ijfatigue.2020.105811.

[247] MIL-STD-1530C, Standard Practice Aircraft Structural Integrity Program (ASIP), US Department of Defence (2004) 7.

[248] N. Shamsaei, J. Simsiriwong, Fatigue behaviour of additively-manufactured metallic parts, Procedia Struct. Integr. 7 (2017) 3–10. https://doi.org/10.1016/j.prostr.2017.11.053.

[249] G.A. Longhitano, M.A. Larosa, A.L. Jardini, C.A. de C. Zavaglia, M.C.F. Ierardi, Correlation between microstructures and mechanical properties under tensile and compression tests of heat-treated Ti-6Al–4 V ELI alloy produced by additive manufacturing for biomedical applications, J. Mater. Process. Technol. 252 (2018) 202–210. https://doi.org/10.1016/j.jmatprotec.2017.09.022.

[250] T. Hermann, P. Kumar, U. Ramamurty, Fracture and fatigue in additively manufactured metals, Acta Mater. 219 (2021) 117240.

https://doi.org/10.1016/j.actamat.2021.117240.

[251] MIL-STD-810G, Test Method Standard - Environmental Engineering Considerations and Laboratory Tests, US Department of Defence, Method 514.6 Annex A, (2008) 514.6A-3 – 514.6A-5.

[252] M.D. Chapetti, Fatigue propagation threshold of short cracks under constant amplitude loading, Int. J. Fatigue. 25 (2003) 1319–1326. https://doi.org/10.1016/S0142-1123(03)00065-3.

[253] R. Jones, J.G. Michopoulos, A.P. Iliopoulos, R.K. Singh Raman, N. Phan, T. Nguyen, Representing crack growth in additively manufactured Ti-6Al-4V, Int. J. Fatigue. 116 (2018) 610–622. https://doi.org/10.1016/j.ijfatigue.2018.07.019.

[254] H. Gong, Effect of defects on fatigue tests of as-built TI-6AL-4V parts fabricated by selective laser melting, 23rd Annual International Solid Freeform Fabrication Symposium - An Additive Manufacturing Conference (2012) 499-506.

[255] K. Sadananda, A.K. Vasudevan, Fatigue crack growth behavior of titanium alloys, Int. J. Fatigue. 27 (2005) 1255–1266. https://doi.org/10.1016/j.ijfatigue.2005.07.001.

[256] Z. Zhan, H. Li, K. Y. Lam, Development of a novel fatigue damage model with AM effects for life prediction of commonly-used alloys in aerospace, International Journal of Mechanical Sciences 155 (2019) 110-124. https://doi.org/10.1016/j.ijmecsci.2019.02.032.

[257] F. Fomin, M. Horstmann, N. Huber, N. Kashaev, Probabilistic fatigue-life assessment model for laser-welded Ti-6Al-4V butt joints in the high-cycle fatigue regime, Int. J. Fatigue. 116 (2018) 22–35. https://doi.org/10.1016/j.ijfatigue.2018.06.012.

[258] U. Zerbst, M. Vormwald, R. Pippan, H.P. Gänser, C. Sarrazin-Baudoux, M. Madia, About the fatigue crack propagation threshold of metals as a design criterion - A review, Eng. Fract. Mech. 153 (2016) 190–243. https://doi.org/10.1016/j.engfracmech.2015.12.002.

[259] U. Zerbst, M. Madia, M. Vormwald, H.T. Beier, Fatigue strength and fracture mechanics – A general perspective, Eng. Fract. Mech. 198 (2018) 2–23. https://doi.org/10.1016/j.engfracmech.2017.04.030.

[260] H. Kitagawa, S. Takahashi, Applicability of fracture mechanics to very small cracks or the cracks in the early stage. Proceedings of the 2nd International Conference on Mechanical Behaviour of Materials, Boston, MA (1976) 627-631.

[261] Y. Zhai, D.A. Lados, E.J. Brown, G.N. Vigilante, Fatigue crack growth behavior and microstructural mechanisms in Ti-6Al-4V manufactured by laser engineered net shaping, Int. J. Fatigue. 93 (2016) 51–63. https://doi.org/10.1016/j.ijfatigue.2016.08.009.

[262] A.G. Gavras, D.A. Lados, J. Keith Donald, A unified method of design for fatigue crack growth resistance in structural materials, Int. J. Fatigue. 47 (2013) 58–70. https://doi.org/10.1016/j.ijfatigue.2012.07.009.

[263] S. Suresh, R.O. Ritchie, Propagation of short fatigue cracks, International Metal Reviews 29(1) (1984) 445-475. https://doi.org/10.1179/imtr.1984.29.1.445.

[264] W. Cui, A State-of-the art review on fatigue life prediction methods for metal structures, Journal of Marine Science and Technology 7(1) (2002) 43-56. https://doi-org.imeche.idm.oclc.org/10.1007/s007730200012.

[265] R.J.H. Wanhill, Chapter Two - Fatigue requirements for aircraft structures, in: Rhys Jones, Alan Baker, Neil Matthews, Victor Champagne(Eds.), Aircraft Sustainment and Repair, Butterworth-Heinemann, (2018) 17-40.

https://doi.org/10.1016/B978-0-08-100540-8.00002-9.

[266] A.K. Vasudevan, K. Sadananda, N. Iyyer, Fatigue damage analysis: Issues and challenges, Int. J. Fatigue. 82 (2016) 120–133. https://doi.org/10.1016/j.ijfatigue.2015.08.026.

[267] A.K. Vasudevan, K. Sadananda, G. Glinka, Critical parameters for fatigue damage, 23 (2001) 39–53. https://doi.org/10.1016/S0142-1123(01)00171-2.

[268] E. Wolf, The significance of fatigue crack closure, Damage Tolerance in Aircraft Structures , ASTM STP 486, American Society for Testing and Materials, (1971) 230-242. https://doi.org/10.1520/STP26680S.

[269] J.K Donald., G.H. Bray, R.W. Bush, An evaluation of the adjusted compliance ratio technique for determining the effective stress intensity factor. in: T.L. Panontin , S.D. Sheppard (Eds.), Fatigue and Fracture Mechanics: Twenty-Ninth volume, ASTM STP 1332, American Society for Testing and Materials, West Conshohocken, PA (1999).

[270] V. Sinha, C. Mercer, W.O. Soboyejo, An investigation of short and long fatigue crack growth behavior of Ti-6Al-4V, Mater. Sci. Eng. A. 287 (2000) 30–42. https://doi.org/10.1016/S0921-5093(00)00817-0.

[271] C. Gaëlle, S. Christine, L. Laurie, H. Zeline, Near-threshold fatigue propagation of physically short and long cracks in Titanium alloy, Procedia Struct. Integr. 2 (2016) 950–957. https://doi.org/10.1016/j.prostr.2016.06.122.

[272] L. Lawson, E.Y. Chen, M. Meshii, Near-threshold fatigue : a review, International Journal of Fatigue 21 (1999) 15–34. https://doi.org/10.1016/S0142-1123(99)00053-5.

[273] W. Zhang, Q. Wang, X. Li, J. He, A simple fatigue life prediction algorithm Using the Modified NASGRO Equation, Mathematical Problems in Engineering (2016) 1-8. https://doi.org/10.1128/JVI.05444-11.

[274] R. Jones, D. Peng, A. J. McMillan, Chapter Five - Crack growth from naturally occurring material discontinuities, in: Rhys Jones, Alan Baker, Neil Matthews, Victor Champagne(Eds.), Aircraft Sustainment and Repair, Butterworth-Heinemann (2018) 129-189. https://doi.org/10.1016/B978-0-08-100540-8.00005-4.

[275] Ansys - SMART Fracture white paper (2018). https://www.ansys.com/-/media/Ansys/corporate/resourcelibrary/whitepaper/smart-fracture.pdf

[276] ASTM F1472-14, Standard specification for wrought Titanium-6Aluminum-4Vanadium alloy for surgical implant applications (UNS R56400), ASTM International (2019). www.astm.org.

[277] ASTM E647-15, Standard test method for measurement of fatigue crack growth rates, ASTM International (2015). www.astm.org.

[278] J.J. Lewandowski, M. Seifi, Metal Additive Manufacturing: A Review of Mechanical Properties, Annual Review of Materials Research 46(1) (2016) 151-186. https://doi.org/10.1146/annurev-matsci-070115-032024.

-----x x x x x x-----